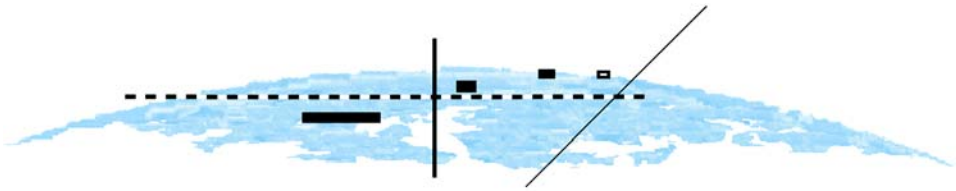

GeoForschungsZentrum Potsdam

STIFTUNG DES ÖFFENTLICHEN RECHTS

Scientific Technical Report

ISSN 1610-0956

GFZ

POTSDAM
Helmholtz-Zentrum

David Mozzoni

The Changing Geomagnetic Field from the Ionosphere to the Core-Mantle Boundary

Scientific Technical Report STR08/02

DOI: 10.2312/GFZ.b103-08029

Dissertation Advisory Committee

Director: Dr. David Van Winkle
Co-Director: Dr. Joseph Cain
Committee Member: Dr. Bernd Berg
Committee Member: Dr. Mark Riley
Outside Committee Member: Dr. Philip Cunningham

GFZ Supervisor: Prof. Dr. Mioara Mandea

Imprint
GeoForschungsZentrum Potsdam
a Helmholtz Centre
Telegrafenberg
D-14473 Potsdam

e-mail: postmaster@gfz-potsdam.de
www: http://www.gfz-potsdam.de

Printed in Potsdam, Germany
January 2008

ISSN 1610-0956

This text is available in electronic form:
http://www.gfz-potsdam.de/bib/zbstr.htm

DOI: 10.2312/GFZ.b103-08029

David Mozzoni

The Changing Geomagnetic Field from the Ionosphere to the Core-Mantle Boundary

Dissertation submitted to the
Department of Physics, Florida State University,
in partial fulfillment of the requirements for the degree of
Doctor of Philosophy
2007

Defense: 9 November 2007

Scientific Technical Report STR08/02

DOI: 10.2312/GFZ.b103-08029

THE FLORIDA STATE UNIVERSITY

COLLEGE OF ARTS AND SCIENCES

THE CHANGING GEOMAGNETIC FIELD FROM THE IONOSPHERE TO THE CORE-MANTLE BOUNDARY

By

DAVID T. MOZZONI

A Dissertation submitted to the
Department of Physics
in partial fulfillment of the
requirements for the degree of
Doctor of Philosophy

Degree Awarded:
Fall Semester, 2007

DOI: 10.2312/GFZ.b103-08029

The members of the Committee approve the Dissertation of David T. Mozzoni defended on November 9, 2007.

David Van Winkle
Professor Directing Dissertation

Philip Cunningham
Outside Committee Member

Bernd Berg
Committee Member

Joseph Cain
Committee Member

Mark Riley
Committee Member

The Office of Graduate Studies has verified and approved the above named committee members.

DOI: 10.2312/GFZ.b103-08029

This thesis is dedicated to my family and friends for their unwavering support over these many long years.

DOI: 10.2312/GFZ.b103-08029

ACKNOWLEDGEMENTS

I would like to thank members of the High Altitude Observatory, including Drs. Richmond, Maute, and Foster, for access to and instruction in the use of the TIE–GCM and its associated programs, while hosting me for seven months in Boulder. I would also like to thank Dr. Mandea for her guidance and support, while providing me with a student position at the GeoForschungsZentrum Potsdam in Section 2.3 (Earth's Magnetic Field), where I also had many fruitful discussions with other group members. I would like to thank members of the Geophysical Fluid Dynamics Institute for access to their administrative and computational resources, which were instrumental throughout nearly every aspect of this research. Many thanks go to Dr. Cain for his guidance and help as a mentor and friend (treating me as member of his family), beginning from my early days as an undergraduate student and continuing right through to the present day.

This research was partially supported by the FSU School for Computational Science and Information Technology (CSIT), by a grant of resources on the IBM pSeries 690 Power4-based supercomputer "Eclipse". This research was also supported, in part, by the NASA Fellowship Grant: NGT5-30454.

DOI: 10.2312/GFZ.b103-08029

TABLE OF CONTENTS

DOI: 10.2312/GFZ.b103-08029

DOI: 10.2312/GFZ.b103-08029

LIST OF TABLES

DOI: 10.2312/GFZ.b103-08029

DOI: 10.2312/GFZ.b103-08029

LIST OF FIGURES

DOI: 10.2312/GFZ.b103-08029

DOI: 10.2312/GFZ.b103-08029

DOI: 10.2312/GFZ.b103-08029

DOI: 10.2312/GFZ.b103-08029

ABSTRACT

In this study two aspects of the geomagnetic field have been investigated. The first part focuses on perturbations of the external field, as seen by the CHAMP satellite and predicted by the Thermosphere-Ionosphere Electrodynamic General Circulation Model, for the purpose of helping to separate out ionospheric sources from the ambient geomagnetic field using a physics based approach. Part two looks at variations of the internal field through an examination of the South Atlantic Anomaly.

The NCAR Thermosphere-Ionosphere Electrodynamic General Circulation Model (TIE–GCM) is a self-consistent, global, atmospheric model that can be used to estimate magnetic perturbations at satellite altitude. These computed perturbations can then be compared with the magnetic vector data provided by low-earth orbiting satellites. Analogous CHAMP magnetic vector residuals were computed for these intervals using the CHAOS model to remove the core and crustal geomagnetic contributions. Under various input parameters, the TIE–GCM predictions were compared with the CHAMP residuals on an orbit by orbit basis demonstrating a reasonable agreement between the TIE–GCM estimates and the CHAMP residuals in non-polar, dayside regions ($\pm 50^\circ$ magnetic latitude). Although no clear component or temporal correlation was discerned, evidence showing overall residual decrease in the comparisons presents the possibility of using the TIE–GCM to preprocess geomagnetic data for main field modeling purposes. A group of spherical harmonic field test models, developed utilizing this correction, verify the feasibility of this application.

Variations of the internal field are investigated through study of the South Atlantic Anomaly, a region of low geomagnetic field measured at the Earth's surface. The time evolution of this feature is tracked at the surface over the last 400 years. Subsequently, its associations with the axial dipole moment and radial geomagnetic flux are examined at the core-mantle boundary, revealing in the process, a possible link between total unsigned flux and geomagnetic jerks.

DOI: 10.2312/GFZ.b103-08029

CHAPTER 1

Introduction & Background

1.1 Introduction

Apart from the Earth's roundness, geomagnetism was the first property to be attributed to the body of the Earth as a whole, a full 87 years before Isaac Newton introduced gravitation in his *Principia* [1]. Despite this early realization, Albert Einstein (nearly 300 years later) still ranked the problem of explaining the origin of the Earth's magnetic field as among the most important unsolved problems in physics [1][1]. While the solution to this problem has proved quite elusive, strides have been made [2, 3, 4] and today we know that when either a magnetic observatory or a satellite takes a geomagnetic field measurement, it represents the superposition of many sources. The largest contribution arises from the approximately dipolar main (or core) field being generated by geodynamic processes within the fluid, iron-rich, outer core of the Earth. However, depending upon the altitude and location of the reading, it may contain sizable contributions from the static lithospheric field, originating largely from rock and remnant magnetism within the Earth's crust. Yet another significant portion comes from external field sources, which are produced in the ionosphere and magnetosphere. These variable sources include the daily solar quiet (Sq) and ring current variations, the contributions from the Disturbance Storm Time (D_{st}) deviations, and the many other current systems present in the geospace region (e.g., the field-aligned currents and the auroral and equatorial electro-jets). Sporadic magnetic storms and pulses, which have short-term effects, also play a role in the measured magnetic field values. Currents induced in the solid Earth by these external fields must also be considered. In satellite data it is even possible to resolve small signals attributable to the electrical currents generated by ocean flow [5]. Most of these field sources undergo temporal variations, both periodic and non-periodic, ranging from the secular variation of the main field on decadal scales down to the sub-second variations during geomagnetic storms in

[1] A secondary source.

DOI: 10.2312/GFZ.b103-08029

the magnetosphere. Understanding and interpreting these magnetic field contributions and their origins is a major task; however, significant progress has recently been achieved using a combination of ground and satellite based data.

The present study is an effort to better understand the external sources of the geomagnetic field by first evaluating the prospect of comparing a physics-based atmospheric model derived using limited direct observational input with that of actual, observed, geomagnetic data. In particular, it is the characterization of the ionospheric component of the ambient field under varying conditions, which will be the main focus. Another aim is to see if this comparison may help with the development of future geomagnetic models. For this I have used the Thermosphere-Ionosphere Electrodynamics General Circulation Model (TIE–GCM) [6], developed at the National Center for Atmospheric Research (NCAR) in Boulder, Colorado. This model can be used to predict many different atmospheric quantities, such as wind velocities, various atmospheric species concentrations, temperatures, electric fields, and current densities. The current densities can later be post-processed to compute magnetic perturbations both above and below the ionosphere.

In order to validate these model results, comparisons of the predicted perturbations calculated at the average altitude of the CHAMP satellite (for this study taken to be 430 km) with vector residuals computed from the difference in the CHAMP data and the CHAOS geomagnetic model [7] were studied. The quietest day of each month from 2001–2005 according to the list of international Q–days, was selected. New residuals were then computed between the original CHAMP and CHAOS data residuals and estimates from the different TIE–GCM model runs for these quiet days. It is shown that the TIE–GCM model can, to some degree, reproduce the residuals computed from CHAMP geomagnetic vector data, and that it should be possible to use the TIE–GCM to preprocess dayside satellite data in order to supplement geomagnetic modeling efforts, especially when there is a scarcity of quality data. In order to verify this claim, a series of basic spherical harmonic models were developed incorporating either TIE–GCM corrected or uncorrected dayside data during a two month span in 2004. The results of this analysis indicate that this correction procedure does provide a tangible improvement to data residuals in the equatorial region.

While the first half of this study examines external field sources, the second part looks more closely at internal variations of the geomagnetic field. Specifically, the South Atlantic Anomaly (SAA) is examined and its location on the surface is tracked over the past 400 years using the gufm1 model [8]. Also, changes associated with the SAA are examined at the core-mantle boundary through investigation of the change in the axial dipole moment and total unsigned magnetic flux

DOI: 10.2312/GFZ.b103-08029

(with a possible link found with geomagnetic jerks).

Accurately measuring the geomagnetic field is one of the few ways in which to remotely probe properties of the Earth's core, mantle, crust and atmosphere. Because the core field must diffuse through Earth's mantle, the geomagnetic field yields information both on the region of its generation in the outer core and on the electrical conductivity of the mantle [9]. The lithospheric field emanating from the crust can provide geological structure, composition and dynamics information, while similarly, the structure, composition and dynamics of the atmosphere can also be studied, in part, through external geomagnetic field measurements. Because of this, the Earth's magnetic field is an important subject to study and understand, since it touches in some manner many other disciplines (especially, but not limited to the Earth sciences). The geomagnetic field gives information about various aspects of the development of the Earth itself, its geology, and its atmosphere. Similarly it can provide insights into the workings and histories of other planetary bodies.

From the perspective of everyday life, the geomagnetic field acts as a magnetic shield protecting the Earth from the cosmic and solar winds (and the worst of their accompanying radiation), while controlling the energy-momentum transfer (having near-Earth effects like inducing surges in long power lines and, more generally, positioning the auroral zone) into the Earth system. Biologically speaking, this shelter may have played a role in the evolution of life itself on Earth. Even today, the migratory patterns of many biological creatures are guided by the influence of the geomagnetic field [10]. Humans alike rely upon it for the important role it plays in navigation, both past and present (e.g. aircraft today rely upon magnetic field maps in their navigation systems, as do ocean-going ships, and even hikers). Therefore, knowledge of the geomagnetic field is vital for forecasting the effects of space weather phenomena on spacecraft as well as on ground based infrastructure (e.g. pipelines and the power grid).

1.2 Background

The vector geomagnetic field $\mathbf{B}$ can be described by its strength in particular directions (northwards ($X = -B_\theta$), eastwards ($Y = B_\phi$) and radially inwards ($Z = -B_r$)), or by the angle between its orientation in the horizontal plane and the northward direction (declination D), the angle between its orientation and the horizontal plane at Earth's surface (inclination I), and the total intensity of the field ($F = |\mathbf{B}| = \sqrt{X^2 + Y^2 + Z^2}$). Examples are shown in Fig. 1.1 of both the Z and F components of the geomagnetic field. However, taken together the full geomagnetic field has

DOI: 10.2312/GFZ.b103-08029

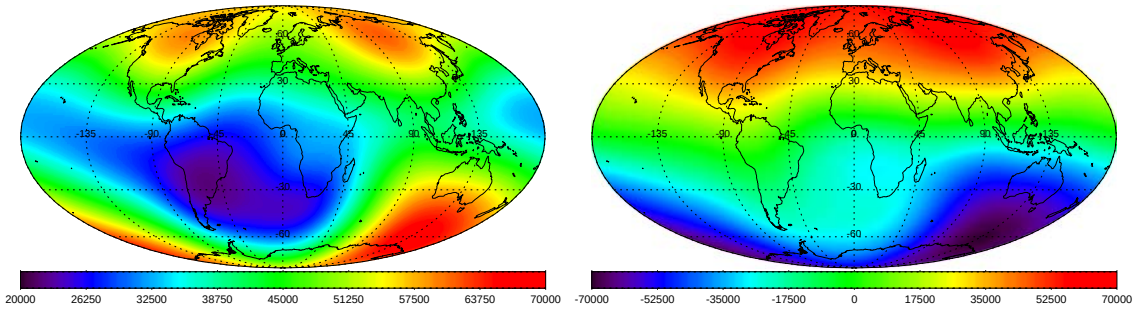

Figure 1.1: A plot of the geomagnetic field using the CHAOS model for the year 2005 at the Earth's surface: total field (left) and vertical component (right). Note the different scales for each plot. The large low over the south Atlantic visible in the total field is known as the South Atlantic Anomaly (SAA) and is discussed later in Sec. 3.1.

a 3-D structure (Fig. 1.2) that fully envelops the entire globe and is composed of a very complex superposition of disparate magnetic field sources. These sources (see Sec. 1.5) include both the static lithospheric field and the strong, slowly morphing core field. Also contributing are the external sources, which can range from the smoothly regular, daily periodic variations to the frenetically varying transient external fields. Moreover, when coupled with other sources, these can induce secondary fields like those caused by the ocean tides. The geomagnetic field extends outward from the Earth, in the form of the magnetosphere, taking a general shape reminiscent of a comet: compressed on the dayside (sunward) by the solar wind (10–12 R_E) and tapering off on the nightside (anti-sunward) for over 200 R_E. The direct and indirect study of these fields has had a long and diverse history from its infancy in oceanic navigation during the age of exploration to the current set of space-based satellites (POGO [11], Magsat [12], Ørsted [13], CHAMP [14], SAC-C [15], etc) used to make global models (which have been further extended to other planetary bodies like Mars [16]).

1.3 Historical Context

The natural ability of lodestone to attract bits of iron introduced the ancients to the magnetic force. This property may have been recognized as early as 4000 years ago in China, and was familiar shortly thereafter to the Greeks and Romans having been mentioned by Homer [17]. Although the first known observations concerning magnets were made by the Greek philosopher Thales in the sixth century B.C. [1].

DOI: 10.2312/GFZ.b103-08029

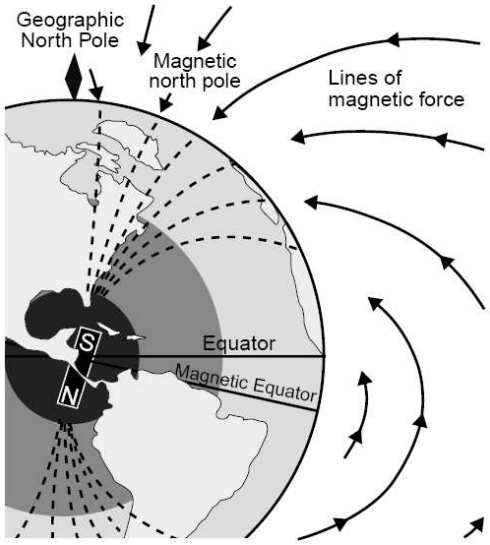

Figure 1.2: A rough sketch of geomagnetic field lines, which highlight the displacement of the magnetic poles from the true poles, also known as declination [10].

The earliest form of the compass was introduced by the Chinese in at least the first century A.D., and perhaps as early as the second century B.C. [1]. Although, recognition that the magnetic force could be harnessed, by means of the compass needle, to aid in the determination of north and south for purposes of navigation, was first reliably noted by the Chinese encyclopedist Shen-Kau around 1088 when he wrote "fortune-tellers rub the point of a needle with the stone of the magnet in order to make it properly indicate the south" [18] in his *Meng Ch'i Pi T'an* (Dream Pool Essays). Similarly, the monk Alexander Neckam in his works *De naturis rerum* and *De utensilibus*, around 1190, described how the use of a pivoted-needle compass (and its application for maritime navigation) was already in common usage in Europe by the twelfth century [1, 18].

Declination, the difference between magnetic north, given by the compass needle, and true north (Fig. 1.2), was known in Europe by the middle of the 15^{th} century, but the earliest precise recording of this value dates to 1510 when Georg Hartmann determined the value in Rome to be 6° E [18, 1]. However, knowledge of declination and its measurement can be traced as far back as 720 A.D. in China by the Buddhist astronomer Yi-Xing [19, 1]. Inclination, the local angle between the horizontal and the direction of the magnetic force (also called dip angle), was discovered by Hartmann in 1544, but his discovery was evidently lost to science. Luckily, Robert Norman independently rediscovered this property of the compass again not long thereafter in 1576

DOI: 10.2312/GFZ.b103-08029

[1].

Through experiments using a terrella (magnetized sphere made of lodestone) and a pivoted needle, the English physician and natural philosopher William Gilbert, building on the ever accumulating knowledge concerning the workings of the compass (especially inclination) and the earlier work of Petrus Peregrinus (his 1269 experimental discourse *Epistola de magnete* discusses the nature of a spherical lodestone [20]) and others, came to the realization that "magnus magnes ipse est globus terrestris" (the Earth globe itself is a great magnet) [1]. Gilbert used this revelation to describe the previously known but unexplained properties of the compass: declination and inclination [21]. So his treatise *De Magnete* published in 1600 [22] introduced this novel concept and established geomagnetism as a meaningful field of science worthy of the deep, rigorous study that continues to this day.

Nearly a century later, Edmond Halley conducted the first magnetic survey between 1698–1700, which charted the declination in the Atlantic Ocean. The variations of the geomagnetic field, as seen at the surface, have been studied as far back as the 18^{th} century, but it was the discovery of diurnal variations that prompted Coulomb to develop his highly sensitive torsion balance in 1777 in order to measure the detailed aspects of these variations. While investigating electric batteries in 1820, Ørsted discovered that electric currents can produce magnetism, and Ampère later that same year used this discovery to explain magnetism in terms of forces between electric currents. A few years later in 1828, Gauss developed a method to measure magnetic intensity and subsequently devised an application of spherical harmonic analysis to study the scalar magnetic potential. His studies were the first to show that the Earth's magnetic field could be described as the gradient of a scalar potential

$$\mathbf{B} = -\nabla\Phi = -\nabla\left(\Phi^i + \Phi^e\right), \tag{1.1}$$

where Φ^i and Φ^e denote the scalar potential due to internal and external sources, respectively. From this he was able to demonstrate that nearly 99% of the field (measured at the Earth's surface) originates from within the Earth. However, it was Faraday who went on to discern magnetic induction and formulate a dynamo theory that attempts to describe the source of this internal field [23, 24].

1.4 Observing the Geomagnetic Field

The Earth's magnetic field can be measured in a number of ways, each having its own set of advantages and disadvantages. For instance, magnetic observatories can provide a very long-term

DOI: 10.2312/GFZ.b103-08029

(nearly 2 centuries in some cases), systematic, stationary time-series with high resolution, ideal for certain secular variation studies (time evolution of the field), however their spatial distribution is less than ideal [25]. Aeromagnetic surveys can provide snapshots of high resolution magnetic anomaly maps, but only for relativity small localized areas. Indirect observations of the Earth's magnetic field prior to the 17^{th} century are possible today by sampling archaeological and paleomagnetic remains. However, these studies rely on indirect measurements of magnetic sediments (e.g., lake sediments or lava flows) and artifact samples, which can be difficult to reliably acquire and process, but allow models like CALS7K.2 [26] to give insights into the distant past of the geomagnetic field. Ship-track data (mainly declination and inclination) over the past 400 years has been able to provide information in remote, under sampled areas of the ocean and has been used to good effect in the gufm1 model [8, 27]. Satellites are the best means of acquiring data on global scales, however, they suffer from relatively poor surface level resolutions and have only modest operational lifetimes. Mandea (2006) [28] offers a good summary outlining many of the satellite missions that have and are currently being used in the field of geomagnetic research as well as highlighting some of the resulting science.

1.4.1 Magnetic Observatories

Magnetic observatories are a network of globally distributed facilities for accurately and continuously monitoring the geomagnetic field at stationary locations (often with time resolutions of one minute or less). The earliest dedicated magnetic observatories date back to the 1840's. From these measurements, hourly, monthly and annual means are often computed. As is evident in Figs. 1.3 and 1.9, they can provide long time-series field data that are well suited for high resolution secular variation studies. Many of the better magnetic observatories, which maintain a higher-level standard for data measurement and distribution, collectively form the INTERMAGNET [29] network of observatories. For global magnetic field modeling, one problem with geomagnetic observatories is that their global coverage can be uneven, as Fig. 1.4 readily demonstrates. A high concentration exists in Europe and North America, but a dearth in the southern hemisphere and oceans. A novel new approach to partially combat this shortcoming is to introduce the notion of a virtual observatory by means of carefully reducing the global satellite data in order to extract monthly mean values analogous to those from stationary observatories [30].

DOI: 10.2312/GFZ.b103-08029

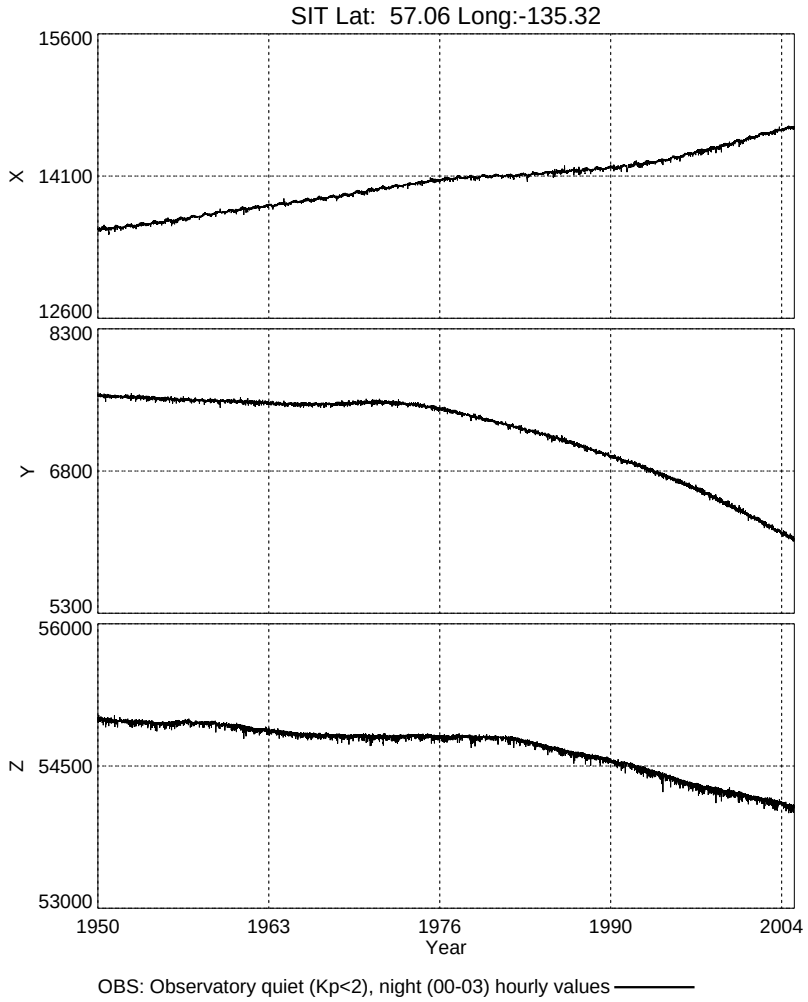

Figure 1.3: The quiet night-time geomagnetic X, Y, and Z field components in units of nT from the Sitka, Alaska (SIT) Geomagnetic Observatory, part of INTERMAGNET, from 1950–2004. Notice how the magnetic field varies over time, known as secular variation, despite being a stationary observatory.

1.4.2 Satellite

Early Satellite Missions

The early satellite missions that had a focus on measuring the magnetic field, like the Polar Orbiting Geophysical Observatory (POGO) series, recorded only scalar field values [11, 31]. But in October of 1979, NASA launched its "Magnetic Field Satellite" (Magsat) [12] which was the first spacecraft to supply precise, global vector magnetic field measurements of near-Earth space. It flew in a near polar orbit at an altitude of 300–550 km with an inclination of 96.8°, basically fixing it

DOI: 10.2312/GFZ.b103-08029

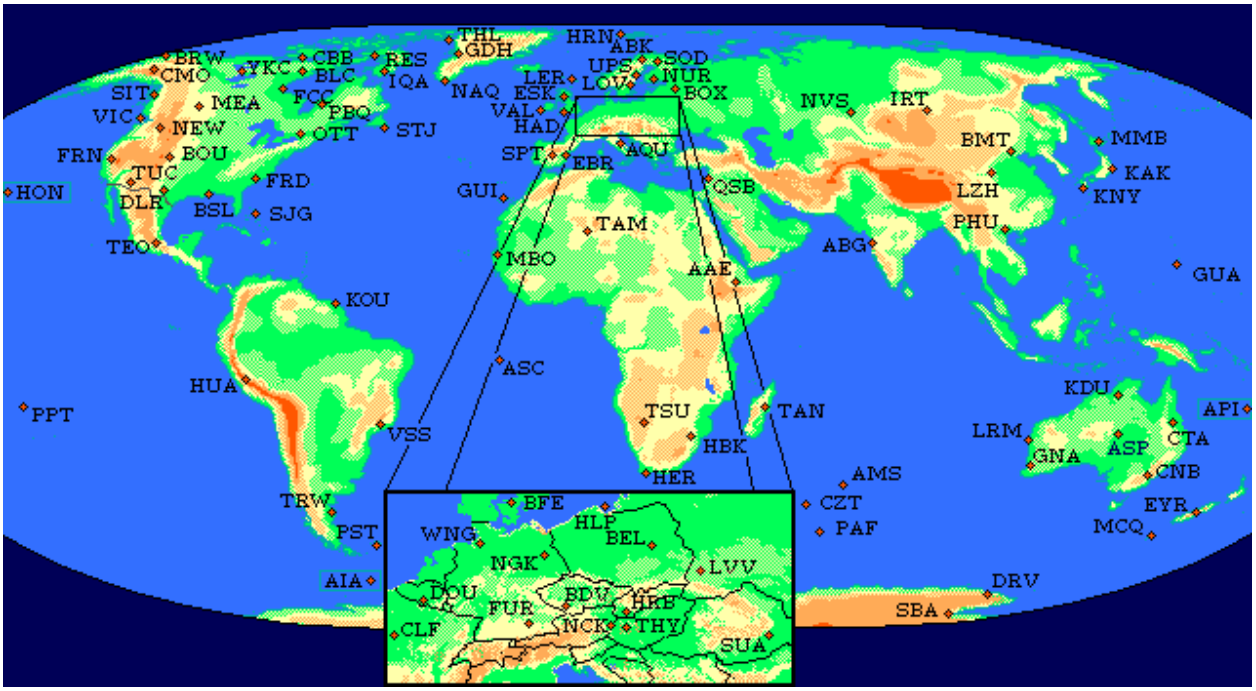

Figure 1.4: A global distribution map of the INTERMAGNET observatories, highlighting their uneven spacial distribution. Figure taken from INTERMAGNET website [29].

into a dawn/dusk local time plane (6/18 LT). Having already a rather brief lifespan, the mission survived only from October of 1979 through June of 1980, the data availability was further limited to just November–April. It carried both a scalar (cesium vapor) and vector (tri-axial fluxgate) magnetometer on the end of a 6 m long boom (to minimize interference from the main body). The data has been used to produce global spherical harmonic models of the internal main field, and has proved useful in understanding the ionospheric magnetic field, and the meridional current systems.

Ørsted and SAC-C

The acquisition of measurements of the near-Earth magnetic vector field, analogous to those of Magsat, were not revisited until some 20 years later, with the launching of the Ørsted satellite mission [13] operated by the Danish Space Institute in February of 1999, thus ushering in a resurgence of magnetic field modeling research. The spacecraft has an elliptical polar orbit, ranging in altitude from 650–860 km with an inclination of 96.5°. Unlike Magsat, Ørsted samples all local times with a 470-day period. Measurements are made using a compact spherical coil (CSC) fluxgate vector magnetometer and an Overhauser scalar magnetometer, both of which are mounted on an

DOI: 10.2312/GFZ.b103-08029

8 m boom pointing away from the Earth. A year later, the Argentinian SAC-C mission (primarily a biosphere/vegetation monitoring satellite) launched with a similar experimental package to that of Ørsted's (referred to as Ørsted 2), however it returns only scalar data due to problems with its star camera. With the introduction of this data, new satellite-based, global secular variation studies could be performed comparing with the earlier Magsat results. In addition, because of the quality of data, newer higher resolution models were developed like OIFM [32] and OSVM [33].

CHAMP

The Challenging Minisatellite Payload (CHAMP) is a low-earth orbiting German satellite [14, 34]. Since its launch on July 15, 2000, this multi-mission satellite has supplied invaluable, high precision, magnetic, gravity, and ion drift measurements. It has two magnetic fluxgate sensors mounted together with star cameras on a common optical bench (about 2 meters away from the main spacecraft body), which provides the necessary mechanical stability required between these systems. A scalar Overhauser Magnetometer, located at the end of a 4-meter boom, enables an absolute in-flight calibration capability for the vector magnetic field measurements.

The more than six years worth of CHAMP geomagnetic field measurements, coupled with the other orbiting missions, have paved the way for the development of global magnetic field models with unprecedented resolutions of the core, its secular variation and the lithosphere. Recent examples would include internal field models like CHAOS [7] and POMME [35], and static lithospheric field models such as MF4 [36] and MF5 [37].

Although for this work only the magnetic field data is directly used, it is worth briefly describing the rest of the main instruments because they all work in concert together in an integrated fashion. The satellite itself, despite its name, is quite large with the following instrument payload (see Fig. 1.5 for layout) and physical parameters, which are listed and condensed from the CHAMP GFZ website [34].

- CHAMP physical parameters

Total Mass:	522 kg (with 20 kg Boom)
Height:	750 mm (with 224 mm Boom)
Length	8333 mm (with 4044 mm Boom)
Width:	1621 m (with 224 mm Boom)

- Electrostatic STAR Accelerometer

  The STAR accelerometer measures the non-gravitational accelerations of the spacecraft

DOI: 10.2312/GFZ.b103-08029

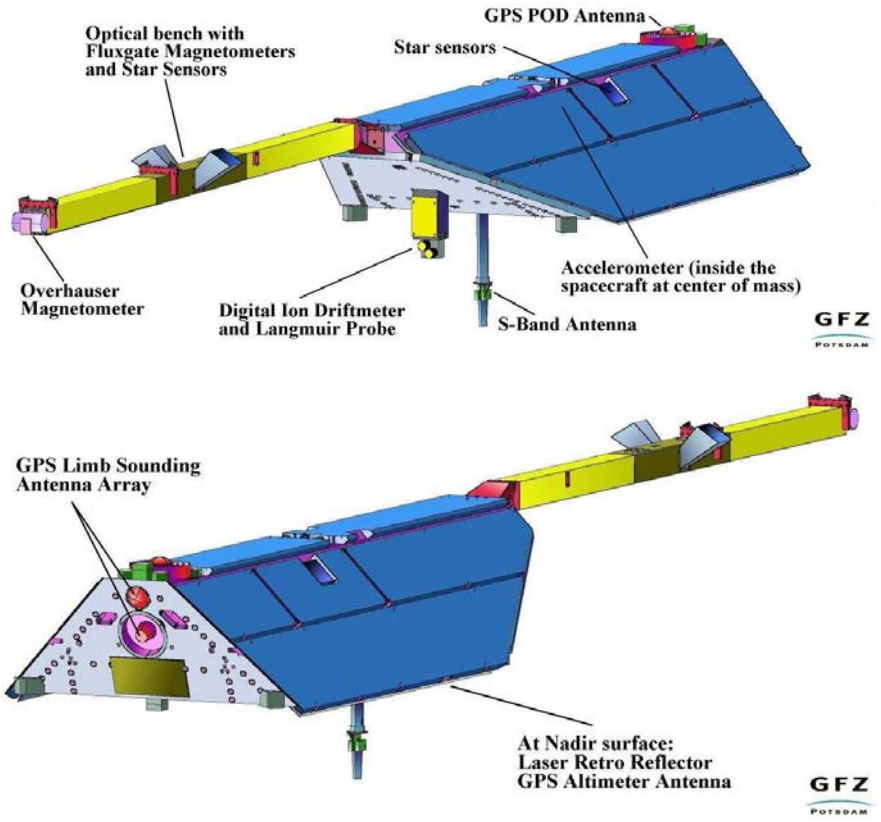

Figure 1.5: Diagram of the CHAMP satellite with locations for the main instrument packages, from the CHAMP GFZ Website [34].

caused by, for example, air drag and solar radiation. At the heart of the sensor is a micro-accelerometer which regulates the power required to keep a proof-mass electrostatically suspended inside a cavity. It does this by having embedded servo-loops and electrodes along the cavity's three-axes, which both generate an electrostatic force and give capacitive sensing of the proof-mass. Applying the correct pattern of voltage over the loops, translationally and rotationally controls the proof-mass and keeps it motionless in the center of the cage.

The detected acceleration is proportional to these required forces and supports the recovery of the orbit from GPS data (from which it is possible to estimate the gravity field). The accelerometer sensor is located precisely at the center of gravity in order to minimize the influence of measurement disturbances due to rotational accelerations and gravity gradients. The STAR accelerometer sensor is provided by the Centre National d'Etudes Spatiales (CNES) and was manufactured by the Office National d'Etudes et de Recherches Aerospatials

DOI: 10.2312/GFZ.b103-08029

(ONERA).

- GPS Receiver TRSR-2

  The Global Positioning System (GPS) Receiver TRSR-2 onboard CHAMP is a fully autonomous sixteen-channel GPS receiver provided by NASA and manufactured at NASA's Jet Propulsion Laboratory (JPL). Coupled with the STAR accelerometer, it serves as the main tool for the high-precision orbit determination of the CHAMP satellite. It works by establishing a high-low satellite-to-satellite (SST) link whereby the higher orbiting GPS satellites transmit a pseudorandom number modulated L1 and L2 signal, which is received (maximum of 12 simultaneous satellites) by the TRSR-2 receiver onboard CHAMP. From these signals the orbiting receiver generates pseudo-ranges and carrier phases for all satellites which were in lock. By using pseudo-ranges from at least 4 different GPS satellites with known ephemeris, a navigation solution for CHAMP can be determined for both the three-dimensional coordinates and the rate of change.

  Additional features are implemented for atmospheric limb sounding and the experimental use of specular reflections of GPS signals from ocean surfaces for GPS-altimetry. A synchronization pulse delivered every second is used for precise onboard timing purposes, and the autonomously generated navigation information is used by both the CHAMP Attitude and Orbit Control System and the star sensors to update their orbital position.

- Laser Retro Reflector

  The Laser Retro Reflector instrument consists of 4 cube corner prisms which reflect short laser pulses back to a transmitting ground station, making it possible to measure the direct two-way range between ground station and satellite. These data are used for precise orbit determination in connection with GPS for gravity field recovery, calibration of the onboard microwave orbit determination system and two-color ranging experiments to verify existing atmospheric correction models. The Laser Retro Reflector was developed and manufactured at GFZ.

- Fluxgate Magnetometer

  The Fluxgate Magnetometer (FGM) probes the vector components of the Earth's magnetic field, and is therefore regarded as the prime instrument for the mission's magnetic field investigations. The FGM was developed and manufactured under contract by the DTU

DOI: 10.2312/GFZ.b103-08029

(Technical University of Denmark, Lyngby). It is the same Compact Spherical Coil (CSC) sensor design used for the Ørsted mission. The interpretation of the vector readings requires the knowledge of the sensor attitude at the time of measurement, so for that reason the FGM is mounted rigidly together with the Advanced Stellar Compass on an optical bench.

The operational principle of fluxgate magnetometers is well known and has been used on many different spacecraft. This particular instrument utilizes three orthogonal sets of coils (tri-axial) wound on the surface of a sphere to generate a homogeneous field within the whole spherical volume. The current through these coils is controlled by a feedback loop which tries to cancel the ambient magnetic field in the interior. Three ring core sensors in the center act as null-indicators.

The FGM covers the full range of the Earth's field, $\pm 65,000\,\mathrm{nT}$, in all three components. Deviations from linearity are found to be in the range of $\pm 100\,\mathrm{pT}$ and the overall noise level is of the order of $50\,\mathrm{pT}$ (rms). In the nominal operation mode, the field vector is sampled at a rate of $50\,\mathrm{Hz}$ providing a spatial resolution along the orbit of approximately $150\,\mathrm{m}$.

For redundancy reasons a second FGM is accommodated on the optical bench, $60\,\mathrm{cm}$ inward from the primary sensor, which can also be used as a gradiometer. Both CSC sensors are mounted together with the star cameras (ASC) on a common optical bench providing a mechanical stability between these systems of better than 10 arcsec. The optical bench, as a part of the boom, is placed about halfway between the satellite body and the Overhauser Magnetometer (OVM) at the tip. This location is a compromise between avoidance of magnetic interference from the spacecraft and cross-talk between the FGM and the OVM.

- Overhauser Magnetometer

  The Overhauser Magnetometer (OVM) was developed and manufactured under contract by LETI (Laboratoire d'Electronique de Technologie et d'Instrumentation) in Grenoble, France. It serves as the magnetic field standard for the CHAMP mission. The purpose of this scalar magnetometer is to provide an absolute in-flight calibration capability for the FGM vector magnetic field measurements. The OVM samples continuously the ambient field strength in any direction at a rate of $1\,\mathrm{Hz}$ and because of a dedicated program ensuring the magnetic cleanliness of the spacecraft, allows for a reading with an absolute accuracy of $< 0.5\,\mathrm{nT}$. In order to keep the influence of stray magnetic fields from the spacecraft as low as possible the OVM sensor is mounted at the tip of the $4\,\mathrm{m}$ long deployable boom.

DOI: 10.2312/GFZ.b103-08029

It works on the principle of proton magnetic resonance, where a proton-rich liquid is exposed to a DC magnetic field causing the protons to precess around the field direction with a frequency strictly proportional to the applied field magnitude. In principle there is no dependency on field direction, temperature, or drift. By exactly measuring the precession frequency an absolute figure of the ambient magnetic field strength can be derived (the ratio between the two is called the gyromagnetic ratio).

- Advanced Stellar Compass

  The Advanced Stellar Compass (ASC) has been developed and fabricated under contract by the DTU (Technical University of Denmark, Lyngby). It uses the same design as does the Ørsted satellite mission. On CHAMP there are two ASC systems (each consisting of two Camera Head Units (CHU) and a common Data Processing Unit (DPU)) with one on the main spacecraft body and the other mounted to the magnetometry optical bench unit on the boom.

  The magnetic cleanliness of the CHU enables one of them to be mounted near to the magnetometer on a rigid structure which significantly improves the validity of attitude solutions transferred from one system to the other. The ASC on the boom provides the high attitude precision needed for the magnetic field vector measurements. The ASC on the spacecraft body provides attitude data primarily for the three component STAR accelerometer and the Digital Ion Drift Meter. However, this information is also utilized for the proper reduction of the GPS data, laser ranging data and the attitude control.

  An image of the stars within the field-of-view is acquired by integrating the light focused onto a photo-sensitive charge coupled device (CCD) array. The image is digitized, fed to a microprocessor, sifted for stars brighter than $mV = 6$ and then corrected for lens distortions all of which culminates in a list of calculated star centroids with sub-pixel precision. A best fit comparison of the determined star centroids with real star positions derived from an on-board HIPPARCOS star catalogue yields the attitude. The two transverse directions, right-ascension and declination, can be determined with an accuracy of about 1 arcsecond. However, the rotation angle about the boresite is poorer by about a factor of 5, but this can be partially mitigated when both star cameras are in service.

- Digital Ion Drift Meter

  The Digital Ion Drift Meter (DIDM) is provided by the AFRL (Air Force Research Laboratory,

DOI: 10.2312/GFZ.b103-08029

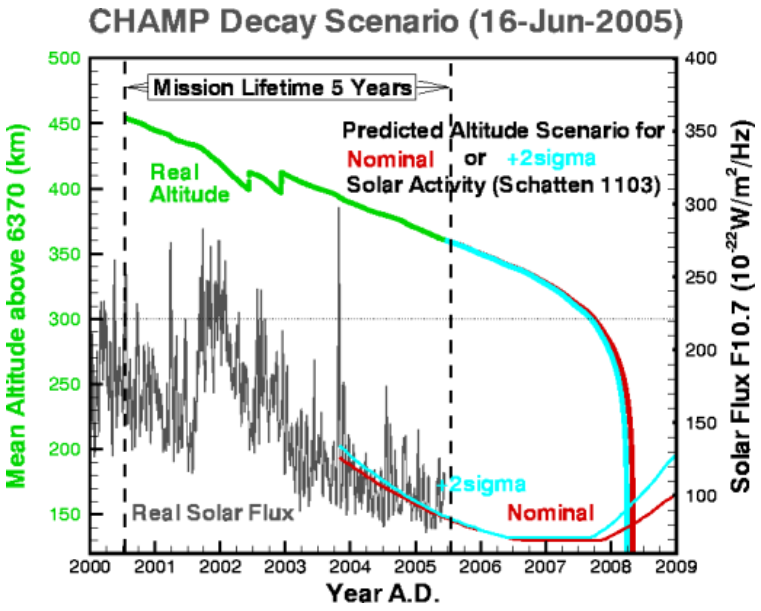

Figure 1.6: A plot and forecast of the CHAMP satellite orbit decay as of June 16, 2005. The two jogs in the altitude (green curve) in 2002 are adjustments to raise the spacecraft in order to prolong the mission [34].

Hanscom). The purpose of this instrument is to make in-situ measurements of the ion distribution within the ionosphere. A number of key parameters can be determined from the readings, such as the ion density and temperature, the drift velocity and the electric field by applying the $(\mathbf{v} \times \mathbf{B})$-relation. Together with the magnetic field measurements these quantities can be used to estimate the ionospheric current distribution. Knowing these currents helps in separating internal and external magnetic field contributions. In conjunction, a Planar Langmuir Probe (PLP) provides auxiliary data needed to interpret the ion drift measurements. Quantities that can be derived from the PLP sweeps include spacecraft potential, electron temperature and density.

CHAMP was launched into an essentially circular, near-polar orbit with an initial altitude of 454 km and an inclination of 87.3° with respect to the Equator. This orbit allows the satellite to have an almost complete, homogeneous global coverage granting it the local time variation needed to separate out periodic phenomena like atmospheric tides and diurnal variations (and is a good compromise between the magnetic, gravitational, and atmospheric mission goals). The spacecraft orbits the entire globe with a period of 93.55 minutes, which corresponds to 15.4 orbits per day.

DOI: 10.2312/GFZ.b103-08029

Over time the orbit decays because of atmospheric drag and increased solar activity exacerbates this decay rate, thus shortening its stated 5-year lifetime (which has already been exceeded). Once the satellite passes below an altitude of 300 km it will quickly descend. In a effort to extend its lifetime, an onboard cold gas thruster was used to raise the spacecraft's orbit twice in 2002 (Fig. 1.6) and again more recently in 2006 (but not shown in the figure), which should allow the spacecraft to operate until 2009.

1.5 Sources of the Geomagnetic Field

The measured magnetic field of the Earth is actually composed of fields originating from several separate source regions, the dominant ones of which are illustrated in Fig. 1.7. As this figure demonstrates the largest contributor is from the core field originating in the fluid outer core, which reaches intensities of around 55,000 nT at satellite altitude (in this case 400 km). While in the upper crust, the lithospheric field typically ranges ±20 nT when measured at satellite altitudes, but can be much higher at the surface where it is closer to its source region. In the atmosphere currents generated in the ionosphere and magnetosphere also produce their own magnetic fields, which can vary widely in intensity, both spatially and temporally, due to the solar inputs. These sources are examined and further discussed in the remainder of the section.

1.5.1 The Internal Field

The main field

The main field, often referred to as the core field, represents more than 90% of the geomagnetic field measured at the Earth's surface and ranges in magnitude from approximately 30,000 nT at the Equator up to 60,000 nT at the poles. Because most of the interior of the Earth is hotter than the Curie point temperature (1043 K), the aligned electron and nuclei spins in iron atoms are randomized, thus neutralizing the magnetic properties of magnetized iron deposits. Instead the field originates from geodynamo processes in the fluid outer core. A first order approximation of the structure of the main field indicates a dipole symmetry located near the center of the Earth, but inclined relative to the geographic poles (the 2005 Magnetic North Pole is (82.7° N, 114.4° W)). However, the main field is not static, instead exhibiting significant spatial and temporal variation when viewed on long timescales. For example, the poles undergo what is known as polar wander whereby their positions are constantly in a state of motion with average velocity around 9 km/yr, but since 1970 this movement has accelerated to 40 km/yr in 2001 [40]; this acceleration has continued

DOI: 10.2312/GFZ.b103-08029

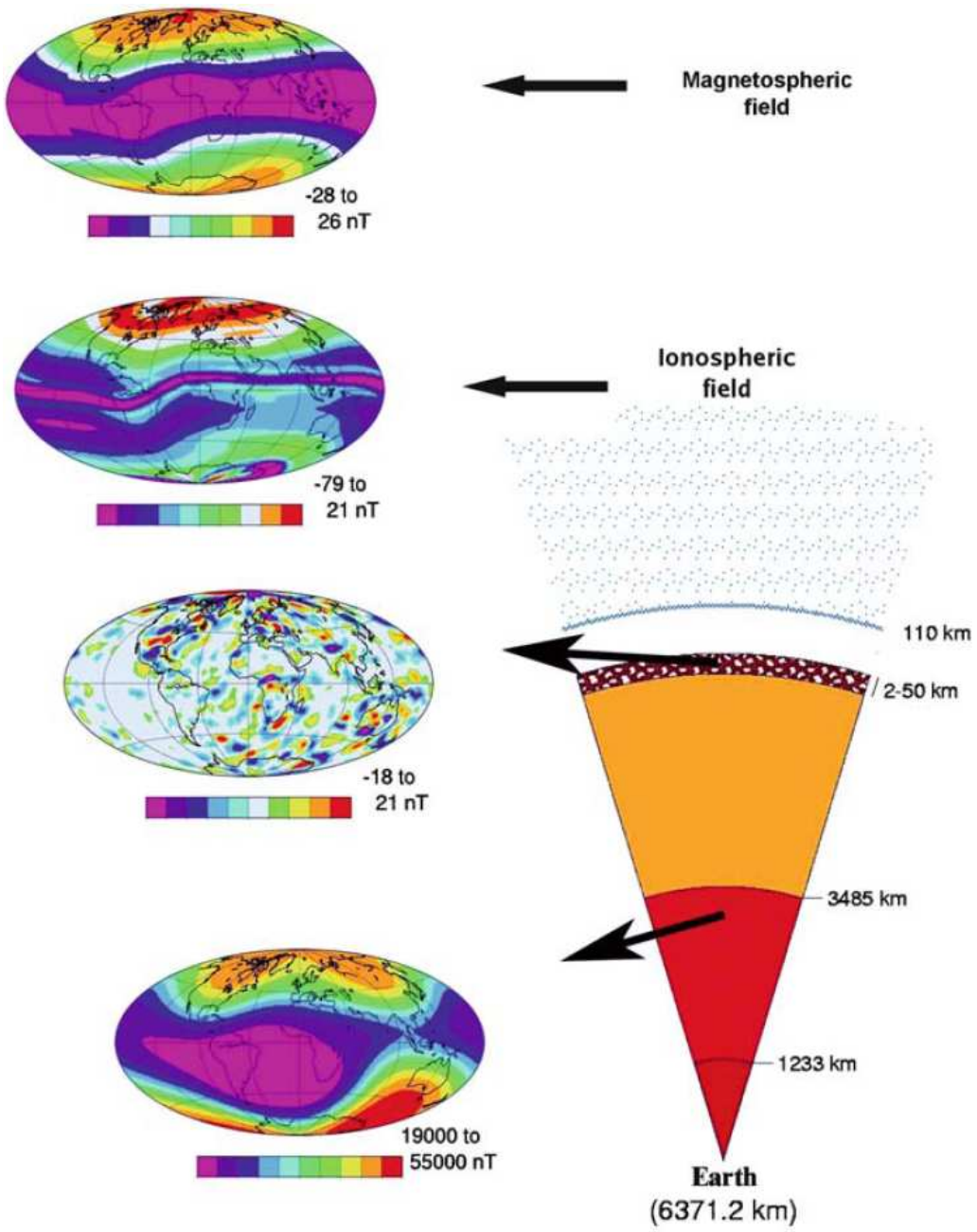

Figure 1.7: Dominant magnetic fields and their associated source regions within the Earth's system, including those originating in the core (bottom), lithosphere (2^{nd} from bottom), ionosphere (2^{nd} from top) and magnetosphere (top). The fields were computed using the CM4 model (see Sec. 1.7.2) for 2002 at 400 km, where the core field is the scalar intensity of the main field between spherical harmonic degrees 1 and 13. The lithospheric field in the direction of the main field is shown between spherical harmonic degrees 15 and 65. The ionospheric and magnetospheric fields are for 13:30 LT on January 5, 2002 and again are the fields in the direction of the main field [38].

DOI: 10.2312/GFZ.b103-08029

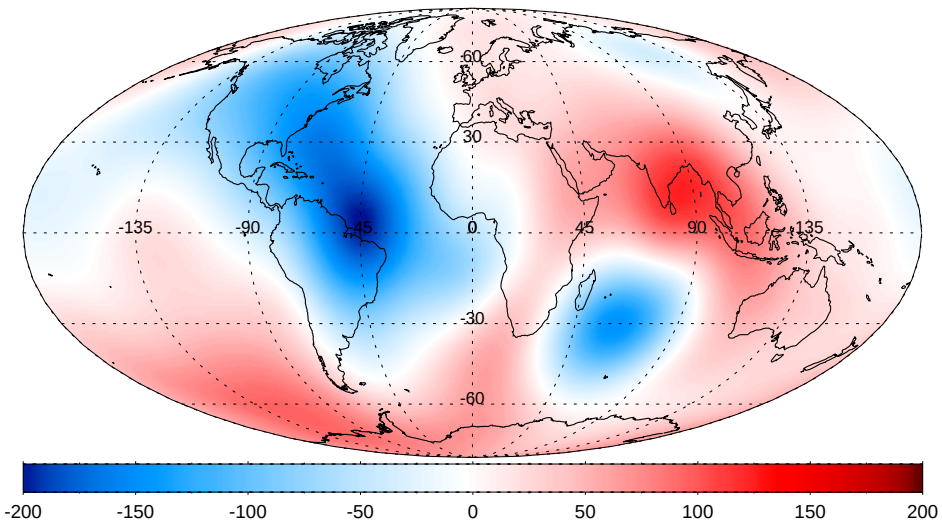

Figure 1.8: A plot of the global secular variation in the vertical component in 2005 at the Earth's surface using the CHAOS model. Notice the high rates of change in nT/yr in the mid-Atlantic, off the coast of Madagascar and over India.

in recent years [41]. Furthermore, the strength of the dipole is currently (since 1840) decaying at a rate of about 15 nT/yr [42]. In fact, the paleomagnetic record abounds with instances of complete polarity reversals. While at the same time there is a general westward drift of the entire field, as well as smaller range regional change. Halley first discovered this phenomenon during his famous voyages that charted the declination between 1698–1700 [1].

Much of this change (known as secular variation), despite not being fully understood, is clearly evident in the time-series of magnetic vector field data from geomagnetic observatories. Fig. 1.9 is a good example of secular change from around the area of Berlin, Germany, spanning almost 200 years in the declination, Z, and horizontal geomagnetic components (discussed in Sec. 1.6.1). The declination measured in Freiberg (later relocated to Potsdam, Seddin and Niemegk in 1890), starting around 1810, increases fairly linearly from $-19°$ to $2°$ in 2005. The Z component also increases, but not in such a clear linear fashion from $43,000$–$45,000$ nT during the interval from 1890–2000. The horizontal component, H, demonstrates an oscillatory behavior fluctuating between $18,400$–$18,800$ nT. Fig. 1.8 depicts the global extent of the secular variation from 2000–2005 and highlights its heterogeneous regional nature. There are models like the gufm1 [8] which use historical data dating back to the late 1500's and other paleomagnetic models dating back even further, like the

DOI: 10.2312/GFZ.b103-08029

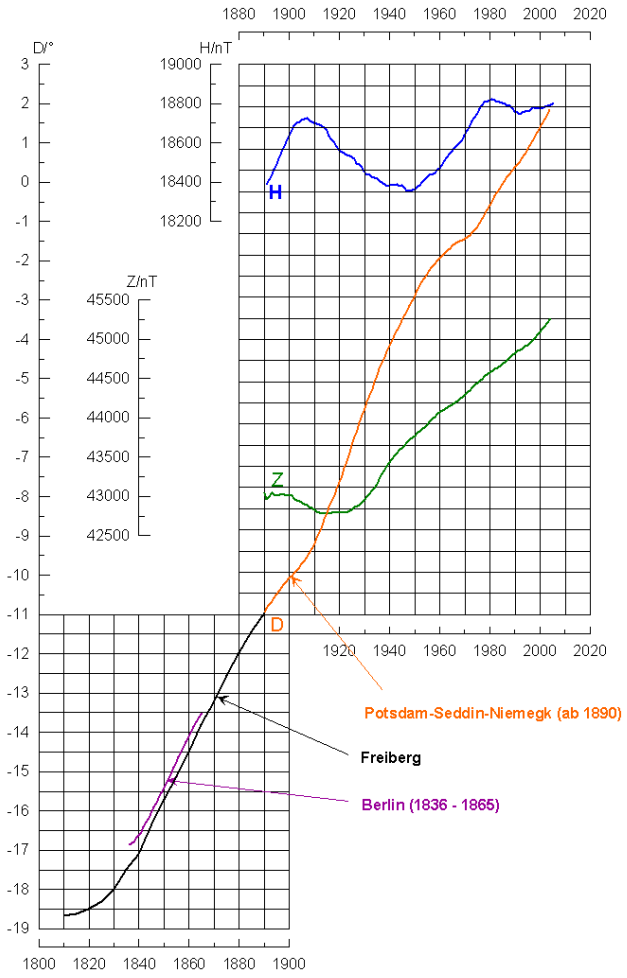

Figure 1.9: An example of secular variation from the magnetic observatories Freiberg, Berlin, and Potsdam-Seddin-Niemegk of the Z, D, and H geomagnetic field components from 1810–2005 [39].

CALS7K.2 model [26].

Abrupt, discontinuous changes in the second time-derivative (secular acceleration) of the Earth's magnetic field are known as geomagnetic jerks [44], an example is shown in Fig. 1.10. While the true nature of these jerks is still unknown they are believed to be internal to the Earth and may have to do with core flow changes, possibly torsional oscillations [45]. There is also evidence for a correlation with changes in the length-of-day (LOD – is a measure of the rotation rate of the mantle and it provides information about the changes in the mantle's moment of inertia or the axial torques acting on the mantle, from external or internal influences such as the dynamical coupling with the atmosphere or the Earth's core, respectively), which is demonstrated in Fig. 1.11 [46].

DOI: 10.2312/GFZ.b103-08029

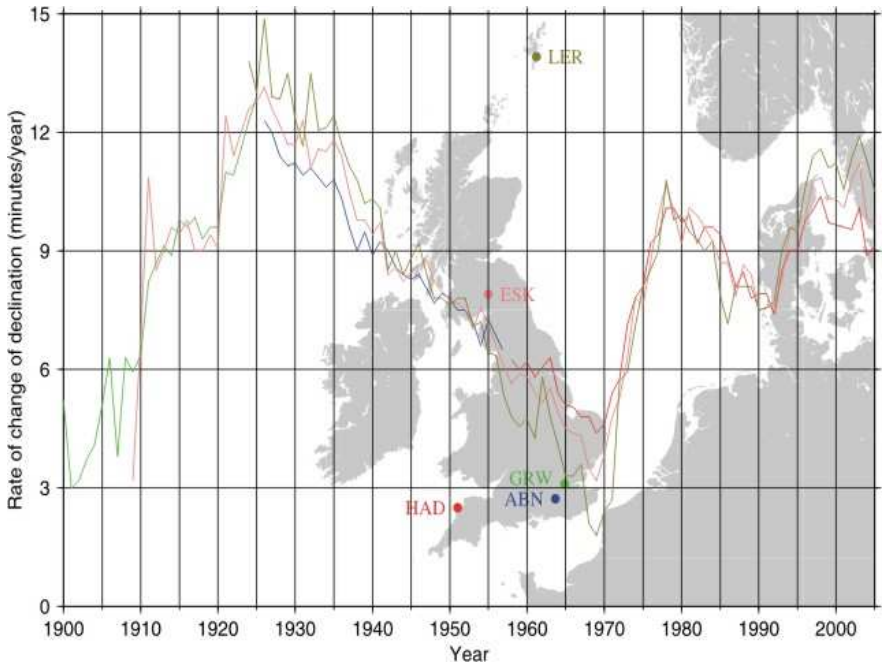

Figure 1.10: An example of some geomagnetic jerks (e.g. around 1970 and 1980) from several magnetic observatories in Europe [43].

This subject is discussed further in Sec. 3.7.

The lithospheric field

While not nearly having the same level of intensity as the core, the Earth's lithosphere has an associated magnetic field, commonly referred to as the crustal or lithospheric field, which arises from the remnant magnetism in the magnetic minerals of the crust and upper mantle (primarily magnetite with varying degrees of titanium content). This field source is spatially limited to a relatively thin layer (10–50 km thick depending on the local heat flow) since below it the internal temperature of the Earth rises to a level above the Curie temperature which mitigates the formation and maintenance of remnant magnetic fields (titano-magnetites have Curie temperatures of 400°–600° C). The magnitude of the field is highly variable ranging from essentially zero up to 1000's of nT and is highly dependent upon the characteristic geology of the region (e.g., there are many strong features like the Bangui Anomaly in the Central African Republic and the Kursk Anomaly in Russia). A mapping of this field on its own is often referred to as an anomaly map (Fig. 1.12) because it is essentially static over time, at least on time scales comparable to the core and atmospheric

DOI: 10.2312/GFZ.b103-08029

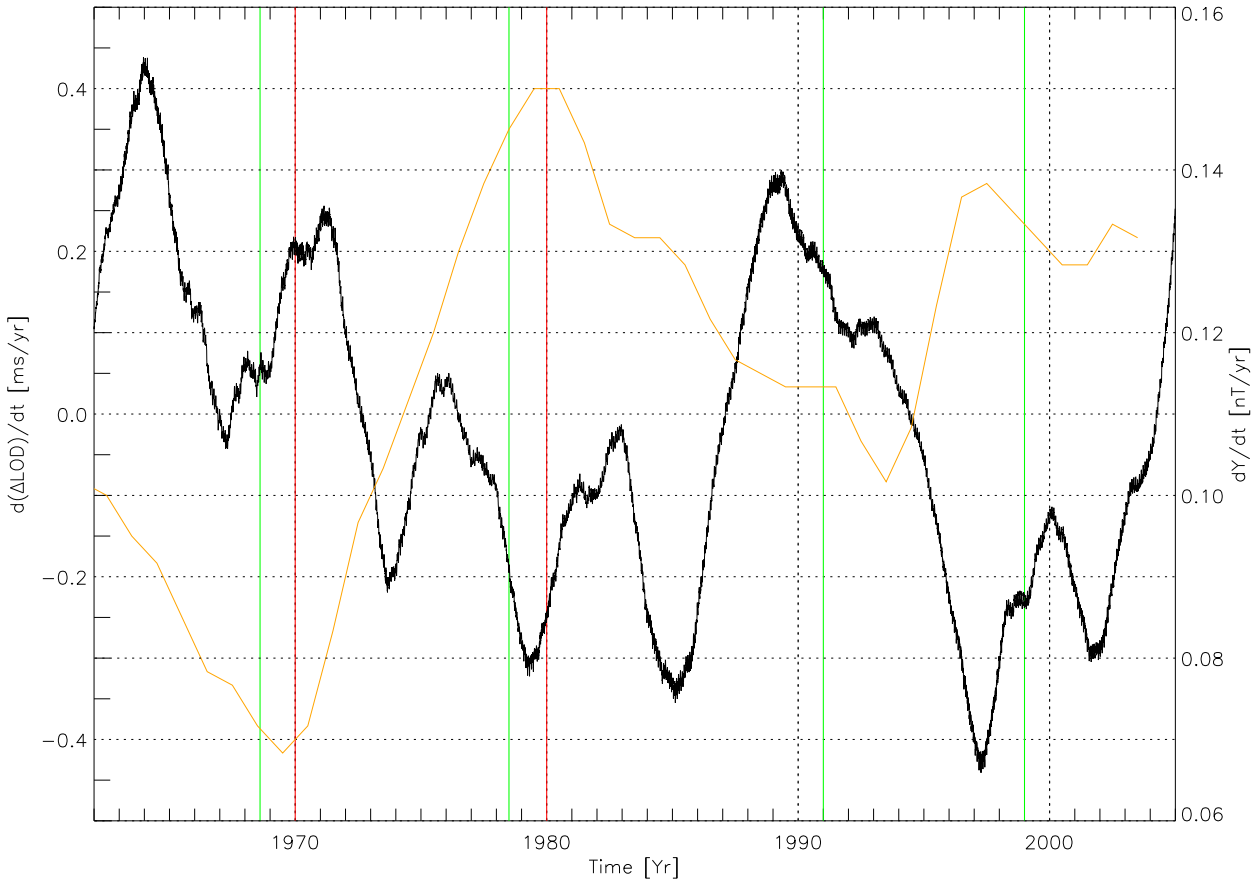

Figure 1.11: The time derivative of the length of day variation in ms/yr for 1962–2005 showing its correlation with some known jerks (vertical lines, red–strong jerks and green–derived from monthly means). The orange curve (right scale, in nT/yr) represents the secular variation in the East component of the geomagnetic field, the primary indicator of jerks, from the Chambon la Forêt magnetic observatory.

sources. However, it is worth noting that only the shorter wavelengths are resolvable (less than 2500 km or above spherical harmonic coefficient degree $n = 13$) since longer wavelengths are masked by the much larger core field (see the power spectrum in Fig. 1.20). This makes it difficult to see large scale features like coastlines, despite the differing crustal magnetization and thickness for oceanic (weaker) and continental (stronger) crust. The lithospheric field shows a tendency to scale with the strength of the main field; hence, it is particularly weak in the South Atlantic Ocean and strong at the poles. Anomaly maps can have many uses, ranging from geologic prospecting to paleomagnetic studies. For instance, examining the magnetic signature in volcanic sediments involved with seafloor spreading has revealed geomagnetic field reversals (as the molten lava cools

DOI: 10.2312/GFZ.b103-08029

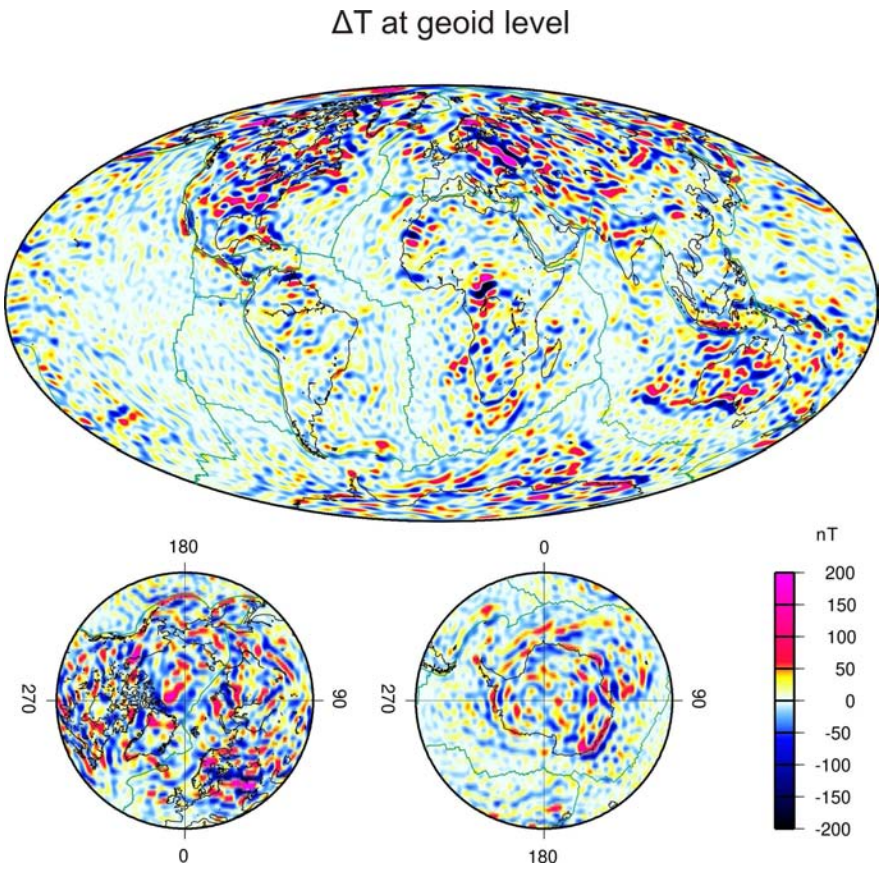

Figure 1.12: The total intensity anomaly of the Earth's lithospheric field using the MF5 model [47].

it acquires an imprint of the ambient magnetic field). Global anomaly maps can be produced from satellite data, e.g. MF5, however they have a lower resolution than when aeromagnetic surveys are used (but with reduced spatial coverage). The World Digital Magnetic Anomaly Map (WDMAM) [48, 49] is an effort to combine the various scattered aeromagnetic surveys into a comprehensive high resolution global anomaly map.

1.5.2 The external field

The source of the remaining contribution of the geomagnetic field, not from within the Earth, comes from currents in the ionosphere and magnetosphere. Here the temporal variations occur on a much shorter time span compared to the secular variation of the internal field. There exist annual, semiannual, and daily period variations as well as non-periodic transient effects that affect the external field contribution.

DOI: 10.2312/GFZ.b103-08029

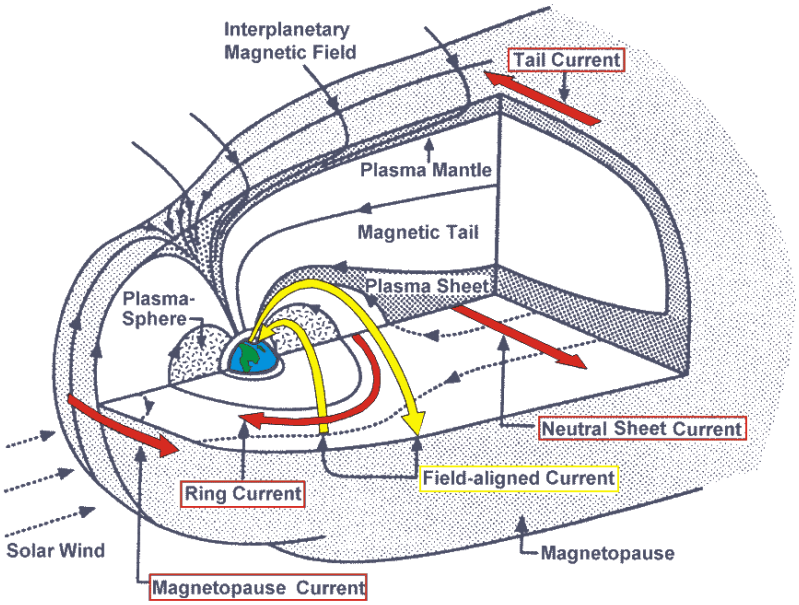

Figure 1.13: A diagram of the magnetosphere highlighting some of the important current systems, from [18].

The driving force that powers much of the external field phenomena on Earth arises directly or indirectly from the sun. Radiating outward from the sun, with an average velocity of about 450 km/s, is a plasma of ionized atoms and electrons called the solar wind. The highly conductive nature of the plasma allows it to carry along with it the sun's magnetic field, called the Interplanetary Magnetic Field (IMF), (which is why the measured IMF (a few nT's) is roughly 100 times greater near the Earth than a simple r^{-3} dipole decay law would naively predict) creating a very complex, Archimedean spiral-like, magnetic field configuration. Along with this are the actual ions themselves, which contribute to the input and generation of the aurora. The input light radiation itself is the principle mechanism that drives the atmospheric wind dynamo, which is the impetus for many of the atmospheric current systems.

The magnetospheric field

The magnetosphere is the region carved out of the solar wind plasma flow by the interaction with the geomagnetic field (see Fig. 1.13). It takes a general cometary shape with compression of the geomagnetic field lines ($\sim$ 10 Earth radii during low activity) in the sunward direction and a

DOI: 10.2312/GFZ.b103-08029

long stretched out magnetotail in the anti-sunward direction (100's of Earth radii). Its shape is highly dynamic as it responds to changes in both the solar wind density and field direction. The magnetosphere consists of plasma mainly from the solar wind, but also large contributions come from the ionosphere. A transfer of energy from the solar wind drives the magnetosphere in a process called reconnection, whereby the field lines in the IMF and the geomagnetic field merge transferring energy, mass, and momentum [50].

When the IMF embedded in the solar wind impinges upon the Earth's intrinsic magnetic field, a substantial transfer of energy into the terrestrial magnetosphere occurs. If this condition persists for several hours, the entire magnetosphere becomes disturbed. The term geomagnetic storm is used when the magnetosphere is in such a state. The primary measure of the intensity of a geomagnetic storm is the strength of the ring current, which is quantified by the D_{st} index (see Sec. 1.5.3) [51, 52]. The ring current, first characterized by Arthur Schuster in 1911, was the first major external current system discovered. It resides in the inner magnetosphere circling the Earth near the equatorial plane, flowing along the magnetopause on the sunward side and the magnetotail on the anti-sunward side. It arises from trapped ions drifting longitudinally westward across the geomagnetic field lines [23]. The magnetic field of the ring current decreases the field measured at the Earth's surface, and it is this depression that gets recorded as D_{st} [52]. It is detectable at the surface, but during low activity normally represents just a few nT; however, it may be enhanced during magnetic storms when the fields can intensify up to 100's of nT (see Fig. 1.17 for an example two strong geomagnetic storms in October of 2003). A typical storm includes a substantial ring current that develops over a few hours and then recovers over several days. Forecasting the state of the ring current is a necessity for forecasting the magnetic field in the magnetosphere [52].

The ionospheric field

The ionosphere is an ionized region of the upper atmosphere divided into three main strata (Fig. 1.14). Each layer is independently produced mainly via the absorption of solar radiation (solar heating) by specific constituents of the neutral atmosphere, which responds differently to different parts of the incident solar photon spectrum. They include, with approximate altitude ranges [53, 17]:

- The F-region (130–600 km) is usually further subdivided into the F_1 and F_2 regions, although the F_1 region merges into the F_2 region during the night. The highest ionospheric plasma

DOI: 10.2312/GFZ.b103-08029

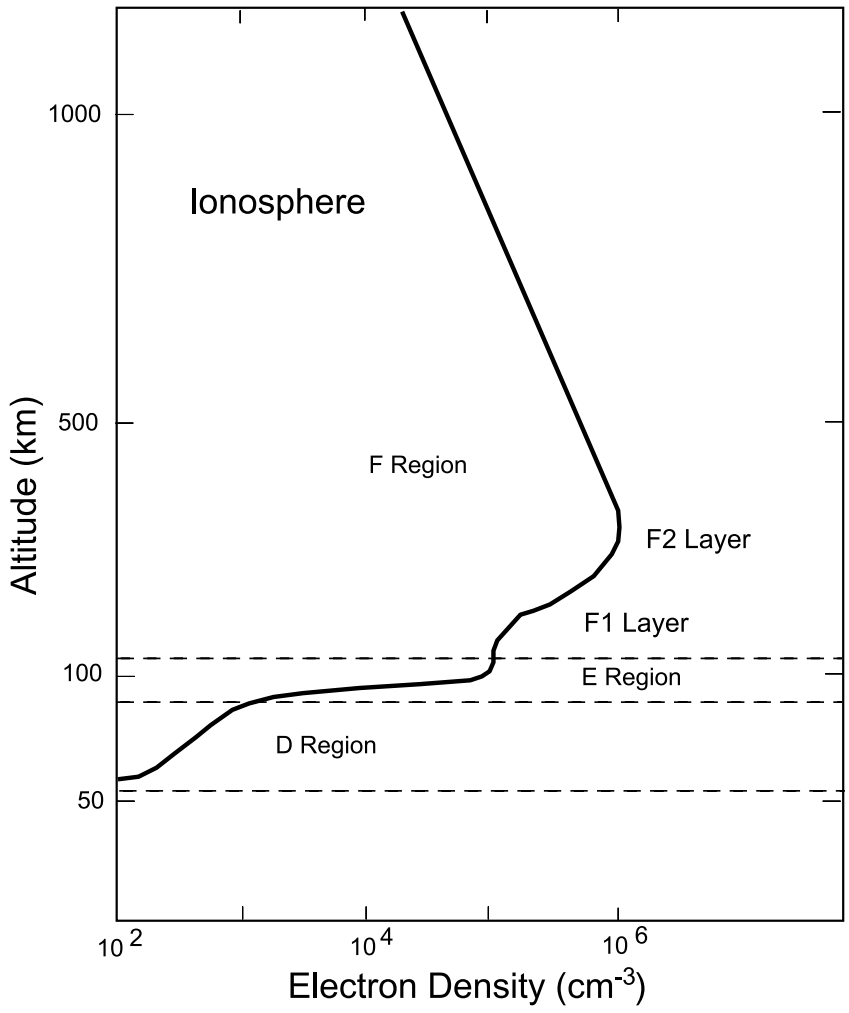

Figure 1.14: Election density profiles showing the various ionospheric layers: D, E, and F (which splits into F_1 and F_2 on the dayside) [18].

densities reside in the F-region (primarily e^- and O^+) during noon in the 170 km and 250–300 km altitude range for F_1 and F_2, respectively.

- The E-region (90–130 km) is ionized predominately by solar 1–10 nm x-rays and ultraviolet radiation in the 100–150 nm range, producing the primary ion constituents e^-, NO^+ and O_2^+.

- The D-region (50–90 km), the deepest of the layers, is maintained by the most energetic radiation which can penetrate to this low altitude. The primary ions produced in the D-region include e^-, NO^+ and O_2^+. Solar 0.1–1 nm x-rays dominate at the highest reaches

DOI: 10.2312/GFZ.b103-08029

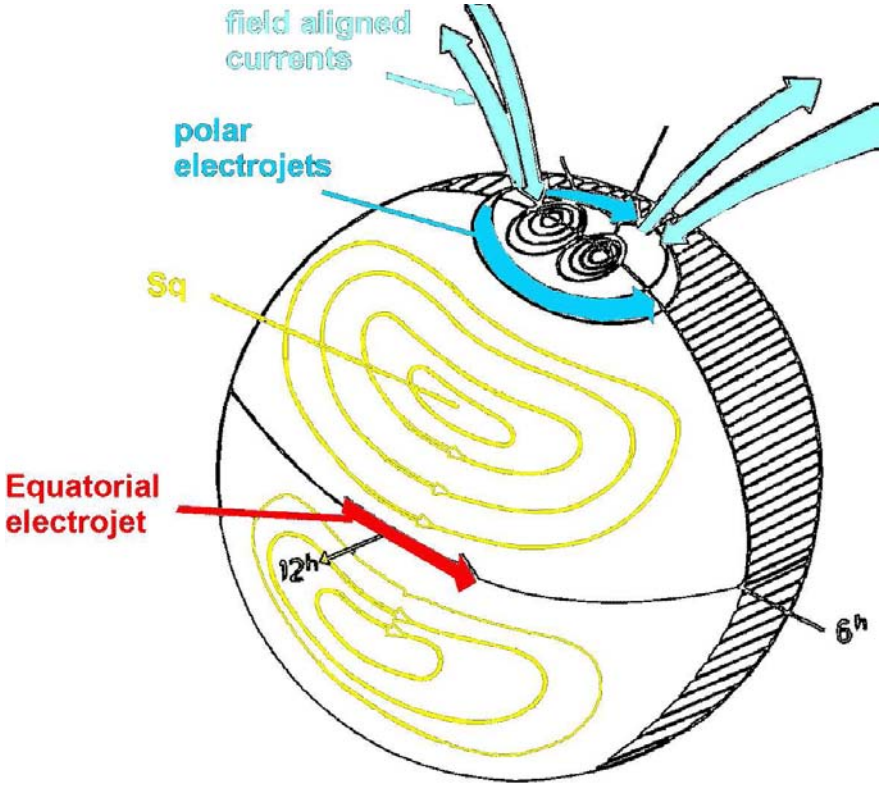

Figure 1.15: A diagram of the ionosphere highlighting some of the important current systems.

of its altitude range (80–90 km), while the solar Lyman-α radiation predominates in middle around 70–80 km. Descending even further down, cosmic-ray particles begin to dominate the ionization process, which are active even during the night. The D-region is of particular importance for radio communication.

The plasma densities in the ionosphere vary greatly between noon and midnight as well as with season, solar cycle and solar activity, because of the changing influx of ultraviolet radiation that drives the bulk of the ionization process. This contributes to the development of ionospheric currents (Fig. 1.15), which track the position of the sun. In turn, these current systems contribute to the diurnal magnetic field variations observed at the surface (up to around 80 nT). Among these dayside current systems, the most intense is the Equatorial Electro-Jet (EEJ), which flows eastward near the magnetic equator in the E-region. The EEJ is a narrow current system that varies somewhat with longitude, being particularly intense over South America and Indonesia and weaker over Africa. Closely related to the EEJ, although less intense, is the large-scale solar quiet

DOI: 10.2312/GFZ.b103-08029

(Sq) current system. It consists of two current vortices or lobes, one in each hemisphere, covering essentially the entire sunlit part of the ionosphere. The thermospheric neutral winds, modulated by atmospheric waves, move ionospheric plasma across geomagnetic field lines thus creating an atmospheric dynamo that sets up the Sq and the EEJ current systems [9, 50, 53, 17]. Currents in the Polar Regions are derived from the ionospheric–magnetospheric coupling that takes place along the geomagnetic field lines connecting the ionosphere and the magnetopause [9].

1.5.3 Geomagnetic Activity Indices

While the main magnetic field has a slow secular variation, the external field is characterized by transient variations having time scales on the order of days to minutes (or less). These geomagnetic disturbances can be monitored by ground-based magnetic observatories recording the three magnetic field components, which can give some information about much of the magnetospheric and ionospheric phenomena. The solar wind, including both plasma and the IMF, is the source of energy for the Earth's magnetosphere. Solar wind characteristics are highly variable and directly influence the shape, size and morphology of the magnetosphere, the amount of transferred energy, and how that energy gets dissipated. The transient variations of the geomagnetic field measured at the Earth's surface are a signature of currents flowing in the magnetosphere, as the result of the solar wind magnetosphere coupling processes. They result from both external currents flowing in the ionosphere and in the magnetosphere, including field aligned currents, magnetopause currents and internal induced currents. The high degree of complexity of the solar wind - magnetosphere - ionosphere coupling results in a large variety in magnetic signatures measured at surface level, which depend upon the state of the magnetosphere, and differ with the geographic and geomagnetic location of the observatory. It is possible to track basic features of these ground observed perturbations, and to attempt to relate them to ionospheric and magnetospheric sources. These transient variations can be decomposed into regular and irregular components. The smooth and periodic regular variations are mainly related to the atmospheric dynamo processes, while the irregular variations are mostly due to the energy input to the magnetosphere. Much of this variation is recorded and distilled down into different indices, which attempt to record the irregular variability in geomagnetic activity. They are important for many reasons and, as such, are used in various, different research domains. Geomagnetic indices constitute data series, which attempt to describe, on a planetary scale, the magnetic activity or some of its components. They allow for statistical studies over long time periods and make it possible to characterize the physical

DOI: 10.2312/GFZ.b103-08029

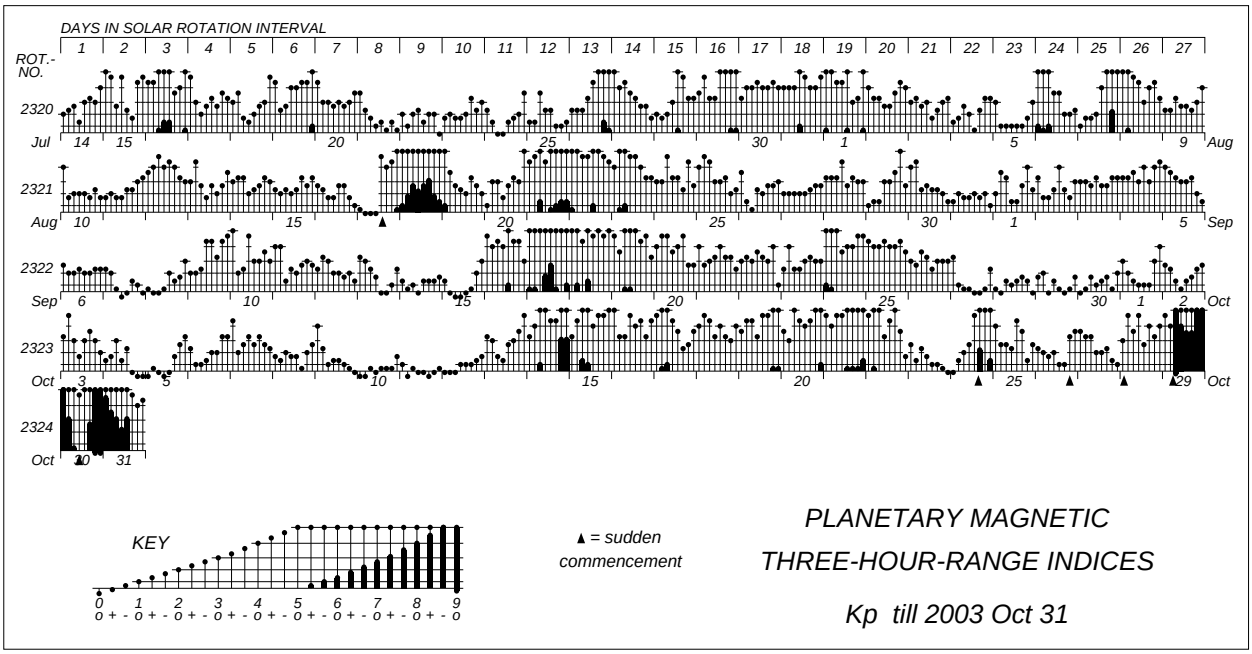

Figure 1.16: The K_p index for July through October 2003 presented in the Bartel's musical diagram format. Notice the exceptionally strong magnetic activity during the last part of October from the 29^{th}–31^{st}, which corresponds to the Halloween solar flare events [55].

processes driving the coupling, and its dependence on solar wind parameters [54].

Listed below are some of the indices utilized in the present study.

K_p Index

The K_p index, introduced by Julius Bartels in 1949, attempts to provide an approximate worldwide proxy of overall geomagnetic activity by measuring the magnetic effects of solar particle radiation. It divides the day equally into eight three-hour intervals. Its derivation is based on the measurements of the two horizontal geomagnetic field components made at a selection of 13 subauroral magnetic observatories [55].

At its root, the index relies upon the K index also introduced by Bartels [56], which records the maximum local disturbance (range in variation) in either of the two horizontal geomagnetic field components (after subtraction of the diurnal variations resulting from ionization of the ionosphere and its tides) during each time interval. This range is coded according to a quasi-logarithmic scale whereby each K index value is assigned an integer ranging from 0 to 9 [57]. One problem is that this index is locally bound to each observatory, so through statistical methods and conversion tables

DOI: 10.2312/GFZ.b103-08029

this index is translated into a standardized form, K_s, which is common across all the involved observatories. This K_s is more granular, still covering the same 0–9 range, but instead is quantized into units of $\frac{1}{3}$, totaling 27 gradations. The planetary index, K_p (from the German "*planetarische Kennziffer*"), is then computed from the arithmetic mean of the K_s values from the 13 standardized observatories [58].

Currently the K_p index is produced and maintained by the GFZ-Potsdam's Adolf-Schmidt-Observatorium für Geomagnetismus, and can be retrieved from their website [55]. The index series spans the years 1932 to the present.

$F_{10.7}$ Index

The 10.7 cm Solar Flux, or $F_{10.7}$, is measured using two fully automated radio telescopes operated by the Dominion Radio Astrophysical Observatory in British Columbia, Canada. It is a measurement of the integrated emission at a wavelength of 10.7 cm from all visible sources present on the solar disc. It has a thermal origin and relates to magnetically trapped plasma over active solar regions and, in turn, to the amount of magnetic flux. The 10.7 cm Solar Flux correlates well with indices of solar activity such as sunspot number and total sunspot area, and since solar irradiance is modulated by solar magnetic activity it correlates well with Earth based magnetic activity indices [59].

International Q-Days

The list of International Q-Days (Quiet-Days) and D-Days (Disturbed-Days) is a ranking of the days in a particular month, based on the K_p index, for the purpose of classifying them by their relative level of geomagnetic activity. Each day is assigned an ordered rank on the basis of the sum, sum of squares, and the maximum of the eight daily K_p values. The mean of these three rank values is computed and assigned as the overall rank for that day. The ten lowest ranks represent the Q-Days and the five highest ranks represent the D-Days. It is important to note that these ranks are only relative to other days in the same month and bear no relation to other months or years which may have vastly different absolute levels of geomagnetic activity (e.g., Jan 8, 2004 is the quietest day of its month but the K_p for the day ranges as high as 3^+). The list of International Q-Days is currently maintained by GFZ-Potsdam and can be obtained from their website [60].

DOI: 10.2312/GFZ.b103-08029

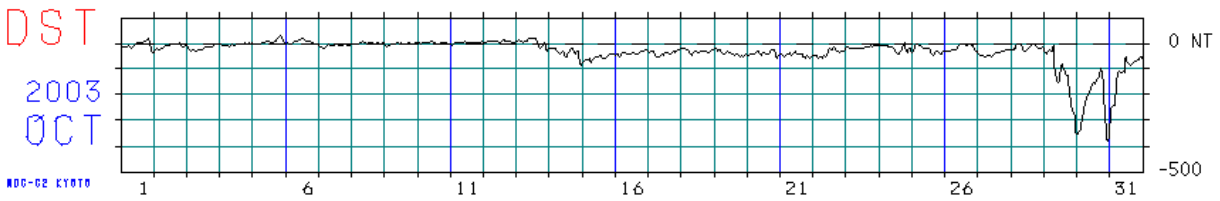

Figure 1.17: The D_{st} index for October 2003. Notice the strong negative deflections on the 29^{th} and 31^{st}, which correspond to the Halloween solar flare events [61].

$\mathbf{D}_{st}$ Index

The disturbance storm time index, known as D_{st}, monitors the world wide magnetic storm level. It does this by measuring the axisymmetric component of the ring current through the magnetic field disturbances near the dipole equator on the Earth's surface as recorded by magnetic observatories [62]. At such latitudes the H component of the magnetic perturbation is dominated by the intensity of the magnetospheric ring current. The magnetic field of the ring current, which is affected by geomagnetic storms, decreases the geomagnetic field at the surface of the Earth, and this depression is measured as D_{st} [52]; however, Campbell (1996) [63] points out that it is not purely just a ring current contribution. The D_{st} index is a direct measure of the hourly average of this perturbation across multiple geomagnetic observatories, however, the computation involves careful removal of quiet time values from the H component traces and an adjustment for location [58]. Negative perturbations indicate storm conditions and the greater the perturbation, the more intense the storm. D_{st} values still above $-20\,\mathrm{nT}$ are associated with quiet geomagnetic activity, but values below $-50\,\mathrm{nT}$ indicate a moderate disturbance in the geomagnetic field, and in extreme cases the D_{st} can drop to below $-400\,\mathrm{nT}$ as seen in Fig. 1.17.

1.6 Mathematical Description of the Geomagnetic Field

1.6.1 Coordinate Systems

The geomagnetic field is a 3D vector field and as such can be represented at any point in space and time by a vector magnitude and its direction. Typically, magnetic observatory field observations are decomposed into geographic coordinates, either X, Y, Z or D, I, H, and F. Where F represents the total magnetic field intensity. Helping to visualize the orientation, Fig. 1.18 illustrates how the X (north) and Y (east) components are both aligned parallel to the Earth's surface but are

DOI: 10.2312/GFZ.b103-08029

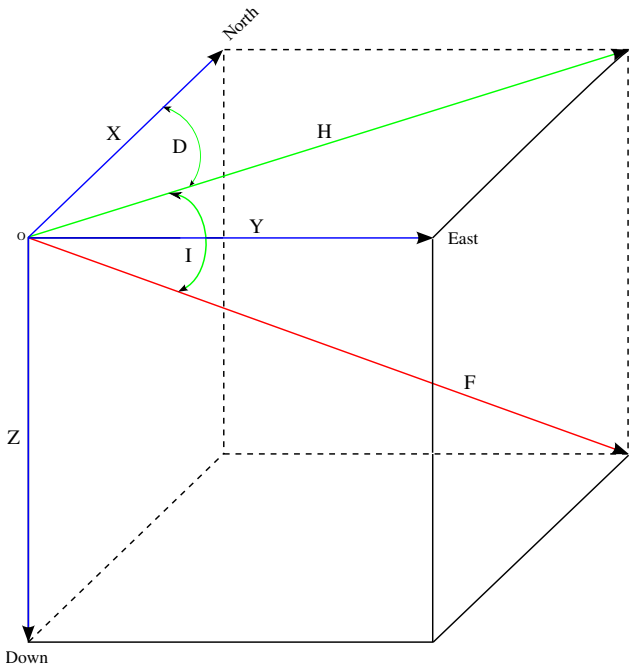

Figure 1.18: The magnetic-field components (X, Y, Z) define the Cartesian components (north, east, down), where the usual observatory components (H, D, Z) are (horizontal intensity, declination, down), the angle of the magnetic vector with respect to the horizontal plane (I) is inclination, and (F) is the total field intensity (after [64]).

directed either geographically northward (X) or eastward (Y). H is the horizontal component vector parallel to the Earth's surface and directed toward magnetic north and Z is the vertical analogue pointing downward toward the surface. The inclination (I) is the angle between H and F, and represents the downward vertical dip seen in the compass needle, while the declination (D) is the angle between magnetic north (H) and geographic north (X).

This geographic coordinate frame is altered slightly when referencing satellite data, in that Z rather than pointing downward points instead to the center of a spheroid Earth, becoming a geocentric frame. In this way it is easy to transform the components directly to spherical geocentric coordinates.

$$X = -B_\theta, \tag{1.2}$$

$$Y = B_\phi, \tag{1.3}$$

$$Z = -B_r \tag{1.4}$$

The geocentric NEC (North, East, Center) frame (Fig. 1.19) is an Earth-fixed reference frame

DOI: 10.2312/GFZ.b103-08029

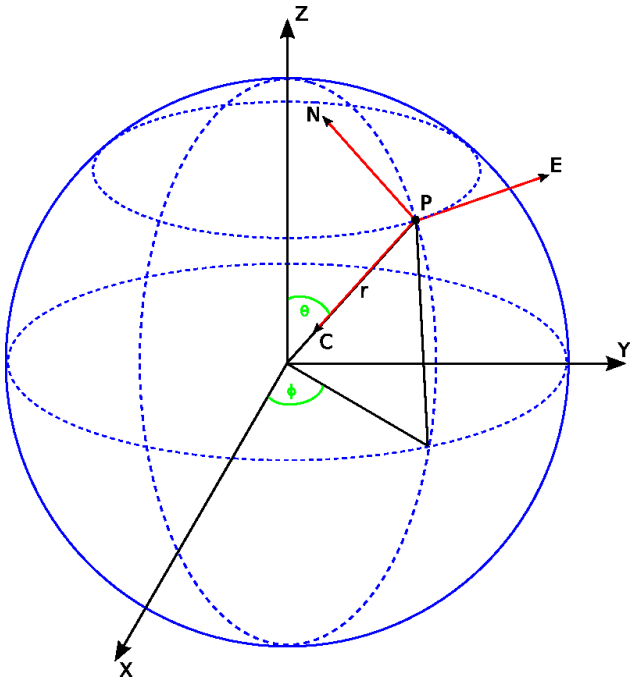

Figure 1.19: Geocentric North, East, Center coordinate system.

which is the usual coordinate system used with the CHAMP data (although it is not the internal spacecraft coordinate frame, which is a spacecraft specific coordinate frame based on the fluxgate magnetometers, denoted FGM). The northward component points toward the North Pole along $\mathbf{e}_\theta$, the center component points toward the center of the Earth along $\mathbf{e}_r$, and the east component points eastward along $\mathbf{e}_\phi$, thus completing the orthogonal coordinate frame.

The TIE–GCM (see Sec. 1.7.2) internally uses modified apex coordinates as a means of simplifying its ionospheric calculations. Briefly, apex coordinates follow a geomagnetic field line to its maximum point (apex) above the surface of the Earth. The geomagnetic-dipole longitude of this apex point is defined to be the apex longitude ϕ_A. The altitude of the apex point defines the apex altitude (h_A) and the apex radius is defined as:

$$A = 1 + \frac{h_A}{R_{eq}}, \tag{1.5}$$

where R_{eq} is the equatorial radius of the Earth, 6378.16 km. From this, the apex latitude can be defined as:

$$\lambda_A = \pm cos^{-1}(A)^{-1/2}, \tag{1.6}$$

where the positive and negative signs reflect positions either north (+) or south (-) of the magnetic

DOI: 10.2312/GFZ.b103-08029

equator. If the Earth were truly a sphere and the geomagnetic field were truly just a dipole then λ_A would simply be reduced to the geomagnetic-dipole latitude. Eq. (1.6) reveals the convenient property that for field lines with a given h_A, the apex latitude will be constant. Lastly, an arbitrary coordinate is then chosen that varies along the field line. So in summary the coordinates are firstly the apex longitude, secondly, some function of apex altitude, like the apex latitude, and thirdly a quantity that varies along the given field line, like the altitude or a function of the magnetic potential. The TIE–GCM internally uses modified apex coordinates as a means of simplifying its ionospheric calculations,

$$\lambda_m = \pm cos^{-1}\left(\frac{R_E + h_r}{R_E + h_A}\right)^{1/2}, \tag{1.7}$$

where R_E is the mean Earth radius (6371 km) and h_R is a constant reference altitude. This modification allows for a continuous latitude coordinate across the magnetic equator. [65, 66]

1.6.2 Spherical Harmonic Analysis

A convenient and useful method of describing the geomagnetic field is by performing a spherical harmonic analysis on the magnetic data. This technique, first applied to geomagnetism by Gauss in 1839, lends itself well to working with spherical coordinates and has the added side benefit of easily separating internal and external sources of magnetic field. It is generally considered that at the Earth's surface the internal field consists of sources from the core and crust, and external sources arise from atmospheric current systems. The chosen separation level is somewhat arbitrary, because when seen from satellite altitude, those same ionospheric current systems are now below the spacecraft and thus are reclassified as internal sources; therefore, care must be taken when satellite data is used.

Following the derivation of Mandea (2007) [67], Maxwell's equations can be used as the starting point for the development of the field components from spherical harmonics [68]:

$$\nabla \times \mathbf{B} = \mu_0 \mathbf{J}, \tag{1.8}$$

$$\nabla \cdot \mathbf{B} = 0, \tag{1.9}$$

where μ_0 is the permeability of free space, $\mathbf{J}$ is the current density, and $\mathbf{B}$ is the magnetic field. Considering that $\mathbf{J}$ is negligible between the Earth's surface and the ionosphere because of the lack of field sources, it is valid to assume the geomagnetic field is curl-free, allowing $\mathbf{B}$ to be written as the gradient of a scalar potential,

$$\mathbf{B} = -\nabla V, \tag{1.10}$$

DOI: 10.2312/GFZ.b103-08029

which must satisfy the Laplace equation

$$\nabla^2 V = 0. \tag{1.11}$$

Casting Eq. (1.11) in to spherical coordinates with co-latitude, θ, longitude, ϕ, and radius, r, yields:

$$\frac{1}{r}\frac{\partial^2 (rV)}{\partial r^2} + \frac{1}{r^2 sin\theta}\frac{\partial}{\partial\theta}\left(\sin\theta\frac{\partial V}{\partial\theta}\right) + \frac{1}{r^2 sin^2\theta}\frac{\partial^2 V}{\partial\phi^2} = 0, \tag{1.12}$$

which can be solved using separation of variables into the general form:

$$\begin{aligned} V(r,\theta,\phi) = a\sum_{n=1}^{\infty}\sum_{m=0}^{n}\Big\{&\left[A_n^m\cos(m\phi) + B_n^m\sin(m\phi)\right]\left(\frac{a}{r}\right)^{n+1} \\ &+ \left[C_n^m\cos(m\phi) + D_n^m\sin(m\phi)\right]\left(\frac{r}{a}\right)^{n}\Big\} P_{n,m}(\cos\theta), \end{aligned} \tag{1.13}$$

where a is the radius of the Earth (usually taken to be $a = 6371.2\,\mathrm{km}$), $P_n^m(\cos\theta)$ are the associated Legendre polynomials, and A_n^m, B_n^m, C_n^m and D_n^m are spherical harmonic coefficients of degree n and order m. The terms with $m = 0$ are referred to as zonal surface harmonics, while $m = n$ terms refer to sectorial harmonics. Intermediate terms with $0 < m < n$ are the tesseral harmonics.

In order to apply Eq. (1.13) to geomagnetism the potential function is separated and written as the sum of internal and external contributions:

$$V = V_{int} + V_{ext}. \tag{1.14}$$

Represented in their expanded form with the associated Schmidt quasi-normalized Legendre polynomials (P_n^m) substituted and internal and external series limits truncated to N_{int}^{Max} and N_{ext}^{Max}, Eq. (1.14) takes the form:

$$V_{int} = a\sum_{n=1}^{N_{int}^{Max}}\left(\frac{a}{r}\right)^{n+1}\sum_{m=0}^{n}\left[g_n^m\cos(m\phi) + h_n^m\sin(m\phi)\right]P_n^m(\cos\theta), \tag{1.15}$$

$$V_{ext} = a\sum_{n=1}^{N_{ext}^{Max}}\left(\frac{r}{a}\right)^{n}\sum_{m=0}^{n}\left[q_n^m\cos(m\phi) + s_n^m\sin(m\phi)\right]P_n^m(\cos\theta), \tag{1.16}$$

where now the g_n^m and h_n^m are the internal while q_n^m and s_n^m are the external Gauss spherical harmonic coefficients of degree n and order m.

Assuming no magnetic monopoles exist, the g_0^0 term is set to zero. So from this formalism a dipole field can be represented simply by considering only the internal $n = 1$ terms, representing geocentric dipoles located at the center of the Earth with g_1^0 along the z-axis, g_1^1 along the x-axis and h_1^1 along the y-axis. Higher degree coefficients represent geocentric quadrupoles ($n = 2$),

DOI: 10.2312/GFZ.b103-08029

octupoles ($n = 3$), *etc.* It is not uncommon for magnetic field models to have term limits as high as $N_{int}^{Max} = 50$ and similar gravity field models can easily have terms well into the hundreds, but these limits usually depend on the nature and quality of the input data. When considering the scale of the Earth a useful rule of thumb is that the wavelength of the g_n^m term is roughly $\frac{2\pi a}{(n+\frac{1}{2})}$, so that a $n = 10$ model is limited to resolutions of about 3800 km at the surface [17].

In actuality the internal geomagnetic field is not static, rather it changes over time in a process know as secular variation. This process can be accounted for in the scheme of spherical harmonic analysis by the addition of a potential, which assumes the Gauss coefficients are time dependent, and then taking the time-derivative:

$$V_{SV} = a \sum_{n=1}^{N_{SV}^{Max}} \left(\frac{a}{r}\right)^{n+1} \sum_{m=0}^{n} (t - T_0) \left[\dot{g}_n^m \cos(m\phi) + \dot{h}_n^m \sin(m\phi)\right] P_n^m(\cos\theta), \tag{1.17}$$

where N_{SV}^{Max} is the series truncation limit, $\dot{g}_n^m$ and $\dot{h}_n^m$ are the time derivatives of the Gauss coefficients, T_0 is a reference epoch and t is the desired epoch. Higher degree secular variation can be applied to this linear secular variation term by applying higher degree derivatives (e.g. the Magsat model m102389 [69] only uses first order time-derivatives, while the CHAOS model takes third order time-derivatives parameterized via splines rather than polynomials).

Calculating the gradient of Eq. (1.13) following Eq. (1.10) yields the spherical components of the geomagnetic field:

$$\begin{aligned} B_r = \frac{-\partial V}{\partial r} = &\sum_{n=1}^{\infty} \sum_{m=0}^{n} \left\{ (n+1) \left[g_n^m \cos(m\phi) + h_n^m \sin(m\phi)\right] \left(\frac{a}{r}\right)^{n+2} \right. \\ &\left. -n \left[q_n^m \cos(m\phi) + s_n^m \sin(m\phi)\right] \left(\frac{r}{a}\right)^{n-1} \right\} P_n^m(\cos\theta), \end{aligned} \tag{1.18}$$

$$\begin{aligned} B_\theta = \frac{-\partial V}{r\partial\theta} = &-\sum_{n=1}^{\infty} \sum_{m=0}^{n} \left\{ \left[g_n^m \cos(m\phi) + h_n^m \sin(m\phi)\right] \left(\frac{a}{r}\right)^{n+2} \right. \\ &\left. + \left[q_n^m \cos(m\phi) + s_n^m \sin(m\phi)\right] \left(\frac{r}{a}\right)^{n-1} \right\} \frac{dP_n^m(\cos\theta)}{d\theta}, \end{aligned} \tag{1.19}$$

$$\begin{aligned} B_\phi = \frac{-1}{r sin\theta} \frac{-\partial V}{\partial \phi} = &\frac{1}{\sin\theta} \sum_{n=1}^{\infty} \sum_{m=0}^{n} m \left\{ \left[g_n^m \sin(m\phi) + h_n^m \cos(m\phi)\right] \left(\frac{a}{r}\right)^{n+2} \right. \\ &\left. + \left[q_n^m \sin(m\phi) + s_n^m \cos(m\phi)\right] \left(\frac{r}{a}\right)^{n-1} \right\} P_n^m(\cos\theta). \end{aligned} \tag{1.20}$$

One way to judge the relative contribution that is provided by the Gauss coefficients is to calculate their power spectrum. For this the Lowes-Mauersberger power spectrum is applied [70]

DOI: 10.2312/GFZ.b103-08029

for spherical harmonic degree, n:

$$W_n = (n+1)\sum_m \left((g_n^m)^2 + (h_n^m)^2 \right). \tag{1.21}$$

Plotting Eq. (1.21) for different models demonstrates its utility in seeing the separation between core and crustal field sources, it can also give a measure of relative noise levels for higher degree terms. One clear observation is that the core field dipole term carries most of the power. It is also clear that the slope of power spectrum changes abruptly in a transition zone between $13 < n < 15$ where the relative contribution of the core field gives way to the crustal field and the power levels off. The lack of power in the low degree terms of the Mars model, m071801, indicates that Mars no longer generates a core field. The Magsat model, m102389, shows a slight increase in power at higher terms, more so than the CHAOS model. This is an indication of higher noise in these terms, which should be expected considering the quality and breadth of the differing input datasets.

Normally, a spherical harmonic expansion allows one to study the magnetic field and its change at the Earth's surface. However, it is often required that information is needed at something different from the reference radius. This can be accommodated though the procedure of upward or downward continuation where measurements made at one source distance are adjusted to that of another. In effect, upward continuation is a smoothing function and maps, at the higher altitudes, the contribution of the most extended sources. On the other hand, downward continuation strongly amplifies the smallest variations in the signal and as a result is critically sensitive to any noise in the original data.

1.7 Geomagnetic Field Models

Geomagnetic field models are useful tools for describing the state of the magnetic field during different epochs and under different conditions. The methods utilized vary across the different models. Some, like the TIE–GCM, are based almost solely on physical principles, while most are empirically based utilizing various sources of data and incorporating differing levels of physical assumptions. Here I briefly mention some of the models that are used in some context during the course of this study, but more detailed descriptions are included in the relevant sections.

1.7.1 Previous main field modeling experience

Prior to commencement of the research at hand, I was fortunate enough to be involved with the development of some main field modeling research. The models developed were relatively high

DOI: 10.2312/GFZ.b103-08029

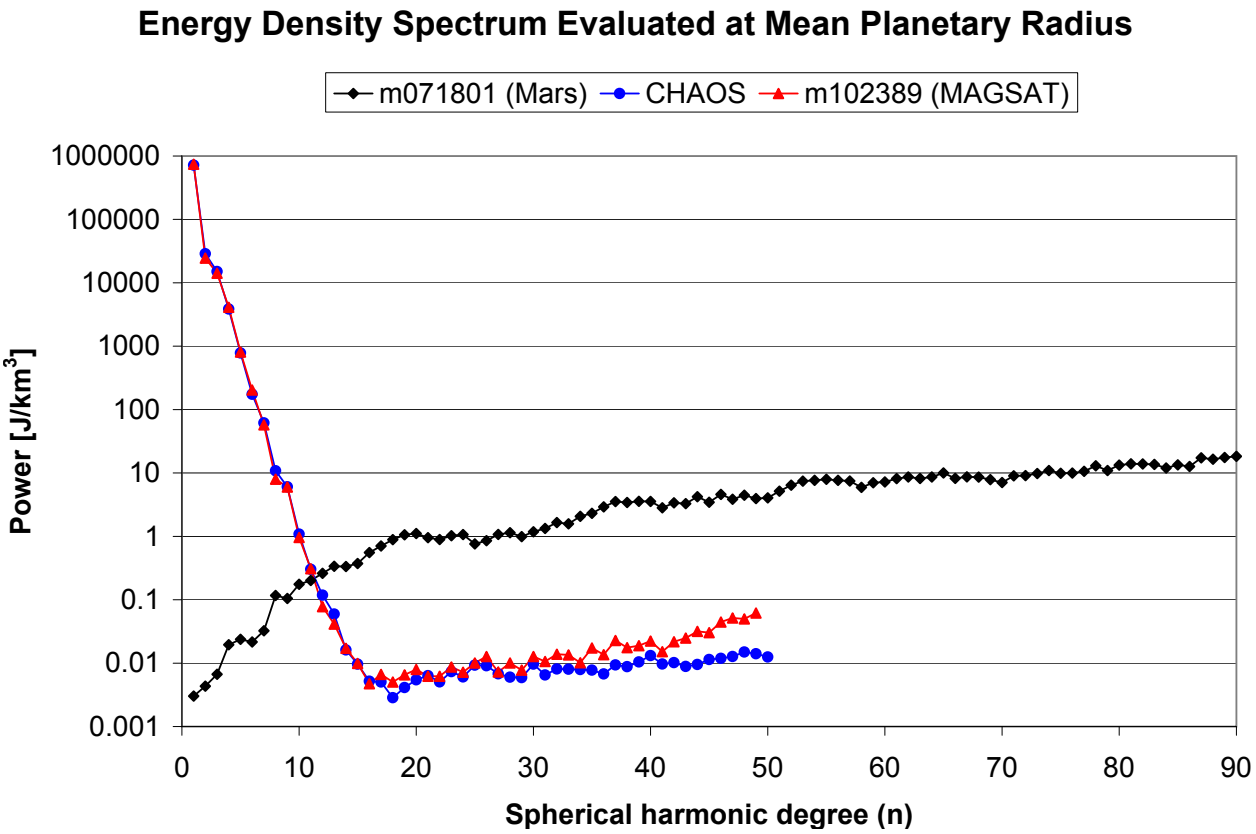

Figure 1.20: The Lowes-Mauersberger Power Spectrum for the m102389 (Magsat), CHAOS (Ørsted/CHAMP) and m071801 (Mars) models. The Earth models show a strong disparity in power between the early degrees, approximately 1–13, which are dominated by the core field and the crustal sources dominating thereafter. The lack of a Martian core field is reflected in the absence of strong power in low degree terms of the m071801 model.

degree spherical harmonic models, which included up to second order secular variation terms. These models were derived using mostly highly selected Ørsted and CHAMP scalar and vector data, but also included were data from magnetic observatories in the form of secular change values. The observatory secular change data (minute, monthly means, and annual means) were computed by fitting to a function, the rate of change (slope) of the individual vector component time-series, which depending upon the specific circumstances could include up to a second order polynomial plus a sinusoid. This research was able to show how the secular variation changed over the period from 1995–2000, and based on an error analysis of the data inversion's co-variance matrix, we were able to show a prediction of the propagation of errors over time [71].

The modeling methodology developed for the Earth's geomagnetic field was adapted to model

DOI: 10.2312/GFZ.b103-08029

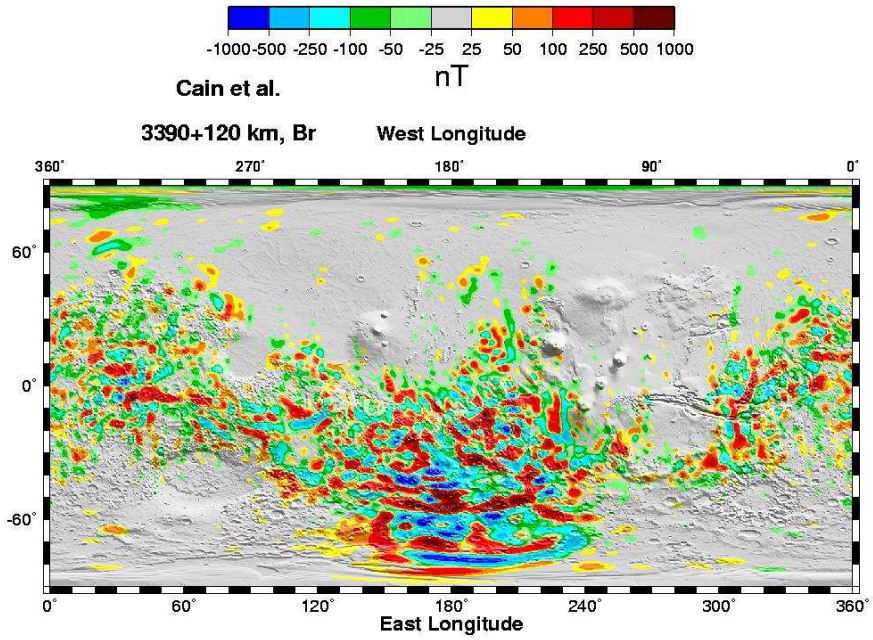

Figure 1.21: A B_r field anomaly map based on the Cain model [16] of the Martian surface, which highlights the relatively low magnetic field in the newer crust of the northern hemisphere and the small scale, high intensity magnetic anomalies in the southern hemisphere [72].

the Martian magnetic field using Mars Global Surveyor data. This resulted in a very high degree $n = 90$ SHC model which was useful in studying the Martian internal field, which today arises solely from remnant magnetization in the crust, because the dynamo processes in the core of Mars have essential shut down. The Martian magnetic field (see Fig. 1.21) displays a strong dichotomy whereby the northern lowlands are relatively devoid of any strong magnetic field signatures, because it is believed that the surface geology in this region is newer and developed after the cessation of the dynamo. The southern highlands, on the other hand, indicate older crust, which contains a highly variable, high intensity, anomaly field [16].

1.7.2 Models utilized in this project

TIE–GCM

The Thermosphere-Ionosphere Electrodynamics General Circulation Model (TIE–GCM) [6], developed at the National Center for Atmospheric Research (NCAR), is a self-consistent, physics-based simulation of neutral winds, conductivities, electric fields, various atmospheric species concentrations, temperatures, and current densities having minimal direct observational input data. At the

DOI: 10.2312/GFZ.b103-08029

heart of the model, with regards to ionospheric electrodynamics, is the ionospheric wind dynamo, which is a process whereby thermospheric winds in the upper atmosphere transport the charged ions in the ionosphere through the geomagnetic field generating electric fields and currents [73]. An important aspect is that the modeled current densities can later be post-processed to compute magnetic perturbations both above and below the ionosphere. Comparing these perturbations with CHAMP residuals is the basis for the external perturbation investigation of Chap. 2.

CHAOS

The CHAOS (CHAMP, Ørsted and SAC-C) [7] model describes the Earth's magnetic field over the time frame of the current epoch (1999–2005). It models the geomagnetic field using spherical harmonics up to degree $n = 50$ for the static field, $n = 18$ for the first time derivative (secular variation), and $n = 14$ for the quadratic and cubic time derivatives. The temporal variation of the core field is described using splines (for $n \leq 14$). It was developed using high-precision, geomagnetic measurements from the Ørsted, CHAMP and SAC-C satellite missions. I use this model extensively throughout both parts of this study; however, it plays its most important role in the external perturbation study. Geomagnetic field values computed from this model are subtracted from CHAMP data to calculate the residuals, which in turn are compared with the TIE–GCM predictions.

gufm1

The gufm1 is a model of the magnetic field for the interval spanning 1590–1990. The model's early data is largely based on historical observations of the magnetic field by mariners engaged in merchant and naval shipping. The time-dependent field model constructed from the dataset is parameterized spatially in terms of spherical harmonics and temporally in B-splines. The fact that the model was specifically designed to aid in core field modeling, and represents the longest continuous model of the field available (from direct observation) [8, 27], makes it ideal for studying the South Atlantic Anomaly (SAA) in Chap. 3.

CM4

The Comprehensive Model – Phase 4 (CM4) [74] is a SHC model of the quiet-time, near-Earth magnetic field that has been derived using a comprehensive approach, covering the years from 1960 through mid-2002. As such, this one model is able to describe field contributions from core,

DOI: 10.2312/GFZ.b103-08029

lithosphere, external and induced sources. It incorporates satellite data from the POGO, Magsat, Ørsted and CHAMP missions, as well as quiet-time observatory hourly mean data from 1960 through 2000. This model is also utilized in the SAA study of Chap. 3.

IGRF

The International Geomagnetic Reference Field (IGRF/DGRF models) is a relatively low degree spherical harmonic (SHC) model, which the international geomagnetic community at large has developed as a general purpose main field and secular variation model [75]. It covers the range 1900–2005 and is recomputed every five years along with a new five-year secular variation prediction. The TIE–GCM uses this model for calculating magnetic field lines during its modified apex coordinate computation. I also use this model while investigating the SAA.

CALS7K.2

CALS7K.2 [26, 76] is a main field model covering the past 7000 years based on archeomagnetic, lava and lake sediment data. The spatial and temporal resolution is significantly lower than that of current epoch models, but it describes the general, large-scale evolution of the dipole moment and secular variation of the geomagnetic field over the past several millennia. I make use of this model in Chap. 3 when attempting to study the long-term nature of the SAA.

DOI: 10.2312/GFZ.b103-08029

CHAPTER 2

External Perturbations: As seen by the CHAMP satellite & the TIE–GCM

2.1 Introduction

The present study is an effort to better understand the external sources of the geomagnetic field by first evaluating the prospect of comparing a physics based model with limited direct observational data with that of observed data, hoping that it may in turn help with the development of future geomagnetic main field models. The results during the initial stage are described in proceedings paper [77] and then further developed in a journal article [78]. The Thermosphere-Ionosphere Electrodynamics General Circulation Model (TIE–GCM) [6] is a self-consistent global atmospheric model being developed at the National Center for Atmospheric Research (NCAR) in Boulder, Colorado. This model can be used to predict many different atmospheric quantities, such as wind velocities, various atmospheric species concentrations, temperatures, electric fields, and current densities. The current densities can later be post-processed to compute magnetic perturbations both above and below the ionosphere.

In order to validate these model results, one can compare the predicted perturbations calculated at the altitude of the CHAMP satellite (taken to be 430 km) with vector residuals computed from the difference of the CHAMP data and the CHAOS geomagnetic model [7]. For the first comparison, the quietest day of each month from 2001–2005 according to the list of international Q–days, was selected. New residuals can then be computed between the original CHAMP/CHAOS residuals and estimates from the different TIE–GCM model runs for these quiet days. A subsequent study takes a look at the effect of changing the K_p value while everything else is fixed for the quietest day of each year. After demonstrating that the TIE–GCM is able to reproduce, to some degree, the CHAMP residuals, I look to see if correcting the field data for the TIE–GCM prediction is of overall benefit while developing a new spherical harmonic main field model.

DOI: 10.2312/GFZ.b103-08029

2.1.1 TIE–GCM

The TIE–GCM [6] is a self-consistent, physics-based simulation of neutral winds, conductivities, electric fields, various atmospheric species concentrations, and current densities having minimal direct observational input data. With only the highlights discussed herein, please consult the literature [6, 65] for a proper treatment of this multifaceted model.

At the heart of the model, with regards to ionospheric electrodynamics, is the ionospheric wind dynamo. It is a process whereby thermospheric winds in the upper atmosphere transport charged ions in the ionosphere through the geomagnetic field, which generates electric fields and currents [73].

$$\mathbf{J} = \sigma_P(\mathbf{E} + \mathbf{u} \times \mathbf{B}) + \sigma_H \mathbf{b} \times (\mathbf{E} + \mathbf{u} \times \mathbf{B}) + \mathbf{J}_{\parallel} + \mathbf{J}_M \tag{2.1}$$

The Ohm's law expression for the current density in Eq. (2.1) is used to solve for the electric field equatorward of 60° magnetic latitude (imposed otherwise). In Eq. 2.1, $\mathbf{B}$ is the magnetic field with parallel unit vector $\mathbf{b}$, $\mathbf{E}$ is the electric field, $\mathbf{u}$ is the neutral wind velocity, and σ_P and σ_H are the Pedersen and Hall conductivities. Also included is a field aligned component of the current density $\mathbf{J}_{\parallel}$ and a non-ohmic, magnetospheric component $\mathbf{J}_M$.

The International Geomagnetic Reference Field (IGRF/DGRF models, see Sec. 1.7.2 or Sec. 3.3) [75] is used for the purpose of casting the formulation into modified magnetic apex coordinates [65], which is a more convenient coordinate frame for performing the calculations. As a simplifying measure, geomagnetic field lines are assumed to be equipotential, which reduces the electrodynamic equations to two dimensions. In order to ensure that the divergence of the total current vanishes, it is assumed that field-aligned current flows between both hemispheres. Induced Earth currents are simulated assuming a perfectly conducting layer at a depth of 600 km below the Earth's surface. Height-integrated horizontal ionospheric currents are treated as currents in a thin shell at an altitude of 110 km, connected to field-aligned currents. Atmospheric tides from the Global Scale Wave Model (GSWM) [79, 80] can be used as a lower boundary condition and magnetic activity index values, like K_p and $F_{10.7}$ (see Secs. 1.5.3–1.5.3), can be varied to simulate desired atmospheric conditions and configurations [81].

2.1.2 CHAOS

Briefly stated, the CHAOS (CHAMP, Ørsted and SAC-C) [7] model describes the Earth's magnetic field over the time frame of the current epoch. It models the geomagnetic field using spherical

DOI: 10.2312/GFZ.b103-08029

harmonics up to degree $n = 50$ for the static field, $n = 18$ for the first time derivative (secular variation), and $n = 14$ for the quadratic and cubic time derivatives. The temporal variation of the core field is described using splines (for $n \leq 14$). It was developed using high-precision, geomagnetic measurements from the Ørsted, CHAMP and SAC-C satellite missions spanning over 6.5 years (including data between March, 1999 - December, 2005). It incorporates into its dataset higher than usual geomagnetic activity ($K_p \leq 2$). It uses magnetometer vector data in the instrument frame and simultaneously estimates the Euler angles that describe the transformation from the magnetometer frame to the star camera frame, thus avoiding the potential inconsistency of using vector data that have been aligned with another field model. The slight bending of the CHAMP optical bench, connecting the magnetometer and star camera, is taken into account by estimating Euler angles in 10 day segments. It also determines $n = 1$ external fields separately for every 12-hour interval. The model coefficients and codes required to compute field values at arbitrary times and locations are available for download from either the GeoForschungsZentrum Potsdam [82] or the Danish National Space Center [83].

2.2 Dates Selected for Investigation

Table 2.1: The selected dates used in this comparison study represent the quietest day of each month from 2001–2005 as determined by the list of International Q–days.

Date (2001)	**Date (2002)**	**Date (2003)**	**Date (2004)**	**Date (2005)**
Jan 01, 2001	Jan 03, 2002	Jan 09, 2003	Jan 08, 2004	Jan 26, 2005
Feb 03, 2001	Feb 14, 2002	Feb 25, 2003	Feb 26, 2004	Feb 05, 2005
Mar 15, 2001	Mar 17, 2002	Mar 25, 2003	Mar 24, 2004	Mar 04, 2005
Apr 30, 2001	Apr 08, 2002	Apr 07, 2003	Apr 02, 2004	Apr 10, 2005
May 31, 2001	May 24, 2002	May 04, 2003	May 26, 2004	May 26, 2005
Jun 28, 2001	Jun 28, 2002	Jun 12, 2003	Jun 22, 2004	Jun 21, 2005
Jul 28, 2001	Jul 14, 2002	Jul 08, 2003	Jul 08, 2004	Jul 06, 2005
Aug 16, 2001	Aug 06, 2002	Aug 31, 2003	Aug 04, 2004	Aug 11, 2005
Sep 10, 2001	Sep 23, 2002	Sep 28, 2003	Sep 11, 2004	Sep 24, 2005
Oct 24, 2001	Oct 13, 2002	Oct 11, 2003	Oct 17, 2004	Oct 15, 2005
Nov 03, 2001	Nov 08, 2002	Nov 28, 2003	Nov 06, 2004	Nov 16, 2005
Dec 09, 2001	Dec 18, 2002	Dec 19, 2003	Dec 04, 2004	Dec 23, 2005

Generally speaking, most main field modeling tends to restrict its input datasets to include only

DOI: 10.2312/GFZ.b103-08029

Table 2.2: The quietest day for each month in 2001 as determined by the list of International Q–days and its associated model and magnetic activity parameters. June 28, 2001 (star) was selected as the quietest day of the year.

Date (2001)	**MJD2000**	**DOY**	**Model Date**	$\mathbf{K}_p$	$\mathbf{F}_{10.7}$	**SLT**	$\mathbf{Q}_{Rank}$
Jan 1	366	1	01-02	$0\ -1$	165.3	11.0, 23.0	1
Feb 3	399	34	32-35	$0\ -1^-$	159.0	8.0, 20.0	1
Mar 15	439	74	72-75	$0\ -1$	134.7	4.4, 16.4	1
Apr 30	485	120	118-121	$0\ -1$	190.7	0.2, 12.2	1
May 31	516	151	149-152	$0\ -1$	136.6	9.3, 21.3	1
⋆Jun 28	544	179	177-180	$0\ -1^-$	144.9	6.8, 18.8	1
Jul 28	574	209	207-210	$0^+ - 1$	119.0	4.1, 16.1	1
Aug 16	593	228	226-229	$0^+ - 1$	146.2	2.4, 14.4	1
Sep 10	618	253	251-254	$0^+ - 1^+$	247.8	2.0, 12.1	1
Oct 24	662	297	295-298	$0\ -1^-$	236.0	8.1, 20.1	1
Nov 3	672	307	305-308	$0\ -1^-$	212.5	7.2, 19.2	1
Dec 9	708	343	341-344	$0\ -2^-$	217.5	3.9, 15.9	1

Table 2.3: The quietest day for each month in 2002 as determined by the list of International Q–days and its associated model and magnetic activity parameters. May 24, 2002 (star) was selected as the quietest day of the year.

Date (2002)	**MJD2000**	**DOY**	**Model Date**	$\mathbf{K}_p$	$\mathbf{F}_{10.7}$	**SLT**	$\mathbf{Q}_{Rank}$
Jan 3	733	3	01-04	$0\ -1$	213.0	1.7, 13.7	1
Feb 14	775	45	43-46	$0\ -2^-$	191.3	9.8, 21.8	1
Mar 17	806	76	74-77	$0\ -1$	182.7	7.0, 19.0	1
Apr 8	828	98	96-99	$0\ -1^-$	206.8	5.0, 17.0	1
⋆May 24	874	144	142-145	$0\ -1^-$	193.9	0.8, 12.8	1
Jun 28	909	179	177-180	$0^+ - 1^-$	141.9	9.6, 21.6	1
Jul 14	925	195	193-196	$0^+ - 1^-$	148.6	8.1, 20.1	1
Aug 6	948	218	216-219	$0^+ - 2$	148.8	6.0, 18.0	1
Sep 23	996	266	264-267	$0\ -1$	154.8	1.6, 13.6	1
Oct 13	1016	286	284-287	$1\ -2^-$	178.3	11.8, 21.0	1
Nov 8	1042	312	310-313	$0^+ - 2$	185.5	9.4, 21.4	1
Dec 18	1082	352	350-353	$0^+ - 1^+$	190.6	5.7, 17.8	1

DOI: 10.2312/GFZ.b103-08029

Table 2.4: The quietest day for each month in 2003 as determined by the list of International Q–days and its associated model and magnetic activity parameters. December 19, 2003 (star) was selected as the quietest day of the year.

Date (2003)	**MJD2000**	**DOY**	**Model Date**	$\mathbf{K}_p$	$\mathbf{F}_{10.7}$	**SLT**	$\mathbf{Q}_{Rank}$
Jan 9	1104	9	07-10	$0 - 2^+$	176.9	3.8, 15.8	1
Feb 25	1151	56	54-57	$1^- - 2$	99.5	11.5, 23.5	1
Mar 25	1179	84	82-85	$0 - 1^+$	108.2	8.9, 20.9	1
Apr 7	1192	97	95-98	$0^+ - 3^-$	115.9	7.7, 19.7	1
May 4	1219	124	122-125	$0 - 2$	144.4	5.3, 17.3	1
Jun 12	1258	163	161-164	$1^+ - 2^+$	168.6	1.7, 13.7	1A
Jul 8	1284	189	187-190	$0 - 2^-$	135.7	11.3, 23.3	1
Aug 31	1338	243	241-244	$1 - 2$	111.8	6.4, 18.4	1
Sep 28	1366	271	269-272	$0^+ - 2^-$	137.6	3.8, 15.8	1
Oct 11	1379	284	282-285	$0 - 1$	105.4	2.6, 14.6	1
Nov 28	1427	332	330-333	$0^+ - 2^+$	163.2	10.2, 22.2	1
⋆Dec 19	1448	353	351-354	$0 - 1^-$	118.6	8.3, 20.3	1

Table 2.5: The quietest day for each month in 2004 as determined by the list of International Q–days and its associated model and magnetic activity parameters. December 4, 2004 (star) was selected as the quietest day of the year.

Date (2004)	**MJD2000**	**DOY**	**Model Date**	$\mathbf{K}_p$	$\mathbf{F}_{10.7}$	**SLT**	$\mathbf{Q}_{Rank}$
Jan 8	1468	8	06-09	$0^+ - 3^+$	116.1	6.5, 18.5	1A
Feb 26	1517	57	55-58	$0 - 2^-$	118.4	1.9, 14.0	1
Mar 24	1544	84	82-85	$0^+ - 1^+$	119.0	11.5, 23.5	1
Apr 2	1553	93	91-94	$0^+ - 2^-$	108.1	10.7, 22.7	1
May 26	1607	147	145-148	$0^+ - 1^+$	106.1	5.7, 17.7	1
Jun 22	1634	174	172-175	$0^+ - 1^-$	120.5	3.2, 15.2	1
Jul 8	1650	190	188-191	$0^+ - 1^-$	84.6	1.8, 13.8	1
Aug 4	1677	217	215-218	$0 - 1^+$	87.9	11.2, 23.3	1
Sep 11	1715	255	253-256	$0 - 1$	117.9	7.8, 19.8	1
Oct 17	1751	291	289-292	$0 - 1^-$	91.2	4.5, 16.5	1
Nov 6	1771	311	309-312	$0 - 1^-$	126.5	2.7, 14.7	1
⋆Dec 4	1799	339	337-340	$0 - 0$	94.6	4.0, 12.1	1

DOI: 10.2312/GFZ.b103-08029

Table 2.6: The quietest day for each month in 2005 as determined by the list of International Q–days and its associated model and magnetic activity parameters. December 23, 2005 (star) was selected as the quietest day of the year.

Date (2005)	**MJD2000**	**DOY**	**Model Date**	$\mathbf{K}_p$	$\mathbf{F}_{10.7}$	**SLT**	$\mathbf{Q}_{Rank}$
Jan 26	1852	26	24-27	$0^+ - 1^-$	86.6	7.2, 19.2	1
Feb 05	1862	36	34-37	$0 - 1$	92.0	6.3, 18.3	1
Mar 04	1889	63	61-64	$0 - 1$	77.7	3.8, 15.8	1
Apr 10	1926	100	98-101	$0 - 1$	88.6	0.4, 12.4	1
May 26	1972	146	144-147	$0 - 0^+$	92.8	17.5, 17.5	1
Jun 21	1998	172	170-173	$0 - 1$	85.5	5.8, 17.8	1
Jul 06	2013	187	185-188	$1^- - 1^+$	127.2	4.4, 16.4	1
Aug 11	2049	223	221-224	$0 - 1^+$	77.9	1.1, 13.1	1
Sep 24	2093	267	265-268	$0^+ - 1^+$	81.9	9.0, 21.0	1
Oct 15	2114	288	286-289	$0 - 1^-$	79.1	7.1, 19.1	1
Nov 16	2146	320	318-321	$0^+ - 1^+$	91.8	4.1, 16.1	1
⋆Dec 23	2183	357	355-358	$0 - 0^+$	90.1	0.7, 12.7	1

data taken during local night-time hours under low magnetic activity conditions, in an effort to minimize external and other transient effects. For this reason it was decided to use only days with low geomagnetic activity for this initial comparison study since it is the most likely category of data to have immediate use in the modeling community. The dates selected represent the quietest day of each month, in terms of geomagnetic activity, spanning the years 2001–2005 as determined by the list of International Q–days. Tab. 2.1 lists the actual dates investigated while Tabs. 2.2-2.6 further detail their corresponding magnetic activity (with a graphic representation displayed in Fig. 2.1). Listed also in these tables is the range of dates over which the TIE–GCM was run, which usually includes a two day initial buffer so as to allow the model to achieve an equilibrium state by the time the dates of interest are reached. A column is included that lists the across-the-day average of the two CHAMP solar local time orbit planes for each day. An A under the Q_{Rank} column means that while that particular day was the quietest during the month, it relatively speaking, would not be called very quiet. For example, Jan 8, 2004 in Tab. 2.5 is the quietest day of the month but the K_p for the day ranges as high as 3^+. There is also a column of the Modified Julian Day (MJD2000) [84, 85] referenced to the year 2000 and a column of the corresponding Day of Year (DOY) number.

DOI: 10.2312/GFZ.b103-08029

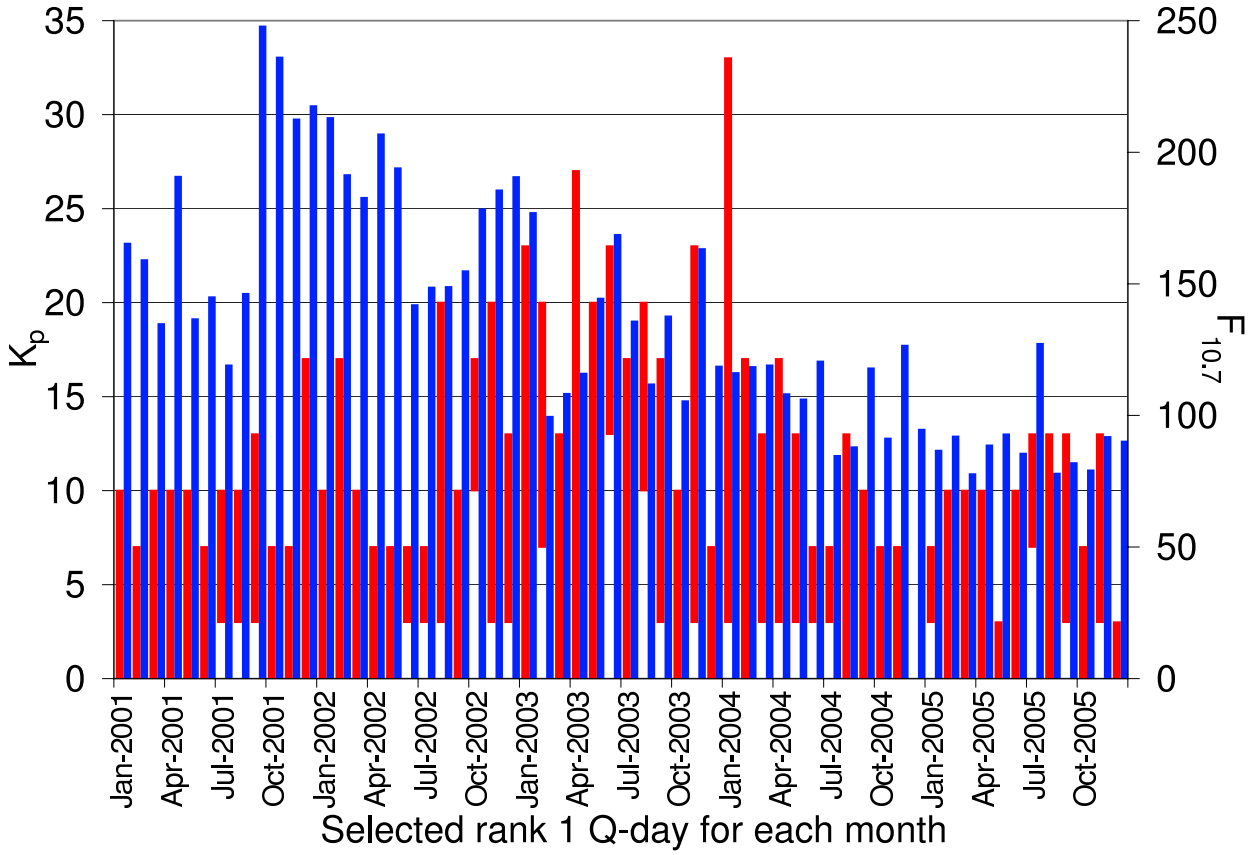

Figure 2.1: Activity indices including the K_p range (red) and $F_{10.7}$ (blue) for the selected rank 1 Q–days of each month.

2.3 TIE–GCM Method

The procedure utilized in comparing the model results with that of the CHAMP data involved using the TIE–GCM to model each of the 60 quiet days from 2001 to 2005 listed in Tab. 2.1. In order to investigate the model's sensitivity across a wide range of magnetic activity, the following five cases of the input parameter $F_{10.7}$ (measured in solar flux units, $1\,\mathrm{sfu} = 10^{-22}\,\mathrm{Wm^{-2}Hz^{-1}}$, see Sec. 1.5.3) were used for each day: $F_{10.7} = 70$, 90, 150, 190 and GPI (where GPI uses a geophysical indices database to compute real-time values, interpolating for every time-step). $F_{10.7}$ is a proxy for the solar UV flux impinging on the atmosphere and so plays a major role in the atmospheric processes, like the wind dynamo, which govern the interactions ultimately responsible for the development of the ionospheric magnetic fields measured by spacecraft like CHAMP. While the true landscape of the current systems in the atmosphere exists in an assorted array of complex

DOI: 10.2312/GFZ.b103-08029

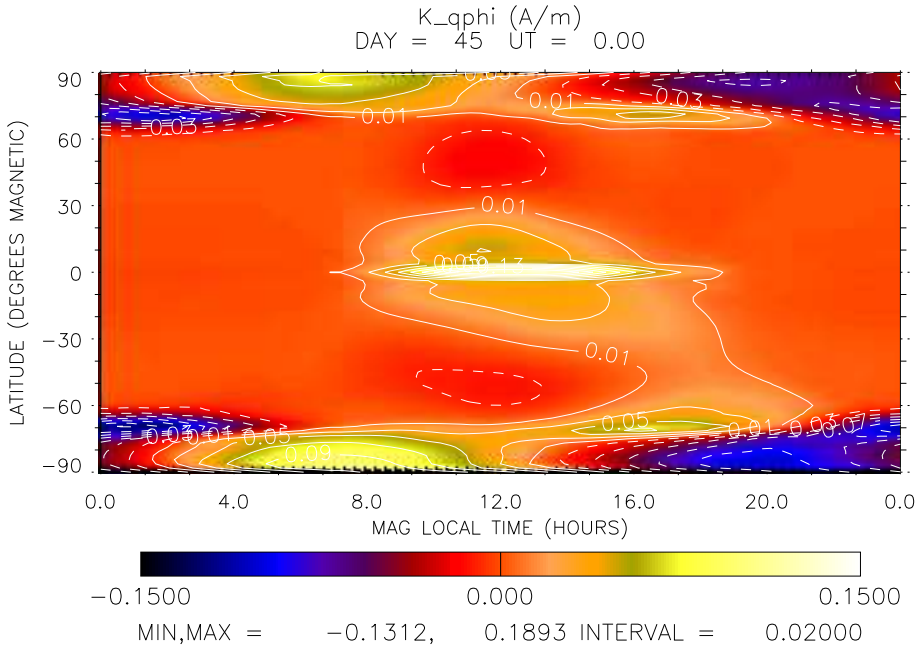

(a) Eastward component

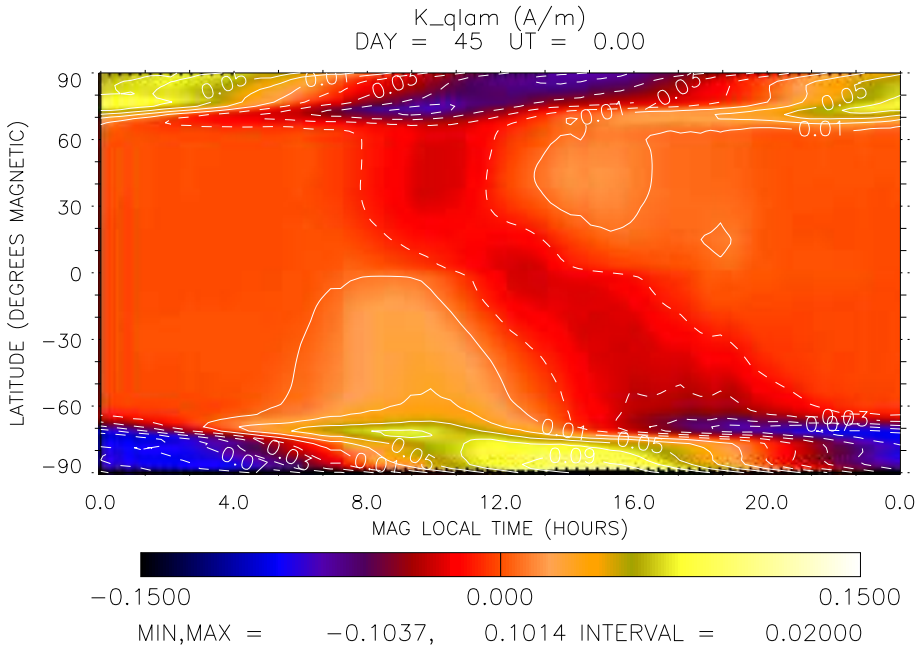

(b) Northward component

Figure 2.2: The eastward and northward components of the height-integrated horizontal current density, in A/m, predicted by the TIE–GCM for February 14, 2002 using GPI inputs.

DOI: 10.2312/GFZ.b103-08029

3D configurations, the TIE–GCM reduces this complexity down to a height-integrated current sheet. However this simplifying measure, when viewed from above or below the ionosphere, has little effect when measured a distance away from the ionosphere.

The model permits its lower boundary condition to be specified by the Global Scale Wave model (GSWM); therefore, included were the full complement of both the migrating (diurnal and semidiurnal) and non-migrating (diurnal and semidiurnal) atmospheric tides, which are global, periodic density variations of the atmosphere. The default integrated Heelis electric potential model [86] was invoked. In addition, a two-day initial buffer was considered so as to allow the model to achieve an equilibrium state by the time the dates of interest were reached. The model internally calculates all quantities at every time-step (2 minutes) but the output was only recorded to disk once per modeled hour due to data file size constraints.

Fig. 2.2 represents the TIE–GCM prediction of the height-integrated horizontal current density for February 14, 2002 using real-time GPI inputs rather than fixed activity index values for the northward and eastward components. There exists a great deal of variability in the polar regions, however, so in the forthcoming analyses only the mid-latitude region between $\pm 50^\circ$ magnetic latitude will be considered. The reason for this is two-fold: firstly the model is less reliable in the polar region since it imposes an electric field distribution, and secondly the strongly variable and unpredictable nature of the polar regions make the CHAMP vector data less consistent. Being restricted to the mid-latitudes during quiet-times helps to maximize the visibility of the more consistent systems like Sq and the Equatorial Electro-Jet (EEJ). Most importantly the EEJ signature has been reproduced in the eastward component, with amplitude of around 0.15 A/m, centered, as expected, on the magnetic equator around 12 magnetic local time.

2.4 A Quick Solar Quiet Verification

The most thoroughly studied and best understood of the various types of geomagnetic activity is that of the diurnal Sq variation (it is primarily solar diurnal, with a smaller semidiurnal component and a weak lunar semidiurnal component) [58]. The Sq system (briefly mentioned back in Sec. 1.5.2), approximately symmetric about the noontime magnetic equator (sun synchronous), is comprised of two large vortices flowing on the dayside of the Earth, counterclockwise in the northern hemisphere and clockwise in the southern hemisphere (centered about $\pm 30^\circ$ magnetic latitude, respectively). On average, the total current in each vortex is around 150 kA, although this varies with solar cycle (being a somewhat higher -207 to 252 kA for the solar-maximum conditions in Fig. 2.3(a)) and

DOI: 10.2312/GFZ.b103-08029

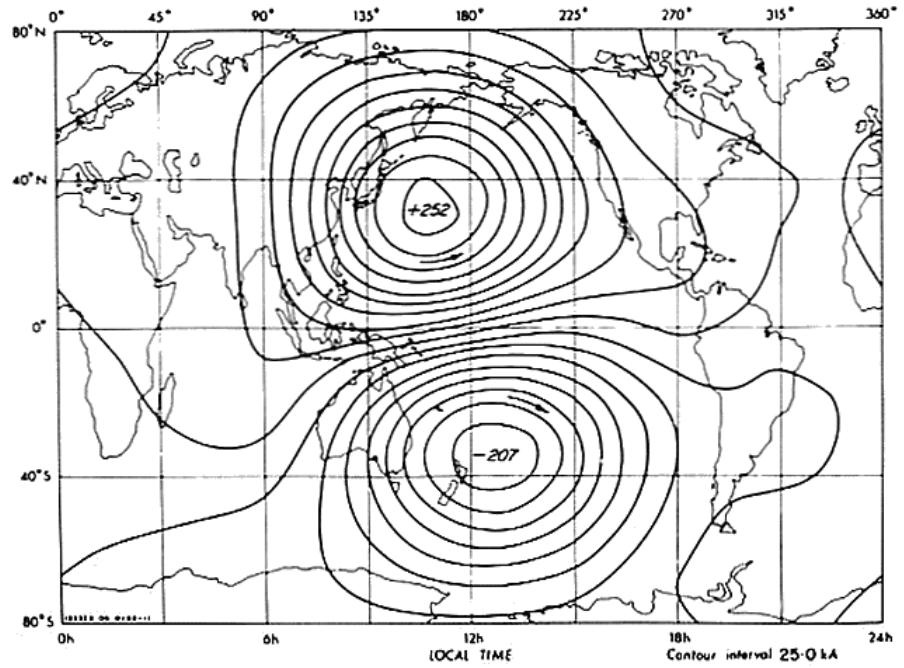

(a) Classic Sq current system

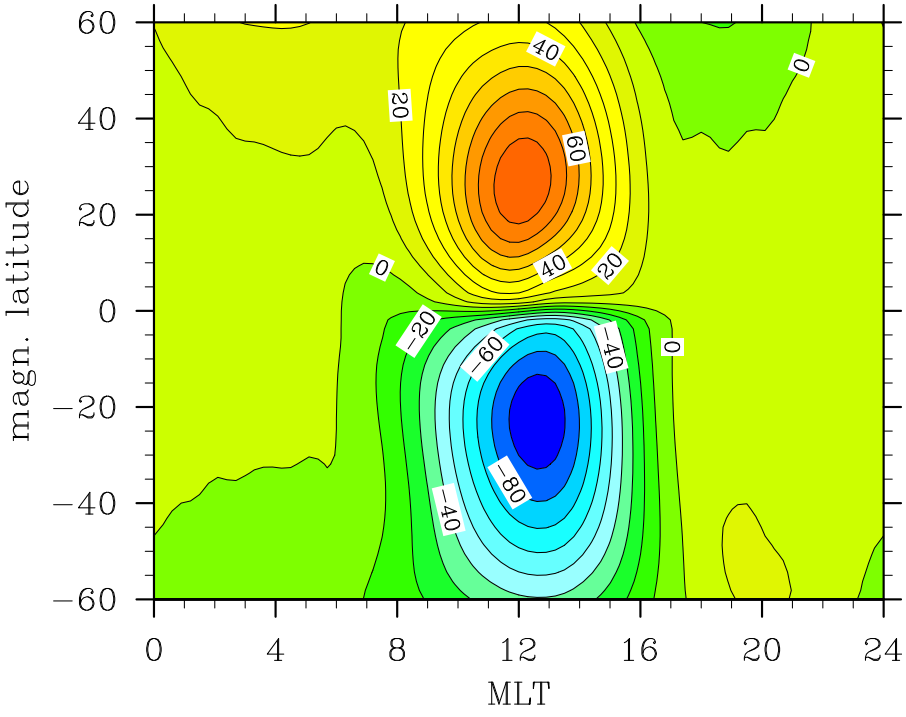

(b) TIE–GCM equivalent current

Figure 2.3: The Sq current system for equinox conditions in units of kA: (a) the classic picture [58, 87] and (b) as calculated by the TIE–GCM [81].

DOI: 10.2312/GFZ.b103-08029

with season (being stronger in summer than winter) [88]. The primary cause of the diurnal variation is a dynamo created by motion of electric charges in the ionosphere across the Earth's magnetic field lines. This motion is driven by winds in the ionosphere, which in turn are mostly driven by solar heating and to a lesser extent lunar and solar tides [58].

Fig. 2.3(a) illustrates the ionospheric current system responsible for the diurnal magnetic field variations evident in the geomagnetic field record at the surface as the observatories rotate beneath the current system. In order to have any confidence in the TIE–GCM's ability to compute reliable magnetic field perturbations, this current system should be reasonably well reproduced. The TIE–GCM computation in Fig. 2.3(b), most importantly, is able to reproduce the general Sq pattern, although the intensity is somewhat reduced, in part because it was not computed during solar maximum conditions. One should note also that the plot for the TIE–GCM calculation is in coordinates of magnetic latitude, which accounts for the absence of the tilt seen in the classic picture about the equatorial region.

2.5 Calculation of Magnetic Perturbations

Reassured by the TIE–GCM's ability to reproduce a reasonable approximation of the Sq current system, the magnetic perturbations are investigated. The calculation process for magnetic perturbations involves making a few assumptions [89]. As noted before, the height-integrated horizontal ionospheric currents are treated as currents in a thin shell located at an altitude of 110 km, and connected to field-aligned currents. The field-aligned currents are treated as though they are flowing on dipolar field lines, while zonal currents in the magnetosphere are ignored. Induced Earth currents are simulated by a perfectly conducting layer at a depth of 600 km below the surface of the Earth. Calculated ground magnetic effects are used to define equivalent horizontal ionospheric currents in a shell at a height of 110 km [90]. A satellite altitude of 430 km is assumed for this calculation.

From the TIE-GCM, a thin shell of height-integrated horizontal ionospheric current density is produced. The equivalent current system, a fictitious divergence-free current sheet, which produces the same magnetic perturbations at the ground, is then calculated. The equivalent current function can be expressed as an expansion in spherical harmonic coefficients, which are then used to calculate the magnetic potential. From the magnetic potential one can compute the magnetic field perturbations.

DOI: 10.2312/GFZ.b103-08029

A thin shell of height-integrated horizontal ionospheric current density is described [65] as:

$$\mathbf{K} = K_{q\phi}\mathbf{f_1} + K_{q\lambda}\mathbf{f_2} \tag{2.2}$$

with basis functions $\mathbf{f_1}$ and $\mathbf{f_2}$ and northward ($K_{q\phi}$) and eastward ($K_{q\lambda}$) directional components which are calculated by the TIE–GCM (e.g. Fig. 2.2).

These components are used to compute an equivalent current function [91]. The equivalent current system is a non-physical current sheet, yet still has the capability of reproducing the same ground magnetic perturbations as does the true three dimensional current system. The difference between this equivalent current function and $K_{q\phi}$ and $K_{q\lambda}$ yields the unequivalent current function. Each of these two current sheets is used in the magnetic perturbation computation at satellite altitude. The equivalent current function can be expressed as an expansion in spherical harmonic coefficients, which are then used to calculate the magnetic potential. From magnetic potential it is straightforward to compute the magnetic field perturbations.

Fig. 2.4(a) represents the northward component at satellite altitude of the magnetic perturbation, produced by post-processing the TIE–GCM predictions of current densities, for February 14, 2002 using real-time GPI inputs. The EEJ signature seen in the eastward component of the height-integrated current density (Fig. 2.2(a)) produces a negative magnetic perturbation, of order $-30\,\mathrm{nT}$, in the northward magnetic perturbation component centered at the equator around 12 magnetic local time.

2.6 $F_{10.7}$ Variation

2.6.1 The effect of varying the $F_{10.7}$ on the TIE–GCM magnetic perturbation predictions

The main thrust so far has been to do a systematic comparison of the effect of $F_{10.7}$ on the TIE–GCM magnetic perturbation predictions and to see how it relates to observed data. To this end the quietest magnetically active day (as discussed earlier in Sec. 2.2) of each month from 2001–2005 have been used for the TIE–GCM calculation.

For each day the model was executed using the GPI and then again with fixed $F_{10.7}$ magnetic activity inputs equal to $F_{10.7} = 70$, 90, 150 and 190. Also held fixed were the cross-tail potential ($CTPOTEN = 45$) and the hemispheric power ($POWER = 16$), which are parameterized in the model to be functions of K_p (see Eqs. (2.3)-(2.4) and Tab. 2.7 discussed later in Sec. 2.7.1).

DOI: 10.2312/GFZ.b103-08029

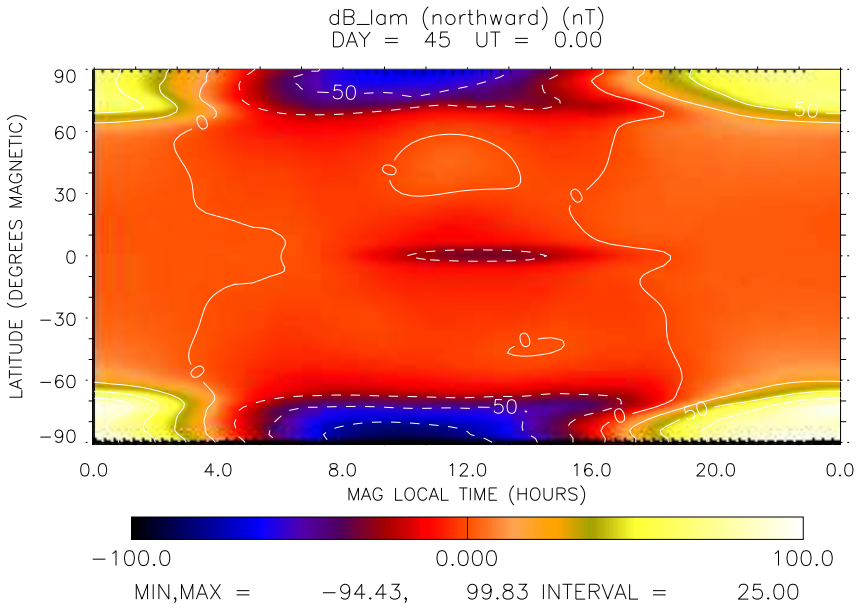

(a) Northward component

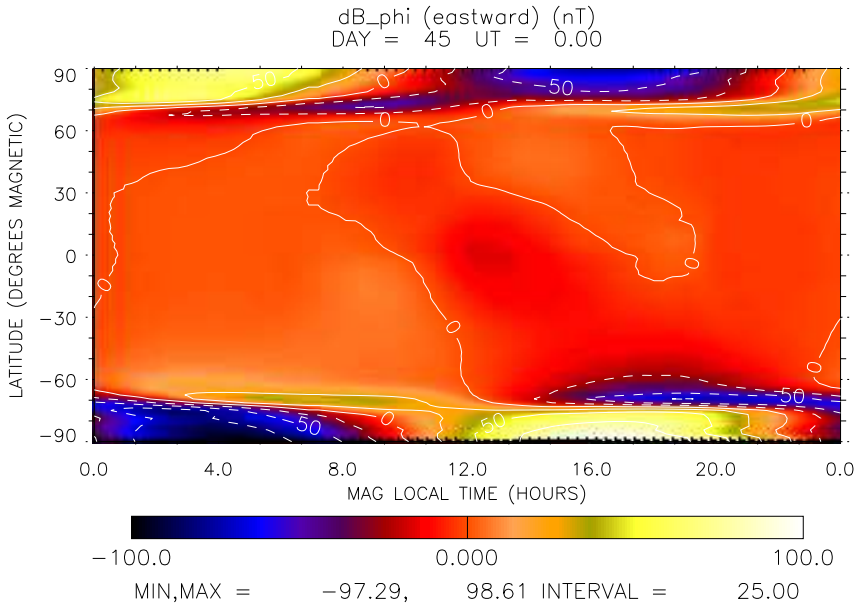

(b) Eastward component

Figure 2.4: The northward and eastward components of the magnetic perturbation, in nT, predicted by the TIE–GCM for February 14, 2002 using GPI inputs.

DOI: 10.2312/GFZ.b103-08029

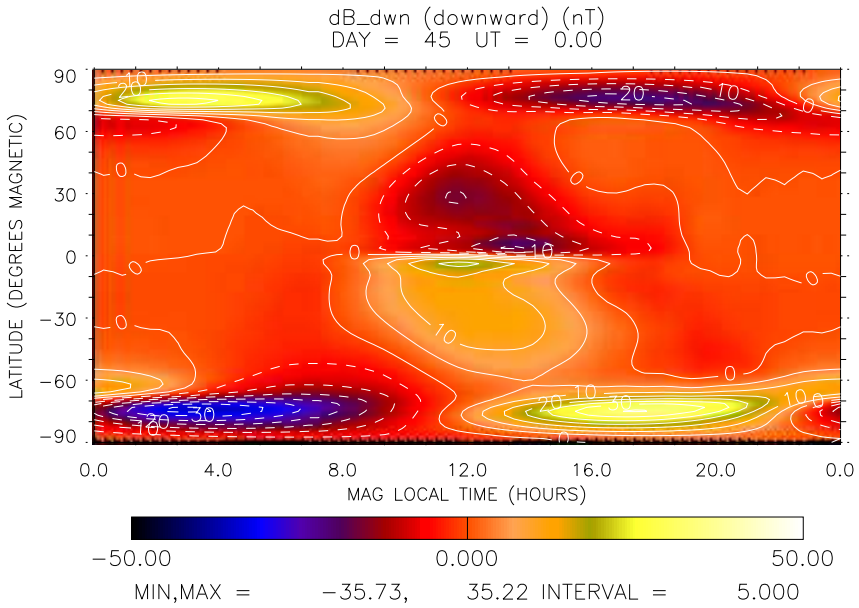

(a) Downward component

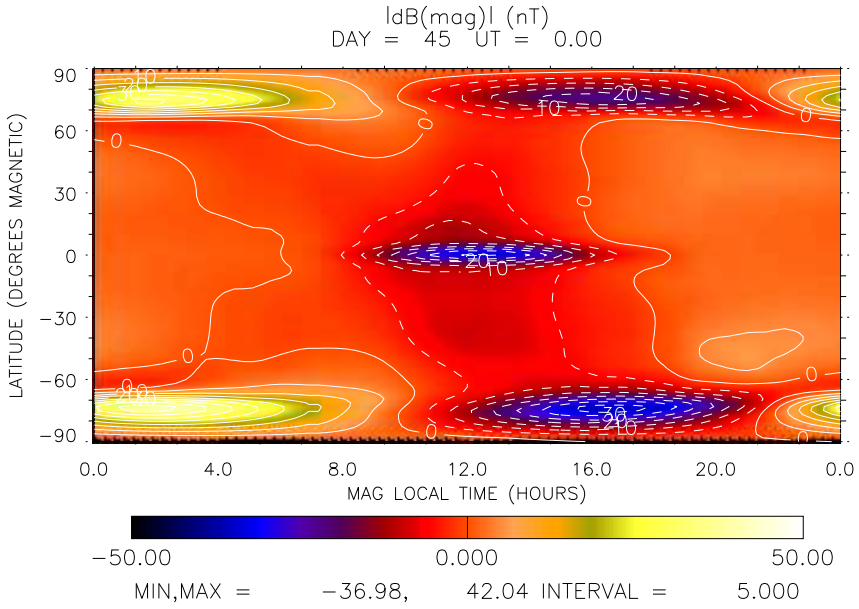

(b) Total field

Figure 2.5: The total field and downward component of the magnetic perturbation, in nT, predicted by the TIE–GCM for February 14, 2002 using GPI inputs.

DOI: 10.2312/GFZ.b103-08029

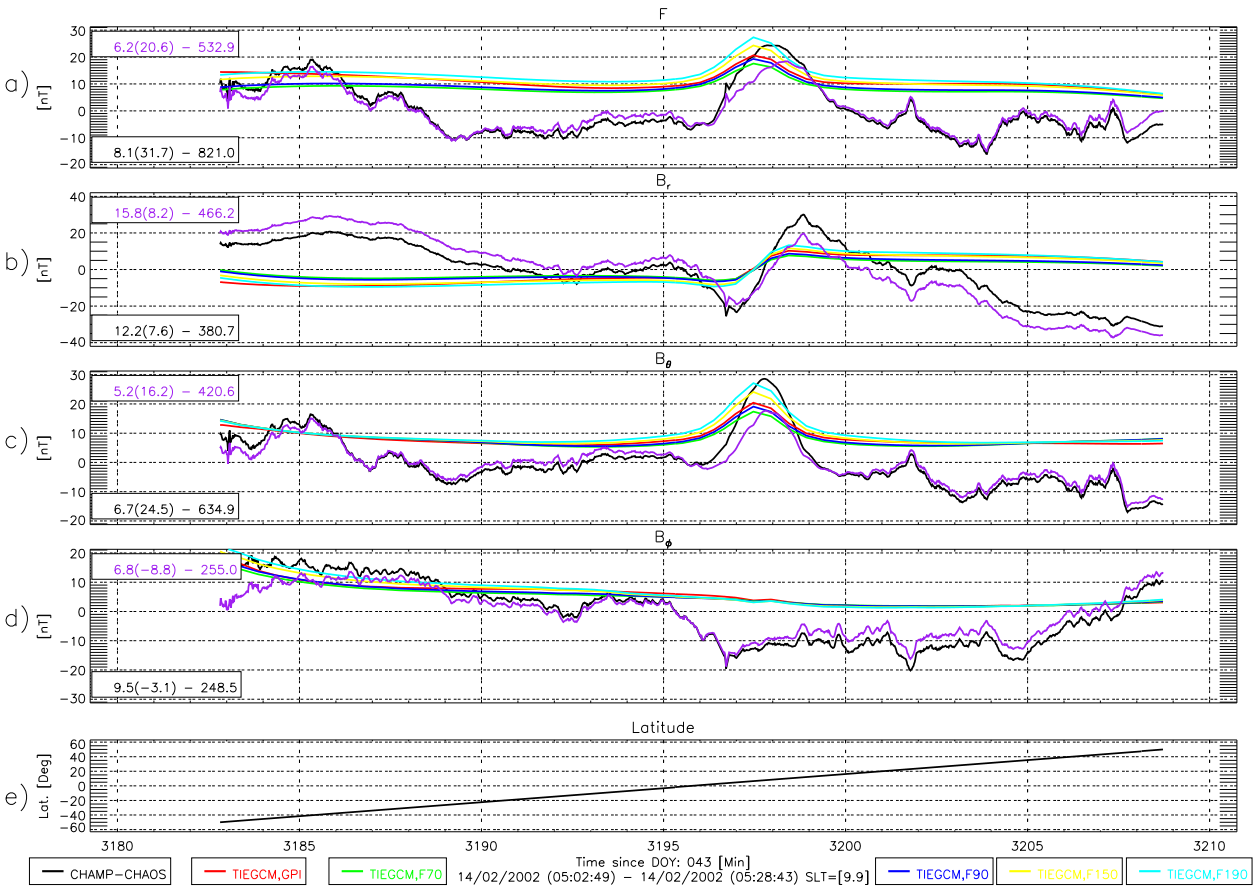

Figure 2.6: The CHAMP residual and TIE–GCM perturbation prediction data along the satellite orbit track for one orbit pass on February 14, 2002 between ±50° latitude. The plot windows correspond to (a) the total field perturbation, (b) the B_r component of the perturbation, (c) the B_θ component, (d) the B_ϕ component, and (e) the satellite latitude. All five TIE–GCM model runs are shown vs. the CHAMP data and perturbation residuals using the following color scheme: $F_{10.7} = 70$ (Green), $F_{10.7} = 90$ (Blue), $F_{10.7} = 150$ (Yellow), $F_{10.7} = 190$ (Cyan), $F_{10.7} = GPI$ (Red), $CHAMP/CHAOS$ Residual (Black), and $CHAMP/CHAOS/TIE\text{–}GCM(GPI)$ Residual (Purple).

2.6.2 Comparison of Model Results

The TIE–GCM magnetic perturbation predictions (Figs. 2.4 and 2.5) were compared with CHAMP/CHAOS residuals along the orbit-track in order to produce Fig. 2.6. The full CHAOS model was used to compute residuals for the corresponding CHAMP vector measurements. Plotted also is a curve representing the residual calculated from the difference of the CHAMP/CHAOS residual and the predicted TIE–GCM magnetic perturbation. The CHAMP/CHAOS and

DOI: 10.2312/GFZ.b103-08029

CHAMP/CHAOS/TIE–GCM residuals have had their mean subtracted so as to remove their offset from zero and bring all datasets to a common level. For this individual plot, the CHAMP satellite was in approximately a 10 AM solar local time (SLT) plane. In the top and bottom left-hand corners, are displayed the absolute mean deviation, mean and area under the curve in the following format: $[MDEV(MEAN) - AREA]$. The MEAN represents an important quantity in terms of the overall offsets. Ideally a CHAMP/CHAOS residual MEAN would be zero, indicating that the model and the data are of equivalent amplitude, but this of course is not the case because of errors as well as unresolved and unmodeled phenomena. Instead an offset is observed, which ideally the TIE–GCM perturbation can partially ameliorate. The MDEV is also important in that it is a measure of the variation in the time series. A residual MDEV of zero would correspond to a straight line and indicate that the CHAMP and CHAOS exactly mirror each other in terms of small scale variations. Again from a practicality standpoint this is not possible and is evidenced by the EEJ signatures visible in the CHAMP/CHAOS residuals because CHAOS does not model such systems. The TIE–GCM, however, does model the EEJ and so if an accurate magnetic perturbation prediction can be computed and is then subtracted out, a reduction in the EEJ signature should be visible, which in turn would reduce (all things being equal) the MDEV value. The AREA statistic is a measure of the area under the residual time-series and so is an amalgamation of the MEAN and MDEV, but can be heavily skewed by a large MEAN value.

The EEJ signature seen in B_θ (Fig. 2.6(c)) for this particular orbit pass is fairly well reproduced in location, even though the amplitude is quite a bit smaller. After the application of the TIE–GCM magnetic perturbation prediction, this component yields both a reduction in MDEV (spread) and MEAN (offset), likewise for the total field (Fig. 2.6(a)). In this case the run with the $F_{10.7}$ held fixed at 190 seems to have produced the best overall fit (the actual $F_{10.7}$ for this date was 191.3). The plot window for the B_r component (Fig. 2.6(b)) shows the ability of the TIE–GCM to reproduce the low/high transition centered around the magnetic equator associated with Sq, however its poorer job in the tail region has it netting a worse overall MDEV and MEAN. The B_ϕ component (Fig. 2.6(d)) has a mixed result whereby the model matched a slight trend but the amplitude was off causing a better MDEV but worse MEAN. But overall Fig. 2.6 actually represents a relatively good fit, whereas many individual day comparisons can show more inconsistent results.

DOI: 10.2312/GFZ.b103-08029

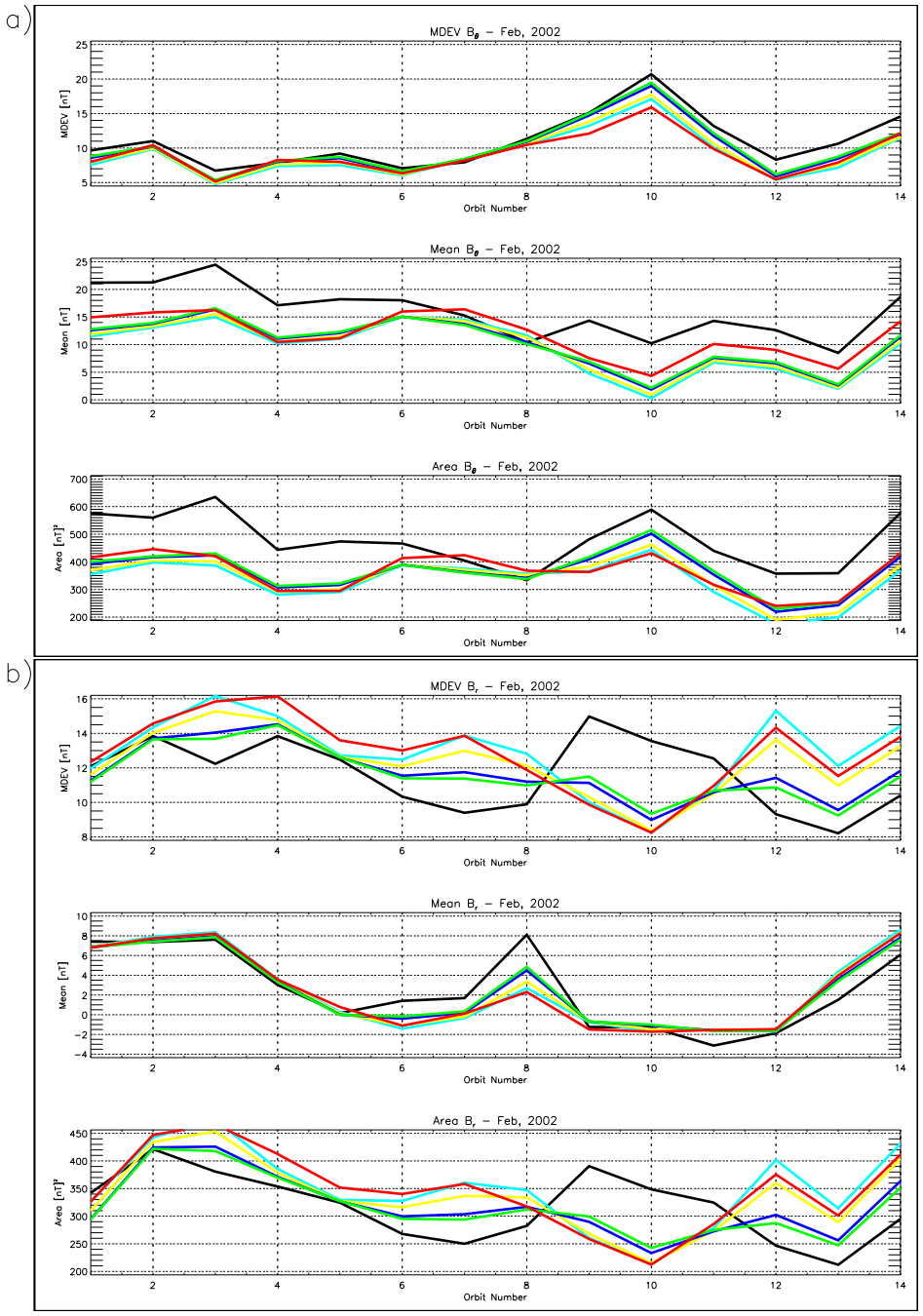

Figure 2.7: These plots show the statistics of the dayside orbit passes for February 14, 2002: MDEV (top), Mean (middle), and Area (bottom)). The CHAMP/CHAOS/TIE–GCM B_θ (a) and B_r (b) residuals from Fig. 2.6 are shown vs. the orbit number. All five TIE–GCM model runs (*GPI* (Red), $F_{10.7} = 70$ (Green), $F_{10.7} = 90$ (Blue), $F_{10.7} = 150$ (Yellow), $F_{10.7} = 190$ (Cyan)) and the CHAMP residuals (Black) are displayed.

DOI: 10.2312/GFZ.b103-08029

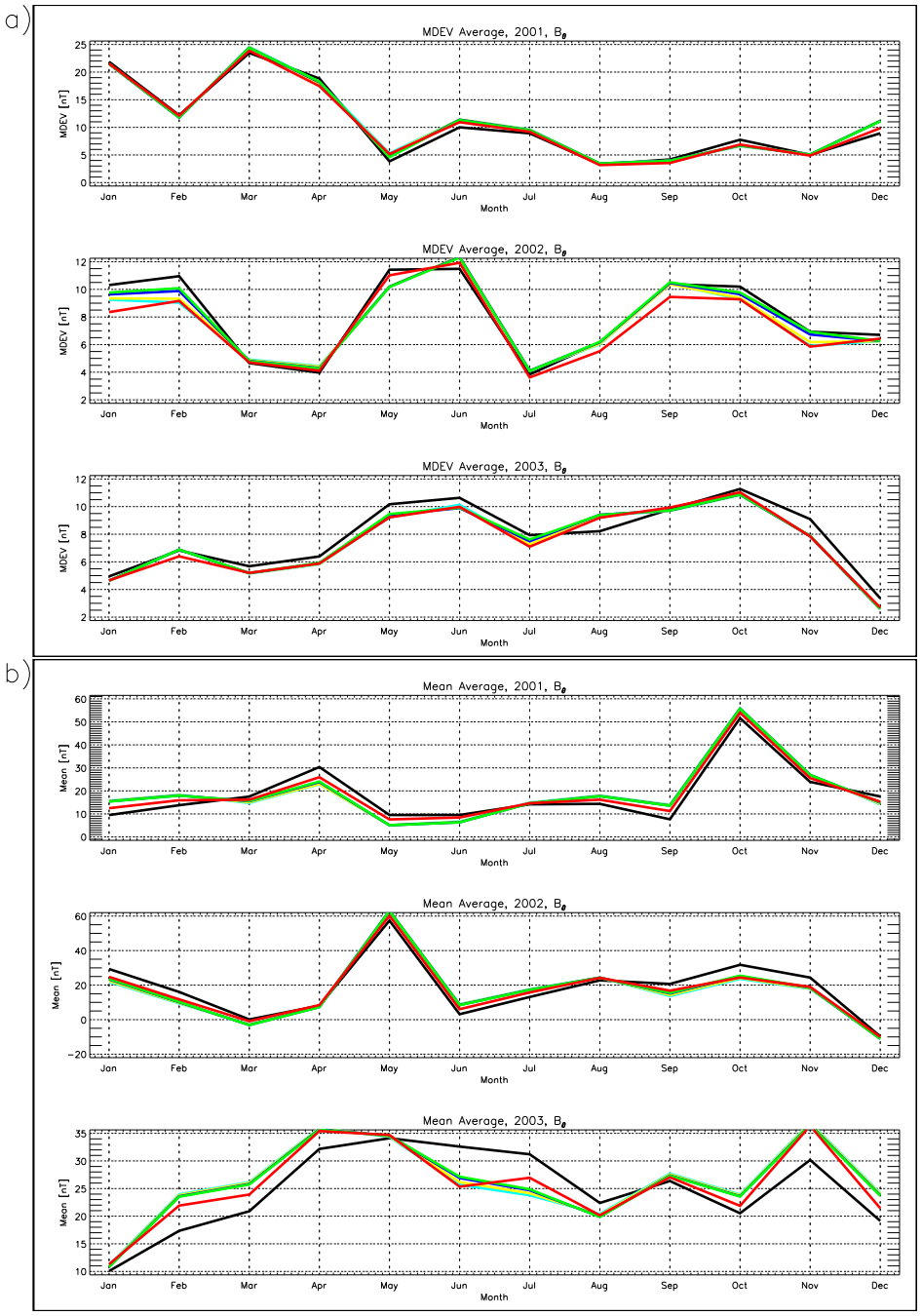

Figure 2.8: These plots show the time-series of the average orbit pass statistics MDEV (a) and Mean (b) (nT vs. Month) for each of the selected days spanning the years 2001 (top), 2002 (middle), and 2003 (bottom) for the B_θ component. All five TIE–GCM model runs are represented (GPI (Red), $F_{10.7} = 70$ (Green), $F_{10.7} = 90$ (Blue), $F_{10.7} = 150$ (Yellow), $F_{10.7} = 190$ (Cyan)) as well as the CHAMP residuals (Black).

DOI: 10.2312/GFZ.b103-08029

2.6.3 Summary of Results

Fig. 2.7 is a summary plot of Fig. 2.6 (corresponding to orbit number 3) across all orbits in the day. In Fig. 2.7(a) the TIE–GCM models generally show an improvement by reducing the MDEV and Mean for the B_θ component. Though not displayed, the total field B_F shows similar character. As is typical, the B_r (Fig. 2.7(b)) and B_ϕ (not shown) components are more inconsistent, varying from having a positive influence to having a negative influence over the course of the day.

Although not conclusive, the TIE–GCM models seem to bring an improvement in the final residuals (Fig. 2.8 is only the average for one day during the month). For instance, the 2003 MDEV Average for B_θ is consistently lower than the data alone, save for the month of August.

2.7 K_p Variation

2.7.1 The effect of varying the K_p on the TIE–GCM magnetic perturbation predictions

In an effort to better characterize the TIE–GCM model results in relation to CHAMP data, I have selected a few days and varied the K_p parameter. It should be noted that when the GPI is used, all the magnetic activity parameters are recomputed and updated at each new time step. The $F_{10.7}$ is interpolated to the current model time step using data from ± 2 days. While K_p is interpolated using a ± 1 day window of the eight daily 3-hour values. In this particular test only constant values of K_p were used and were varied from 0–8 with a fixed $F_{10.7}$ for all runs. The model does not directly take K_p as an input, but rather indirectly through the parameters POWER and CTPOTEN. Therefore, the values of 0–8 were substituted for the interpolated K_p value K_p^i in Eq. (2.3) and Eq. (2.4). The resulting values, listed in Tab. 2.7, were used as the inputs to the TIE–GCM model runs, in order to see the effects of changing just the K_p, while other parameters were held fixed.

$$\text{POWER} = MAX(3.0, -2.78 + 9.33K_p^i) \tag{2.3}$$

$$\text{CTPOTEN} = 29.0 + 11.0K_p^i \tag{2.4}$$

Of the model runs plotted in Fig 2.9, the best fit for the total field (B_F) visually appears to be the Blue $K_p = 2$ which is close to the upper limit of the actual K_p range of 0–2^-. The next best fit corresponds to the curve for $K_p = 1$, followed by the $K_p = 0$, $K_p = 4$, and $K_p = 8$. However, it should be remembered that in Fig 2.9 the black CHAMP/CHAOS residual has had

DOI: 10.2312/GFZ.b103-08029

Table 2.7: The constant values for POWER and CTPOTEN used in the TIE–GCM as a way of varying the K_p.

K_p^i	**POWER**	**CTPOTEN**
0	3.00	29
1	6.55	40
2	15.88	51
3	25.21	62
4	34.54	73
5	43.87	84
6	53.20	95
7	62.53	106
8	71.86	117

its mean removed so as to center the curve about zero, but the magnetic perturbation curves have not. Examining Tab 2.8 (Fig 2.9 corresponds to orbit number 2) actually reveals that in terms of MEAN and AREA, the higher K_p values are generally better and the goodness of fit decreases with decreasing K_p values. It is not surprising that MEAN and AREA give a similar pattern, since the MEAN values exert a strong influence in the AREA calculation. In terms of MDEV the best fit does not seem to have a consistent pattern. Sometimes the high K_p runs are best, but other times it is the low values. The B_ϕ component shows better agreement in the MEAN and AREA with TIE–GCM runs of smaller K_p value. The agreement generally tends to degrade with increasing K_p. This also seems to be the trend seen in the MDEV of the B_θ component.

The B_ϕ component shows better agreement in the MEAN and AREA with TIE–GCM runs with smaller K_p values. The agreement generally tends to degrade with increasing K_p. This also seems to be the trend seen in the MDEV of the B_θ component.

Curiously it appears that generally the $K_p = 4$ curve is the best for the B_θ component in the MEAN and AREA statistic (see Tab 2.8), probably because it tends to show the best approximation of the EEJ in terms of signal amplitude, without having the tail diverge as much as does the $K_p = 8$ curve. All the other components have no clear patterns.

Performing this same procedure for Aug 2004 shows a different pattern, where the $K_p = 8$ generally shows the best fit, which degrades down to the $K_p = 0$ run for the B_F and B_r components (except for the B_F MDEV). The remaining components seem rather mixed (see Appendix B).

DOI: 10.2312/GFZ.b103-08029

Table 2.8: Goodness of Fit Rankings of individual dayside orbit tracks for different values of K_p runs for TIE–GCM for Feb 14, 2002 for the B_F and B_θ components. The Values are the K_p used and 1^{st} is the best fit while 5^{th} is the worse fit in terms of either the MDEV, MEAN or AREA. SLT is about 9.88

Orbit	**1**	**2**	**3**	**4**	**5**	**6**	**7**	**8**	**9**	**10**	**11**	**12**	**13**	**14**
B_F MDEV														
1^{st}	1	0	2	8	8	4	8	8	8	0	2	0	0	1
2^{nd}	0	1	1	4	4	0	4	0	4	1	1	1	1	2
3^{rd}	4	2	0	2	0	2	2	1	2	2	0	2	2	0
4^{th}	2	4	4	1	1	1	1	4	1	4	4	4	4	4
5^{th}	8	8	8	0	2	8	0	2	0	8	8	8	8	8
B_F MEAN														
1^{st}	8	8	8	8	8	8	8	8	4	8	4	4	8	4
2^{nd}	4	4	4	4	4	4	4	4	8	4	2	2	4	2
3^{rd}	2	2	2	2	2	2	2	2	2	2	8	1	2	8
4^{th}	1	1	1	1	1	1	1	1	1	1	1	0	1	1
5^{th}	0	0	0	0	0	0	0	0	0	0	0	8	0	0
B_F AREA														
1^{st}	8	8	4	8	8	8	8	8	4	4	4	4	8	4
2^{nd}	4	4	8	4	4	4	4	4	8	8	2	2	4	2
3^{rd}	2	2	2	2	2	2	2	2	2	2	1	1	2	1
4^{th}	1	1	1	1	1	1	1	1	1	1	8	0	1	0
5^{th}	0	0	0	0	0	0	0	0	0	0	0	8	0	8
B_θ MDEV														
1^{st}	0	2	2	0	0	0	0	0	0	0	0	1	4	4
2^{nd}	1	1	4	1	1	1	1	1	1	1	1	2	2	2
3^{rd}	2	0	1	2	2	4	2	2	2	2	2	0	1	1
4^{th}	4	4	0	4	4	2	4	4	4	4	4	4	0	0
5^{th}	8	8	8	8	8	8	8	8	8	8	8	8	8	8
B_θ MEAN														
1^{st}	4	4	4	4	4	4	8	4	2	2	4	4	2	4
2^{nd}	2	2	2	2	2	8	4	8	4	1	2	2	1	2
3^{rd}	1	1	1	1	1	2	2	2	1	0	1	1	0	1
4^{th}	0	0	0	0	0	1	1	1	0	4	0	0	4	0
5^{th}	8	8	8	8	8	0	0	0	8	8	8	8	8	8
B_θ AREA														
1^{st}	4	4	4	4	4	4	4	0	2	0	2	4	2	4
2^{nd}	2	2	2	2	2	8	2	4	1	1	4	2	4	2
3^{rd}	1	1	1	1	1	2	8	1	0	2	1	1	1	1
4^{th}	0	0	0	0	0	1	1	2	4	4	0	0	0	0
5^{th}	8	8	8	8	8	0	0	8	8	8	8	8	8	8

DOI: 10.2312/GFZ.b103-08029

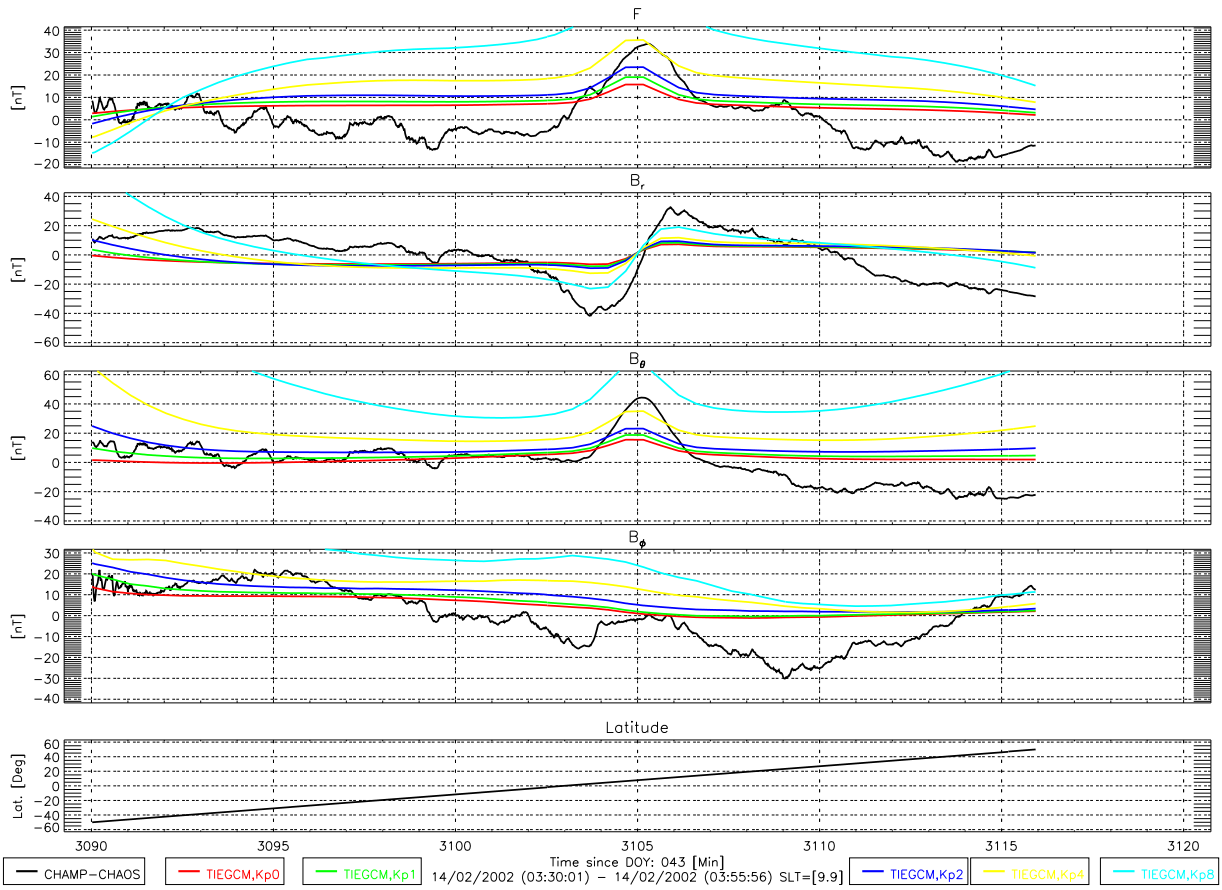

Figure 2.9: A comparison of the effects of varying K_p on the TIE–GCM prediction for a dayside orbit pass on February 14, 2002, using a constant $F_{10.7}$ of 190. Black is the CHAMP/CHAOS residual, Red is the TIE–GCM using $K_p = 0$, Green is $K_p = 1$, Blue is $K_p = 2$, Yellow is $K_p = 4$, and Cyan is $K_p = 8$.

2.7.2 Examining the quietest day of each year from 2001–2005 by varying K_p

In order to examine the effects of K_p, the quietest day of each year from 2001–2005 was selected for further study. These days were selected by first examining the K_p range for each of the days, then selecting the days with the lowest value for the high end K_p value. In case of duplicates, the one with the smaller $F_{10.7}$ value was selected. The dates selected are listed in Tab. 2.9.

Tab. 2.10 tries to show some commonalities between the different years and the role of K_p. Numbers in parenthesis represent other K_p values that also minimize the given statistics, but are fewer in number of orbit passes than the main number. As an example, the MDEV for the B_F component in 2004 (see first row of Tab. C.7) has 7 orbits minimized by $K_p = 0$, 5 orbits minimized

DOI: 10.2312/GFZ.b103-08029

Table 2.9: The quietest geomagnetically active day of the year from 2001–2005 with its associated K_p value range and $F_{10.7}$

Date	**Year**	$\mathbf{K}_p$	$\mathbf{F}_{10.7}$
Jun 28	2001	$0\ -1^-$	144.9
May 24	2002	$0\ -1^-$	193.9
Dec 19	2003	$0\ -1^-$	118.6
Dec 4	2004	$0\ -0$	94.6
Dec 23	2005	$0\ -0^+$	90.1

Table 2.10: The overall most highly ranked K_p values for each component, year and statistic. K_p values in parenthesis, while not the most common, are ranked first for a significant number of orbits.

	$\mathbf{B}_F$			$\mathbf{B}_r$		
Date	**MDEV**	**MEAN**	**AREA**	**MDEV**	**MEAN**	**AREA**
Jun 28, 2001	0	8	8	2(0)	0(8)	4
May 24, 2002	0	8	8	0(8)	8	0(8)
Dec 19, 2003	0	8	8	0	8(4)	0(8)
Dec 4, 2004	0(2)	8	8	0	8(4)	0
Dec 23, 2005	0	8	8	0	8	0(4)

	$\mathbf{B}_\theta$			$\mathbf{B}_\phi$		
Date	**MDEV**	**MEAN**	**AREA**	**MDEV**	**MEAN**	**AREA**
Jun 28, 2001	0	8	4(0)	0	4(0)	0
May 24, 2002	0	8	8	0(4)	8	0(2,4)
Dec 19, 2003	4(0)	4	4	0	0	0
Dec 4, 2004	0	4(8)	4	0	0(8)	0(2)
Dec 23, 2005	0(4)	2	4	0	0	0

by $K_p = 2$, and 3 orbits minimized by $K_p = 4$. In this case the ratio 7:5:3 is significant and thus noted in the table, but the 13:1:1 ratio for the MEAN does not seem significant. This determination is rather arbitrary when applying the secondary number. Some patterns are evident, for instance the B_F component shows that the lowest $K_p = 0$ run minimizes the MDEV for each year, whereas it is the highest $K_p = 8$ run that minimizes the MEAN and AREA statistics. However, the larger inherent offsets associated with the higher K_p runs probably explain the better MEAN and AREA statistics, more so than a better actual fit to the data.

DOI: 10.2312/GFZ.b103-08029

2.8 The TIE–GCM as a possibility for correcting magnetic field data

Generally during the process of developing a geomagnetic main field model, only night-time values are taken into account during the inversion process. The reason for this is that nighttime values are usually the quietest available, however, this can lead to data coverage issues. One way to increase the number of data available for geomagnetic field modeling is to simply include dayside data, however, due to the nature of the dayside geomagnetic field this tends to introduce increased levels of noise in the form of external field source contamination, as discussed in Sec. 1.5.2. One prospect here is to see if the TIE–GCM can be used to partially correct dayside data, so as to supplement the geomagnetic datasets currently being used with dayside data, especially during times and places where there are insufficient quiet nighttime data available. To this end, a series of main field models were developed to investigate this supposition.

2.8.1 Lesur Model: Initial Proof of Concept Case Study

The above performed tests suggest that the TIE–GCM model may be used in the selection criteria of satellite magnetic data. One prospect here is to see if the TIE–GCM can be used to partially correct dayside data so as to supplement the current geomagnetic datasets, especially during times and places where there are insufficient quiet nighttime data available. Lesur computed a test snapshot model following the basic procedure outlined in Sec. 1.6.2 [92] of 5 days of CHAMP data between August 14–18, 2001, and supplied the dataset and model predictions. Using the same procedures already described, the TIE–GCM was used to compute analogous model predictions. The difference between the dataset/model residuals and the TIE–GCM predictions was computed to see if any of the statistical quantities could be improved.

A main objective was to see if the TIE–GCM "correction" would reduce the residuals on the dayside to the same level as the residuals on the nightside. In this way the TIE–GCM could be used as a way of correcting dayside data so that it could be used for magnetic field modeling, when it normally would not be used. This did not appear to be the case, the dayside residuals were slightly reduced, but not to the nightside level. Fig. 2.10 shows the obtained residuals, with the dayside residuals slightly reduced, but not to the nightside level. Even if the dayside residuals are not reduced all the way down to the nightside level, there are tangible improvements that might prove useful in future studies.

When the entire orbit is considered (Tab. 2.11), improvement was generally narrow or actually

DOI: 10.2312/GFZ.b103-08029

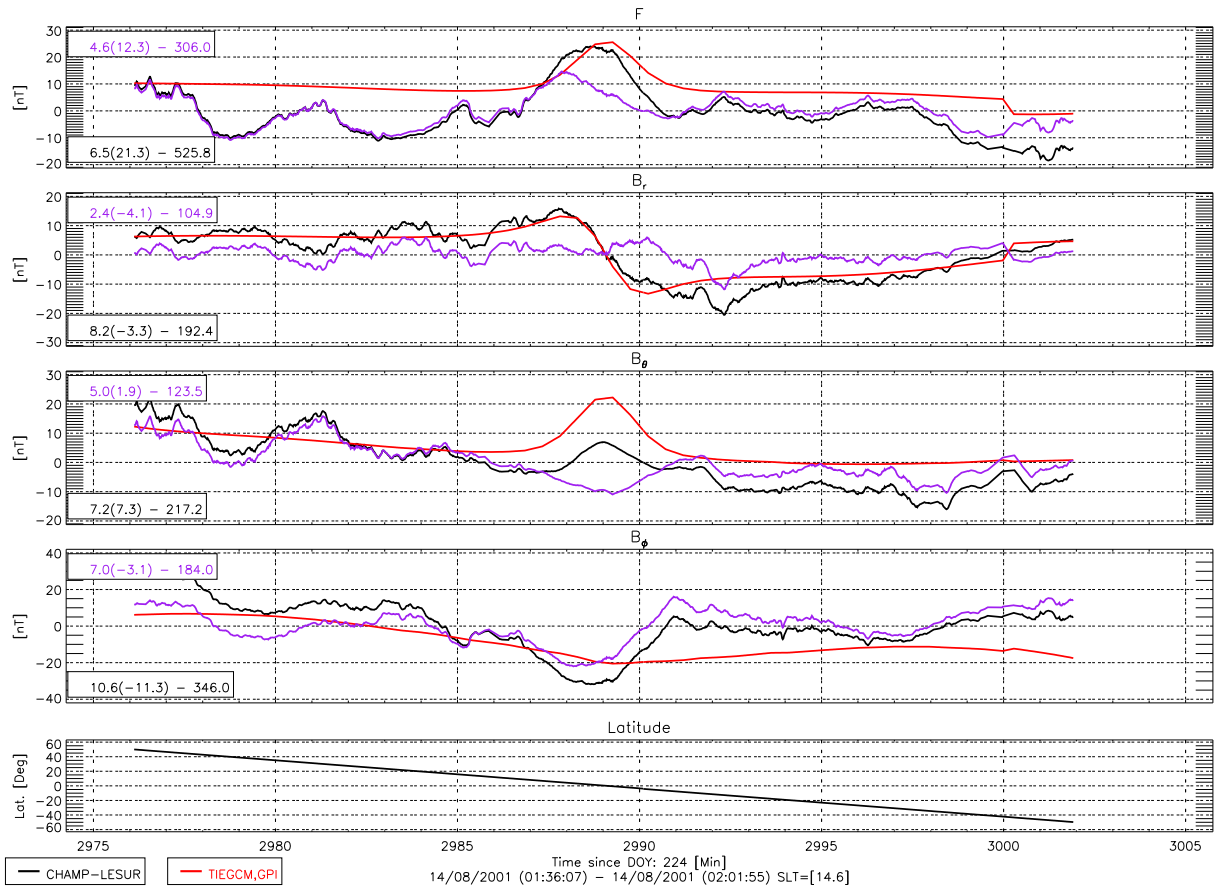

Figure 2.10: A sample dayside orbit plot for August 14, 2001 showing the comparison of the Lesur/CHAMP data residuals (Black) and the Lesur/CHAMP/TIE–GCM residuals (Purple) between ±50° latitude. The TIE–GCM alone is in red. The numbers on the left side of each window represent the MDEV(MEAN) – AREA. For this particular orbit the TIE–GCM reduces the MDEV from 8.2 to 2.4 for the B_r component.

made worse, for instance the Mean and Variance increased for the B_ϕ component, whereas the opposite is true when the B_θ component is considered (quite a large decrease). However, when just the mid-latitudes (±50°) are considered, which is more appropriate considering the limitations of the models, Tab. 2.12 shows a substantial improvement across the board for virtually all the components.

2.8.2 MAGFIT Models: Case Study

A more detailed study was undertaken building upon the rather positive results indicated using the Lesur Model. In this case two months of CHAMP data were used to develop models to characterize

DOI: 10.2312/GFZ.b103-08029

Table 2.11: Comparisons of the Lesur Model and the TIE–GCM for all data on August 14, 2001. The inclusion of the polar region in the dataset causes the scatter in the statistics to be quite high. The TIE–GCM does not model the polar regions very well and this is reflected in the fact that the statistics are often higher when the TIE–GCM correction is included. For instance the variance is higher after the TIE–GCM values are applied to the residuals of the B_F component.

TYPE	**Data** B_F	**TIE–GCM** B_F	**Data** B_r	**TIE–GCM** B_r
Mean	58.3	57.7	4.8	4.3
Vari	9380.2	9776.3	997.1	963.2
Skew	3.3	3.0	3.0	2.2
Kurt	13.8	10.7	12.4	7.8
MDev	59.7	64.9	16.6	17.7
SDev	96.9	98.9	31.6	31.0
TYPE	**Data** B_θ	**TIE–GCM** B_θ	**Data** B_ϕ	**TIE–GCM** B_ϕ
Mean	15.3	12.8	9.8	10.5
Vari	4218.2	2484.5	7212.2	8060.8
Skew	2.1	1.8	3.3	3.5
Kurt	14.8	16.7	20.7	22.7
MDev	33.9	26.4	42.4	43.9
SDev	64.9	49.8	84.9	89.8

Table 2.12: Comparisons of the Lesur Model and the TIE–GCM for mid-latitudes between ±50° on August 14, 2001. The exclusion of the polar region in the data set reduces the scatter in the statistics seen in Tab. 2.11. The statistics are now usually lower when the TIE–GCM correction is included. For instance the variance drops from 187.0 to 118.2 after the TIE–GCM values are applied to the residuals of the B_F component.

TYPE	**Data** B_F	**TIE–GCM** B_F	**Data** B_r	**TIE–GCM** B_r
Mean	17.3	13.9	-2.0	-2.1
Vari	187.0	118.2	74.8	61.2
Skew	1.0	1.5	-0.6	-0.6
Kurt	1.0	2.4	1.6	1.8
MDev	11.3	8.4	6.4	5.7
SDev	13.7	10.9	8.6	7.8
TYPE	**Data** B_θ	**TIE–GCM** B_θ	**Data** B_ϕ	**TIE–GCM** B_ϕ
Mean	5.9	4.5	-5.7	-5.2
Vari	123.7	89.5	217.3	190.8
Skew	1.1	1.0	0.4	-0.2
Kurt	1.5	4.2	2.6	0.6
MDev	8.5	6.6	10.3	10.3
SDev	11.1	9.5	14.7	13.8

DOI: 10.2312/GFZ.b103-08029

the usefulness of folding TIE–GCM corrected dayside data into modeling datasets. While the Lesur Model investigation looks at a post-modeling TIE–GCM correction, it is more useful in terms of an end product to apply a pre-modeling correction. For this, five new models were derived using the modeling techniques developed in previous work [71]: a standard model with nightside data and no dayside data, a model with nightside data and uncorrected dayside data, and lastly three models with nightside data and dayside data corrected using the TIE–GCM with either GPI, $K_p = 0$ or $K_p = 8$ inputs. Only two months worth of data were used to artificially create a need for the use of dayside data; two months is enough to produce a reasonable model yet will still contain data coverage gaps (Fig. 2.11) that can be filled with dayside data. The five models are outlined herein:

- **Model 1**

  CHAMP FGM-NEC and OVM data from 8/01/2004–9/31/2004 were converted to geodetic X, Y, Z and F vector components. The data were selected for local times between 10 PM–2 AM, $K_p \leq 1$, $F_{10.7} \leq 150$, and a D_{st} correction was applied. The vector data was limited to lie between $\pm 50^\circ$ magnetic latitude, while the scalar data was limited to be poleward of $\pm 50^\circ$ magnetic latitude. Residuals were computed using CHAOS to estimate data class weights and those data differing by more than 100 nT were removed from the dataset. The entire dataset was equal-area shaved down to $\sim 200,000$ data points and corresponding equal-area weight factors were determined. A truncated CHAOS model (limited to spherical harmonic degree $n = 20$ with secular variation terms to degree $n = 10$) was used as an initial state model.

- **Model 2**

  This model is identical to Model 1 with the addition of dayside data. CHAMP FGM-NEC data from 8/01/2004–9/31/2004 were converted to geodetic X, Y, Z and F vector components. The data were selected for local times between 9 AM–3 PM, $K_p \leq 1$, $F_{10.7} \leq 150$, and a D_{st} correction was applied. The vector data were restricted to lie between $\pm 50^\circ$ magnetic latitude. Residuals were computed using CHAOS to establish data class weights and those data differing by more than 100 nT were removed from the dataset. The entire dataset was equal-area shaved down to $\sim 150,000$ data points ($\sim 350,000$ total) and the corresponding equal-area weight factors were determined. A truncated CHAOS model (limited to spherical harmonic degree $n = 20$ with secular variation terms to degree $n = 10$) was used as an initial state model.

DOI: 10.2312/GFZ.b103-08029

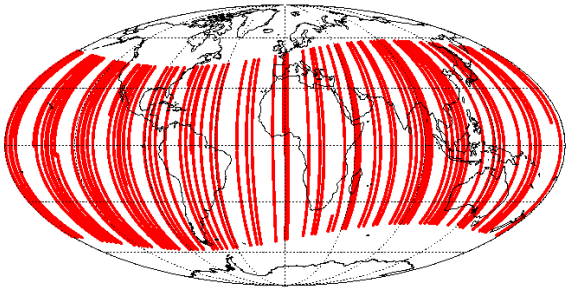

(a) Nighttime Vector Data

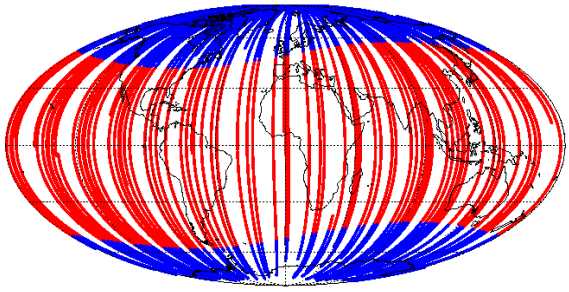

(b) Nighttime Vector and Scalar Data

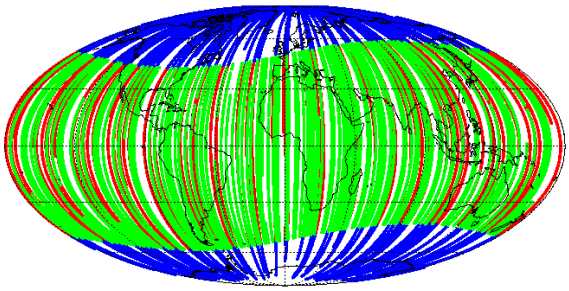

(c) With Daytime Vector Data

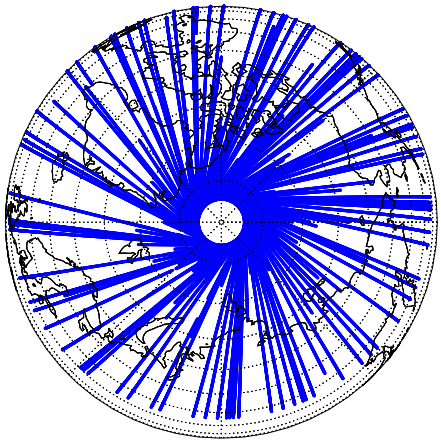

(d) North Pole

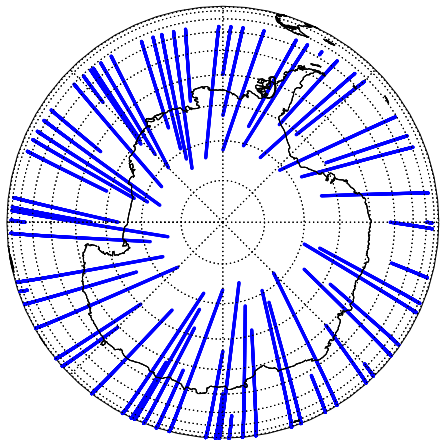

(e) South Pole

Figure 2.11: The data distribution for the Magfit Models, where red is CHAMP vector nightside, blue is CHAMP scalar nightside, and green is CHAMP vector dayside. The window (a) highlights the nightside vector data, window (b) displays both the nightside vector and scalar representing the data distribution of Model 1, while window (c) shows nightside vector and scalar with the addition of dayside vector, which is the data distribution for Model 2 and Model 3. Windows (d) and (e) show the scalar data distribution in the polar regions and demonstrate, especially in the southern polar region, the problem of using such a short time span.

DOI: 10.2312/GFZ.b103-08029

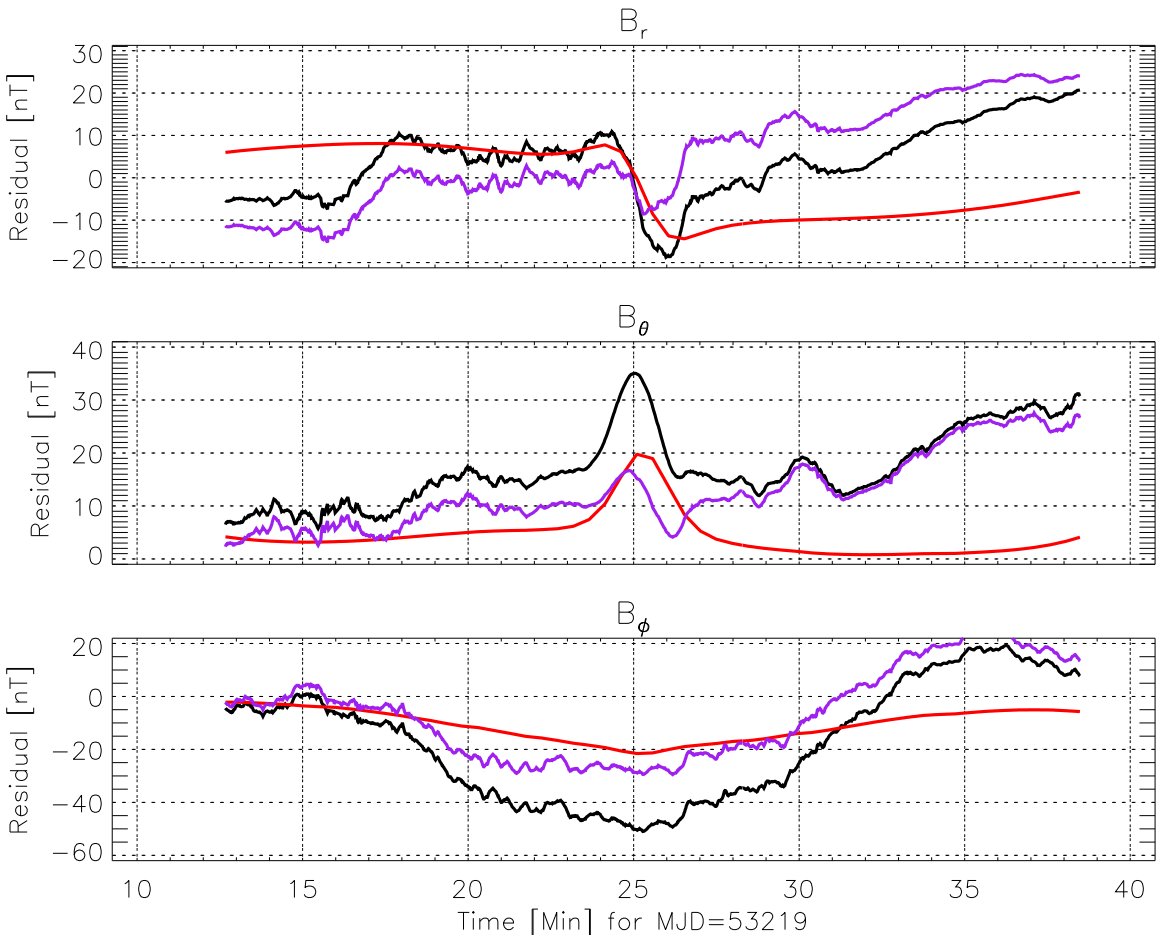

Figure 2.12: The TIE–GCM correction (red) applied to a sample orbit of the dayside data in Model 3. The residual (black) of the dayside data was computed relative to the CHAOS model (residuals used to facilitate clarity). The difference (purple) represents the corrected residual data (the actual data input to the model were not the corrected CHAOS residuals, but rather the true corrected data). While the TIE–GCM correction mirrors the data in a general sense, it can also adversely affect the corrected data by amplifying the misfit in some areas (especially the higher latitude regions).

- **Models 3, 4 and 5**

  These models are identical to Model 2 except the additional dayside data were further corrected using the TIE–GCM perturbations. Model 3 uses GPI TIE–GCM inputs, Model 4 uses fixed $K_p = 0$ and $F_{10.7} = 100$ inputs, and Model 5 uses fixed $K_p = 8$ and $F_{10.7} = 100$ inputs. A sample of the Model 3 correction is displayed in Fig. 2.12 for a sample orbit pass.

DOI: 10.2312/GFZ.b103-08029

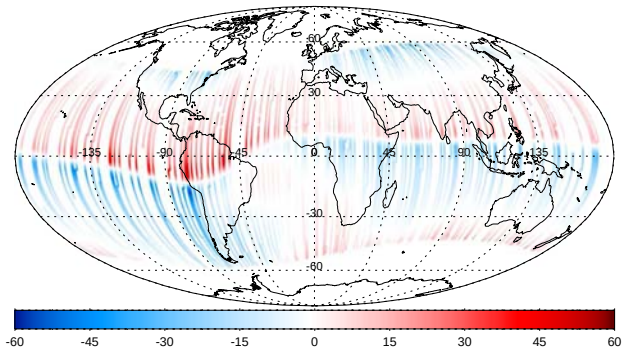

(a) B_r component

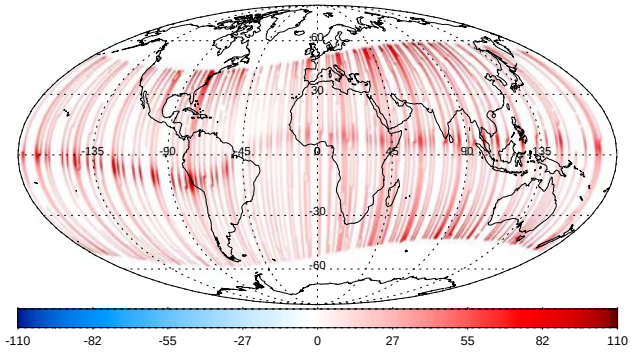

(b) B_θ component

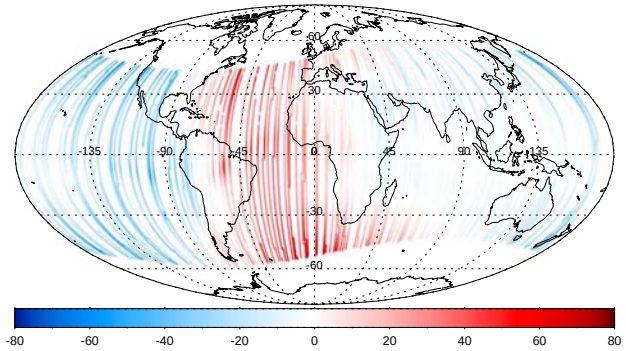

(c) B_ϕ component

Figure 2.13: $1^\circ \times 1^\circ$ binned and averaged maps of the TIE–GCM (with GPI inputs) correction data used in the derivation of Model 3. Compare this with the individual orbit pass correction in Fig. 2.12. The B_r components (a) indicates the attempt to reduce the Sq-like feature by its sign change about the magnetic equator. Similarly, (b) shows its largest values (always positive) along the magnetic equator, which is expected since the B_θ component contains the EEJ signature. Lastly (c) is the B_ϕ component.

DOI: 10.2312/GFZ.b103-08029

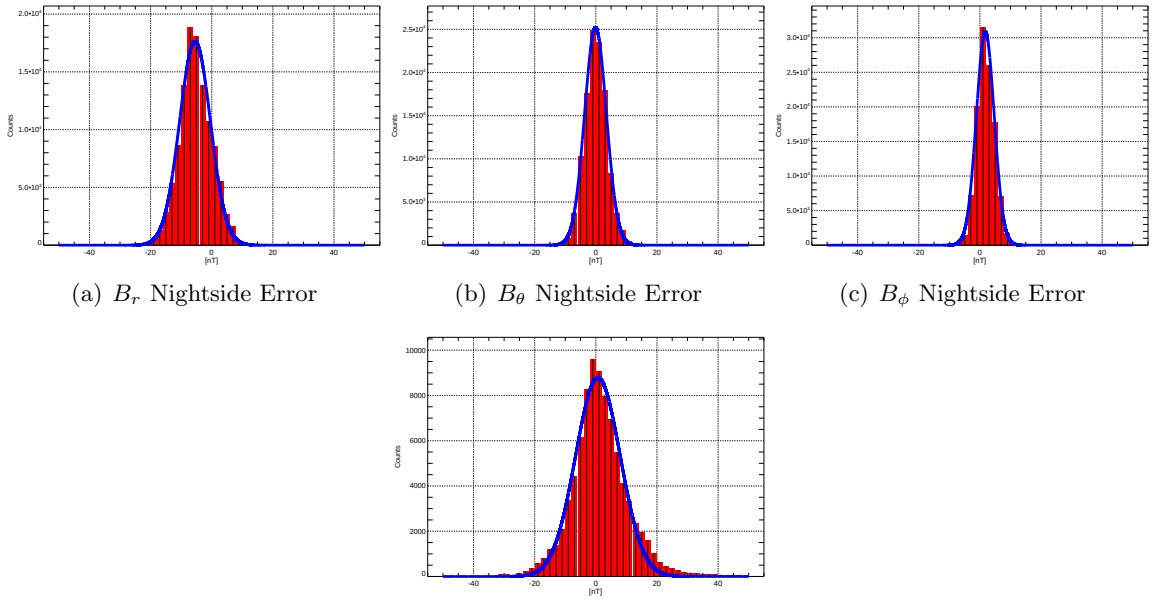

(a) B_r Nightside Error (b) B_θ Nightside Error (c) B_ϕ Nightside Error

(d) B Nightside Error

Figure 2.14: The error distributions for Magfit Model 1 magnetic field components with Gaussian fits.

Table 2.13: Gaussian fit parameters for the residual error distributions of Models 1–5.

Class	**Model**	$\mathbf{B}_r$		$\mathbf{B}_\theta$		$\mathbf{B}_\phi$		**B**	
		Cen	**Wid**	**Cen**	**Wid**	**Cen**	**Wid**	**Cen**	**Wid**
Night/Mid/Vector	Model 1	-5.43	5.16	-0.12	3.70	1.88	3.16	-	-
	Model 2	-5.87	7.38	0.75	4.99	2.12	3.31	-	-
	Model 3	-5.82	5.07	1.23	4.73	2.10	3.24	-	-
	Model 4	-5.85	5.10	1.11	4.76	2.10	3.23	-	-
	Model 5	-5.30	7.39	5.43	5.00	1.86	3.34	-	-
Night/Pole/Scalar	Model 1	-	-	-	-	-	-	0.70	7.43
	Model 2	-	-	-	-	-	-	1.40	8.78
	Model 3	-	-	-	-	-	-	0.84	7.92
	Model 4	-	-	-	-	-	-	0.93	8.06
	Model 5	-	-	-	-	-	-	0.22	9.99
Day/Mid/Vector	Model 1	-	-	-	-	-	-	-	-
	Model 2	5.74	8.39	-2.67	9.92	-1.24	15.28	-	-
	Model 3	7.23	8.49	-5.00	9.89	3.74	12.97	-	-
	Model 4	7.10	8.32	-4.46	9.79	3.77	13.45	-	-
	Model 5	9.46	12.98	-25.94	13.88	-2.67	21.72	-	-

DOI: 10.2312/GFZ.b103-08029

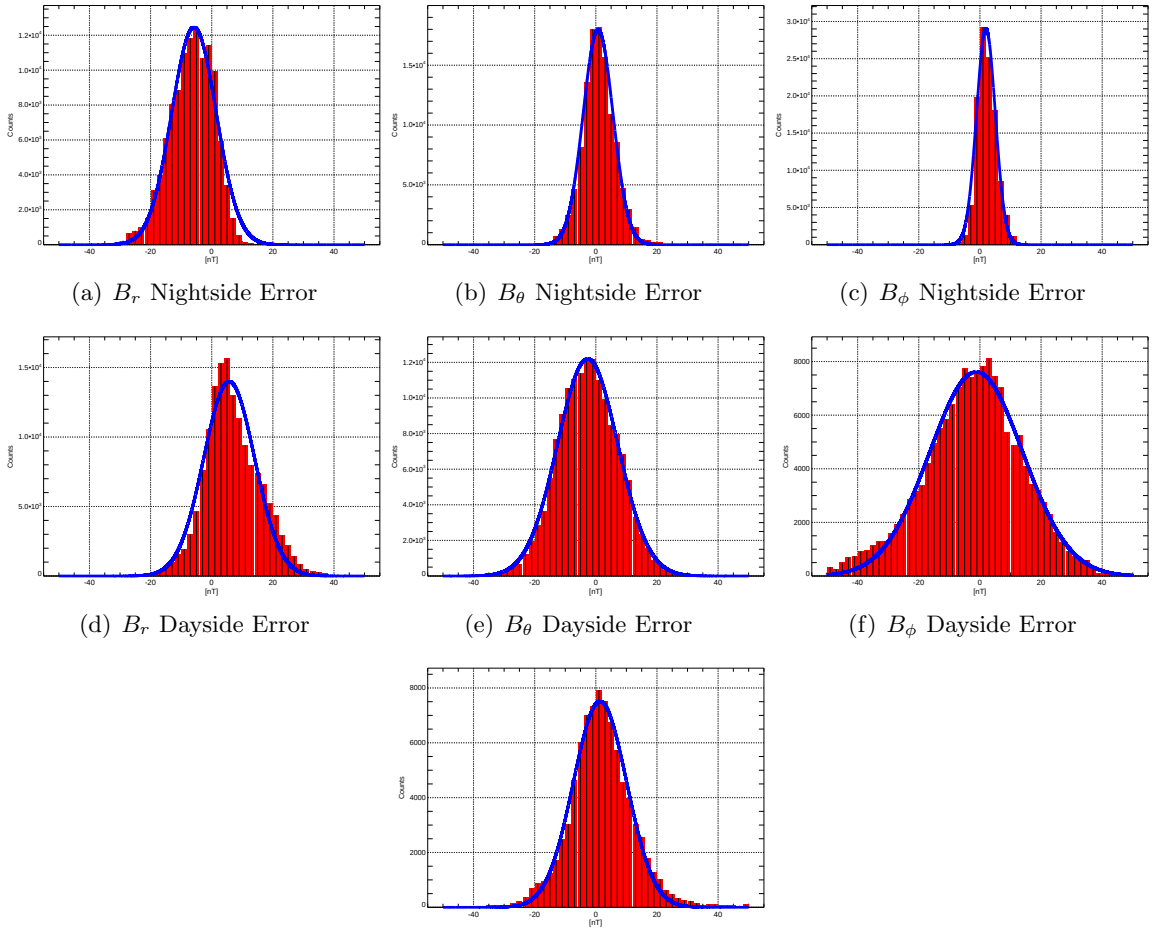

(a) B_r Nightside Error (b) B_θ Nightside Error (c) B_ϕ Nightside Error

(d) B_r Dayside Error (e) B_θ Dayside Error (f) B_ϕ Dayside Error

(g) B Nightside Error

Figure 2.15: The error distributions for Magfit Model 2 magnetic field components with Gaussian fits. It highlights the expected large increase in misfit for the dayside data.

After deriving the models, residuals were computed between the resulting spherical harmonic coefficients and the input datasets. The error distributions of the residuals were fit to a Gaussian function and plotted in Figs. 2.14–2.16 with the results summarized in Tab. 2.13.

Comparing Models 1 and 2 shows that adding uncorrected dayside data increases the Gaussian width of the mid-latitude vector and polar scalar nightside data, which is not unexpected. The misfit for the nightside B_r component data is larger by about 2 nT (from 5.16 nT to 7.38 nT), while the nightside B_θ component and the total field in the polar region increased by about 1 nT. The B_ϕ component showed only a modest gain in misfit. The TIE–GCM corrected dayside data in Model 3 reduces these misfits slightly for the B_θ and B_ϕ components, while the B_r component misfit is

DOI: 10.2312/GFZ.b103-08029

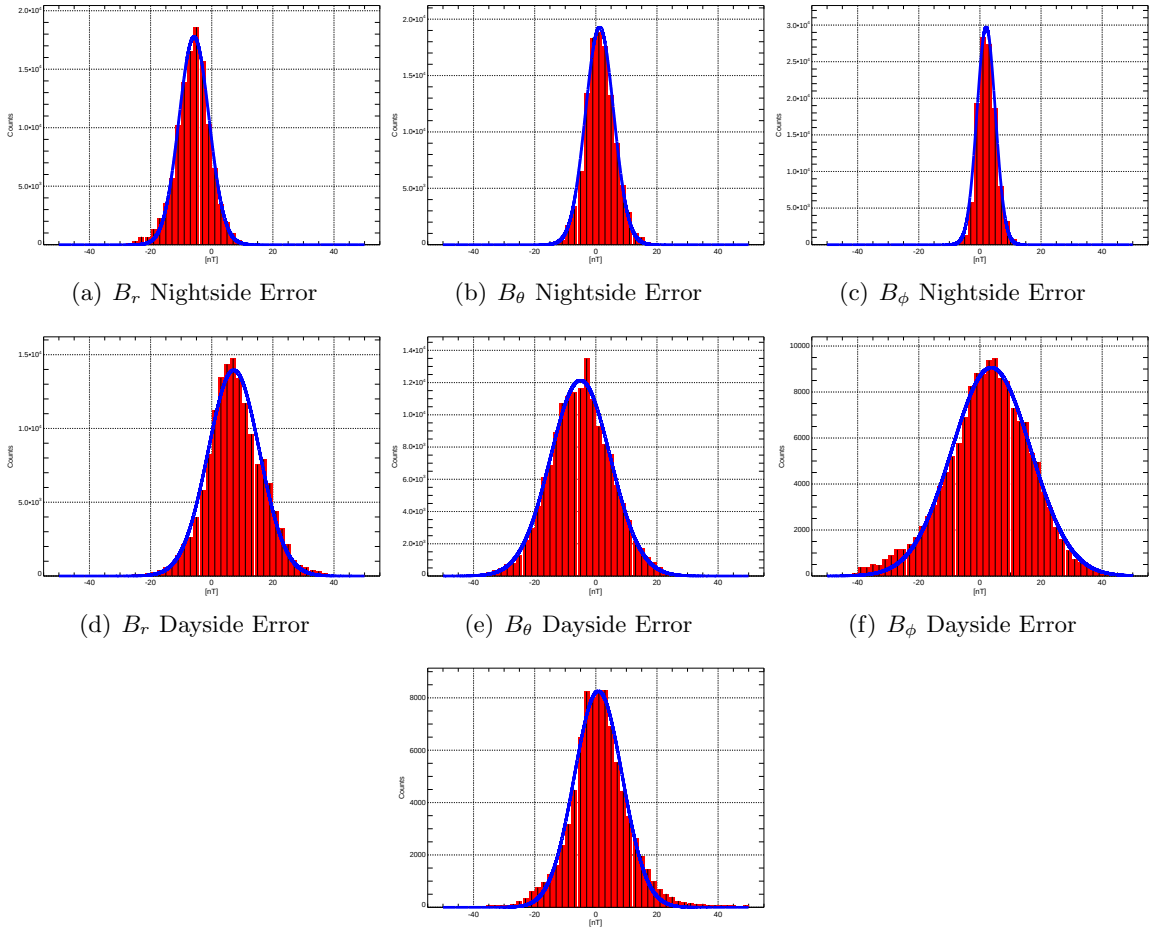

(a) B_r Nightside Error (b) B_θ Nightside Error (c) B_ϕ Nightside Error

(d) B_r Dayside Error (e) B_θ Dayside Error (f) B_ϕ Dayside Error

(g) B Nightside Error

Figure 2.16: The error distributions for Magfit Model 3 magnetic field components with Gaussian fits.

dramatically reduced to be even smaller than that of Model 1, which altogether excludes dayside data. The low magnetic activity TIE–GCM correction used in Model 4 shows similar results to that of Model 3, with generally slightly higher fit errors, although the nightside B_r is still lower than Model 1. The high magnetic activity TIE–GCM correction associated with Model 5 shows a level of misfit on par with that of Model 2 (uncorrected dayside).

The fact that the B_r components in Models 3 & 4, which incorporate corrected dayside data, are roughly as low or lower than that of Model 1 may prove useful in core flow modeling as this component features prominently in such studies.

DOI: 10.2312/GFZ.b103-08029

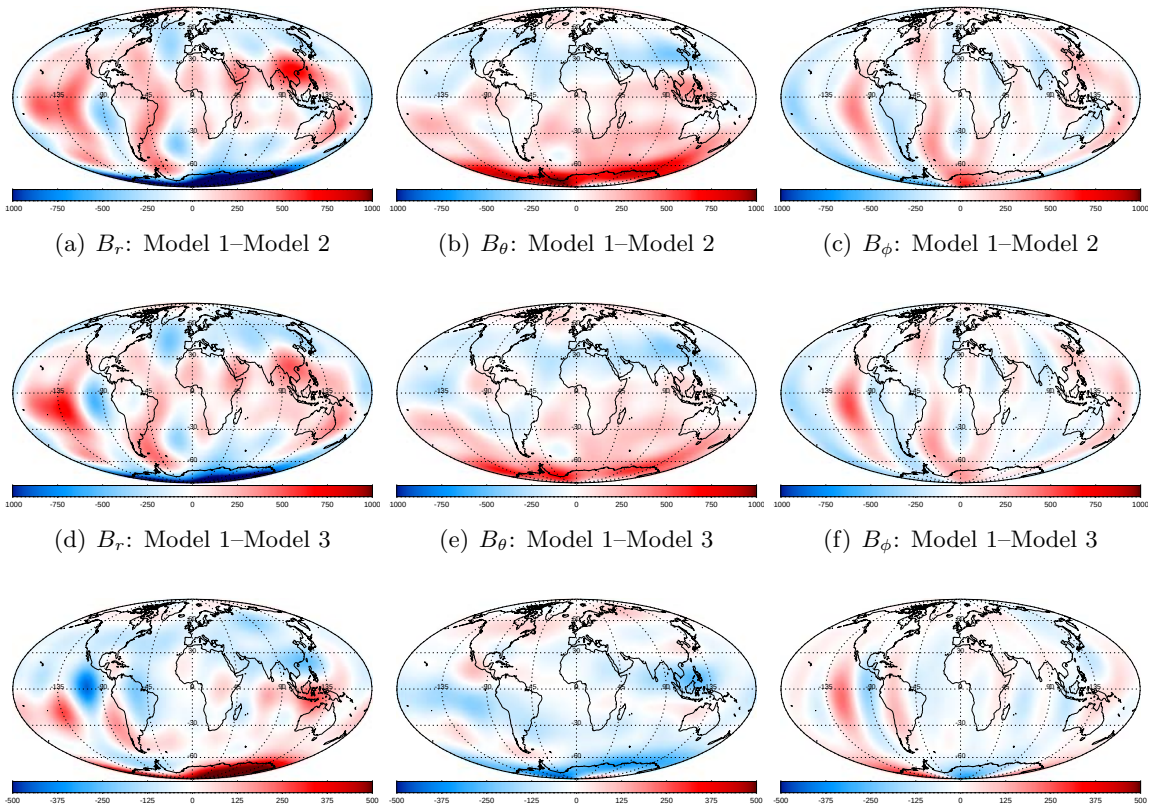

(a) B_r: Model 1–Model 2 (b) B_θ: Model 1–Model 2 (c) B_ϕ: Model 1–Model 2

(d) B_r: Model 1–Model 3 (e) B_θ: Model 1–Model 3 (f) B_ϕ: Model 1–Model 3

(g) B_r: Model 2–Model 3 (h) B_θ: Model 2–Model 3 (i) B_ϕ: Model 2–Model 3

Figure 2.17: Difference plots for Model 1–Model 2 (a-c) [±1000nT], Model 1–Model 3 (d-f) [±1000 nT], and Model 2–Model 3 (g-i) [±500 nT]. Model 2 (uncorrected dayside data) and Model 3 (TIE–GCM corrected dayside data) show the largest difference in the southern polar region.

The absolute misfit for mid-latitude dayside data is, of course, higher than that of the corresponding nightside data (greater by a factor anywhere from 1.5× for B_r to 5× for B_ϕ), but that is consistent with the expected higher noise characteristic of dayside measurements. However, the data show similar misfits in each component across Models 2, 3 and 4 with Model 4 having marginally better misfits in the B_r and B_θ components and Model 3 having the best B_ϕ component misfit. Model 5 consistently demonstrates the highest misfit for each component, roughly 65% higher than the other models.

The differences between Model 2 and Model 3 shown in Figs. 2.17(g)–2.17(i) reveal that the largest and most noticeable misfit appears in the sparsely sampled southern polar region, which unfortunately is unavoidable with a dataset of such limited temporal extent. The differences

DOI: 10.2312/GFZ.b103-08029

elsewhere, however, are fairly diffuse, although they seem to be associated with the orbit track lines. One of the stronger differences is located of the western coast of Central and South America.

2.9 Conclusions

For this study, the TIE–GCM was used to simulate the magnetic perturbations at CHAMP satellite altitude during the lowest geomagnetically active days of each month from 2001–2005. For each of these days the modeling was carried out using five different cases of the input parameter $F_{10.7}$. The model results were then compared with residuals of vector geomagnetic field measurements computed from the difference of CHAMP data and the CHAOS geomagnetic field model.

From the above plots in this initial study, one can see that the TIE–GCM can, to some degree, reproduce the residuals computed from CHAMP geomagnetic vector data. However, the quality of the comparison is rather inconsistent, sometimes the improvements being noticeable, sometimes not. This is evidenced, for example, in the mean average of the B_θ component for 2003 (Fig. 2.8), where there is a marked improvement from May until September, but an equally marked worsening for the other months. For that same component however, the MDEV is consistently better for the years 2002 and 2001, but not in B_F.

But overall, the fact that a model derived using no *in-situ* magnetic data can match features in satellite data is promising. This modeling approach better lends itself to an understanding of the physics of the ionospheric sources than would a purely parameterized model. The results suggest that under the right circumstances it might be possible to use the TIE–GCM to preprocess dayside satellite data in order to supplement geomagnetic modeling efforts, especially when the availability of data is insufficient. This possibility was further investigated, first the feasibility was assessed by looking at a snapshot model supplied by Dr. Lesur and then a more involved, but simple, model was derived. Initially, it was shown that the TIE–GCM perturbation predictions, when subtracted from the Lesur model, could yield lower data residuals than the model alone. In order to follow-up this result, five new spherical harmonic models were derived (1– night-time data only, 2– night-time and day-time, and 3,4 and 5– night-time and TIE–GCM corrected day-time). These models demonstrate the potential usefulness of preprocessing the dayside data prior to modeling, since the TIE–GCM corrected Models 3 and 4 produced smaller residuals than did the uncorrected model.

DOI: 10.2312/GFZ.b103-08029

CHAPTER 3

Internal Variations: South Atlantic Anomaly from the Earth's Surface to the Core-Mantle Boundary

Instead of further discussing perturbations of the external field, this chapter deals with looking at variations of the internal field. In particular, I look specifically at aspects of the South Atlantic Anomaly. For this I proceed in three basic stages, beginning with a cursory introduction, which will define this feature and discuss its impact, followed by an attempt to track its position on the Earth's surface over the recent past. I next look below the surface to the core-mantle boundary (CMB) to see if there is any interplay with the axial dipole. Lastly an examination of the total magnetic flux emanating from the CMB to see what role it might serve in the evolution of the SAA. Parts of this chapter were developed for and used in a collaborative paper [93] that discusses the magnetic field changing over the southern portion of the African continent and a submitted paper [94], which discusses the relation between total unsigned flux and geomagnetic jerks.

3.1 The South Atlantic Anomaly

The South Atlantic Anomaly (SAA) is an extended, roughly elliptical region (currently located generally over the South Atlantic Ocean with its minimum in 2005 centered inland from the east coast of Brazil, at approximately 26.5° S Lat., 55.3° W Lon.). In this region, the shielding effects of the geomagnetic field have been severely compromised, thus allowing high energy particles trapped in the inner van Allen radiation belt to penetrate deep into the upper atmosphere (to altitudes below 100 km). The main feature visible in Fig. 3.1 is represented by the large red region, indicating an elevated proton flux count corresponding to the SAA, which arises from the relative proximity of the inner radiation belt. The bands of elevated count rates at the poles are a result of the outer radiation belt which has its closest approach in the polar regions. The van Allen belts are a pair of low-latitude, torus-shaped magnetospheric regions containing charged particles trapped from the solar wind. The inner belt (mostly elections and protons) extends from about 2 earth radii down

DOI: 10.2312/GFZ.b103-08029

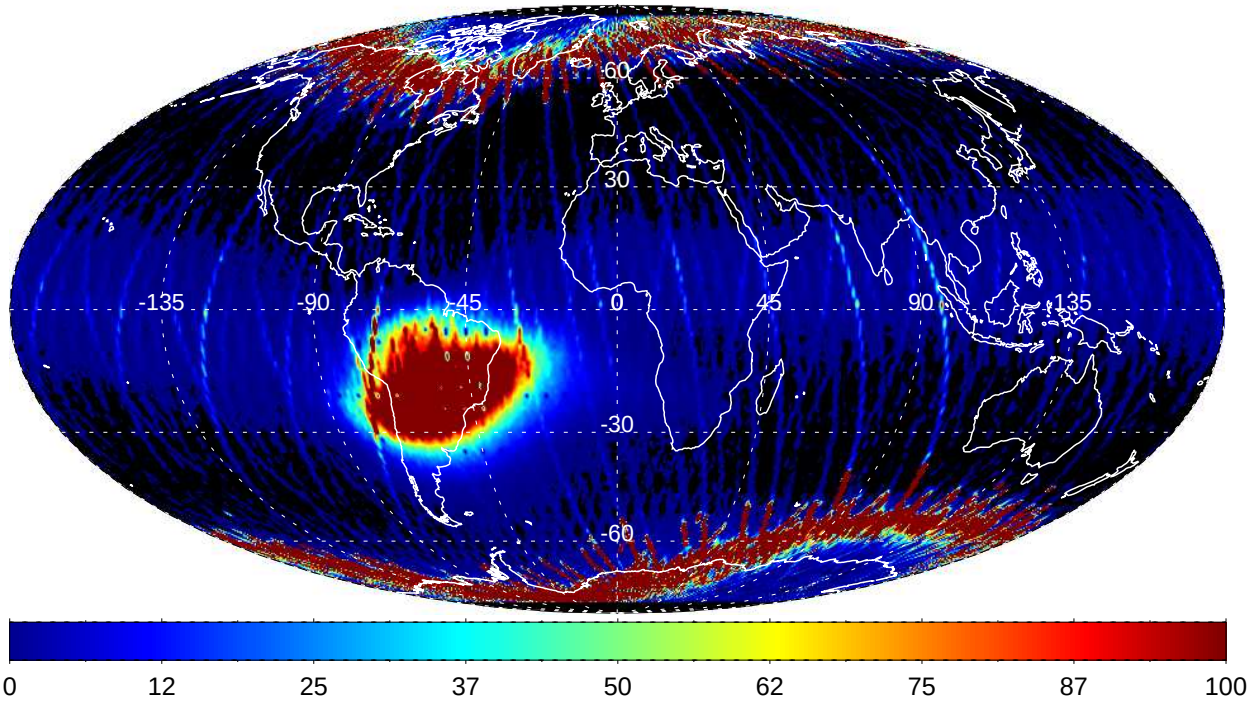

Figure 3.1: Flux count (i.e., counts per second) for protons with energies between 30–80 keV for August 2005. This shows the localized extent of the SAA, which is represented by the large red region with elevated proton flux count. The data is from the NOAA POES-15 spacecraft [95].

to 200–800 km altitude above the SAA region, while the outer belt (mostly electrons) extends to about 10 earth radii [97, 98]. The perpendicular view in Fig. 3.2 is a vertical slice through the SAA highlighting the penetration depth of the inner radiation belt.

The anomaly arises from the eccentric displacement between the magnetic and geographic poles of the Earth, which ultimately conspire to produce a region of relatively weak geomagnetic field intensity (roughly 22,700 nT at the Earth's surface in 2005 according to the CHAOS model, compared an antipodal value around 45,000 nT) that in turn permits the increased radiation. To a first approximation the geomagnetic field can be represented by a dipole inclined 11° from the Earth's rotation axis and offset from the center by about 500 km in the direction of the northwest Pacific. However, this description is insufficient when viewed in finer detail and possibly points toward the need for the incorporation of higher order field terms and a possible association with reverse flux patches at the core-mantle boundary. The SAA changes on short time scales in response to variations in solar activity and magnetospheric conditions, while on longer time scales it follows the westward drift associated with the secular variation [98, 99, 100, 101].

DOI: 10.2312/GFZ.b103-08029

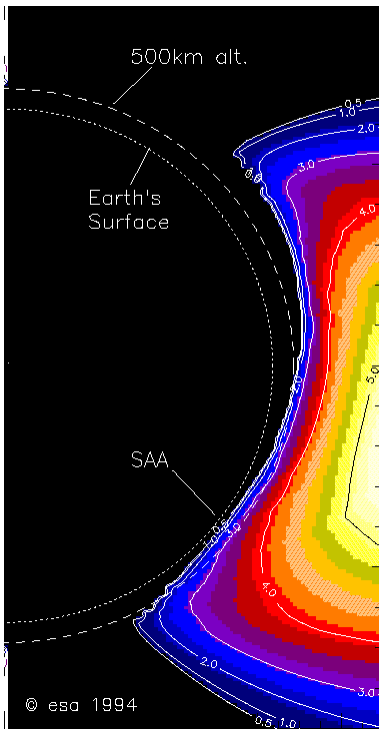

Figure 3.2: The proton flux through a slice of the Earth which demonstrates the radiation penetration enhancement over the SAA, from the ESA website [96].

This lack of the natural shelter afforded by the geomagnetic field is more than simply a curiosity of the region. It represents a real hazard, which can and does have direct impacts on spacecraft orbiting the Earth with inclinations between 35° and 60°, exposing them to long periods (several minutes) of stronger than usual radiation during each orbit. In fact, orbiting spacecraft, while traversing the region, may be bombarded by particles with energies of up to 10 MeV at rates as high as $3000\,\mathrm{cm}^{-2}\mathrm{s}^{-1}$, but it only takes particle energies of 1 MeV to have the potential to cause spacecraft damage [98, 102]. This can cause malfunctions in the electronic equipment by means of sudden event upsets (like the flipping of data bits) and moreover, the accumulated radiation causes a general reduction in the longevity of the spacecraft. In fact, a number of spacecraft have been rendered inoperative or otherwise have encountered problems, like NASA's Moderate Resolution Imaging Spectroradiometer (MODIS) instrument on TERRA, Denmark's Ørsted, NOAA's POES and DMSP [103]. Humans orbiting in the International Space Station or in spacecraft (like the space shuttle), as a result, are potentially subject to increased ionizing radiation dose rates as well, which can be biologically harmful. This effect can be shown, to a lesser degree, even on airplanes

DOI: 10.2312/GFZ.b103-08029

Table 3.1: Some of the nearest ground magnetic observatories to the South Atlantic Anomaly.

Observatory	**Obs. Code**	**Lat.**	**Lon.**	**Alt.**[km]	**Date Range**
Hartebeesthoek, South Africa	HBK	-25.88	27.71	1.52	1972-2004
Hermanus, South Africa	HER	-34.42	19.23	0.03	1941-2004
Huancayo, Peru	HUA	-12.05	-75.33	3.31	1922-1961 1964-1969 1979-1980 1985-1990 1997-2004
Trelew, Argentina	TRW	-43.25	-65.32	0.00	1957-1959 1964-1968 1993-1995 1997-2004
Tsumeb, Namibia	TSU	-19.22	17.7	1.30	1964-1989 1992-2004
Vassouras, Brazil	VSS	-22.40	-43.65	0.00	1915-1925 1957-1959 1968-1972 1979-1991 1998-2004

that fly through the region. Therefore, special measures must be taken during times of exposure in order to mitigate some of the danger associated with the increased particle flux. For instance, the International Space Station (inclination of 51.6°) was designed to incorporate extra shielding and the Hubble Space Telescope (spending about 15% of its time in the SAA) and other satellites often must shutdown parts of there systems to avoid potential damage [98, 101, 100, 104].

3.2 Magnetic Observatories near the South Atlantic Anomaly

Magnetic observatories can be an important tool for monitoring the time evolution of magnetic field phenomena, including in this case the SAA, and are among the first datasets examined. Some of the observatories that are positioned closest to the region of interest are listed in Tab. 3.1 and their locations are plotted on the map of Fig. 3.3. Unfortunately, the SAA is neither currently, nor has it been in the recent past (short time series relative to the time spanned by the gufm1), near one of these observatories. In fact, it lies basically in the center of a circle surrounded by these observatories. For that reason, it is difficult to use the data to say anything conclusive.

DOI: 10.2312/GFZ.b103-08029

3.3 Field Models Utilized in this Study

gufm1

The gufm1 [8, 27] is a model of the magnetic field for the 400-year interval spanning the years 1590–1990. The model's early data is largely based on a massive compilation of historical observations of the magnetic field. A great amount of this dataset originates from unpublished observations taken by mariners engaged in merchant and naval shipping. Considerable attention is given to both correction of data for possible dislocation (originating from poor knowledge of longitude) and to proper allocation of sizable errors in the data. The time-dependent field model constructed from the dataset is parameterized spatially in terms of spherical harmonics and temporally with B-splines. An important aspect of this model is that while the spherical harmonic expansion allows for the study of the field at the Earth's surface, it was specifically designed with the thought of being downward continued by the simple relation $(a/r)^{n+1}$ (where a is the Earth's radius, r is the desired radius, and n is the degree of the individual spherical harmonic coefficient (SHC)) to the CMB, which gives vital information about core dynamics over a long time span. In this way the model has improved the resolution of the core field, and represents the longest continuous model of the field available (from direct observation) making it ideal for studying the time evolution of the radial flux [8].

Comprehensive Model – Phase 4 (CM4)

The Comprehensive Model – Phase 4 (CM4) [74], an extension of the earlier CM3 [105], is a SHC model to degree $n = 65$ of the quiet-time, near-Earth magnetic field covering the years from 1960 through mid-2002 that has been derived using a comprehensive approach in order to separate spatial and temporal variations. Using this approach the model parameterizes the geomagnetic field and co-estimates fields associated with the major current sources in the near-Earth regime using field measurements from quiet time observatory hourly mean data (1960 through 2000) and data from the POGO, Magsat, Ørsted and CHAMP satellite missions. Most importantly, it also takes into account the crucial covariance between these disparate fields. Because of the comprehensive breadth of data used and the rigorous scope of its modeled physics, this one model is able to describe and discern field contributions that originate from the core, lithosphere, current systems of magnetospheric and ionospheric origin along with their associated induced contributions, and toroidal magnetic fields produced by in situ poloidal currents that impinge the thin sampling shells

DOI: 10.2312/GFZ.b103-08029

of the satellites [74].

The International Geomagnetic Reference Field (IGRF)

The International Geomagnetic Reference Field (IGRF) [75, 106] is a relatively low degree SHC model, which the international geomagnetic community at large has developed as a standard main field and secular variation model suitable for general consumption. It is derived using available data sources from satellites, magnetic observatories, ships and aircraft. It is recomputed every five years with a new five-year secular variation prediction. Prior models that have been extensively tested and shown to have acceptable levels of accuracy are reclassified as DGRF (Definitive Geomagnetic Reference Field) and exist for each 5-year epoch dating back to 1900. With the current addition of high quality satellite data the IGRF has been extended to SHC degree $n = 13$ for the main field and $n = 10$ for secular variation (up from $n = 10$ and $n = 8$, respectively).

CALS7K.2

CALS7K [26, 76] is a main field model for the past 7000 years (5000 B.C. – 1950 A.D.) based on archeomagnetic, lava and lake sediment data. The spatial and temporal resolution is significantly lower than that of current epoch models, but it describes the general, large-scale evolution of the dipole moment and secular variation of the geomagnetic field over the past several millennia. Original versions of the model [107] were based solely on directional (declination and inclination) data with a constraint on the axial dipole moment evolution to account for the lack of intensity information. However, with the subsequent inclusion of intensity data, the model can now provide an estimate of the dipole moment evolution. Yet despite this, the model is still rather limited due to the very uneven distribution and quality of the available data.

CHAOS

CHAOS [7] is a current epoch (1999–2005) SHC main field geomagnetic model of the Earth, which incorporates data from the Ørsted, CHAMP and SAC-C satellites missions (refer back to Sec. 2.1.2).

3.4 Tracking the Center of the South Atlantic Anomaly

The South Atlantic Anomaly (SAA) is easily observed today when the magnetic field intensity is computed from satellite measurements, which is clearly evident as the large dark area in Fig. 3.3. However, its existence was not recognized until the advent of early twentieth century magnetic field

DOI: 10.2312/GFZ.b103-08029

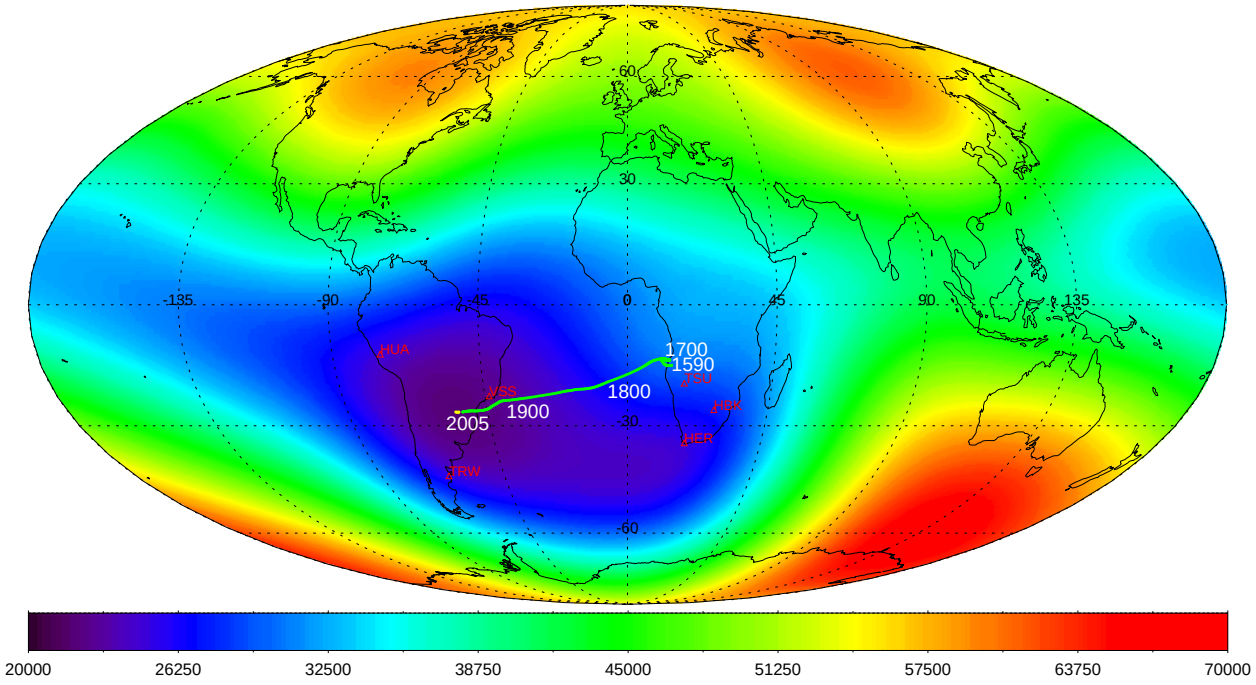

Figure 3.3: Map of the total field intensity (nT) for epoch 2005 computed using the CHAOS model. The South Atlantic Anomaly is well defined by its weaker field values. The track of the minimum of this anomaly over the last four centuries is shown by the green (gufm1) and yellow (CHAOS) lines with white labels indicating the approximate year. Several nearby magnetic observatories are highlighted in red (HUA - Huancayo, VSS - Vassouras, TRW - Trelew, TSU - Tsumeb, HBK - Hartebeesthoek, HER - Hermanus).

maps [99], like those of Chapman (1940) [108]. In this study the SAA position is defined as the location of the minimum of the total field intensity as computed by various field models, however, other possible definitions exist [109]. The method employed to calculate the SAA position involved computing a global $1^\circ \times 1^\circ$ grid of the total field, B_F, using each of the models of interest (gufm1, CM4, IGRF or CHAOS). A simple refinement approach was then employed, whereby, the latitude and longitude location of the minimum field value was used to recompute a new $0.1^\circ \times 0.1^\circ$ grid extending $\pm 7^\circ$ centered about that minimum location. Similarly, that position was then recursively used to compute another $0.01^\circ \times 0.01^\circ$ grid to determine the final minimum location and strength. The resulting parameters are plotted in Fig. 3.3 and Fig. 3.4.

These figures show that the magnetic field is becoming generally weaker in this specific region. The values computed here are based on three models, covering various timespans: 1590–1990 from

DOI: 10.2312/GFZ.b103-08029

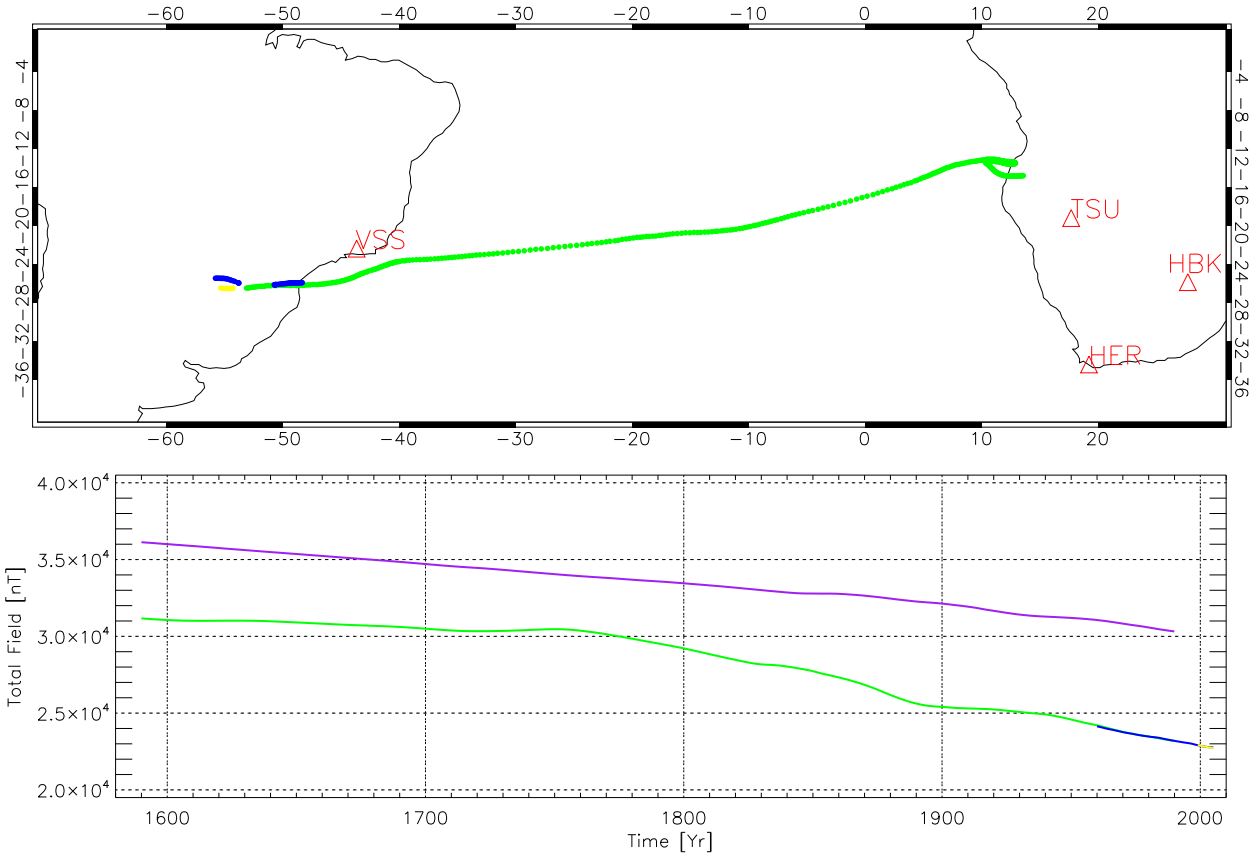

Figure 3.4: The ground track and strength of the SAA from 1590–2005. Green = gufm1(1590–1990), Blue = CM4(1960–2005), and Yellow = CHAOS(1999–2005). The position track of the SAA starts over Africa (1590) then migrates toward South America (2005). The CM4 seems to disagree slightly in position of the SAA but agrees in strength. The purple line depicts the decay of the tilted dipole, which has a shallower slope than the decrease seen in the SAA total field.

the gufm1 model, 1960–2005 from the CM4 and 1999–2005 from the CHAOS model. The SAA minimum has moved over the last four centuries, from the southern African continent to South America, at a noteworthy rate during the last few centuries. The blue curve represents values computed using the CM4, and it seems to not smoothly match the values computed using the CHAOS (Yellow) and the gufm1 (Green) model in position, but does match in field strength. The purple line uses Eq. (3.1) (where g_1^0, g_1^1 and h_1^1 are the model axial and equatorial dipole Gauss coefficients) to calculate the tilted dipole using the gufm1 model, as a way of seeing how much of the SAA decay is attributable to overall dipole decay.

DOI: 10.2312/GFZ.b103-08029

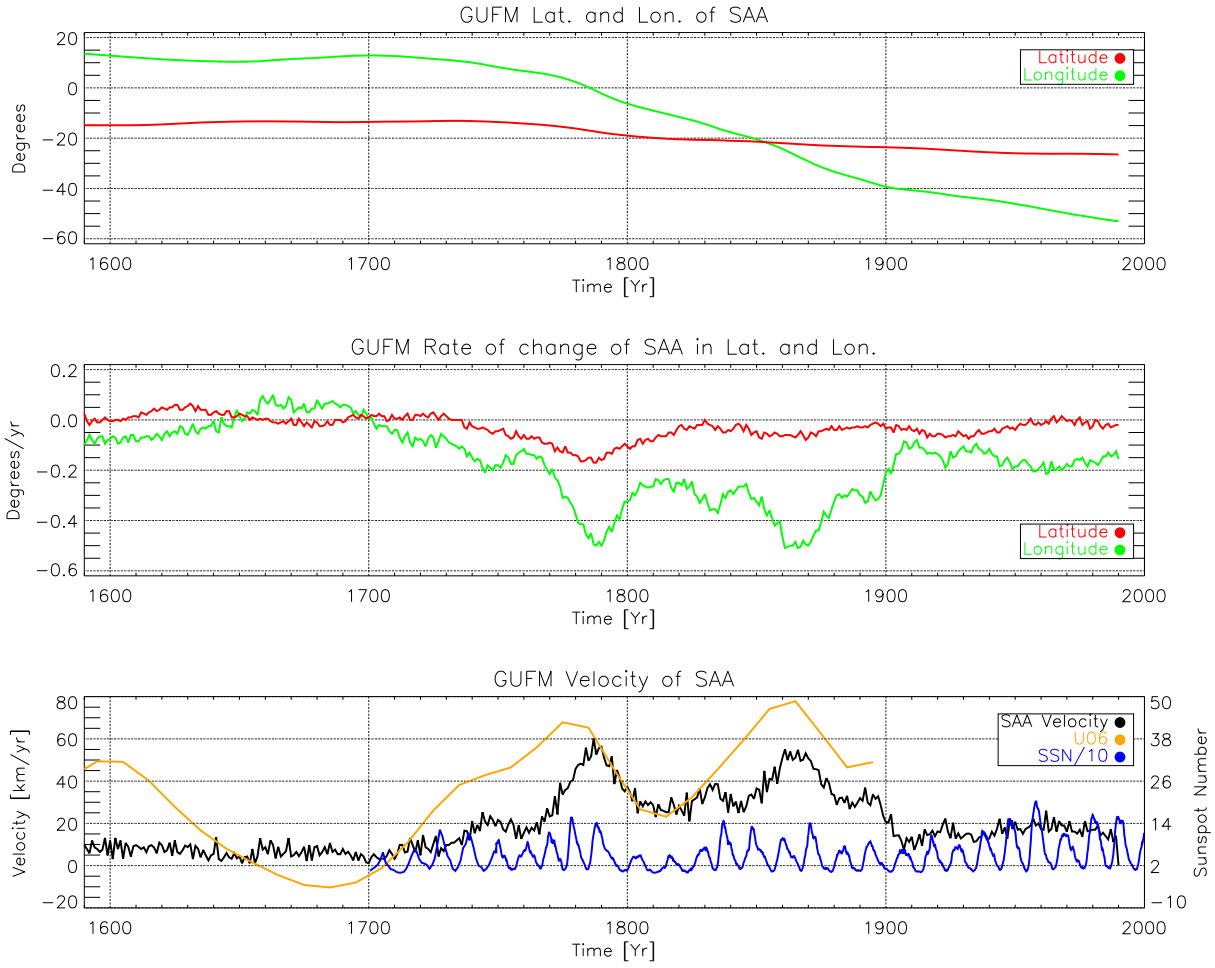

Figure 3.5: Top window – Latitude (red) and Longitude (green) of the SAA over the period 1590–1990 as computed by the gufm1. Middle window – Rate of change of the latitude and longitude in degrees/yr of the SAA. Bottom window – Rate of change in the surface distance of the SAA compared with the U06 (orange) sunspot number reconstruction and the actual SSN (blue, divided by 10). The two periods with rapid change around 1790 and 1870 show correlation with elevated SSN and U06.

$$G_{TD} = \sqrt{(g_1^0)^2 + (g_1^1)^2 + (h_1^1)^2}\,, \tag{3.1}$$

$$\dot{G}_{TD} = \frac{(g_1^0 \dot{g}_1^0) + (g_1^1 \dot{g}_1^1) + (h_1^1 \dot{h}_1^1)}{G}, \tag{3.2}$$

The SAA drifts generally to the west at a speed of about 0.3°/yr, and is noticeable in the track evolution in Fig. 3.3 and more directly in plots of the gufm1 SAA position velocity in Fig. 3.5 (Figs. 3.22–3.23 also demonstrate this movement between 1600–1990 in 50-year intervals). The

DOI: 10.2312/GFZ.b103-08029

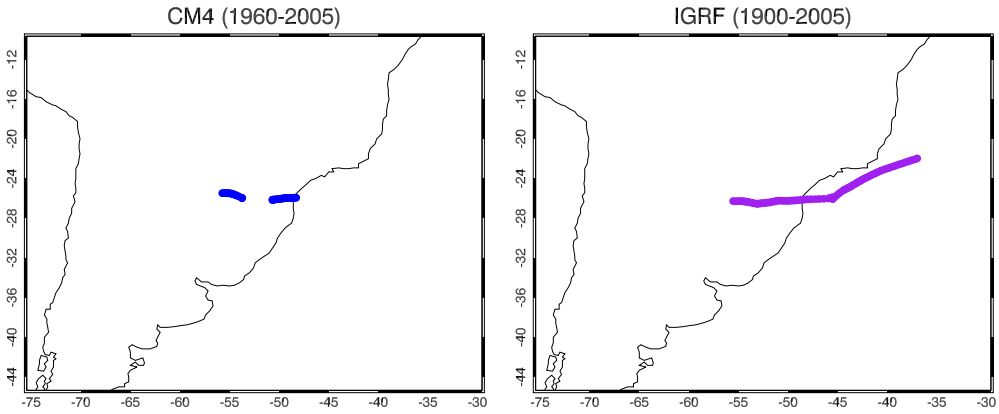

(a) CM4 SAA Track (b) IGRF SAA Track

Figure 3.6: The CM4 (a) has a peculiar jump (first seen in Fig. 3.4) in the longitude track of the SAA between the years 1986 and 1987 where the location jumps by 3.03° between the start of September (50.69° W Lon.) and the beginning of October (53.72° W Lon.). This jump appears to be an artifact caused by the interaction of shape of the minimum and the SAA track grid resolution. The IGRF (b) does not show an analogous jump, but does show a jog in the track at around 1945; however the gufm1 also shows a similar occurrence, but not as sharp.

latitude (red) of the SAA in the top window stays consistently close to 20° S latitude (±5°), and similarly its position velocity fluctuates only minimally about 0. On the other hand the longitude (green) shows a large swing in position over this same time period ranging from 15° W to 55° E (Africa to South America), with peaks in velocity at 1790 and 1870. The bottom window depicts the rate of change of the point to point surface distance showing the same two peaks in velocity. Overlain on this bottom window is the sunspot number [110] and a longer period sunspot reconstruction (U06) [111], both of which seem to show similarities to the SAA velocity.

The drift rate of the SAA closely matches the differential rotation between the Earth's core and lithosphere, estimated to be between 0.3°/yr – 0.5°/yr [112]. This westward drift of the SAA has also been shown, at least in the near term, by measurement of particle flux dose rates on orbiting manned spacecraft [101]. It has been suggested [99] that the SAA drifts westward in the equatorial region, circumnavigating the globe with a period of approximately 2300 yr.

Although first noted in Fig. 3.4, the close-up of Fig. 3.6 better demonstrates some peculiar behavior in the SAA track of the CM4 (and also the IGRF). CM4 (a) has a pronounced jump in the longitude track of the SAA between the years 1986 to 1987 where the location jumps by 3.03° between the start of September (50.69° W Lon.) and the start of October (53.72° W Lon.).

DOI: 10.2312/GFZ.b103-08029

However, upon closer inspection this jump appears to arise from the topography of the field intensity surface, which displays a relatively long longitudinally extended area of the lowest field, and so has more to do with the limited resolution of the SAA position calculation than an actual jump. When a higher resolution test grid was applied to the appropriate area and time, the jump was not as evident. The IGRF does not show an analogous jump, but does show a jog in the track at around 1945. Possible reasons for this are discussed by others [113], where irregularities are pointed out in secular variation studies derived using the IGRF. However it should be pointed out that the gufm1 also displays a similar change in track, but it is not as sharp.

Wanting to extend the SAA track even further backward in time, the CALS7K.2 model was used to calculate the SAA over its temporal range (5000 B.C.–1950 A.D.). However, as seen in Fig. 3.7 the CALS7K.2 is unfortunately unable to resolve properly the SAA even during the period of overlap with the other models showing a different location and opposite intensity trend (bottom panel). The calculation would have long periods of an essentially stationary SAA, followed by the development of a new stationary low elsewhere. This pattern would cycle back and forth with lobes developing and decaying, but with little of the expected lateral movement. This behavior, however, is consistent with the dataset when considering the sparseness and nature of the data involved. It should be noted that the development of new lows is not in and of itself bad, because this behavior could be expected [100] in the future (off the southern tip of Africa by 2100) assuming secular variation follows the predictions of the IGRF-1995 model. Also plotted in the middle panel of this figure are some sunspot number reconstructions [111] with a 24-year running average. Despite the inability of the CALS7K.2 to determine the SAA location, a correlation is evident (particularly after 2000 B.C.) when the strength of the SAA is compared with the inverse of the 24-year running average of the sunspot reconstruction U06. Although, this correlation is not entirely clear since the corresponding local extrema are not consistent in time (that is to say, the sunspot number extrema tend to vary from initially leading to then lagging those of the SAA strength).

This correlation indicates that SAA may, in part, respond to external inputs, in that higher solar activity leads to more activity in the radiation belt, which in turn grants deeper penetration of the resulting generated external fields, further reducing the already weakened geomagnetic field measured at the surface. In a similar vein, some [114, 115] have pointed to a link between solar activity and LOD studies (which has been related to geomagnetic jerks). However, because it is thought that the SAA ultimately arises from physics in the core, in the next sections it should be interesting to investigate some of the parameters at the CMB in order to look for some indication

DOI: 10.2312/GFZ.b103-08029

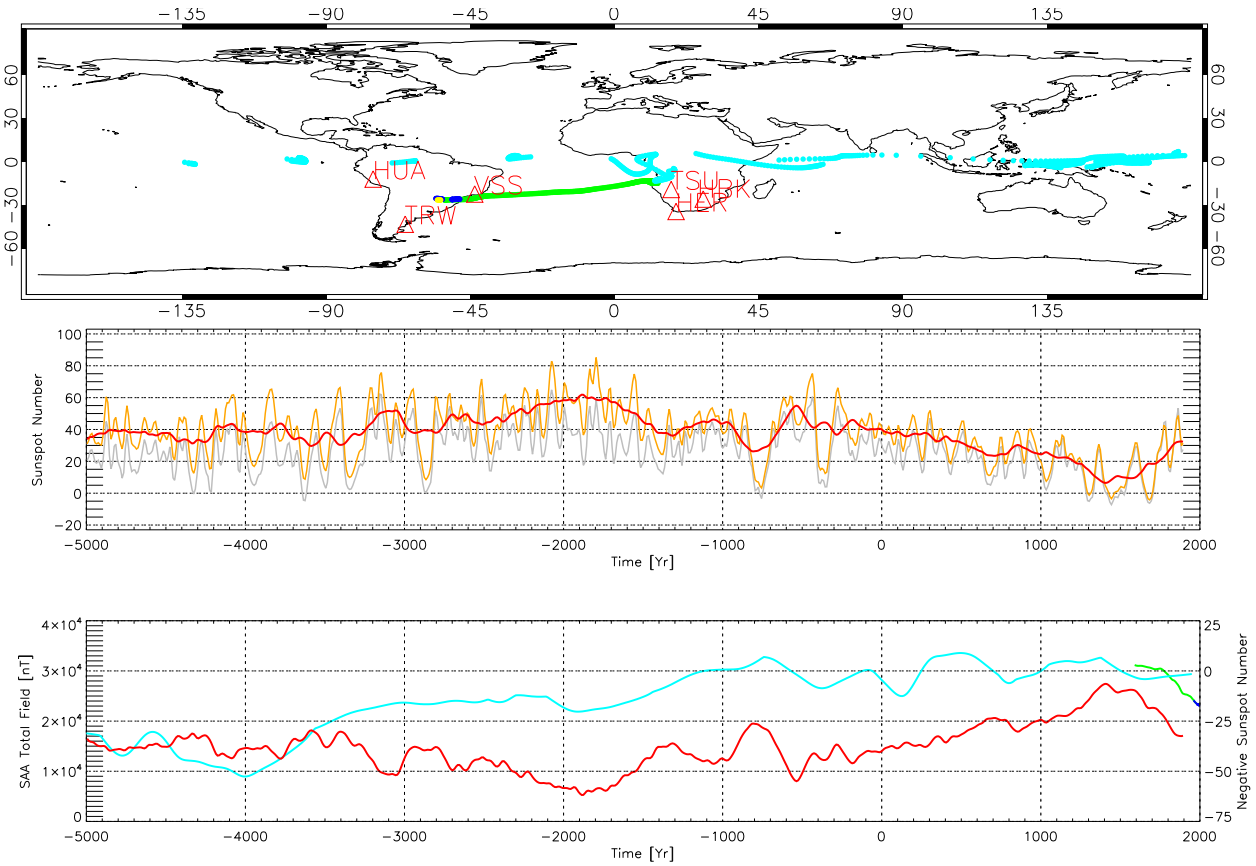

Figure 3.7: The ground track and strength of the SAA from 5000 B.C.–2005 A.D. with Cyan = CALS7K.2(5000 B.C.–1950 A.D.), Green = gufm1(1590–1990), Blue = CM4(1960–2005) and Yellow = CHAOS(1999–2005). The position track of the SAA starts over Africa (1590) with the gufm1 then migrates toward South America (2005). The CALS7K.2 due to the nature of its dataset is unable to reliably resolve the SAA. The locations of the observatories listed in Tab. 3.1 are also displayed. The middle panel displays the sunspot number reconstructions series, S04 (grey) and U06 (orange), with a 24-year running average of the U06 in red. The bottom panel shows the strength of the SAA with the negative of the averaged sunspot number, which shows after about 2000 B.C. a loose correlation.

of a correspondence.

3.5 Axial Dipole Moment - A Role in the SAA?

The geomagnetic field, according to geodynamo theory, has a very complex structure within the core, but outside near the surface it is a relatively simple tilted dipole. Of which approximately 80% of the total is dipole in nature, with the remaining 20% being of a weaker nondipole contribution. However, the time-averaged field tends to reduce this nondipole portion, instead leaving what

DOI: 10.2312/GFZ.b103-08029

approaches a geocentric axial dipole. Of course it takes geologic times scales for this effect to be realized, about 5 Ma to get to within 95% and 120 Ma before it is essentially a dipole. An important measurable quantity of the dipole is its moment [98]:

$$m \equiv (m_x\hat{x} + m_y\hat{y} + m_z\hat{z}) \tag{3.3}$$

$$= \frac{3r}{2\mu_0}\int B_r\,(sin(\theta)cos(\phi)\hat{x} + sin(\theta)sin(\phi)\hat{y} + cos(\theta)\hat{z})\,dS \tag{3.4}$$

$$= \frac{4\pi r_e^3}{\mu_0}\left(g_1^1\hat{x} + h_1^1\hat{y} + g_1^0\hat{z}\right). \tag{3.5}$$

From these, the axial moment, m_z, is straightforwardly determined either as a function of the dipole SHC or the B_r component of the field, both of which are readily available from geomagnetic models. Similarly the rate of change of the axial moment is calculated in Eq. (3.6) by taking the time-derivative of the axial component of Eq. (3.5), where θ is the co-latitude and $\dot{B}_r$ is the first time-derivative of the B_r component of the magnetic field computed using either the gufm1, CHAOS, CM4, OSVM (Ørsted Secular Variation Model [33]), or M102389 (Magsat model [69]) models.

$$\dot{B}_r cos(\theta) \tag{3.6}$$

More specifically, this was accomplished by computing B_r as normal, but substituting, the secular variation or higher time terms in place of the static field coefficients. The computed $\dot{B}_r$ value is downward continued to the core-mantle boundary (CMB) assuming an outer core radius of $R_c = 3480\,\text{km}$.

Understanding the geomagnetic dipole moment and its secular change are important for geodynamo studies for a number of reasons. Firstly and probably most obviously, is the simple observational fact that the geomagnetic field approximates a dipole field. Another reason is that it is an intrinsic, frame-invariant, global property of the Earth. Lastly, from a practicality standpoint, this quantity is one of the few that is easily determined from existing geomagnetic models, which derive solely from surface measurements. In this way, it serves to easily and remotely probe core geodynamic processes [98].

In an effort to visualize the rate of change of the axial dipole moment, Eq. (3.6) was applied to the gufm1 to produce the series of plots in Fig. 3.8. These images show a number of interesting features. For instance, there is a consistent region of relatively strong positive change starting in 1600 around 40° S, 30° W that drifts slowly westward, while intensifying throughout the entire series. Common to all the years is the relative quiet seen in the Pacific and the equatorial regions,

DOI: 10.2312/GFZ.b103-08029

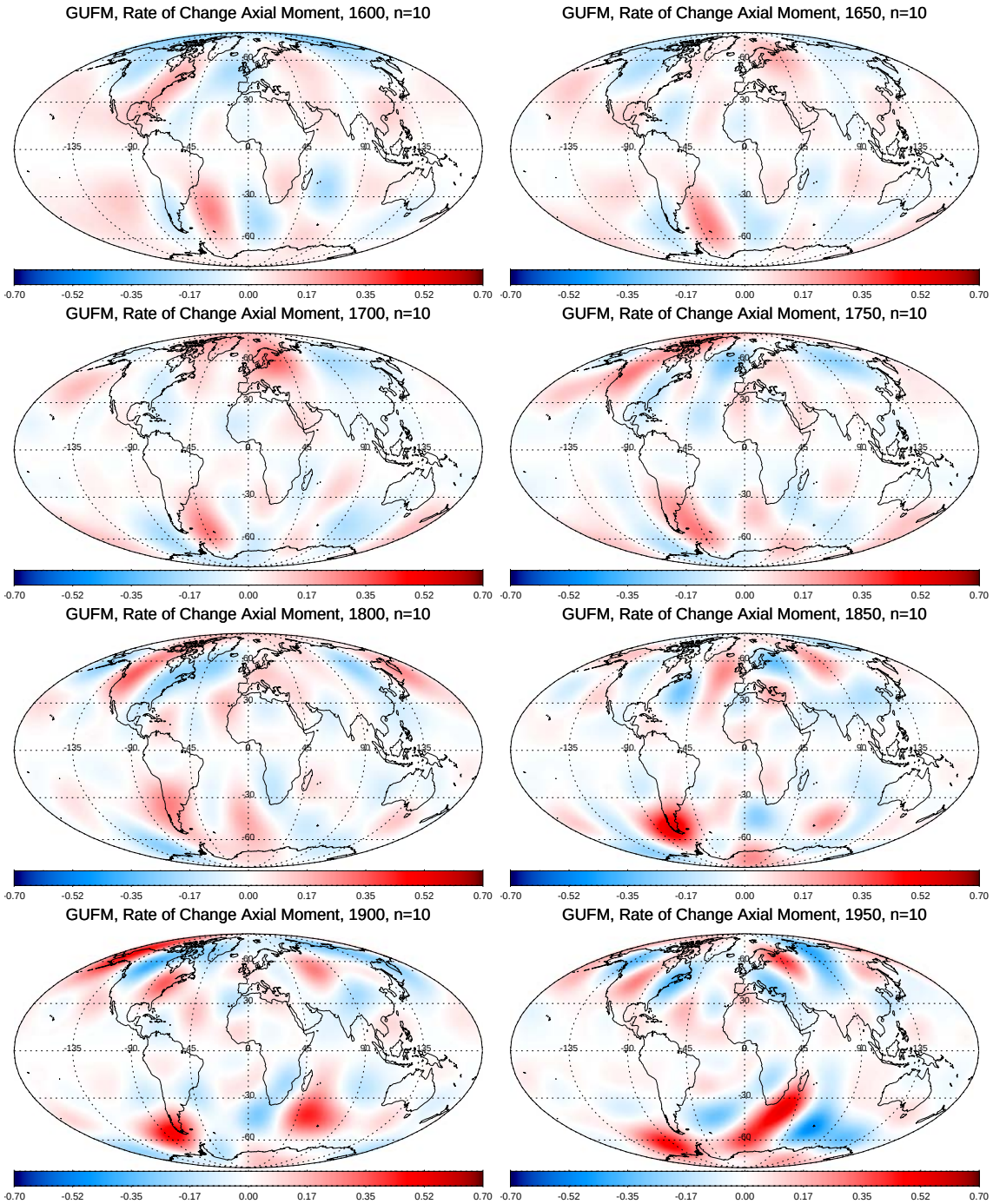

Figure 3.8: The gufm1 Rate of Change of the Axial Moment for every 50 years between 1600 and 1950 at the CMB for spherical harmonic degree $n = 10$ in units of mT/century.

DOI: 10.2312/GFZ.b103-08029

Table 3.2: Ranges for the rate of change of the axial dipole moment at the CMB for every 10 years using gufm1 spherical harmonic degrees 10 and 13 in units of mT/century. The gufm1 above SV $n = 10$ damps which is why the there is little difference in range between the $n = 10$ and $n = 13$ calculations.

Year	Min $n = 10$	Max $n = 10$	Min $n = 13$	Max $n = 13$	Year	Min $n = 10$	Max $n = 10$	Min $n = 13$	Max $n = 13$
1590	-0.31	0.28	-0.31	0.29	1800	-0.27	0.35	-0.31	0.36
1600	-0.29	0.29	-0.29	0.29	1810	-0.27	0.29	-0.27	0.31
1610	-0.27	0.29	-0.26	0.29	1820	-0.25	0.28	-0.25	0.30
1620	-0.24	0.28	-0.23	0.29	1830	-0.20	0.35	-0.21	0.33
1630	-0.22	0.28	-0.22	0.29	1840	-0.31	0.43	-0.33	0.42
1640	-0.21	0.29	-0.20	0.30	1850	-0.33	0.58	-0.35	0.58
1650	-0.19	0.30	-0.19	0.30	1860	-0.33	0.67	-0.33	0.68
1660	-0.19	0.30	-0.19	0.31	1870	-0.33	0.70	-0.38	0.71
1670	-0.20	0.32	-0.20	0.32	1880	-0.33	0.65	-0.42	0.66
1680	-0.21	0.34	-0.20	0.34	1890	-0.40	0.61	-0.47	0.61
1690	-0.21	0.36	-0.20	0.36	1900	-0.41	0.53	-0.47	0.53
1700	-0.21	0.34	-0.21	0.34	1910	-0.46	0.58	-0.47	0.60
1710	-0.22	0.32	-0.23	0.34	1920	-0.48	0.70	-0.46	0.71
1720	-0.23	0.33	-0.25	0.35	1930	-0.43	0.75	-0.43	0.74
1730	-0.25	0.32	-0.27	0.34	1940	-0.42	0.70	-0.43	0.71
1740	-0.26	0.32	-0.29	0.35	1950	-0.51	0.57	-0.48	0.58
1750	-0.29	0.31	-0.31	0.34	1960	-0.65	0.53	-0.64	0.50
1760	-0.32	0.32	-0.34	0.31	1970	-0.62	0.58	-0.64	0.52
1770	-0.33	0.31	-0.35	0.31	1980	-0.65	0.60	-0.68	0.55
1780	-0.32	0.31	-0.37	0.31	1990	-0.68	0.65	-0.71	0.68
1790	-0.31	0.34	-0.35	0.34					

while most of the stronger activity seems generally to be in either the polar regions or the Atlantic sector (which is also associated with the SAA region). There is also another region of very strong positive change that starts in 1850 (40° S, 75° E) and quickly comes to dominate the area 100 years later in 1950. Tab. 3.2 summaries the minimum and maximum in the values of the rate of change in the axial dipole moment, and so is a corollary to Fig. 3.8. The gufm1 damps SV terms above $n = 10$, which accounts for the only slight difference between the computation of $n = 10$ and $n = 13$. The minimum values stay fairly constant around $-0.3\,\mathrm{mT/century}$ up to about 1840 when the value starts to speedily increase. There is a similar character for the maximum values. The date 1840 coincides in the gufm1 model with the elimination of an imposed $-15\,\mathrm{nT/yr}$ dipole decay to rely instead on intensity data [8].

DOI: 10.2312/GFZ.b103-08029

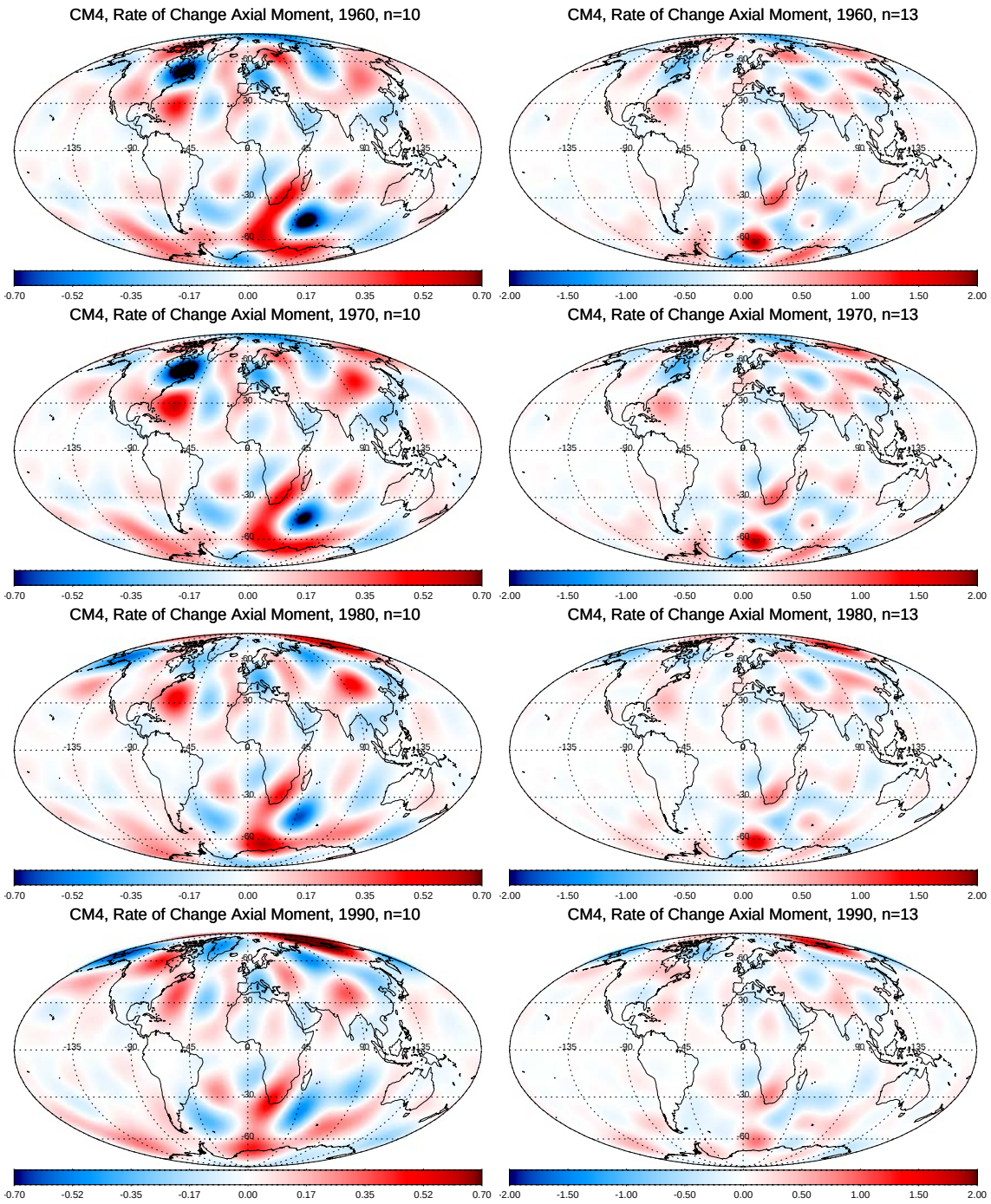

Figure 3.9: CM4 Rate of Change of the Axial Dipole Moment for 1960–1990 at the CMB calculated for $n = 10$ and $n = 13$ in units of mT/century. Despite the change in scale and the more resolved features, the similarities persist from the $n = 10$ to $n = 13$, even if fine detail differs. Common to these plots is the high activity in the Atlantic sector, which in a general sense is co-located with the SAA, albeit, displaced somewhat to the southeast.

DOI: 10.2312/GFZ.b103-08029

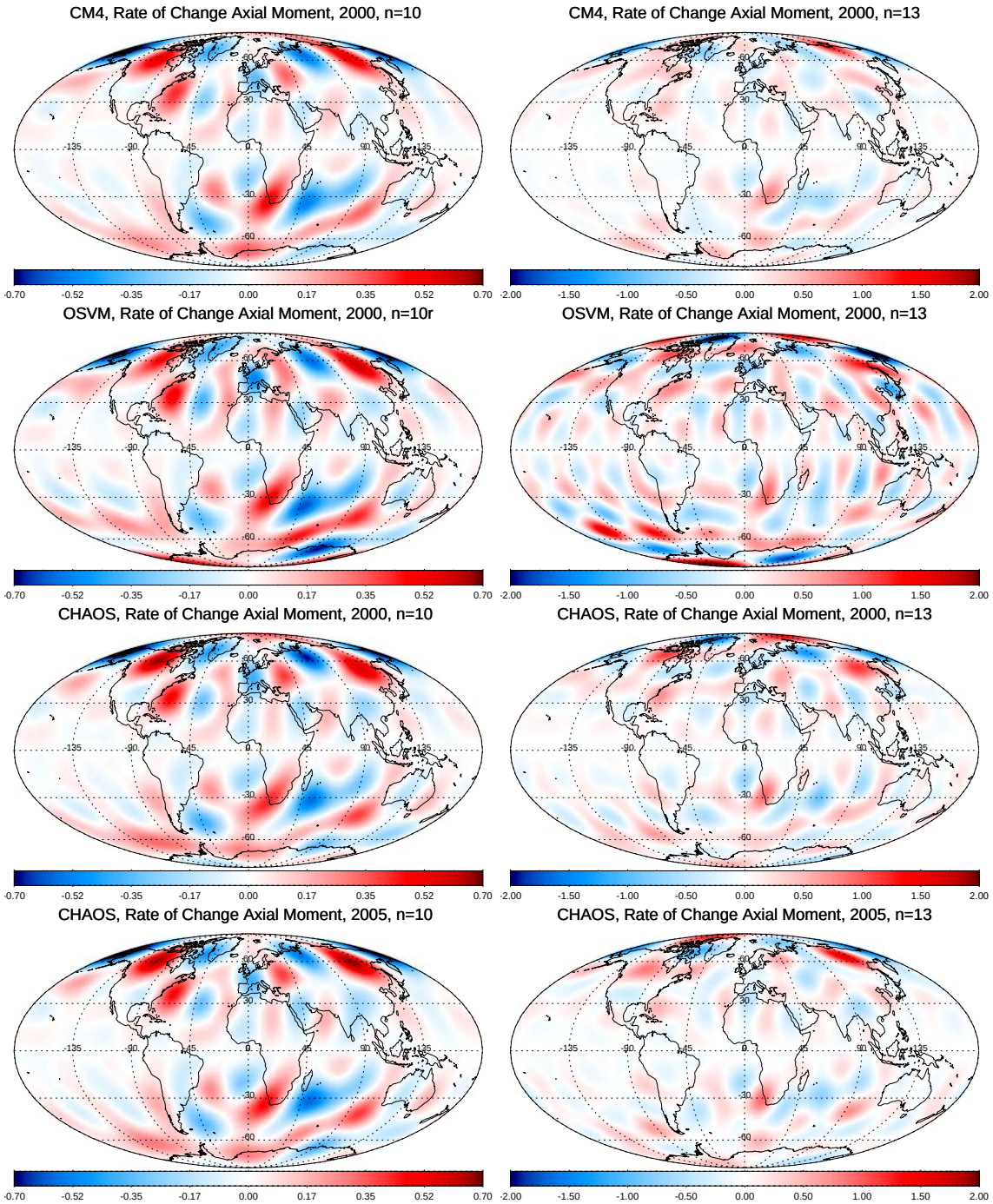

Figure 3.10: CHAOS, CM4 & OSVM Rate of the Change of Axial Moment for 2000 and 2005 at the CMB, $n = 10$, $n = 13$ in units of mT/century.

DOI: 10.2312/GFZ.b103-08029

Table 3.3: Ranges for the rate of change of the axial dipole moment at the CMB for CM4, Magsat, OSVM, and CHAOS in units of mT/century at various dates and spherical harmonic degrees.

Model	**Year**	**Min** $n = 10$	**Max** $n = 10$	**Min** $n = 13$	**Max** $n = 13$	**Min** $n = 18$	**Max** $n = 18$
CM4	1960	-0.84	0.62	-1.21	1.99		
CM4	1965	-0.85	0.61	-1.20	1.98		
CM4	1970	-0.95	0.64	-1.11	1.96		
CM4	1975	-0.69	0.65	-1.01	1.84		
CM4	1980	-0.64	0.66	-0.88	1.67		
CM4	1985	-0.60	0.90	-1.01	1.67		
CM4	1990	-0.66	1.00	-1.25	1.86		
CM4	1995	-0.70	0.82	-1.41	1.75		
CM4	2000	-0.83	0.57	-1.60	1.33		
Magsat	1980	-3.34	4.78				
OSVM	2000	-0.74	0.63	-2.30	2.36		
CHAOS	2000	-0.82	0.69	-1.67	1.35	-6.78	9.68
CHAOS	2005	-0.87	0.70	-1.76	1.62	-9.10	10.6

The Magsat model only has SV terms up to $n = 10$ whereas the OSVM has SV terms going up to $n = 13$. The CHAOS model has SV terms up to $n = 18$, while the CM4 can have arbitrarily high SV terms, but only terms up to $n = 13$ were considered for the purposes of this study. The $n = 10$ values as outlined in Tab. 3.3 are the most consistent values across models (save the Magsat model) and produce global plots with some consistent features (see Figs. 3.9-3.10).

Comparing the common date 1980 across the models gufm1, CM4 and Magsat, one notices similarities between both the minimum and maximum for $n = 10$ rate of change of the axial dipole moment (both about ± 0.6 in Tabs. 3.2–3.3) as well as similar features (gufm1 not shown for 1980). These similarities are altered when jumping to $n = 13$, but as mentioned the damping of the gufm1 limits the comparison. The Magsat model values for the rate of change on the axial moment seem to be inconsistent with the other models (the Magsat $n = 10$ values are more than double the values of most of the other models at $n = 13$), this may be due to a number of reason including the fact that the model was computed from only 6 months of data which had only a narrow selection of local times. While the model produces adequate results during the time-interval of the model, effectively extrapolating outside this range by using solely the SV terms probably produces somewhat less then robust results.

The most striking feature is an "L" shaped three lobed region of high positive change in the

DOI: 10.2312/GFZ.b103-08029

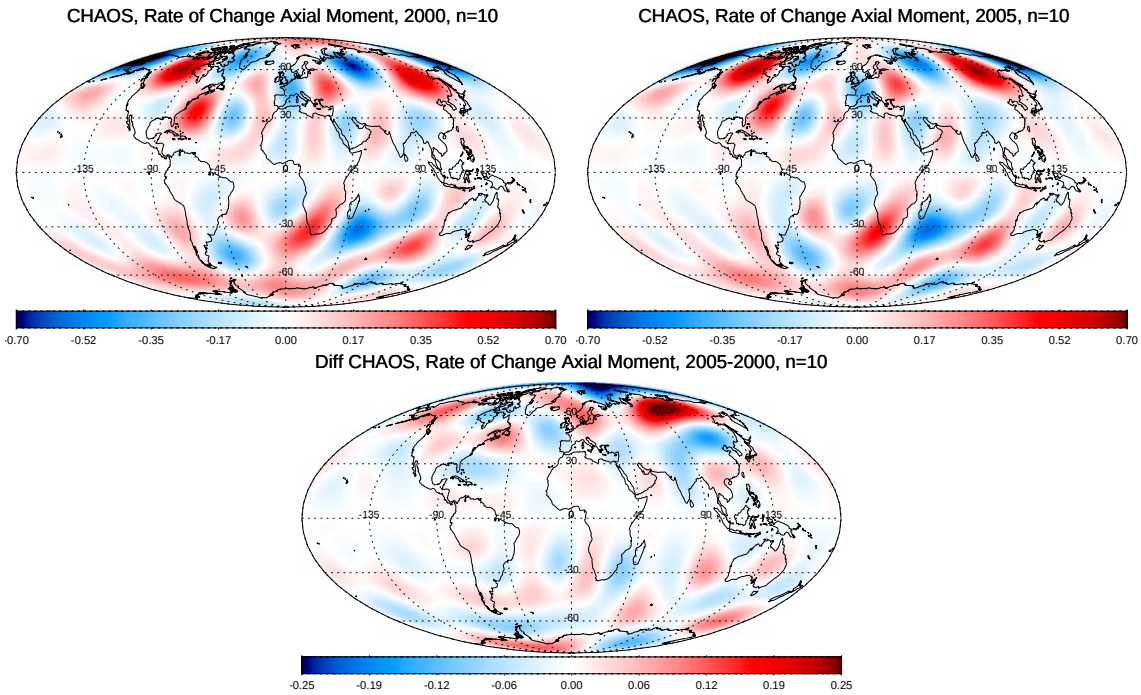

Figure 3.11: CHAOS Rate of Change of the Axial Moment for 2000 & 2005 and the difference at the CMB, $n = 10$ in units of mT/century. Outside of the strong differences in the polar regions, one of the area associated with activity is the south Atlantic, an area in common with the SAA.

southern hemisphere from the tip of South Africa southwest to the Prime Meridian at about 60° S latitude and then back southeast into Antarctica. There is a strong low in the center of this feature. This is consistent with Fig. 4d from the paper of Olson (2006) [98]. Over the time period covered by the CM4, 1960–2005, this entire feature drifts slowly with a counterclockwise rotation and the two more southerly lobes tend to diminish in intensity. Another commonality is a high/low pair of lobes in the Atlantic at about 30° N, with the high to the west near the United States east coast. This high, over the course of time of the CM4 drifts slightly to the north. Just above this, over eastern Canada in 1960, is a very strong low that drifts northward toward the pole and by 1975 starts to significantly diminish in strength.

Even over the short five year period of the CHAOS model, between 2000–2005, Fig. 3.11 shows some evolution in the rate of change of the axial dipole moment. The largest differences are seen in Asia and over the north polar region. The North Pole displays a relatively strong low, while north-central Siberia shows a region of strong positive change. Further southwest, around China, there is another region of elevated negative change that hooks south and tails off toward India. But

DOI: 10.2312/GFZ.b103-08029

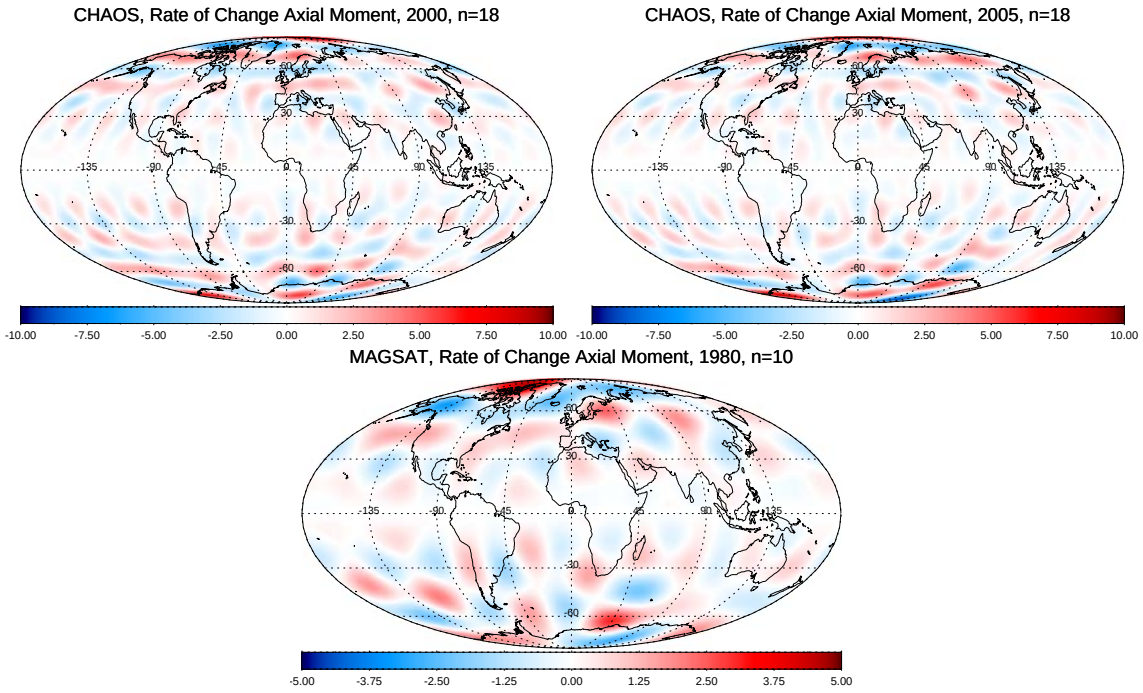

Figure 3.12: Magsat & CHAOS Rate of the Change of Axial Moment for 1980, 2000 & 2005 at the CMB, $n = 10$, $n = 18$ in units of mT/century.

most notable is again the relative lack of significant change in the Pacific regions. Also the south Atlantic area shows a great deal of activity, this area of course, corresponds in general to the area governed by the SAA.

Fig. 3.12 demonstrates the differences and similarities with a low degree representation in the Magsat model ($n = 10$) with that of the higher degree CHAOS model ($n = 18$). Notice the quiet activity in the equatorial regions common to both. Interesting also is the almost alternating horizontal strata of axial dipole change at the poles visible in the CHAOS model; this is only visible in the vaguest sense in the Magsat model. The Magsat model does reproduce to first order the 'L' shape feature south of Africa, which is not so clear in the CHAOS model. It is probably not reasonable, however, to put much weight in any of the plots in this figure, since for reasons already mentioned, the Magsat model is in some disagreement with the other models in strength (as well as pattern), and the CHAOS SV terms, up to $n = 18$, near the limit of trustworthiness.

DOI: 10.2312/GFZ.b103-08029

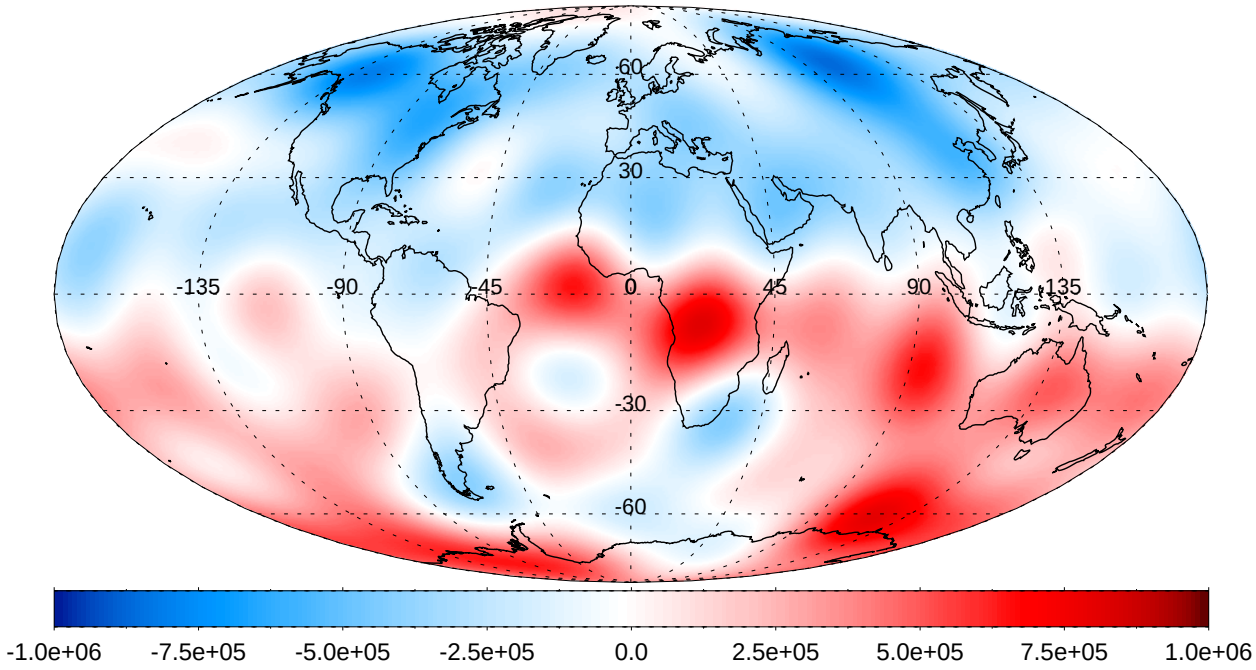

Figure 3.13: The radial magnetic field at the core-mantle boundary (R_{CMB}=3480 km) for epoch 2002.5, computed using the CHAOS model up to SHC degree $n = 10$ in units of nT.

3.6 Magnetic Radial Flux at the Core-Mantle Boundary

The origin of the geomagnetic field in Earth's liquid, outer core has been confirmed by several studies [116, 117, 118] that were able to estimate the radius of the internal source region using geomagnetic and secular variation observations. These results agree very well with the seismologically determined outer core radius, or core-mantle boundary (CMB, approximately 3480 km). These studies also suggest that Earth's mantle must be a rather good electrical insulator, providing a justification for considering Earth's magnetic field in the mantle as a potential field. Further evidence suggesting that the mantle is a good electrical insulator comes from high pressure mineral physics experiments [119], which imply that the electrical conductivity is likely to be between 3–10 Sm^{-1} above the base of the mantle. Adopting this assumption that the mantle is to first order an electrical insulator, it is possible to downward continue the geomagnetic field to the edge of its generation region at the core surface [120].

The largest portion of the geomagnetic field, measured at the Earth's surface, is generated by dynamo processes in the fluid, outer core [4]. To a first order approximation the field exhibits a

DOI: 10.2312/GFZ.b103-08029

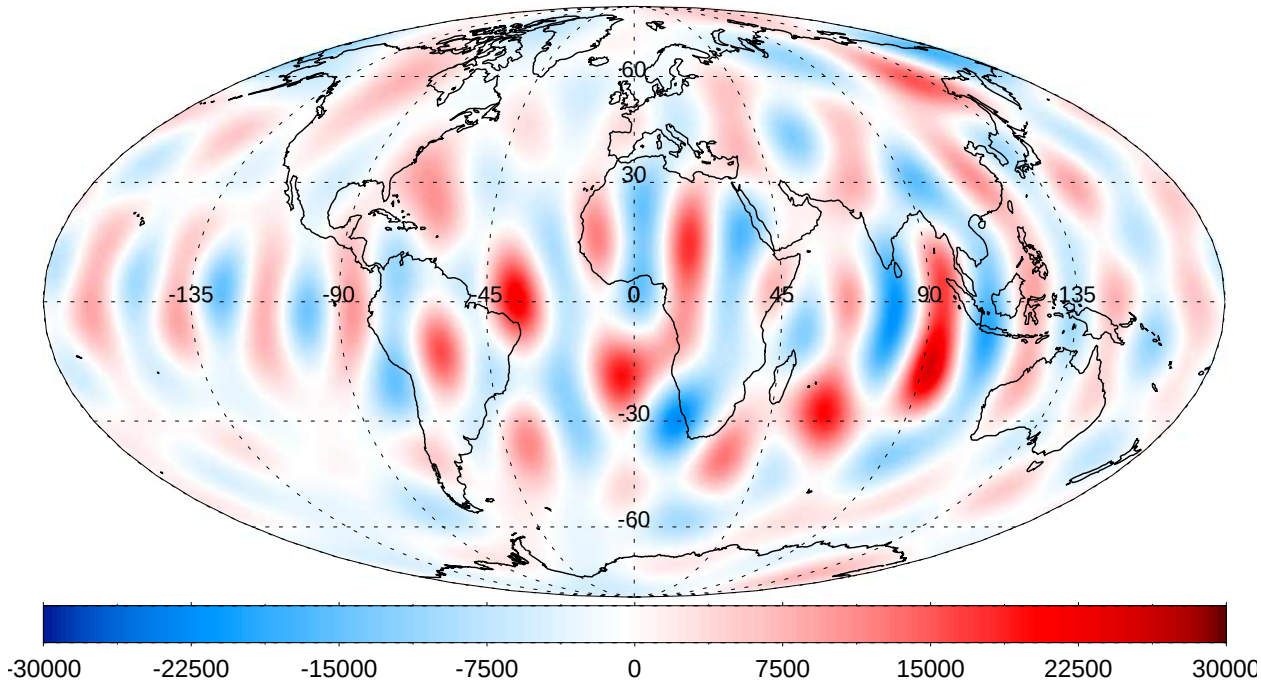

Figure 3.14: The secular variation of the radial field at the core-mantle boundary (R_{CMB}=3480 km) for epoch 2002.5. The field values are computed from the CHAOS secular variation model up to SHC degree $n = 14$ in units of nT/yr. The strongest areas of change are in the Atlantic Ocean west to the Indian Ocean, the same area in Fig. 3.13 showing reversed-flux patches (this is also the area associated with the SAA).

dipolar pattern, whereby the magnetic flux crossing the CMB is generally structured such that field lines presently emanate out from the positive "southern magnetic hemisphere" (referred to as the normal polarity flux Patch P) and enter through the negative "northern magnetic hemisphere" (referred to as the normal polarity flux Patch N). However, a finer analysis reveals that this dichotomy is not so clear when viewed at higher resolutions, since excursions of relatively small patches of oppositely signed flux can exist in either of the two magnetic hemispheres. This is illustrated in Fig. 3.13 where a number of negative patches (in blue), are isolated in the positive southern hemisphere (a strong example being below the tip of Africa and South America – again, this is the area associated with the SAA). Similarly there exist positive patches in the negative northern hemisphere. Collectively these patches are known as reversed-flux patches and like other processes at the core, they tend to evolve in time by varying in size, shape, intensity and position.

Similar maps of the magnetic field at the core surface can be constructed using historical obser-

DOI: 10.2312/GFZ.b103-08029

vations from the past 400 years using the gufm1 and also at lower resolution using archeomagnetic, lava and lake sediment data from the past 7000 years from CALS7K.2 model. These models show that many of the magnetic field features at the core-mantle boundary are not static. This field evolution is the signature at the core surface of the geomagnetic secular variation observed at Earth's surface (Fig. 3.14). At low latitudes and particularly in the Atlantic sector many field features are observed to move azimuthally westwards causing the westward drift of the magnetic field observed at the surface [121]. Poleward motion of reversed-flux features and their simultaneous intensification is also observed, and appears to be correlated with the decay of the axial dipole moment observed at Earth's surface [122, 120].

The full induction equation describes the secular variation that is generated in the core,

$$\frac{\partial \vec{B}}{\partial t} = \nabla \times (\vec{u} \times \vec{B}) + (\mu\sigma)^{-1}\Delta\vec{B}, \tag{3.7}$$

where $\vec{B}$ is the magnetic field, $\vec{u}$ is the fluid velocity at the CMB, σ is the conductivity and μ is the permeability. It can be decomposed into two parts: an advective and a diffusive term. By neglecting diffusion (assuming the core is a perfect conductor), the frozen-flux hypothesis is invoked, which assumes that the magnetic field is locked or frozen into the fluid at the CMB as it evolves on short timescales [123, 124]. By making this assumption, the radial component (B_r) of Eq. (3.7) can be written at the CMB:

$$\frac{\partial B_r}{\partial t} + \nabla_H \cdot (\vec{u} B_r) = 0, \tag{3.8}$$

where ∇_H is the horizontal gradient operator. Integrating Eq. (3.8) over a patch of the core bounded by a null-flux curve and noting that the null-flux curves are material curves, gives:

$$\frac{d}{dt}\left(\int_{S_i} B_r dS\right) = 0 \longrightarrow \int_{S_i} B_r dS = constant, \tag{3.9}$$

where S_i is the surface of a patch delimited by the null-flux curve $B_r = 0$ [125]. Of course at the CMB, there is at least one null-flux curve on S, the magnetic equator, separating the northern and southern magnetic hemispheres. Smaller null-flux curves, which outline the reversed-flux patches, exist within both hemispheres. Before examining how these reversed-flux patches have changed in time, it is acknowledged that the observations are not completely consistent with the frozen-flux assertion, because there are various sources of errors, including limited data accuracy, model truncation, mantle conductivity, diffusion, lithospheric filtering, etc. Despite these limitations, when employed on a large scale, much can still be learned.

DOI: 10.2312/GFZ.b103-08029

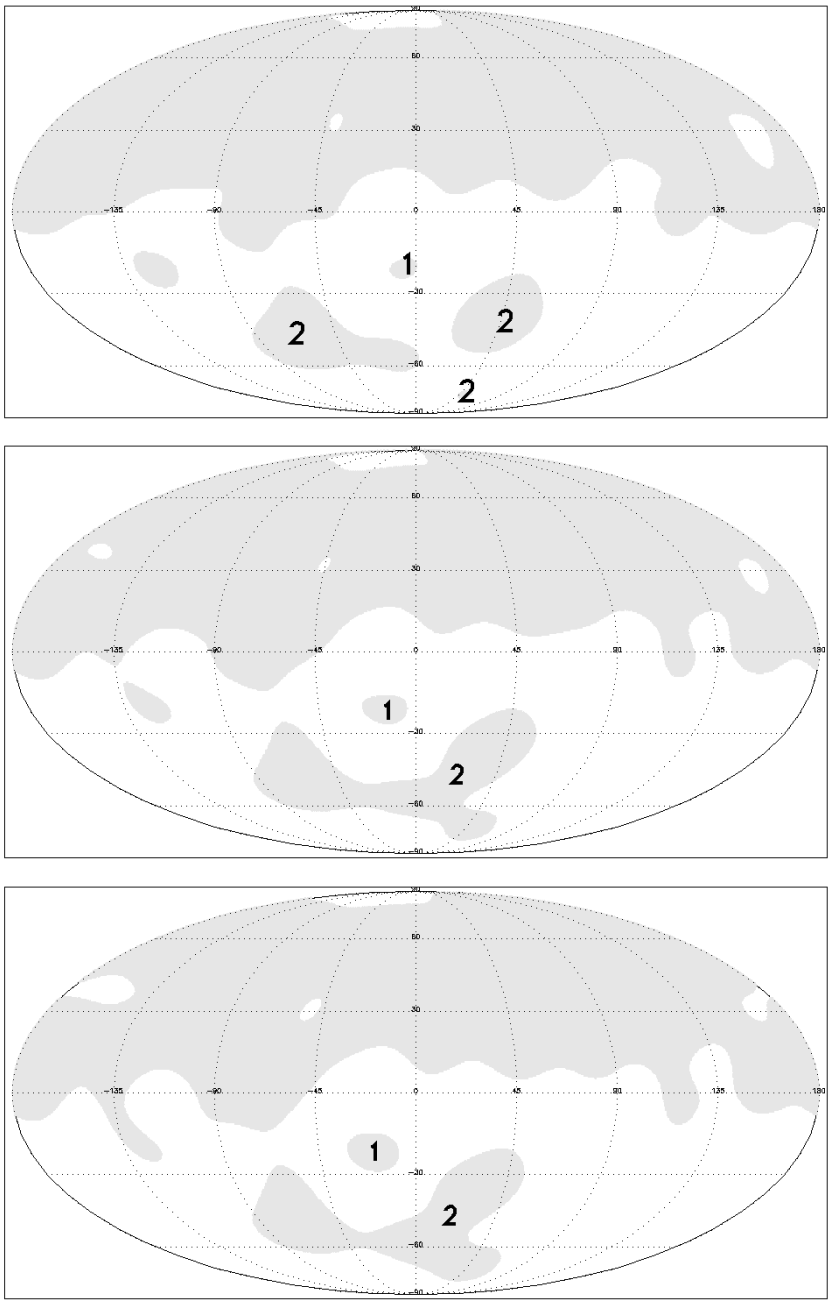

Figure 3.15: Maps of the radial flux calculated from the CM4 for years 1960, 1980, and 2000 with the locations of two reversed-flux patches labeled. Patch 1 is round and centered about 25° S Lat., 25° W Lon., while Patch 2 is more extended and focused about 50° S Lat., 16° E Lon. Note that over the course of time, Patch 2 coalesces from three distinct smaller patches, all of which are considered later as one patch.

DOI: 10.2312/GFZ.b103-08029

The radial flux for the epochs 1960, 1980 and 2000 was computed using the CM4 (Fig. 3.15). A number of negative revered-flux patches, labeled collectively as Patch 1 and Patch 2, are isolated in the positive southern magnetic hemisphere. Analogously there exist positive revered-flux patches in the negative northern magnetic hemisphere. This figure demonstrates that 20 years is a long enough timespan to change the flux patterns. Globally, the most evident change is the transition of the reversed-flux patch in the Pacific Ocean to the north, becoming part of the large northern hemispheric patch. Under the region of interest, Patches 1 and 2 have clear time-dependent evolution. Patch 1 is round and its area increased by nearly 52% over the 20 years between 1980–2000. Patch 2, having previously coalesced from three distinct smaller patches, is more extended and shows only a modest, almost 2%, increase in area. However, its morphology has changed significantly over this time and shows signs that it might split into two segments (near 60° S Lat., 35° W Lon.) [93].

The CHAOS model resolves secular variation coefficients beyond degree $n = 13$, which means that for the first time it is possible to infer the temporal changes of the core field to smaller scales than the field itself and to evaluate structures with short wavelengths at the core-mantle boundary never before observed (Fig. 3.14). This figure shows that the southern African continent is one of two regions of very active variations of the secular variation, where wave-like structures propagate [126]. The magnetic activity within these structures directly relates to the geomagnetic jerks previously reported at the Earth's surface [127].

A series of snapshots of the polarity of the radial field (as in Fig. 3.15), where each frame represents a year of significant change in the layout of the reversed-flux patches (either the creation/vanishing of a patch, or the spawning/merging of patches from other patches), is presented in Fig. 3.16. In total 20 reversed-flux patches have been identified in the radial flux calculated from the gufm1 over the time period from 1590–1990. It should be noted that in this accounting the merging/division of a reversed-flux patch creates all new patches and does not retain the previous patch's numerical label (e.g., Patch 11 splits into Patches 14 and 15). A positive reversed-flux patch (Patch 4) is first noted in 1730 where it develops in the negative normal polarity flux Patch N region and persists thereafter throughout the duration of the gufm1 model. It is interesting to observe that during the years from 1870–1880, reversed-flux Patch 10 recombines with the normal polarity flux Patch N for a short period before detaching again. These observed topological changes indicate that the frozen flux assumption has indeed been violated.

The total unsigned flux was calculated using the gufm1 only up to spherical harmonic degree

DOI: 10.2312/GFZ.b103-08029

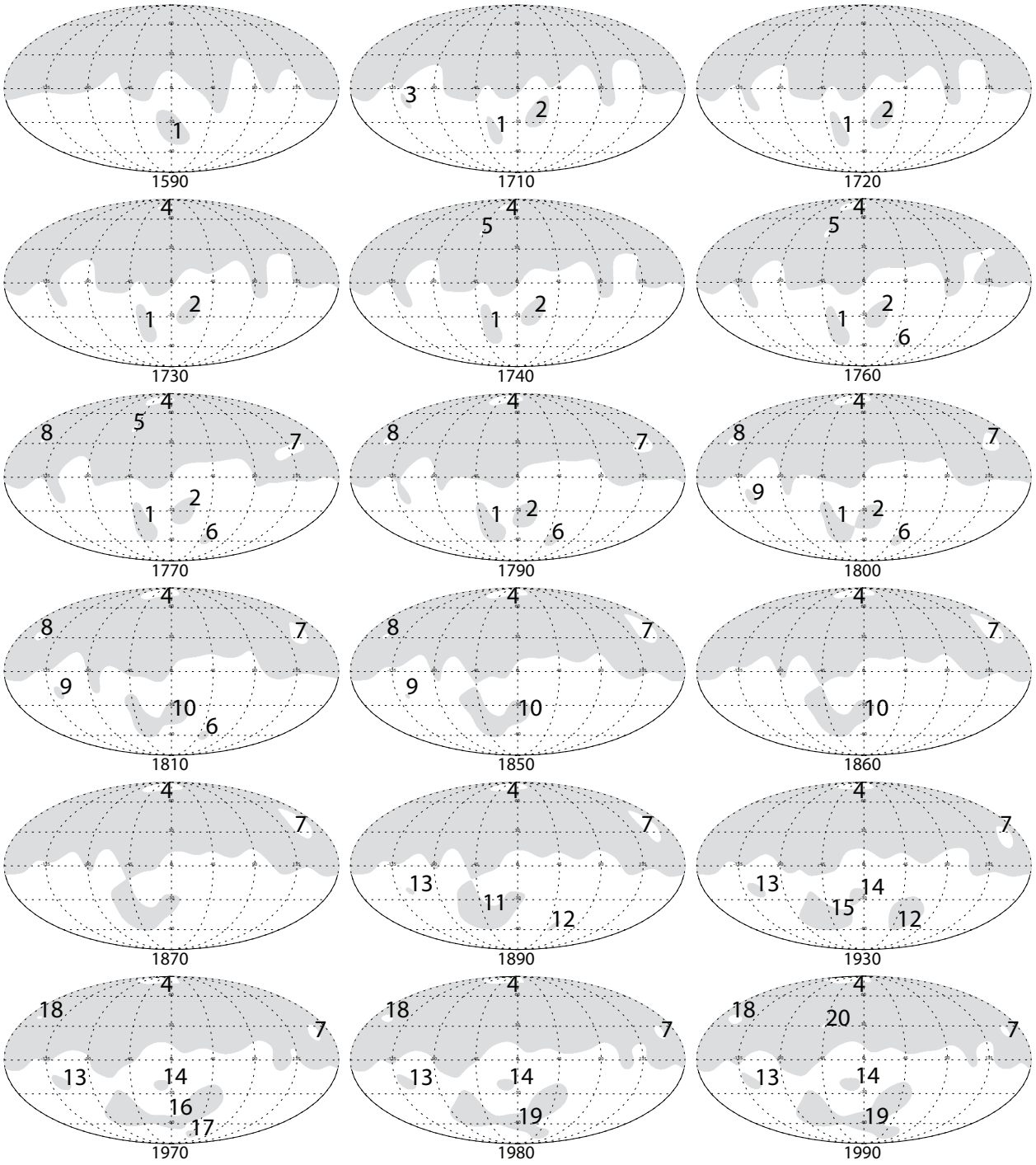

Figure 3.16: A series of plots of flux polarity calculated using the gufm1 for spherical harmonic degree 10. Each year listed coincides with a significant change in the layout of the reversed-flux patches (either an addition, subtraction, merging or division).

DOI: 10.2312/GFZ.b103-08029

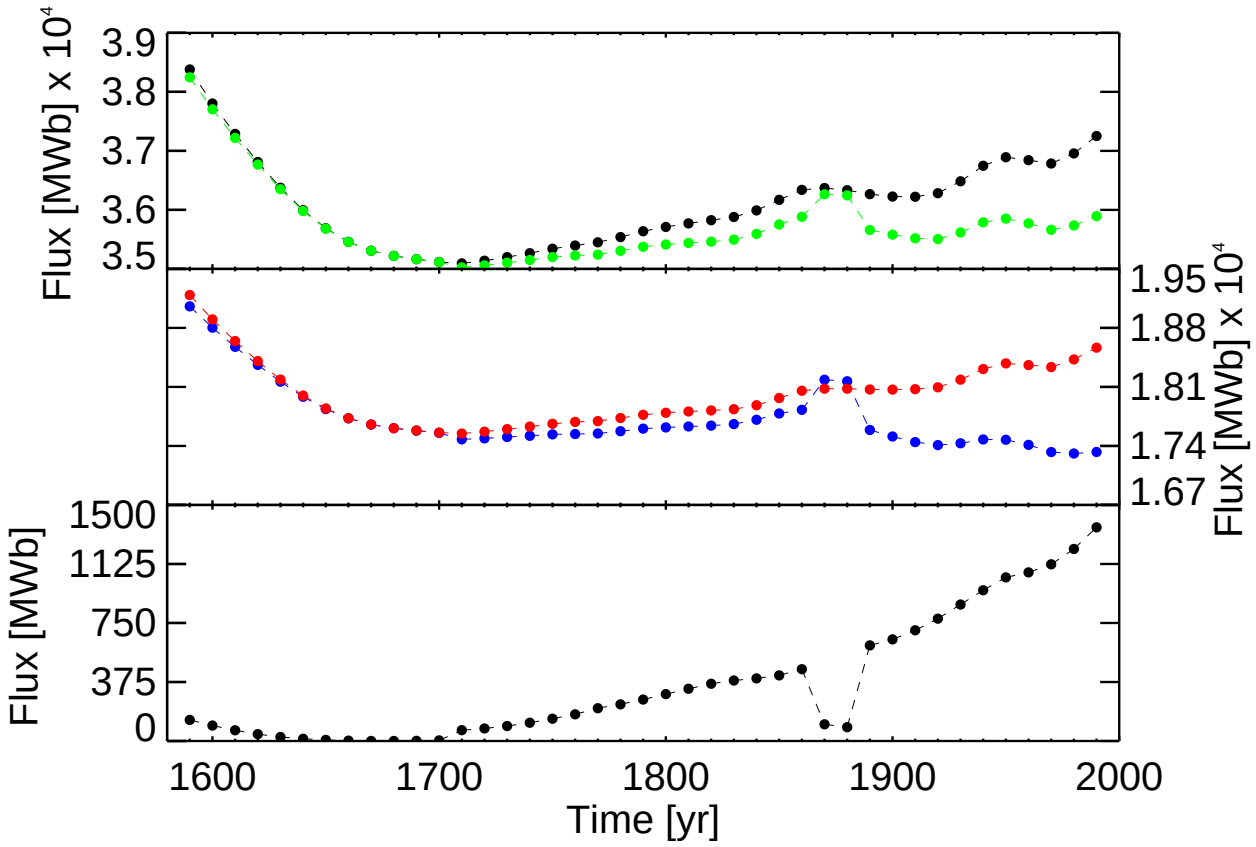

Figure 3.17: Total unsigned flux (black) computed from the gufm1 up to degree 10 from 1590–1990 in units of MWb. Plotted also are the two unsigned normal polarity flux patches: the northern negative Patch N (blue), the southern positive Patch P (red) and their sum (green). The two elevated values in the negative flux for the years 1870–1880 are a consequence of Patch 10 temporarily recombining with Patch N. The bottom plot displays the difference between the total unsigned flux and the normal polarity flux and indicates the contribution of the various small reversed-flux patches to the total unsigned flux.

n=10 at 10-year intervals. Its time-series is exhibited in Fig. 3.17 (top) and brings to light some interesting features. The quick intensity decline from 1590–1710 is probably not a robust feature, having more to do with the nature and quality of the early data associated with this time frame. However, starting in 1710, the total unsigned flux gradually trends upward over 2150 MWb from nearly 35100 MWb to just over 37250 MWb (i.e. 7.7 MWb/yr). The trend from 1710–1840 is linear, after which it oscillates. The date 1840 coincides in the gufm1 model with the elimination of an imposed -15 nT/yr dipole decay to rely instead upon intensity data [8].

The middle window of Fig. 3.17 plots the time series of the unsigned normal polarity flux

DOI: 10.2312/GFZ.b103-08029

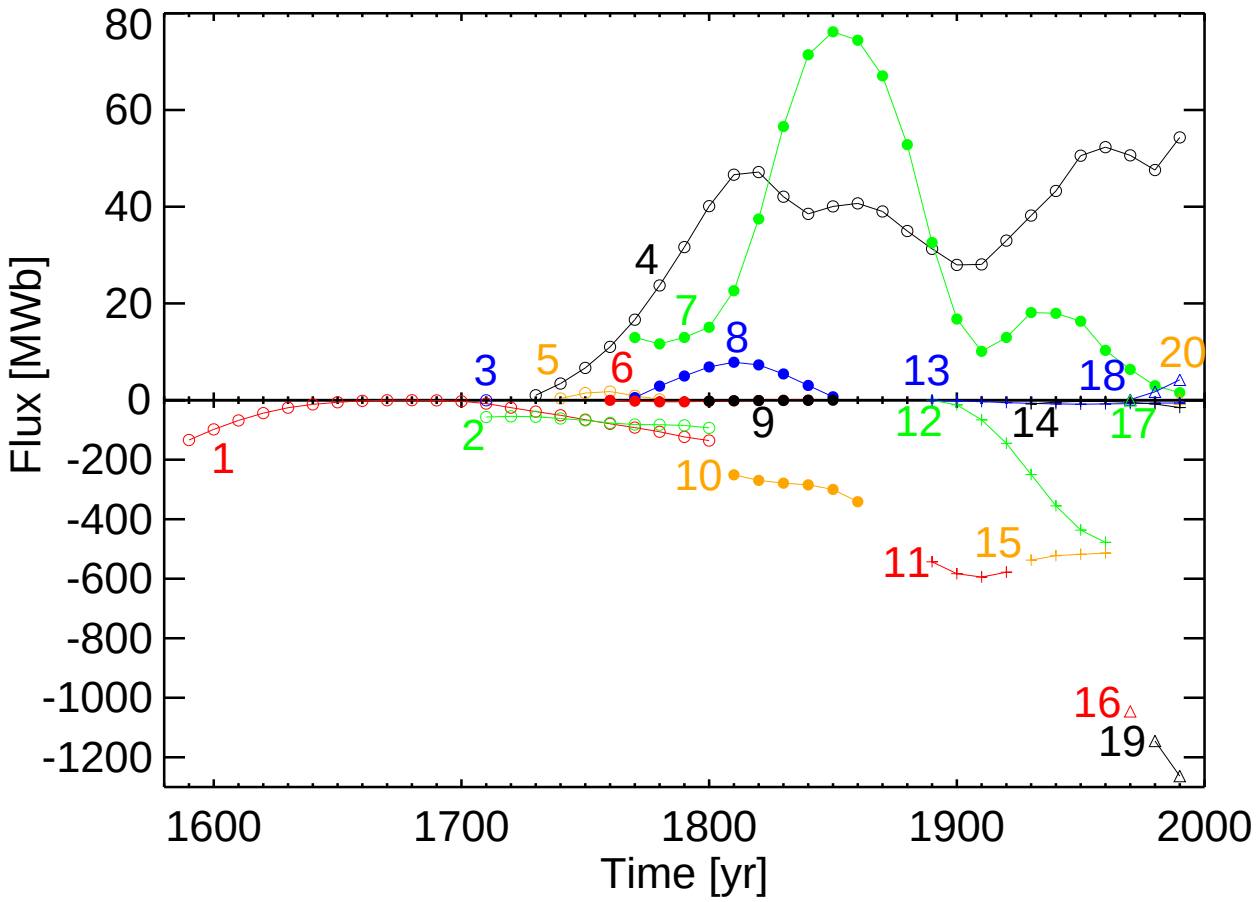

Figure 3.18: Evolution of magnetic flux associated with reversed-flux patches, computed using the gufm1 at degree n=10 from 1590–1990. The labeled patch numbers refer to those displayed in Fig. 3.16.

of Patches P and N. The evolution of Patch P is reminiscent of the total unsigned flux with a similar trend and oscillatory behavior after 1840. Conversely, Patch N, while also showing the oscillatory behavior (most clearly visible after 1890) actually is decreasing in value. Also of note is the apparent discontinuity in the curve between 1870–1880, which corresponds to the negative reversed-flux Patch 10 temporarily recombining with Patch N. Combining the flux of Patches N and P in Fig. 3.17 (top) demonstrates how the contribution of reversed-flux patches to the total unsigned flux has increased over time starting around 1710. The bottom frame of Fig. 3.17 makes this contribution more explicit, clearly showing an increase over time, which matches the decrease evident in Patch P.

The time evolution of the smaller individual positive and negative reversed-flux patches are

DOI: 10.2312/GFZ.b103-08029

Table 3.4: Linear fit parameters of trend segments in the total unsigned flux shown in Fig. 3.19.

Segment	Slope [sigma]	Y-intercept [sigma]
1960–1971	-6.99 [0.69]	50737.64 [1362.57]
1971–1984	12.41 [0.40]	12509.46 [785.09]
1984–1991	5.11 [0.27]	26984.03 [544.85]
1991–2000	13.63 [0.38]	10027.46 [754.2]
2000–2005	23.00 [0.48]	-8734.37 [967.87]

exhibited in Fig. 3.18. Among the positive reversed-flux patches, Patch 7, first appearing in 1770, undergoes the largest change, rapidly reaching a value of 76 MWb in 1850 from its initial 13 MWb. Then just as quickly, it declines to its near original value, after which it has a minor short lived increase on its eventually decay toward zero. Patch 4, appearing in 1730, after attaining a local maximum in 1820 oscillates, but generally has an upward trend. Patches 5 and 8 are shorter lived, rising to modest values before decaying away completely.

The negative reversed-flux patches are dominated by the large patch below the southern tip of Africa and South America. This patch changes a great deal over the 400-year span of the model going through a series of splits and mergers. Starting in 1590 as Patch 1 it combines with Patch 2 in 1810 to form Patch 10. In 1870 this patch temporarily recombines with Patch N, after which it disengages as Patch 11. After this time, Patch 12 emerges and enlarges over time, while Patch 11 splits into Patches 14 and 15. In 1970 Patches 12 and 15 coalesce to form Patch 19. If one considers this long string of associated events as basically one patch then Fig. 3.18 shows how it increases in intensity over the time range of the model. In 1590, starting around -150 MWb, it initially decreases, but by 1700 it quickly starts to intensify and by 1990 the flux value is in excess of -1200 MWb. It is this series that represents the majority of the increase in the proportion of flux in the reversed-flux patches relative to the total unsigned flux as outlined in Fig. 3.17 (bottom).

3.7 Association of Total Unsigned Flux with Geomagnetic Jerks

The total unsigned flux values for 1960–2005 computed using CM4 (1960–2000) and CHAOS (2000–2005), along with single point values from OSVM (2000) [33] and M102389 (1980), are plotted in Fig. 3.19. A cursory visual assessment of the figure illustrates an interesting property, whereby the time-series of the total unsigned flux seems to be constructed from approximately linear segments.

DOI: 10.2312/GFZ.b103-08029

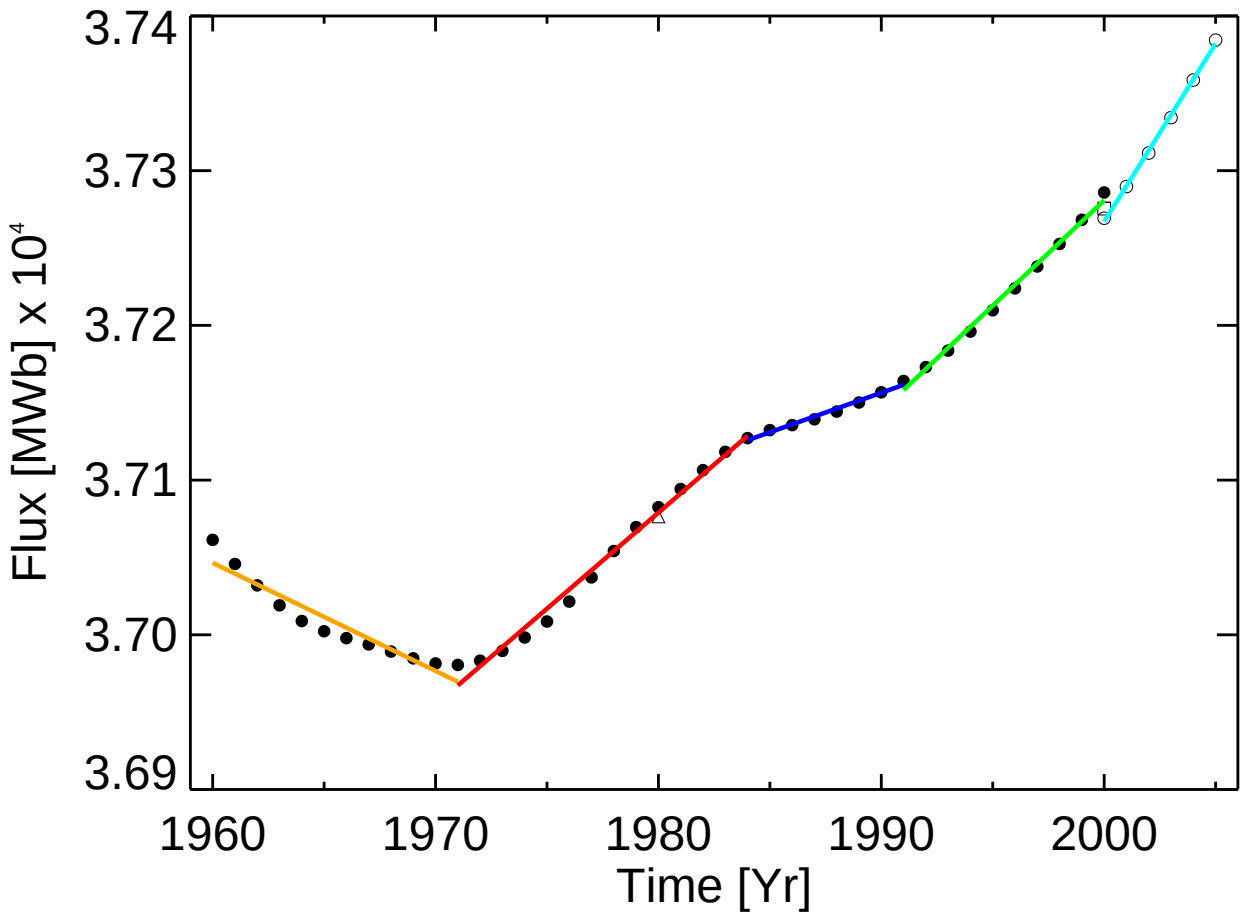

Figure 3.19: The total unsigned magnetic flux computed from various geomagnetic models over the time period 1960–2005, including CM4 (filled circle), CHAOS (open circle), OSVM (square) and M102389 (triangle). Linear trend segments have been fit with the resulting parameters listed in Tab. 3.4.

Therefore, a linear least squares fit was applied to those segments and the resulting parameters are listed in Tab. 3.4. Despite only a small absolute change in the unsigned flux, the crucial aspect is that the intersections of the segments seem to approximately correspond to known dates of geomagnetic jerks, providing observational evidence for a correlation between these two aspects of the field, which are both linked to core dynamics.

Another signature of core processes is the changing of the core field on temporal scales, which is known as secular variation. While it is generally the case that the secular variation evolves slowly, "geomagnetic jerks" on the other hand (refer back to Figs. 1.10–1.11) are characterized by sudden changes in the trend of the secular variation over periods as short as just a few months to a couple

DOI: 10.2312/GFZ.b103-08029

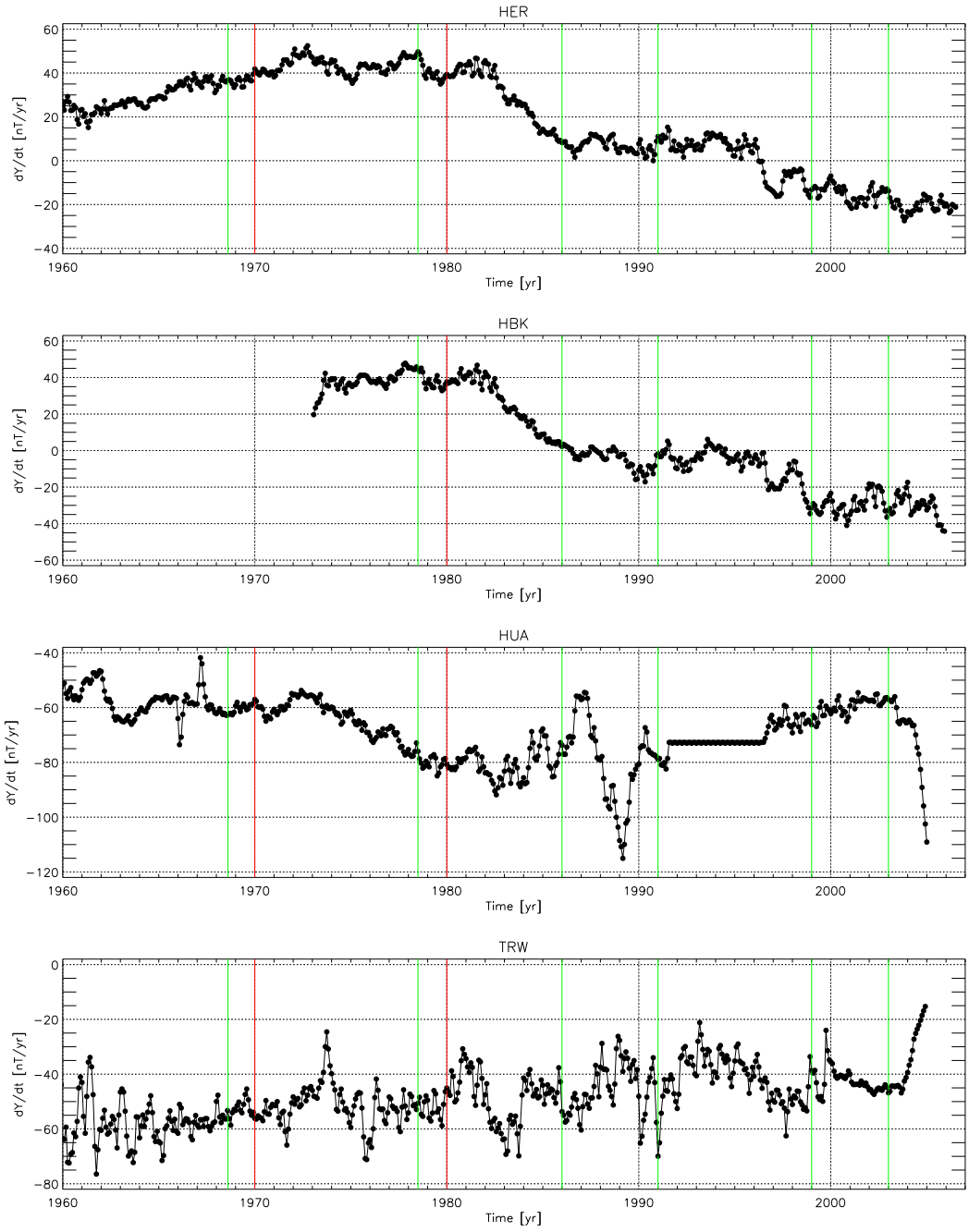

Figure 3.20: The east component (B_y) of the secular variation [nT/yr] measured at the Hartebeesthoek (South Africa), Hermanus (South Africa), Huancayo (Peru) and Trelew (Argentina) magnetic observatories (a selection from the SAA region, see Tab. 3.1) which points out some of recognized geomagnetic jerks (green – CLF monthly means, and red – big five) although most were discovered at other locations so they do not match up well here.

DOI: 10.2312/GFZ.b103-08029

of years. This poorly understood geophysical phenomenon was first recognized from an event in 1969/1970 [128]. It has since been shown rather conclusively that the processes, which result in this phenomenon, are of internal origin [129, 130, 131], possibly having to do with changes in core flow or torsional oscillations [45]. There are now a number of recognized jerks, which have been isolated and documented from different datasets in the magnetic observatory record [25], having varying degrees of spacial extent. There are a least seven jerks considered as possibly having a global extent (1901, 1913, 1925, 1969, 1978, 1991, 1999), and some others suggested to be only of regional extent (1932, 1949, 1958, 1986) [132, 133]. They are usually most clearly seen in the time-derivative of either the east component of the magnetic field (dB_Y/dt, since this component is least disturbed by magnetospheric effects) or the declination, although other components are possible as well, like dB_Z/dt [28]. Some are noted in the B_Y component of the secular variation measured at some of the Tab. 3.1 magnetic observatories in Fig. 3.20. It is also worth noting that the occurrence time for a geomagnetic jerk does not imply a simultaneous event across all observatories [134, 135], but instead the occurrence time is spread over a range of time, which maybe as high as ± 2 years, so different sources may cite slightly different dates for what in all intents and purposes is the same jerk. Recent work [135] demonstrates a procedure of creating virtual observatories from CHAMP satellite data, which has the benefit of constructing virtual observatories in areas not currently covered by existing magnetic observatories and shows the regional occurrence of geomagnetic jerks.

Jerks are important because they potentially have the ability to remotely provide information about the workings of core flow. For that reason it is natural to examine them for correlations with the total unsigned flux at the CMB. Although rather speculative, some researchers [136, 133] even suggest they may play a critical role in anticipating sharp accelerations of global temperature, thus providing information on the future climatic trend.

Fig. 3.21 expands upon Fig. 3.19 by using the gufm1 to plot the first and second time-derivative (via differences) of the total unsigned flux time-series back to 1590 and comparing it with the sign-changed declination component of secular variation from the French magnetic observatory Chambon la Forêt. The figure denotes the geomagnetic jerks observed at Chambon la Forêt from monthly means of the time-derivative of declination (green: 1871, 1901, 1913.6, 1924.6, 1968.6, 1978.5, 1991, and 1999) as well as those isolated in annual means from the Paris declination series (blue: 1700, 1720, 1750, 1766, 1780, 1797, 1813 and 1845). However, the clearest and most widely recognized jerks (red) occurred around 1840, 1870, 1900, 1970 and 1980 ($\pm 2\,\mathrm{yr}$).

The association between geomagnetic jerks and the rate of change of the total unsigned flux

DOI: 10.2312/GFZ.b103-08029

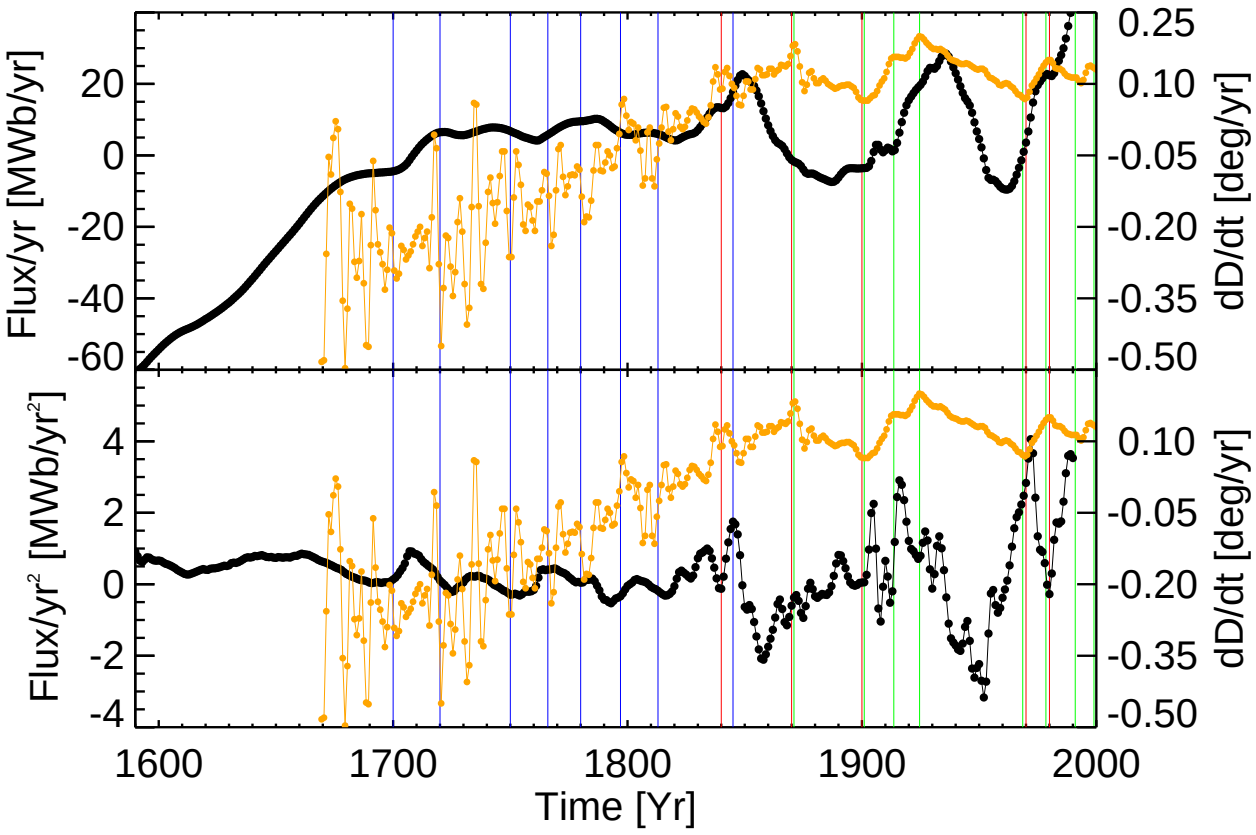

Figure 3.21: The first time-derivative of the total unsigned flux [MWb/yr] (top) and its second time-derivative (bottom) calculated using the gufm1 and compared with the sign-changed declination component of secular variation from the magnetic observatory Chambon la Forêt. Years of known jerks are indicated by vertical lines – CLF Monthly Means (green), Annual Declination (blue) and the most widely recognized (red).

first depicted in Fig. 3.19 is further reinforced by examining the total unsigned flux from the *gufm1* in Fig. 3.17, where oscillation maxima occur in 1870 and 1950 and minima occur in 1910 and 1970. The years 1870, 1910, 1950, 1970 are coincidently near known years of jerks in the magnetic observatory data series of Chambon la Forêt. The year 1870 also corresponds to an extremum in the longitudinal velocity of the South Atlantic Anomaly measured at the Earth's surface.

Furthermore in Fig. 3.21, there are some interesting similarities between the total unsigned flux and secular variation time-series at dates of some of the geomagnetic jerks. For instance, in 1840 there are anti-correlated extrema evident in both the second time-derivative of the total unsigned flux and in the dD/dt series. Around 1980 there are coincident in-phase local extrema. There are also coincident extrema in 1870 and 1970, however, the second time-derivative seems to reach its

DOI: 10.2312/GFZ.b103-08029

extrema two years after that of the dD/dt series. It seems again in 1924 that there are coincident local extrema. Moreover, there are coincident extrema that occur at times when there are no known associated jerks; these dates, both exhibiting in-phase local extrema include 1823 and 1834. Conversely, 1891 and 1952 show clear extrema in the second time-derivative of the total unsigned flux, however the corresponding signal is absent from the dD/dt data.

Because both total unsigned flux generation and geomagnetic jerks are thought ultimately to be manifestations of core flow processes, it should not be surprising to find a general concordance. The geomagnetic jerks are most likely a result of changes in the magnetic field at the top of the core, due to advection. Generally, the diffusion is considered not to be an important factor, because of its larger timescales when compared to advection processes. The clear correlation found here between the changes in the trend of the total unsigned flux and secular variation suggests that diffusion may play a role in the origin of geomagnetic jerks.

The original reason for computing and imaging the radial flux and its patterns on the CMB was to see how it relates to the SAA. This comparison is visible in Figs. 3.22–3.23, which show side by side the radial flux polarity at the CMB and the location of the SAA (red star) for every 50 years starting in 1600. Fig. 3.24 focuses in on two dates, 1790 and 1870, which correspond to extrema in the longitudinal velocity of the SAA measured at the surface as seen in Fig. 3.5.

DOI: 10.2312/GFZ.b103-08029

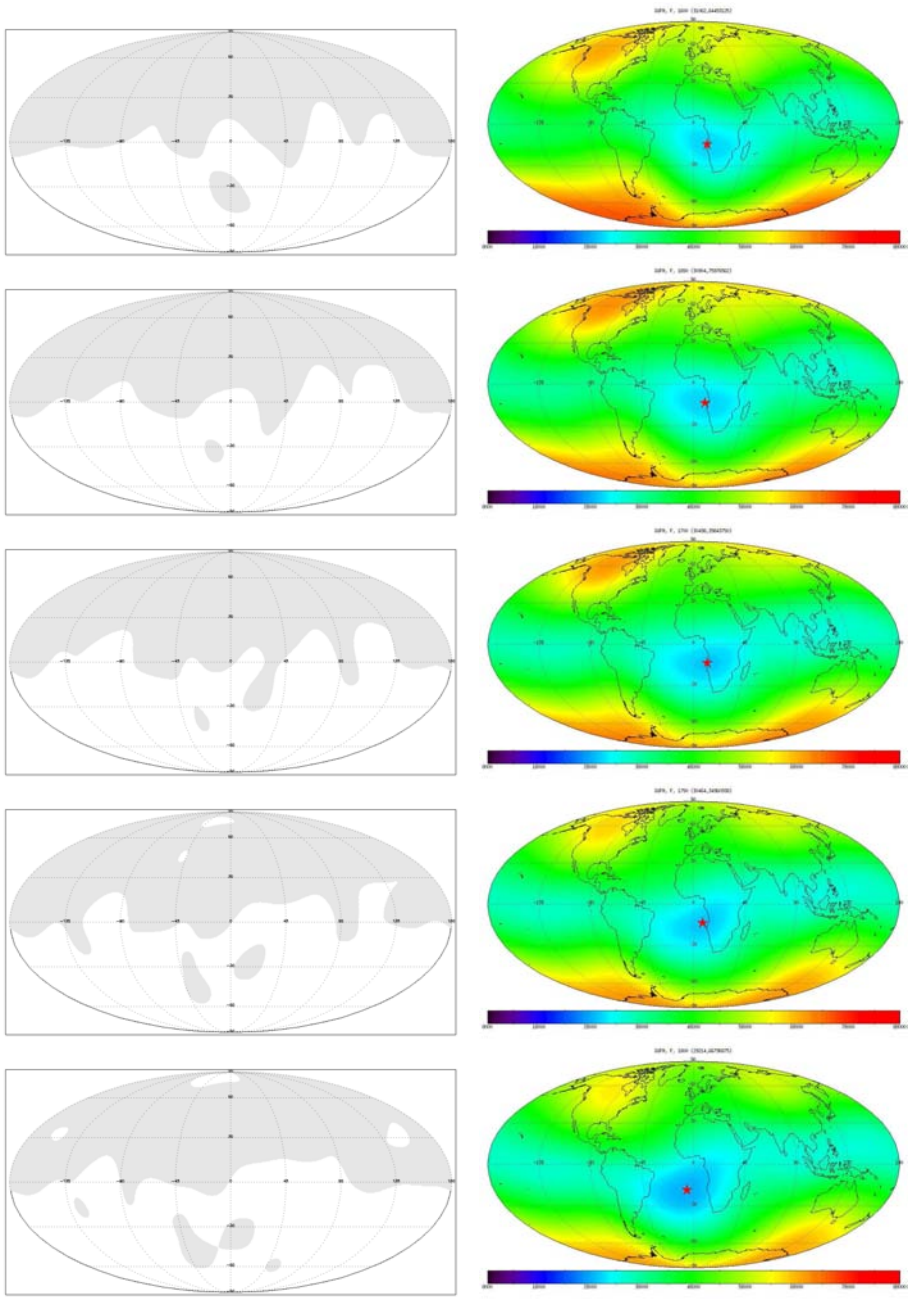

Figure 3.22: Maps of the radial flux polarity at the CMB (left) and surface total field (red star is the location of the SAA) for 1600, 1650, 1700, 1750, and 1800 (top-bottom).

DOI: 10.2312/GFZ.b103-08029

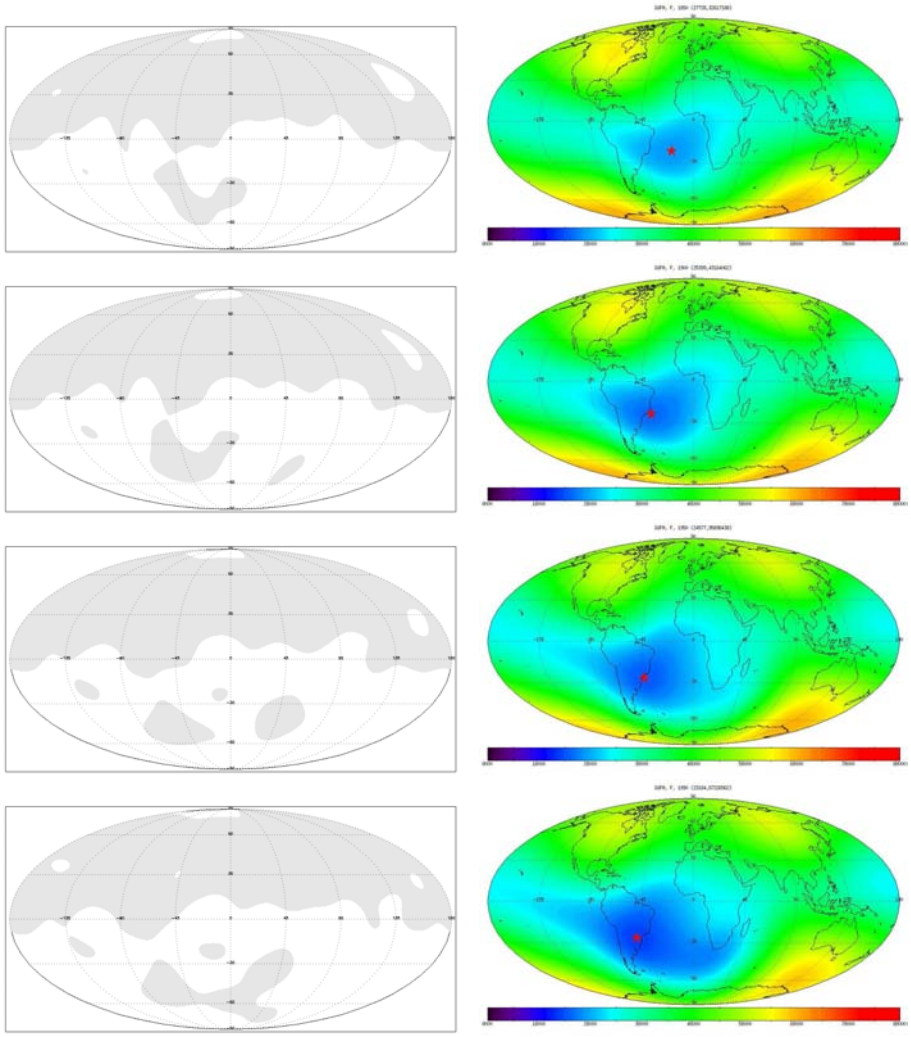

Figure 3.23: Maps of the radial flux polarity at the CMB (left) and surface total field (red star is the location of the SAA) for 1850, 1900, 1950, and 1990 (top-bottom).

DOI: 10.2312/GFZ.b103-08029

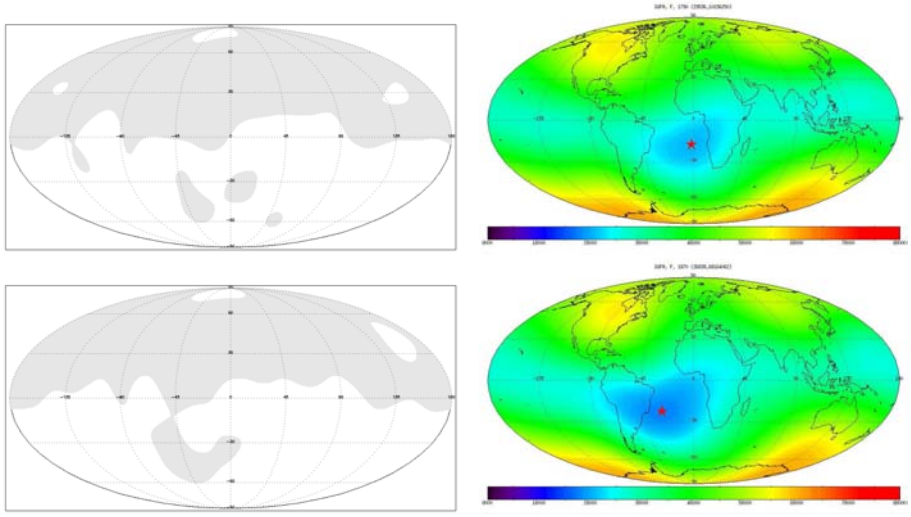

Figure 3.24: Maps of the radial flux polarity at the CMB (left) and surface total field (red star is the location of the SAA) for 1790 and 1870 (top-bottom) which are the approximate dates for maximum velocity of the SAA in the gufm1.

DOI: 10.2312/GFZ.b103-08029

CHAPTER 4

Conclusions & Perspectives ...

4.1 ... for the External Field Perturbations

This study has demonstrated several things about the geomagnetic field. On the external field side, it was shown how the TIE–GCM, a physics based model, is partially able to reproduce perturbations left over in the CHAMP/CHAOS satellite dayside residuals (most clearly evident with Sq and EEJ signatures). The level of agreement was investigated by variation of the model's input parameters corresponding to geomagnetic activity, namely $F_{10.7}$ and K_p. While it was not possible to say conclusively that low activity runs or high activity runs always produce the greatest agreements, some information was gleaned.

Probably the most important result is that these TIE–GCM perturbations are sufficiently good, so that when used to correct dayside CHAMP data, they can yield derived spherical harmonic models with better data residuals (small improvements, but quantifiably noticeable). Part of the goal of such studies is to help sort out the sources of the magnetic field components that come from the crust, core, ionosphere, magnetosphere, induced, etc., by examining the observational data. This is important because while most modeling uses primarily nighttime data, it is conceivable that there are internal currents on the nightside that are induced from the dayside, which can enter such models and be misidentified as internal to the shell of spacecraft measurement. As geomagnetic modeling progresses, this question will become ever more important and will need to be addressed. While it is unresolvable from this approach at the current stage, this application remains a significant goal.

Going forward with the TIE–GCM perturbation study, there are other possible avenues in which to expand the research, including better pinning-down under what conditions the model best predicts the real-world data. To proceed in this direction it is important to expand the tested parameter space to include inputs other than just $F_{10.7}$, K_p and temporal range. These would

DOI: 10.2312/GFZ.b103-08029

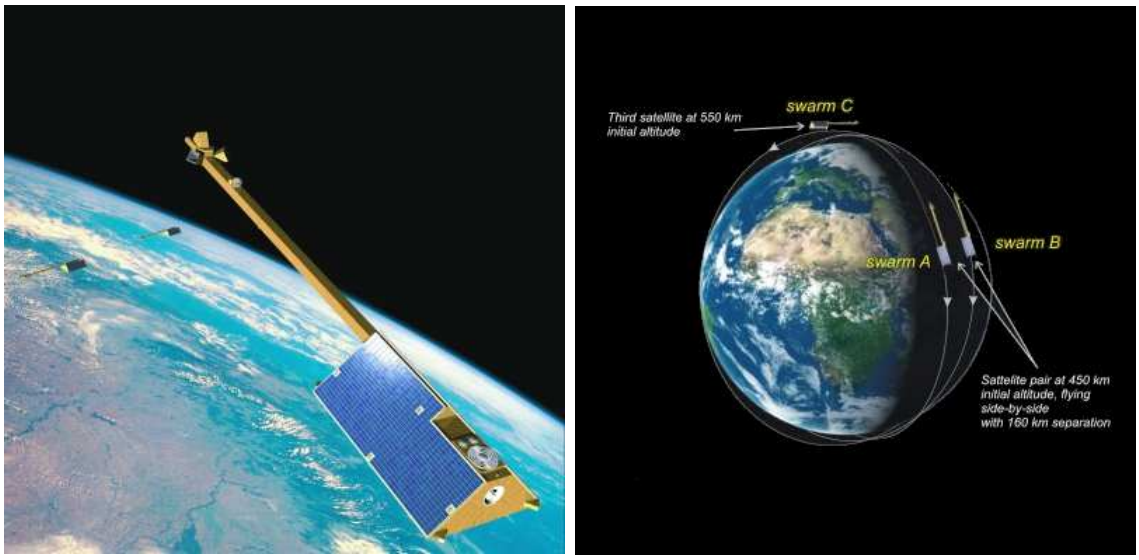

(a) SWARM satellite (b) SWARM constellation

Figure 4.1: An image of one of the SWARM mission satellites (a) and the combined orbit of all three satellites (b), from [138].

include varying TIE–GCM inputs like the atmospheric tides and the electric potential model. Also, broadening the selection criteria to include alternative methods of data selection like those based perhaps on the wavelet power spectrum [137], or conversely it may prove informative to purposely include days with more elevated geomagnetic activity. A more robust way of evaluating the quality of fit also needs to be developed as the current method of using the MDEV and Mean statistics are insufficient and can occasionally be slightly misleading for individual tracks. These new directions should and will be investigated in future work. This may be very important for internal field modeling studies, mainly at high latitudes, where the dayside is so long, causing gaps in datasets.

4.2 . . . for the Internal Field Variations

On the internal field side, it was shown how the SAA could be tracked at the surface over the last 400 years. Also what appears to be a correlation between sunspot number and the strength of the minimum of the SAA was introduced, but this probably points toward a modulation of the surrounding atmospheric region more so than an actual cause. It was further pointed out that at the CMB the rate of change in the axial dipole moment has activity in the same general area. The radial magnetic flux at the CMB was investigated as well, and shows the presence of reversed-flux patches

DOI: 10.2312/GFZ.b103-08029

in the region. The time evolution of these reversed-flux patches were documented. Stemming from that study was the realization that many of the changes noted in the total unsigned flux time-series also correspond to known geomagnetic jerks.

The internal magnetic field studies also have plenty of space to grow. Much of its progress here will proceed in lock-step with the development of ever more precise geomagnetic models, especially those able to determine the nature of core flow. Recently high resolution models based on satellite data have isolated jerks from this satellite data. In this way, the forthcoming SWARM mission [139] will be an unprecedented boon to geomagnetic modeling, because of its three satellites working in conjunction (Fig. 4.1). When they are coupled with the current complement of satellites, it will be possible to undertake a thorough investigation of a complete solar cycle. Moreover, the further augmenting of the current balance of magnetic observatories, with the introduction of sites like the recently installed one in Keetmanshoop, Namibia ($26^\circ 32' 26.1'' \,\mathrm{S}$, $18^\circ 06' 37.3'' \,\mathrm{E}$) [140] and another forthcoming on the South Atlantic island St. Helena (located approximately at $15^\circ 57' \,\mathrm{S}$, $5^\circ 42' \,\mathrm{W}$), is equally important for the continued study of the SAA region.

DOI: 10.2312/GFZ.b103-08029

APPENDIX A

Technical Aspects of Executing the TIE–GCM

A.1 The Eclipse Machine

Because the TIE–GCM is rather computationally intensive, I normally use the School of Computational Science [141] Eclipse machine (csit2.fsu.edu). It is an IBM eServer pSeries 690 computer. Eclipse is made up of 512 processors or CPU's, which are IBM Power4 chips with a clock speed of 1.1 GHz. The processors are arranged into 16 nodes. Each node is a tightly bound set of 32 processors. Fifteen of these nodes are set up so that their processors have access to 32 GB of memory; the remaining node has 24 GB. Each node also has 72 GB of local disk storage.

One node is interactive, and handles all terminal sessions, and immediate execution of small programs. The other nodes are accessible only to batch execution. To run a program on these nodes, a user must prepare a batch file that specifies the processors and time needed. Execution on multiple processors on a single node may be done using OpenMP or MPI. Execution on multiple nodes may be done using MPI.

While any arrangement of processors can be used in parallel, one common arrangement is to have an OpenMP program running on a node, with the 32 processors sharing the entire memory. Another arrangement uses MPI, in which case processors on different nodes can cooperate, but even if the processors share the same node, they divide up the node's memory rather than sharing it. A more elaborate hybrid programming scheme allows MPI to set up several processes, assigning a single process to each node. On each node, OpenMP divides up the task among all the processors.

External storage for Eclipse includes:

- a storage area network (SAN) of 13 TB of disk storage, comprising four IBM FAST 500 Fibre Channel disk arrays
- one 3584 IBM Tape Library with eight Fibre Channel-attached LTO Ultrium tape drives with 200 TB of tape-storage capacity

DOI: 10.2312/GFZ.b103-08029

- a McData ED-6064 Enterprise Fibre Channel Directory
- two McData ES-1000 Fibre Channel switches
- the Tivoli Storage Manager and Tivoli Space Manager software for backup and archiving

The control workstation is a pSeries 620 Model 7025-6F1.

A.2 Procedure for Executing the TIE–GCM

The TIE–GCM is written in Fortran90. The TIE–GCM is coded to take advantage of MPI. In order to spend the least amount of time as possible in the LoadLeveler queue I generally write the LoadLeveler script to use only 4 CPUs and submit it to the interactive parallel queue. Because the runs required for variation of the $F_{10.7}$ and K_p over a day are relatively short it will finish just before the queue time limit of 2 hours is reached. The combination of the interactive queue and requesting only 4 CPUs means the jobs usually start computing right away.

Here is a sample of the LoadLeveler job script and a brief explanation of some of the terms:

```
#
# @ job_name         = mozzoni
# @ class            = interactive
# @ error            = mozzoni.error.log
# @ output           = mozzoni.output.log
#
# @ job_type         = parallel
# @ node             = 1
# @ total_tasks      = 4
# @ node_usage       = shared
# @ network.MPI      = css0,shared,US
#
# @ queue
#
tiegcm < mozzoni.inp  > mozzoni.output
```

- job_name – A name given to the job.
- class – a queue and limits requirement classification (small, medium, large or interactive). Interactive has the smallest CPU requirement and shortest CPU-time requirement.
- error – an output file for error messages.
- output – an output file for normal file output .
- job_type – request either parallel (multiple CPUs) or serial (single CPU) computation.

DOI: 10.2312/GFZ.b103-08029

- node – number of nodes requested. Each node contains 32 CPUs.
- total_tasks – number of tasks (generally refers to the number of CPUs) requested.
- node_usage – allow unused CPUs to be used by other jobs (shared or not_shared).
- network.MPI – specification of MPI off node communication.

The actual run-time parameters are passed to the program via an input file. This is where the output files and input data files are specified, as well as the desired time interval, output species, and activity inputs. Some of the more important items in the input file include:

- SOURCE – A file of initial conditions (usually just a prior run).
- OUTPUT – File names for primary history output files.
- SECOUT – File names for secondary history output files.
- GPI_NCFILE – A file of geomagnetic indices ($F_{10.7}$, K_p). When present the model will look up the values for each timestep. Alternatively one may instead specify values which are held fixed for the entire model run (F107, F107A, POWER, CTPOTEN).
- START – The start date of the model run (DOY, HOUR, MINUTE). I usually begin the modeling run two days before the desired date so as to allow the solution to reach equilibrium. This buffer probably does not need to be quite so large.
- STOP – The end date of the model run (DOY, HOUR, MINUTE).
- START_YEAR – The year of the START date.
- START_DAY – The DOY of the START date.
- SAVE – The intervals at which the calculated results should be written to the output history files.
- STEP – The time step of the model calculation in seconds.
- POTENTIAL_MODEL – Specification of the electric potential model (HEELIS, WEIMAR, or NONE).

Here is a sample input file:

DOI: 10.2312/GFZ.b103-08029

```
&tgcm_input
 LABEL = 'mozzoni'
 TEMPDIR = '.'
 START_YEAR = 2005
 START_DAY  = 34
 CALENDAR_ADVANCE = 1
 MAGVOL = 'TGCM.data.magfield.nc'
 SOURCE = 'MOZZONI.tiegcm1.cyric_init.nc'
 SOURCE_START = 43,0,0
 START = 34,0,0
 STOP = 37,0,0
 HIST =  0,2,0
 SAVE =  1,0,0
 STEP = 120
 OUTPUT = 'MOZZONI.tiegcm1.cyric1.gpi.nc',
          'MOZZONI.tiegcm1.cyric2.gpi.nc'
 MXHIST_PRIM = 48
 SECSTART = 34,0,0
 SECSTOP  = 37,0,0
 SECHIST  = 0,1,0
 SECSAVE  = 0,1,0
 SECOUT = 'MOZZONI.tiegcm1.scyric1.gpi.nc',
          'MOZZONI.tiegcm1.scyric2.gpi.nc',
          'MOZZONI.tiegcm1.scyric3.gpi.nc',
          'MOZZONI.tiegcm1.scyric4.gpi.nc'
 MXHIST_SECH = 24
 SECFLDS = 'TN','UN','VN','W','O1','O2','NO','NE','TE',
           'O2P','POTEN'
 SECFMAG = 'ED1M3D','ED2M3D'
 SECFGEO2D = 'PHIH2D'
 SECFMAG2D = 'PHIM2D','KQPHI','KQLAM','JQR'
 DISPOSE = 0
 MAG = -74.5,127.,79.,-70.
 DIFHOR = 1
 DYNAMO = 2
 TIDE = 0.,0.,0.,0.,0.,0.,0.,0.,0.,0.
 TIDE2 = 0.,0.
 GSWM_DI_NCFILE     = 'TGCM.data.gswm.gswm_diurn_5.0d_99km.nc'
 GSWM_SDI_NCFILE    = 'TGCM.data.gswm.gswm_semi_5.0d_99km.nc'
 GSWM_NMIDI_NCFILE  = 'TGCM.data.gswm.gswm_nonmig_diurn_5.0d_99km.nc'
 GSWM_NMISDI_NCFILE = 'TGCM.data.gswm.gswm_nonmig_semi_5.0d_99km.nc'
 TIDEANN = 0
 AURORA = 1
 COLFAC = 1.5
 GPI_NCFILE = 'gpi.nc'
 BYIMF = 0.
 BZIMF = 0.
 POTENTIAL_MODEL = 'HEELIS'
/
```

A.3 Comparison of the v1.6 and v1.8 TIE–GCM

The two versions are similar in character, although there are some minor differences, especially in the extremities, as the ranges for v1.8 are usually larger than the usual v1.6 results. Also the

DOI: 10.2312/GFZ.b103-08029

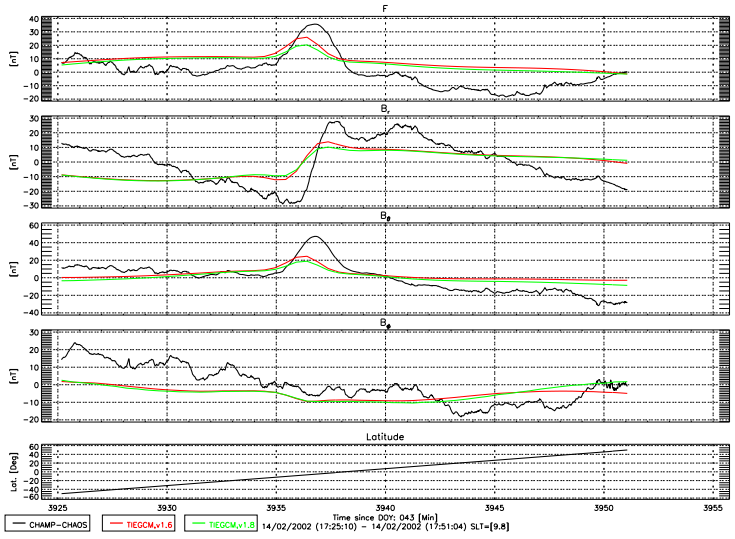

Figure A.1: A comparison of the v1.6 and v1.8 TIE–GCM for a dayside orbit pass on February 14, 2002, using a constant $F_{10.7} = 190$ and constant $K_p = 0$. Black is the CHAMP/CHAOS residual, Red is the TIE–GCM v1.6 result while Green is the v1.8 model result.

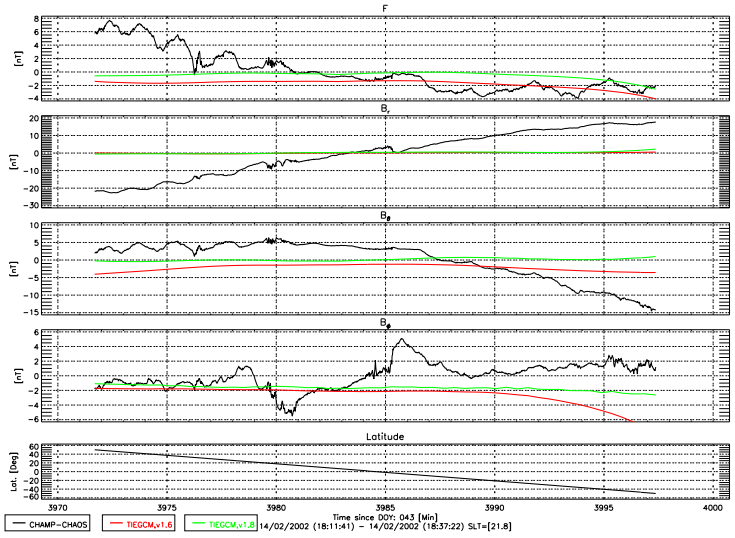

Figure A.2: A comparison of the v1.6 and v1.8 TIE–GCM for a nightside orbit pass on February 14, 2002, using a constant $F_{10.7} = 190$ and a constant $K_p = 0$. Black is the CHAMP/CHAOS residual, Red is the TIE–GCM v1.6 result while Green is the v1.8 model result.

DOI: 10.2312/GFZ.b103-08029

maximum value of the EEJ signature is generally lower. Fig A.1 shows the overall agreement of the two versions of the model for a dayside orbit pass while Fig A.2 shows the analogous result for the nightside orbit pass. The Black curve is the CHAMP/CHAOS residual while the Red curve is the TIE–GCM v1.6 model and the Green curve is TIE–GCM v1.8. These particular plots represent an average comparison, but there are instances where the models do not agree so well. In those cases the v1.6 model usually has a better fit, and under the rarer cases where the v1.8 is better, the margin is usually closer. Despite the similarities, I plan to continue to use v1.6 of the TIE–GCM because the fits do seem to be better and don't warrant recomputing all the previous runs for little to no gain at this point.

A.4 Altitude Variation in the Perturbation Calculation

The magnetic perturbations calculated in Chap. 2 use an altitude of 430 km across all dates. This was done for computational and consistency reasons. While this value is a good approximation for the years 2001–2003, it gradually becomes less precise and by 2005 the difference reaches over 80 km. However, as Fig. A.3 (a worst case scenario) demonstrates, this does not pose a significant problem, because most of the large differences are in the polar regions. Data poleward of $\pm 50^\circ$ magnetic latitude is already excluded from the study in general and the differences in the equatorial region does not represent a large percent difference.

DOI: 10.2312/GFZ.b103-08029

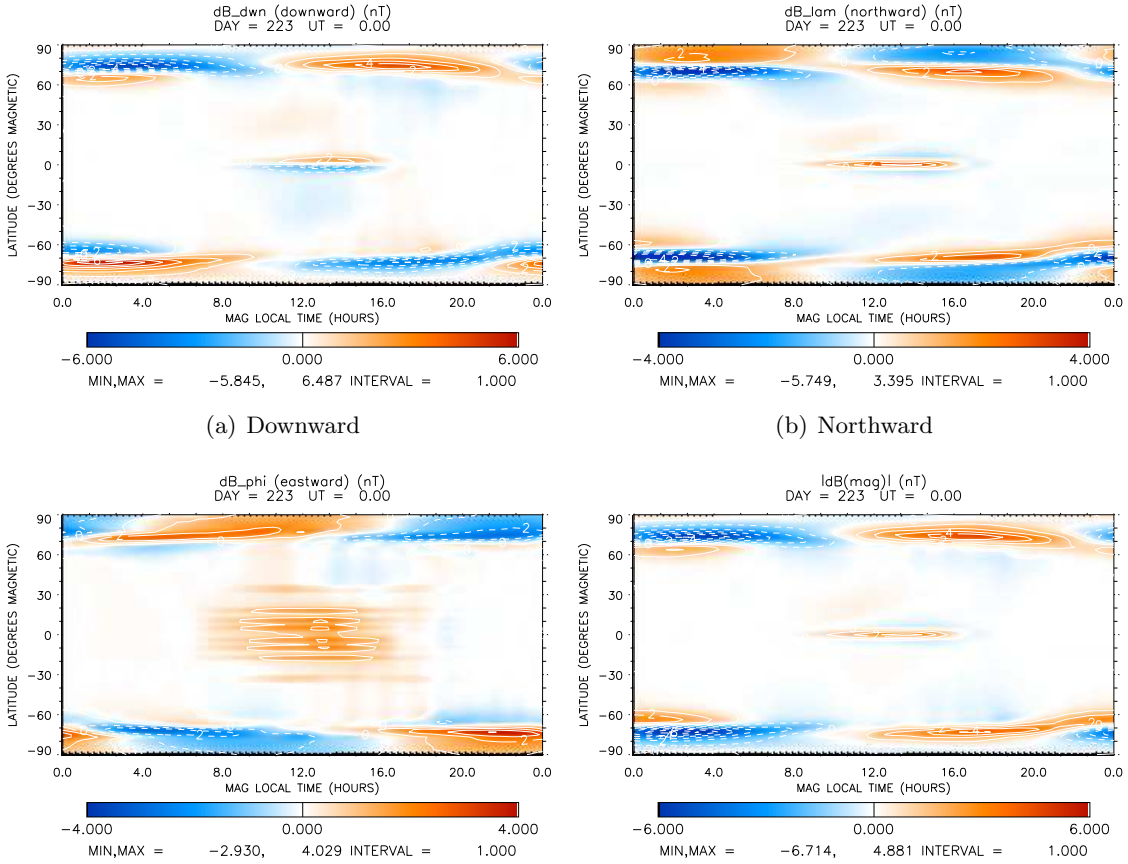

(a) Downward (b) Northward

(c) Eastward (d) Total

Figure A.3: Difference of maximum altitude range in the computation of magnetic perturbation for August 2005. The comparison of the standard altitude, 430 km, and the adjusted altitude, 358 km, show most intense difference in the polar regions, which are not included in the study. The maximum differences in the equatorial region (up to about 3 nT) are smaller and spatially restricted.

DOI: 10.2312/GFZ.b103-08029

APPENDIX B

February 14, 2002 & August 4, 2004 Dayside Orbit Ranks

The tables in this appendix list the orbit ranks for dayside passes on February 14, 2002 and August 4, 2004. The numbers in the tables represent the K_p used for the TIE–GCM run and are ranked from top to bottom where 1^{st} is the best fit and 5^{th} is the worse fit. So in this form the relations depicted are relative only to each individual orbit and from orbit to orbit and day to day the absolute values and differences involved may vary widely.

DOI: 10.2312/GFZ.b103-08029

Table B.1: Goodness of Fit Rankings of individual dayside orbit tracks for TIE–GCM runs using different values of K_p on Feb 14, 2002 for the B_F and B_r components. The values represent the K_p used where 1^{st} is the best fit and 5^{th} is the worse fit in terms of either the MDEV, MEAN or AREA. The SLT is about 9.88 for this day.

Orbit	**1**	**2**	**3**	**4**	**5**	**6**	**7**	**8**	**9**	**10**	**11**	**12**	**13**	**14**
B_F MDEV														
1^{st}	1	0	2	8	8	4	8	8	8	0	2	0	0	1
2^{nd}	0	1	1	4	4	0	4	0	4	1	1	1	1	2
3^{rd}	4	2	0	2	0	2	2	1	2	2	0	2	2	0
4^{th}	2	4	4	1	1	1	1	4	1	4	4	4	4	4
5^{th}	8	8	8	0	2	8	0	2	0	8	8	8	8	8
B_F MEAN														
1^{st}	8	8	8	8	8	8	8	8	4	8	4	4	8	4
2^{nd}	4	4	4	4	4	4	4	4	8	4	2	2	4	2
3^{rd}	2	2	2	2	2	2	2	2	2	2	8	1	2	8
4^{th}	1	1	1	1	1	1	1	1	1	1	1	0	1	1
5^{th}	0	0	0	0	0	0	0	0	0	0	0	8	0	0
B_F AREA														
1^{st}	8	8	4	8	8	8	8	8	4	4	4	4	8	4
2^{nd}	4	4	8	4	4	4	4	4	8	8	2	2	4	2
3^{rd}	2	2	2	2	2	2	2	2	2	2	1	1	2	1
4^{th}	1	1	1	1	1	1	1	1	1	1	8	0	1	0
5^{th}	0	0	0	0	0	0	0	0	0	0	0	8	0	8
B_r MDEV														
1^{st}	4	8	8	8	8	8	0	0	4	4	4	0	0	0
2^{nd}	8	4	0	4	4	4	1	1	2	2	2	1	1	1
3^{rd}	2	2	1	0	0	0	2	2	1	1	1	2	2	2
4^{th}	1	1	2	1	1	1	4	4	0	0	0	4	4	4
5^{th}	0	0	4	2	2	2	8	8	8	8	8	8	8	8
B_r MEAN														
1^{st}	8	8	8	2	2	0	1	4	4	4	4	4	0	8
2^{nd}	4	4	4	4	1	1	2	2	2	2	8	1	1	0
3^{rd}	2	2	2	1	4	2	0	8	1	1	2	2	2	1
4^{th}	1	1	0	0	0	4	4	1	0	0	1	0	4	2
5^{th}	0	0	1	8	8	8	8	0	8	8	0	8	8	4
B_r AREA														
1^{st}	4	8	8	8	8	8	0	0	4	4	4	0	0	0
2^{nd}	8	4	0	4	4	4	1	1	2	2	2	1	1	1
3^{rd}	2	2	4	0	0	0	2	2	1	1	1	2	2	2
4^{th}	1	1	1	1	1	1	4	4	0	0	0	4	4	4
5^{th}	0	0	2	2	2	2	8	8	8	8	8	8	8	8

DOI: 10.2312/GFZ.b103-08029

Table B.2: Goodness of Fit Rankings of individual dayside orbit tracks for TIE–GCM runs using different values of K_p on for Feb 14, 2002 for the B_θ and B_ϕ components. The values are the K_p used where 1^{st} is the best fit and 5^{th} is the worse fit in terms of either the MDEV, MEAN or AREA. The SLT is about 9.88 for this day.

Orbit	**1**	**2**	**3**	**4**	**5**	**6**	**7**	**8**	**9**	**10**	**11**	**12**	**13**	**14**
B_θ MDEV														
1^{st}	0	2	2	0	0	0	0	0	0	0	0	1	4	4
2^{nd}	1	1	4	1	1	1	1	1	1	1	1	2	2	2
3^{rd}	2	0	1	2	2	4	2	2	2	2	2	0	1	1
4^{th}	4	4	0	4	4	2	4	4	4	4	4	4	0	0
5^{th}	8	8	8	8	8	8	8	8	8	8	8	8	8	8
B_θ MEAN														
1^{st}	4	4	4	4	4	4	8	4	2	2	4	4	2	4
2^{nd}	2	2	2	2	2	8	4	8	4	1	2	2	1	2
3^{rd}	1	1	1	1	1	2	2	2	1	0	1	1	0	1
4^{th}	0	0	0	0	0	1	1	1	0	4	0	0	4	0
5^{th}	8	8	8	8	8	0	0	0	8	8	8	8	8	8
B_θ AREA														
1^{st}	4	4	4	4	4	4	4	0	2	0	2	4	2	4
2^{nd}	2	2	2	2	2	8	2	4	1	1	4	2	4	2
3^{rd}	1	1	1	1	1	2	8	1	0	2	1	1	1	1
4^{th}	0	0	0	0	0	1	1	2	4	4	0	0	0	0
5^{th}	8	8	8	8	8	0	0	8	8	8	8	8	8	8
B_ϕ MDEV														
1^{st}	1	8	2	2	0	4	4	2	0	0	2	2	0	4
2^{nd}	2	2	4	4	1	2	8	4	8	1	4	1	1	2
3^{rd}	0	4	1	1	2	1	2	1	1	2	1	0	2	0
4^{th}	8	1	8	0	4	0	1	0	2	4	0	4	4	1
5^{th}	4	0	0	8	8	8	0	8	4	8	8	8	8	8
B_ϕ MEAN														
1^{st}	0	0	0	0	2	0	0	1	0	0	0	0	8	0
2^{nd}	1	1	1	1	4	1	1	2	1	1	1	1	4	1
3^{rd}	2	2	2	2	1	2	2	0	2	2	2	2	2	2
4^{th}	4	4	4	4	0	4	4	4	4	8	4	4	1	4
5^{th}	8	8	8	8	8	8	8	8	8	4	8	8	0	8
B_ϕ AREA														
1^{st}	0	0	1	0	0	1	0	1	0	0	1	0	4	0
2^{nd}	1	1	0	1	1	0	1	2	1	1	2	1	2	1
3^{rd}	2	2	2	2	2	2	2	0	2	2	0	2	1	2
4^{th}	4	4	4	4	4	4	4	4	4	4	4	4	0	4
5^{th}	8	8	8	8	8	8	8	8	8	8	8	8	8	8

DOI: 10.2312/GFZ.b103-08029

Table B.3: Goodness of Fit Rankings of individual dayside orbit tracks for TIE–GCM runs using different values of K_p on Aug 4, 2004 for the B_F and B_r components. The values are the K_p used where 1^{st} is the best fit and 5^{th} is the worse fit in terms of either the MDEV, MEAN or AREA. The SLT is about 11.38 for this day.

Orbit	**1**	**2**	**3**	**4**	**5**	**6**	**7**	**8**	**9**	**10**	**11**	**12**	**13**	**14**	**15**
B_F MDEV															
1^{st}	0	0	1	1	8	8	2	2	4	0	4	0	4	8	8
2^{nd}	1	1	2	2	4	4	1	4	0	1	2	1	2	4	4
3^{rd}	2	2	0	0	2	2	0	1	1	2	1	2	1	2	0
4^{th}	4	4	4	4	1	1	4	0	2	4	0	4	0	0	1
5^{th}	8	8	8	8	0	0	8	8	8	8	8	8	8	1	2
B_F MEAN															
1^{st}	8	8	8	8	8	8	8	8	8	8	8	8	8	8	8
2^{nd}	4	4	4	4	4	4	4	4	4	4	4	4	4	4	4
3^{rd}	2	2	2	2	2	2	2	2	2	2	2	2	2	2	2
4^{th}	1	1	1	1	1	1	1	1	1	1	1	1	1	1	1
5^{th}	0	0	0	0	0	0	0	0	0	0	0	0	0	0	0
B_F AREA															
1^{st}	8	8	8	8	8	8	8	8	8	8	8	4	8	8	8
2^{nd}	4	4	4	4	4	4	4	4	4	4	4	8	4	4	4
3^{rd}	2	2	2	2	2	2	2	2	2	2	2	2	2	2	2
4^{th}	1	1	1	1	1	1	1	1	1	1	1	1	1	1	1
5^{th}	0	0	0	0	0	0	0	0	0	0	0	0	0	0	0
B_r MDEV															
1^{st}	8	8	4	8	8	8	8	8	0	0	0	0	0	0	8
2^{nd}	4	4	8	4	4	4	4	0	1	1	1	1	1	1	0
3^{rd}	0	0	2	0	0	2	2	1	2	2	2	2	2	2	4
4^{th}	2	2	1	1	1	0	0	2	4	4	4	4	4	4	1
5^{th}	1	1	0	2	2	1	1	4	8	8	8	8	8	8	2
B_r MEAN															
1^{st}	8	8	8	8	0	0	8	8	8	4	0	0	1	0	0
2^{nd}	0	4	4	0	1	1	4	4	4	2	1	1	0	1	1
3^{rd}	4	0	0	1	2	2	1	2	2	1	2	2	2	2	2
4^{th}	1	1	1	4	4	4	2	1	1	0	4	4	4	4	4
5^{th}	2	2	2	2	8	8	0	0	0	8	8	8	8	8	8
B_r AREA															
1^{st}	8	8	8	8	0	8	8	8	1	0	0	0	0	0	8
2^{nd}	0	0	4	0	1	0	4	0	0	1	1	1	1	1	0
3^{rd}	1	4	0	1	2	1	2	4	2	2	2	2	2	2	1
4^{th}	4	1	1	4	4	2	1	1	4	4	4	4	4	4	4
5^{th}	2	2	2	2	8	4	0	2	8	8	8	8	8	8	2

DOI: 10.2312/GFZ.b103-08029

Table B.4: Goodness of Fit Rankings of individual dayside orbit tracks for TIE–GCM runs using different values of K_p on Aug 4, 2004 for the B_θ and B_ϕ components. The values are the K_p used where 1^{st} is the best fit and 5^{th} is the worse fit in terms of either the MDEV, MEAN or AREA. The SLT is about 11.38 for this day.

Orbit	**1**	**2**	**3**	**4**	**5**	**6**	**7**	**8**	**9**	**10**	**11**	**12**	**13**	**14**	**15**
B_θ MDEV															
1^{st}	0	1	0	0	0	1	1	0	0	0	0	0	0	0	8
2^{nd}	1	0	1	1	1	0	0	1	1	1	1	1	1	1	0
3^{rd}	2	2	2	2	2	2	2	2	2	2	2	2	2	2	4
4^{th}	4	4	4	4	4	4	4	4	4	4	4	4	4	4	1
5^{th}	8	8	8	8	8	8	8	8	8	8	8	8	8	8	2
B_θ MEAN															
1^{st}	8	4	4	4	4	8	8	4	8	4	4	4	4	4	4
2^{nd}	4	8	2	8	8	4	4	8	4	2	2	2	8	2	2
3^{rd}	2	2	8	2	2	2	2	2	2	1	1	1	2	8	1
4^{th}	1	1	1	1	1	1	1	1	1	0	0	0	1	1	0
5^{th}	0	0	0	0	0	0	0	0	0	8	8	8	0	0	8
B_θ AREA															
1^{st}	8	4	4	4	4	4	8	4	8	4	4	4	4	4	4
2^{nd}	4	8	2	2	2	8	4	8	4	2	2	2	8	2	2
3^{rd}	2	2	1	8	8	2	2	2	2	1	1	1	2	8	1
4^{th}	1	1	8	1	1	1	1	1	1	0	0	0	1	1	0
5^{th}	0	0	0	0	0	0	0	0	0	8	8	8	0	0	8
B_ϕ MDEV															
1^{st}	2	2	2	2	4	4	4	8	4	4	0	2	2	2	2
2^{nd}	1	1	1	4	8	8	8	4	2	2	8	1	1	4	1
3^{rd}	0	0	0	1	2	2	2	2	1	1	1	0	0	1	4
4^{th}	4	4	4	0	1	1	1	1	0	0	2	4	4	0	0
5^{th}	8	8	8	8	0	0	0	0	8	8	4	8	8	8	8
B_ϕ MEAN															
1^{st}	0	0	1	8	2	2	4	4	4	0	8	0	0	8	8
2^{nd}	1	1	2	4	1	1	2	2	2	1	1	1	1	4	4
3^{rd}	2	2	0	0	4	4	0	1	1	2	0	2	2	2	2
4^{th}	4	4	4	2	0	0	1	0	0	4	2	4	4	1	1
5^{th}	8	8	8	1	8	8	8	8	8	8	4	8	8	0	0
B_ϕ AREA															
1^{st}	0	0	2	4	4	4	4	4	4	0	8	0	0	4	4
2^{nd}	1	1	1	2	2	8	8	2	2	1	0	1	1	2	2
3^{rd}	2	2	0	1	8	2	2	1	1	2	1	2	2	1	1
4^{th}	4	4	4	0	1	1	1	0	0	4	2	4	4	0	0
5^{th}	8	8	8	8	0	0	0	8	8	8	4	8	8	8	8

DOI: 10.2312/GFZ.b103-08029

APPENDIX C

K_p Dayside Orbit Ranks for the Quietest Day of Each Year between 2001–2005

This appendix lists the goodness of fit rankings of individual dayside orbit tracks for runs of the TIE–GCM using different values of K_p for the quietest day of each year between 2001–2005. These tables represent the complete set of tables first introduced and discussed in Sec. 2.7.2. The numbers in the tables represent the K_p used for the TIE–GCM run and are ranked from top to bottom where 1^{st} is the best fit and 5^{th} is the worse fit. So in this form the relations depicted are relative only to each individual orbit and from orbit to orbit and day to day the absolute values and differences involved may vary widely.

DOI: 10.2312/GFZ.b103-08029

Table C.1: Goodness of Fit Rankings of individual dayside orbit tracks for TIE–GCM runs using different values of K_p on Jun 28, 2001 for the B_F and B_r components. The values represent the K_p used where 1^{st} is the best fit and 5^{th} is the worse fit in terms of either the MDEV, MEAN or AREA. The SLT is about 6.8 for this day.

Orbit	**1**	**2**	**3**	**4**	**5**	**6**	**7**	**8**	**9**	**10**	**11**	**12**	**13**	**14**
B_F MDEV														
1^{st}	0	0	1	8	2	4	0	0	0	0	0	0	0	0
2^{nd}	1	1	0	4	1	8	1	1	1	1	1	1	1	1
3^{rd}	2	2	2	2	4	2	2	2	2	4	2	2	4	2
4^{th}	4	4	4	1	0	1	4	4	4	2	4	4	2	4
5^{th}	8	8	8	0	8	0	8	8	8	8	8	8	8	8
B_F MEAN														
1^{st}	8	8	8	8	8	8	8	8	8	8	8	8	8	8
2^{nd}	4	4	4	4	4	4	4	4	4	4	4	4	4	4
3^{rd}	2	2	2	2	2	2	2	2	2	2	2	2	2	2
4^{th}	1	1	1	1	1	1	1	1	1	1	1	1	1	1
5^{th}	0	0	0	0	0	0	0	0	0	0	0	0	0	0
B_F AREA														
1^{st}	4	4	8	8	8	8	8	8	8	8	8	8	8	8
2^{nd}	8	8	4	4	4	4	4	4	4	4	4	4	4	4
3^{rd}	2	2	2	2	2	2	2	2	2	2	2	2	2	2
4^{th}	1	1	1	1	1	1	1	1	1	1	1	1	1	1
5^{th}	0	0	0	0	0	0	0	0	0	0	0	0	0	0
B_r MDEV														
1^{st}	1	0	2	2	0	2	4	2	2	0	0	2	4	2
2^{nd}	2	1	1	1	1	4	2	4	4	1	1	8	2	4
3^{rd}	0	2	0	0	2	1	1	1	1	2	2	4	1	1
4^{th}	4	4	4	4	4	0	0	0	0	4	4	1	0	0
5^{th}	8	8	8	8	8	8	8	8	8	8	8	0	8	8
B_r MEAN														
1^{st}	0	8	0	0	0	2	8	2	4	8	8	0	0	0
2^{nd}	1	4	1	1	1	4	4	4	2	4	4	1	1	1
3^{rd}	2	0	2	2	2	1	2	1	8	2	2	2	2	2
4^{th}	4	2	4	4	4	0	1	0	1	1	1	4	4	4
5^{th}	8	1	8	8	8	8	0	8	0	0	0	8	8	8
B_r AREA														
1^{st}	1	0	1	0	0	4	4	4	4	8	8	8	4	1
2^{nd}	0	1	0	1	1	2	8	2	2	4	4	4	2	0
3^{rd}	2	2	2	2	2	1	2	1	1	2	2	2	1	2
4^{th}	4	4	4	4	4	0	1	0	8	1	1	1	0	4
5^{th}	8	8	8	8	8	8	0	8	0	0	0	0	8	8

DOI: 10.2312/GFZ.b103-08029

Table C.2: Goodness of Fit Rankings of individual dayside orbit tracks for TIE–GCM runs using different values of K_p on Jun 28, 2001 for the B_θ and B_ϕ components. The values represent the K_p used where 1^{st} is the best fit and 5^{th} is the worse fit in terms of either the MDEV, MEAN or AREA. The SLT is about 6.8 for this day.

Orbit	**1**	**2**	**3**	**4**	**5**	**6**	**7**	**8**	**9**	**10**	**11**	**12**	**13**	**14**
B_θ MDEV														
1^{st}	0	0	0	8	4	4	2	2	4	0	0	0	0	0
2^{nd}	1	4	1	4	8	8	4	1	2	1	1	1	1	1
3^{rd}	2	1	4	2	2	2	1	4	1	2	2	2	2	2
4^{th}	4	2	2	1	1	1	0	0	0	4	4	4	4	4
5^{th}	8	8	8	0	0	0	8	8	8	8	8	8	8	8
B_θ MEAN														
1^{st}	8	4	8	4	8	8	8	8	4	8	2	1	1	0
2^{nd}	4	2	4	2	4	4	4	4	2	4	1	0	0	1
3^{rd}	2	1	2	1	2	2	2	2	8	2	0	2	2	2
4^{th}	1	8	1	0	1	1	1	1	1	1	4	4	4	4
5^{th}	0	0	0	8	0	0	0	0	0	0	8	8	8	8
B_θ AREA														
1^{st}	0	4	4	4	4	8	4	4	4	0	0	0	0	0
2^{nd}	1	2	8	2	8	4	2	2	2	1	1	1	1	1
3^{rd}	2	1	2	8	2	2	1	1	1	4	2	2	2	2
4^{th}	4	0	1	1	1	1	8	0	0	2	4	4	4	4
5^{th}	8	8	0	0	0	0	0	8	8	8	8	8	8	8
B_ϕ MDEV														
1^{st}	0	0	0	0	0	1	0	0	0	0	0	0	0	0
2^{nd}	1	1	1	1	1	0	1	1	1	1	1	1	1	1
3^{rd}	2	2	2	2	2	2	2	2	2	2	2	2	2	2
4^{th}	4	4	4	4	4	4	4	4	4	4	4	4	4	4
5^{th}	8	8	8	8	8	8	8	8	8	8	8	8	8	8
B_ϕ MEAN														
1^{st}	4	4	4	4	4	4	4	0	0	0	0	0	0	4
2^{nd}	8	0	2	2	2	2	0	1	1	1	1	1	1	2
3^{rd}	2	1	0	1	1	1	2	2	2	2	2	2	2	0
4^{th}	0	2	1	0	0	0	1	4	4	4	4	4	4	1
5^{th}	1	8	8	8	8	8	8	8	8	8	8	8	8	8
B_ϕ AREA														
1^{st}	0	0	0	0	4	4	0	0	0	0	0	0	0	0
2^{nd}	1	1	1	1	2	2	1	1	1	1	1	1	1	1
3^{rd}	2	2	2	2	1	1	2	2	2	2	2	2	2	2
4^{th}	4	4	4	4	0	0	4	4	4	4	4	4	4	4
5^{th}	8	8	8	8	8	8	8	8	8	8	8	8	8	8

DOI: 10.2312/GFZ.b103-08029

Table C.3: Goodness of Fit Rankings of individual dayside orbit tracks for TIE–GCM runs using different values of K_p on May 24, 2002 for the B_F and B_r components. The values represent the K_p used where 1^{st} is the best fit and 5^{th} is the worse fit in terms of either the MDEV, MEAN or AREA. The SLT is about 12.8 for this day.

Orbit	**1**	**2**	**3**	**4**	**5**	**6**	**7**	**8**	**9**	**10**	**11**	**12**	**13**	**14**	**15**
B_F MDEV															
1^{st}	0	0	0	1	0	2	0	8	0	0	0	4	0	0	0
2^{nd}	1	1	1	0	1	1	1	0	1	1	1	8	1	1	1
3^{rd}	2	2	2	2	2	4	8	1	2	2	2	0	2	2	2
4^{th}	4	4	4	4	4	0	2	2	4	4	4	1	4	4	8
5^{th}	8	8	8	8	8	8	4	4	8	8	8	2	8	8	4
B_F MEAN															
1^{st}	8	8	8	8	8	8	8	8	8	8	8	8	8	8	8
2^{nd}	4	4	4	4	4	4	4	4	4	4	4	4	4	4	4
3^{rd}	2	2	2	2	2	2	2	2	2	2	2	2	2	2	2
4^{th}	1	1	1	1	1	1	1	1	1	1	1	1	1	1	1
5^{th}	0	0	0	0	0	0	0	0	0	0	0	0	0	0	0
B_F AREA															
1^{st}	8	8	8	8	8	8	8	8	8	8	8	8	8	8	8
2^{nd}	4	4	4	4	4	4	4	4	4	4	4	4	4	4	4
3^{rd}	2	2	2	2	2	2	2	2	2	2	2	2	2	2	2
4^{th}	1	1	1	1	1	1	1	1	1	1	1	1	1	1	1
5^{th}	0	0	0	0	0	0	0	0	0	0	0	0	0	0	0
B_r MDEV															
1^{st}	0	0	0	0	8	8	8	8	8	0	0	0	0	0	0
2^{nd}	1	1	1	1	0	0	0	0	0	1	1	1	1	1	1
3^{rd}	2	2	2	2	1	1	1	1	1	2	2	2	2	2	2
4^{th}	4	4	4	8	2	2	2	4	2	4	4	4	4	4	4
5^{th}	8	8	8	4	4	4	4	2	4	8	8	8	8	8	8
B_r MEAN															
1^{st}	0	8	8	8	8	0	0	0	8	4	1	4	8	1	8
2^{nd}	4	4	0	0	0	1	1	1	4	2	0	2	4	0	4
3^{rd}	1	0	1	4	1	2	2	2	2	8	2	1	2	2	2
4^{th}	2	2	2	1	2	4	4	8	1	1	4	0	1	4	1
5^{th}	8	1	4	2	4	8	8	4	0	0	8	8	0	8	0
B_r AREA															
1^{st}	0	0	0	8	8	0	0	8	8	0	0	0	0	0	0
2^{nd}	1	1	1	0	0	1	1	0	0	1	1	1	1	1	1
3^{rd}	2	2	2	1	1	2	2	1	1	2	2	2	2	2	2
4^{th}	4	4	4	2	2	4	4	2	2	4	4	4	4	4	4
5^{th}	8	8	8	4	4	8	8	4	4	8	8	8	8	8	8

DOI: 10.2312/GFZ.b103-08029

Table C.4: Goodness of Fit Rankings of individual dayside orbit tracks for TIE–GCM runs using different values of K_p on May 24, 2002 for the B_θ and B_ϕ components. The values represent the K_p used where 1^{st} is the best fit and 5^{th} is the worse fit in terms of either the MDEV, MEAN or AREA. The SLT is about 12.8 for this day.

Orbit	**1**	**2**	**3**	**4**	**5**	**6**	**7**	**8**	**9**	**10**	**11**	**12**	**13**	**14**	**15**
B_θ MDEV															
1^{st}	2	1	0	0	0	0	0	0	0	0	0	0	0	0	0
2^{nd}	1	0	1	1	1	1	1	1	1	1	1	1	1	1	1
3^{rd}	0	2	2	2	2	2	2	2	2	2	2	2	2	2	2
4^{th}	4	4	4	4	4	4	4	4	4	4	4	4	4	4	4
5^{th}	8	8	8	8	8	8	8	8	8	8	8	8	8	8	8
B_θ MEAN															
1^{st}	8	8	8	8	8	8	8	8	8	8	8	8	8	8	8
2^{nd}	4	4	4	4	4	4	4	4	4	4	4	4	4	4	4
3^{rd}	2	2	2	2	2	2	2	2	2	2	2	2	2	2	2
4^{th}	1	1	1	1	1	1	1	1	1	1	1	1	1	1	1
5^{th}	0	0	0	0	0	0	0	0	0	0	0	0	0	0	0
B_θ AREA															
1^{st}	8	8	8	8	8	8	8	8	8	8	8	4	8	8	8
2^{nd}	4	4	4	4	4	4	4	4	4	4	4	8	4	4	4
3^{rd}	2	2	2	2	2	2	2	2	2	2	2	2	2	2	2
4^{th}	1	1	1	1	1	1	1	1	1	1	1	1	1	1	1
5^{th}	0	0	0	0	0	0	0	0	0	0	0	0	0	0	0
B_ϕ MDEV															
1^{st}	0	2	2	0	4	4	4	4	4	0	0	0	0	0	0
2^{nd}	1	1	1	1	2	2	8	8	2	1	1	1	1	1	1
3^{rd}	2	0	0	2	1	1	2	2	1	2	2	2	2	2	2
4^{th}	4	4	4	4	0	0	1	1	0	4	4	4	4	4	4
5^{th}	8	8	8	8	8	8	0	0	8	8	8	8	8	8	8
B_ϕ MEAN															
1^{st}	8	4	2	8	8	8	8	8	8	2	0	0	1	4	2
2^{nd}	4	8	4	4	4	4	0	0	4	1	1	1	0	2	4
3^{rd}	2	2	1	2	0	0	1	1	2	0	2	2	2	1	1
4^{th}	1	1	0	1	1	1	4	4	1	4	4	4	4	0	0
5^{th}	0	0	8	0	2	2	2	2	0	8	8	8	8	8	8
B_ϕ AREA															
1^{st}	2	2	2	4	4	8	8	4	4	1	0	0	0	2	0
2^{nd}	1	1	1	8	2	4	0	8	8	2	1	1	1	1	1
3^{rd}	4	4	0	0	1	0	4	2	2	0	2	2	2	4	2
4^{th}	0	0	4	1	0	2	1	1	1	4	4	4	4	0	4
5^{th}	8	8	8	2	8	1	2	0	0	8	8	8	8	8	8

DOI: 10.2312/GFZ.b103-08029

Table C.5: Goodness of Fit Rankings of individual dayside orbit tracks for TIE–GCM runs using different values of K_p on Dec 19, 2003 for the B_F and B_r components. The values represent the K_p used where 1^{st} is the best fit and 5^{th} is the worse fit in terms of either the MDEV, MEAN or AREA. The SLT is about 8.3 for this day.

Orbit	**1**	**2**	**3**	**4**	**5**	**6**	**7**	**8**	**9**	**10**	**11**	**12**	**13**	**14**	**15**
B_F MDEV															
1^{st}	0	0	8	4	2	2	4	0	0	0	0	2	0	1	0
2^{nd}	1	1	4	2	1	1	2	1	1	1	1	0	1	0	1
3^{rd}	2	2	2	1	0	4	1	4	2	2	2	1	2	2	2
4^{th}	4	4	1	8	4	0	0	2	4	4	4	4	4	4	4
5^{th}	8	8	0	0	8	8	8	8	8	8	8	8	8	8	8
B_F MEAN															
1^{st}	8	8	8	8	8	8	8	8	8	8	8	8	8	8	8
2^{nd}	4	4	4	4	4	4	4	4	4	4	4	4	4	4	4
3^{rd}	2	2	2	2	2	2	2	2	2	2	2	2	2	2	2
4^{th}	1	1	1	1	1	1	1	1	1	1	1	1	1	1	1
5^{th}	0	0	0	0	0	0	0	0	0	0	0	0	0	0	0
B_F AREA															
1^{st}	8	8	8	8	8	8	8	8	8	8	8	8	4	8	8
2^{nd}	4	4	4	4	4	4	4	4	4	4	4	4	8	4	4
3^{rd}	2	2	2	2	2	2	2	2	2	2	2	2	2	2	2
4^{th}	1	1	1	1	1	1	1	1	1	1	1	1	1	1	1
5^{th}	0	0	0	0	0	0	0	0	0	0	0	0	0	0	0
B_r MDEV															
1^{st}	8	4	0	0	8	0	0	0	0	4	0	0	0	8	8
2^{nd}	4	2	1	1	0	1	1	1	1	2	1	1	1	4	4
3^{rd}	2	8	2	2	1	2	2	2	2	1	2	2	2	0	2
4^{th}	1	1	4	4	2	4	4	4	4	0	4	4	4	2	0
5^{th}	0	0	8	8	4	8	8	8	8	8	8	8	8	1	1
B_r MEAN															
1^{st}	8	8	8	2	4	8	4	8	4	4	0	0	0	8	8
2^{nd}	4	4	4	4	2	4	2	4	2	2	1	1	1	0	4
3^{rd}	2	2	2	1	1	2	8	0	1	1	2	2	2	1	2
4^{th}	1	1	0	0	0	1	1	1	0	0	4	4	4	2	1
5^{th}	0	0	1	8	8	0	0	2	8	8	8	8	8	4	0
B_r AREA															
1^{st}	8	8	0	0	8	0	2	0	0	4	0	0	0	8	8
2^{nd}	4	4	1	1	0	1	1	1	1	2	1	1	1	4	4
3^{rd}	2	2	2	2	1	2	0	2	2	1	2	2	2	0	2
4^{th}	1	1	8	4	2	4	4	4	4	0	4	4	4	2	1
5^{th}	0	0	4	8	4	8	8	8	8	8	8	8	8	1	0

DOI: 10.2312/GFZ.b103-08029

Table C.6: Goodness of Fit Rankings of individual dayside orbit tracks for TIE–GCM runs using different values of K_p on Dec 19, 2003 for the B_θ and B_ϕ components. The values represent the K_p used where 1^{st} is the best fit and 5^{th} is the worse fit in terms of either the MDEV, MEAN or AREA. The SLT is about 8.3 for this day.

Orbit	**1**	**2**	**3**	**4**	**5**	**6**	**7**	**8**	**9**	**10**	**11**	**12**	**13**	**14**	**15**
B_θ MDEV															
1^{st}	4	4	4	0	1	0	2	2	0	0	0	4	4	4	4
2^{nd}	2	2	8	1	0	1	1	1	1	1	1	2	8	2	2
3^{rd}	1	1	2	2	2	2	0	4	2	2	2	1	2	1	8
4^{th}	0	8	1	4	4	4	4	0	4	4	4	0	1	0	1
5^{th}	8	0	0	8	8	8	8	8	8	8	8	8	0	8	0
B_θ MEAN															
1^{st}	4	4	4	8	8	8	8	4	4	4	4	4	4	4	4
2^{nd}	2	2	8	4	4	4	4	8	2	2	2	2	2	2	2
3^{rd}	1	1	2	2	2	2	2	2	1	1	1	1	1	1	1
4^{th}	8	0	1	1	1	1	1	1	0	0	8	0	0	8	8
5^{th}	0	8	0	0	0	0	0	0	8	8	0	8	8	0	0
B_θ AREA															
1^{st}	4	4	4	4	8	8	8	4	4	4	4	4	4	4	4
2^{nd}	2	2	8	8	4	4	4	2	2	2	2	2	2	2	2
3^{rd}	1	1	2	2	2	2	2	1	1	1	1	1	1	1	1
4^{th}	8	0	1	1	1	1	1	0	0	0	8	0	0	8	8
5^{th}	0	8	0	0	0	0	0	8	8	8	0	8	8	0	0
B_ϕ MDEV															
1^{st}	0	0	0	0	0	0	0	2	2	0	1	1	0	2	2
2^{nd}	1	1	1	1	1	1	1	4	4	1	2	0	1	0	0
3^{rd}	2	2	2	2	2	2	2	1	1	2	0	2	2	1	1
4^{th}	4	4	4	4	4	4	4	0	0	4	4	4	4	4	4
5^{th}	8	8	8	8	8	8	8	8	8	8	8	8	8	8	8
B_ϕ MEAN															
1^{st}	0	0	0	0	0	0	0	2	0	0	2	4	8	4	0
2^{nd}	1	1	1	1	1	1	1	1	1	1	1	2	4	0	8
3^{rd}	2	2	2	2	2	2	2	4	2	8	0	1	2	1	1
4^{th}	4	4	4	4	4	4	4	0	4	2	4	0	0	2	2
5^{th}	8	8	8	8	8	8	8	8	8	4	8	8	1	8	4
B_ϕ AREA															
1^{st}	0	0	0	0	0	0	0	2	0	0	1	2	0	2	0
2^{nd}	1	1	1	1	1	1	1	1	1	1	0	1	1	0	1
3^{rd}	2	2	2	2	2	2	2	4	2	2	2	0	2	1	8
4^{th}	4	4	4	4	4	4	4	0	4	4	4	4	4	4	2
5^{th}	8	8	8	8	8	8	8	8	8	8	8	8	8	8	4

DOI: 10.2312/GFZ.b103-08029

Table C.7: Goodness of Fit Rankings of individual dayside orbit tracks for TIE–GCM runs using different values of K_p on Dec 4, 2004 for the B_F and B_r components. The values represent the K_p used where 1^{st} is the best fit and 5^{th} is the worse fit in terms of either the MDEV, MEAN or AREA. The SLT is about 12.1 for this day.

Orbit	**1**	**2**	**3**	**4**	**5**	**6**	**7**	**8**	**9**	**10**	**11**	**12**	**13**	**14**	**15**
B_F MDEV															
1^{st}	2	2	2	2	4	0	0	2	4	0	4	0	0	0	0
2^{nd}	4	1	4	1	0	1	1	4	2	1	0	1	1	1	1
3^{rd}	1	0	1	0	2	4	2	1	1	2	1	2	4	4	2
4^{th}	0	4	0	4	1	2	4	0	0	4	2	4	2	2	4
5^{th}	8	8	8	8	8	8	8	8	8	8	8	8	8	8	8
B_F MEAN															
1^{st}	8	8	8	8	8	8	8	8	8	8	8	8	8	0	4
2^{nd}	4	4	4	4	4	4	4	4	4	4	4	4	4	1	8
3^{rd}	2	2	2	2	2	2	2	2	2	2	2	2	2	2	2
4^{th}	1	1	1	1	1	1	1	1	1	1	1	1	1	4	1
5^{th}	0	0	0	0	0	0	0	0	0	0	0	0	0	8	0
B_F AREA															
1^{st}	8	8	8	8	8	8	8	8	8	8	8	8	8	0	4
2^{nd}	4	4	4	4	4	4	4	4	4	4	4	4	4	1	8
3^{rd}	2	2	2	2	2	2	2	2	2	2	2	2	2	2	2
4^{th}	1	1	1	1	1	1	1	1	1	1	1	1	1	4	1
5^{th}	0	0	0	0	0	0	0	0	0	0	0	0	0	8	0
B_r MDEV															
1^{st}	0	0	0	4	0	8	8	8	8	0	0	0	0	0	0
2^{nd}	1	1	1	0	4	4	4	4	0	1	1	1	1	1	1
3^{rd}	2	2	2	2	2	0	1	2	1	2	2	2	2	2	2
4^{th}	4	4	4	1	1	1	0	1	2	4	4	4	4	4	4
5^{th}	8	8	8	8	8	2	2	0	4	8	8	8	8	8	8
B_r MEAN															
1^{st}	4	8	8	8	8	8	0	4	4	2	4	4	8	0	0
2^{nd}	0	4	4	4	4	4	1	2	2	1	2	8	2	1	1
3^{rd}	1	2	2	2	2	2	2	1	1	0	1	0	4	2	2
4^{th}	2	0	0	0	1	1	4	0	0	4	0	1	1	4	4
5^{th}	8	1	1	1	0	0	8	8	8	8	8	2	0	8	8
B_r AREA															
1^{st}	0	4	4	4	8	8	0	8	4	0	0	0	0	0	0
2^{nd}	1	0	0	8	4	4	1	4	2	1	1	1	1	1	1
3^{rd}	2	1	1	0	2	0	4	2	1	2	2	2	2	2	2
4^{th}	4	2	2	2	1	1	2	1	0	4	4	4	4	4	4
5^{th}	8	8	8	1	0	2	8	0	8	8	8	8	8	8	8

DOI: 10.2312/GFZ.b103-08029

Table C.8: Goodness of Fit Rankings of individual dayside orbit tracks for TIE–GCM runs using different values of K_p on Dec 4, 2004 for the B_θ and B_ϕ components. The values represent the K_p used where 1^{st} is the best fit and 5^{th} is the worse fit in terms of either the MDEV, MEAN or AREA. The SLT is about 12.1 for this day.

Orbit	**1**	**2**	**3**	**4**	**5**	**6**	**7**	**8**	**9**	**10**	**11**	**12**	**13**	**14**	**15**
B_θ MDEV															
1^{st}	1	1	0	0	0	0	0	2	4	2	0	0	0	2	0
2^{nd}	2	0	1	1	1	1	1	1	2	1	1	1	1	1	1
3^{rd}	0	2	2	2	2	2	2	0	1	0	2	2	2	0	2
4^{th}	4	4	4	4	4	4	4	4	0	4	4	4	4	4	4
5^{th}	8	8	8	8	8	8	8	8	8	8	8	8	8	8	8
B_θ MEAN															
1^{st}	4	4	4	4	4	8	8	8	8	8	4	4	4	0	4
2^{nd}	2	2	2	2	8	4	4	4	4	4	2	2	8	1	2
3^{rd}	1	8	8	8	2	2	2	2	2	2	1	8	2	2	8
4^{th}	0	1	1	1	1	1	1	1	1	1	0	1	1	4	1
5^{th}	8	0	0	0	0	0	0	0	0	0	8	0	0	8	0
B_θ AREA															
1^{st}	4	4	4	4	4	4	4	8	8	4	4	4	4	0	4
2^{nd}	2	2	2	2	8	8	8	4	4	8	2	2	8	1	2
3^{rd}	1	1	1	1	2	2	2	2	2	2	1	1	2	2	1
4^{th}	0	8	8	8	1	1	1	1	1	1	0	0	1	4	8
5^{th}	8	0	0	0	0	0	0	0	0	0	8	8	0	8	0
B_ϕ MDEV															
1^{st}	0	4	2	8	4	0	0	2	8	1	0	0	0	0	0
2^{nd}	1	8	4	4	0	1	1	4	4	0	1	1	1	1	1
3^{rd}	2	2	1	0	1	2	2	1	2	2	8	2	2	2	2
4^{th}	4	1	0	1	2	4	4	0	1	4	2	4	4	4	4
5^{th}	8	0	8	2	8	8	8	8	0	8	4	8	8	8	8
B_ϕ MEAN															
1^{st}	8	4	8	0	8	8	8	0	0	0	0	4	4	4	2
2^{nd}	4	2	4	1	0	4	4	1	1	1	1	2	2	2	4
3^{rd}	2	1	2	2	1	2	2	2	2	2	2	0	1	1	1
4^{th}	1	0	1	4	4	1	1	4	4	4	4	1	0	0	0
5^{th}	0	8	0	8	2	0	0	8	8	8	8	8	8	8	8
B_ϕ AREA															
1^{st}	0	4	8	4	0	2	4	2	0	0	0	0	2	2	2
2^{nd}	1	2	4	0	1	1	2	1	1	1	1	1	4	1	1
3^{rd}	2	1	2	1	2	0	1	0	2	2	2	2	1	0	0
4^{th}	4	8	1	2	4	4	0	4	4	4	4	4	0	4	4
5^{th}	8	0	0	8	8	8	8	8	8	8	8	8	8	8	8

DOI: 10.2312/GFZ.b103-08029

Table C.9: Goodness of Fit Rankings of individual dayside orbit tracks for TIE–GCM runs using different values of K_p on Dec 23, 2005 for the B_F and B_r components. The values represent the K_p used where 1^{st} is the best fit and 5^{th} is the worse fit in terms of either the MDEV, MEAN or AREA. The SLT is about 12.7 for this day.

Orbit	**1**	**2**	**3**	**4**	**5**	**6**	**7**	**8**	**9**	**10**	**11**	**12**	**13**	**14**	**15**
B_F MDEV															
1^{st}	0	0	4	8	8	8	2	2	0	0	0	0	0	0	1
2^{nd}	1	1	2	4	4	4	1	1	1	1	1	8	1	1	0
3^{rd}	2	2	1	2	2	0	0	0	2	2	2	1	2	2	2
4^{th}	4	4	0	0	0	1	4	4	4	4	4	2	4	4	4
5^{th}	8	8	8	1	1	2	8	8	8	8	8	4	8	8	8
B_F MEAN															
1^{st}	4	8	8	8	8	8	8	8	8	8	8	8	8	8	8
2^{nd}	8	4	4	4	4	4	4	4	4	4	4	4	4	4	4
3^{rd}	2	2	2	2	2	2	2	2	2	2	2	2	2	2	2
4^{th}	1	1	1	1	1	1	1	1	1	1	1	1	1	1	1
5^{th}	0	0	0	0	0	0	0	0	0	0	0	0	0	0	0
B_F AREA															
1^{st}	8	8	8	8	8	8	8	8	8	8	4	8	8	8	8
2^{nd}	4	4	4	4	4	4	4	4	4	4	8	4	4	4	4
3^{rd}	2	2	2	2	2	2	2	2	2	2	2	2	2	2	2
4^{th}	1	1	1	1	1	1	1	1	1	1	1	1	1	1	1
5^{th}	0	0	0	0	0	0	0	0	0	0	0	0	0	0	0
B_r MDEV															
1^{st}	0	0	0	0	0	2	4	4	0	4	0	8	8	0	0
2^{nd}	1	1	1	1	1	1	2	2	1	8	1	4	4	1	1
3^{rd}	2	2	4	2	2	0	1	1	2	2	2	2	2	2	2
4^{th}	4	8	2	4	4	4	0	0	4	1	8	1	1	4	4
5^{th}	8	4	8	8	8	8	8	8	8	0	4	0	0	8	8
B_r MEAN															
1^{st}	8	8	8	8	8	8	8	8	8	4	0	4	0	4	8
2^{nd}	0	4	4	4	4	4	4	4	4	2	1	2	1	2	4
3^{rd}	1	0	0	2	2	2	2	2	2	1	2	1	2	8	2
4^{th}	2	1	1	0	1	1	1	1	1	0	4	0	4	1	1
5^{th}	4	2	2	1	0	0	0	0	0	8	8	8	8	0	0
B_r AREA															
1^{st}	0	0	8	4	4	4	8	8	4	4	0	8	0	0	0
2^{nd}	1	1	4	2	2	2	4	4	2	2	1	4	1	1	1
3^{rd}	2	8	0	0	1	1	2	2	8	1	2	2	2	2	2
4^{th}	4	2	1	1	0	0	1	1	1	0	4	1	4	4	8
5^{th}	8	4	2	8	8	8	0	0	0	8	8	0	8	8	4

DOI: 10.2312/GFZ.b103-08029

Table C.10: Goodness of Fit Rankings of individual dayside orbit tracks for TIE–GCM runs using different values of K_p on Dec 23, 2005 for the B_θ and B_ϕ components. The values represent the K_p used where 1^{st} is the best fit and 5^{th} is the worse fit in terms of either the MDEV, MEAN or AREA. The SLT is about 12.7 for this day.

Orbit	**1**	**2**	**3**	**4**	**5**	**6**	**7**	**8**	**9**	**10**	**11**	**12**	**13**	**14**	**15**
B_θ MDEV															
1^{st}	4	4	2	4	2	2	4	4	2	1	0	0	0	0	0
2^{nd}	8	2	4	2	1	4	2	2	1	2	1	1	1	1	1
3^{rd}	2	1	1	1	0	1	1	1	4	0	2	2	2	2	2
4^{th}	0	0	0	0	4	0	0	0	0	4	4	4	4	4	4
5^{th}	1	8	8	8	8	8	8	8	8	8	8	8	8	8	8
B_θ MEAN															
1^{st}	4	2	2	2	2	1	2	2	4	4	4	2	0	2	4
2^{nd}	2	4	1	1	1	2	1	1	2	2	2	1	1	1	2
3^{rd}	1	1	4	4	0	0	0	4	1	1	1	4	2	0	1
4^{th}	0	0	0	0	4	4	4	0	0	0	0	0	4	4	0
5^{th}	8	8	8	8	8	8	8	8	8	8	8	8	8	8	8
B_θ AREA															
1^{st}	4	4	4	4	2	2	4	4	4	4	2	0	0	1	2
2^{nd}	2	2	2	2	1	4	2	2	2	2	1	1	1	0	1
3^{rd}	1	1	1	1	0	1	1	1	1	1	0	2	2	2	0
4^{th}	0	0	0	0	4	0	0	0	0	0	4	4	4	4	4
5^{th}	8	8	8	8	8	8	8	8	8	8	8	8	8	8	8
B_ϕ MDEV															
1^{st}	0	0	0	0	0	8	8	4	8	8	0	8	0	0	0
2^{nd}	1	1	1	1	1	0	0	2	4	4	1	0	1	1	1
3^{rd}	2	2	2	2	2	1	1	1	2	2	4	1	2	2	2
4^{th}	4	4	4	4	4	2	4	0	1	1	2	2	4	4	4
5^{th}	8	8	8	8	8	4	2	8	0	0	8	4	8	8	8
B_ϕ MEAN															
1^{st}	0	0	0	8	8	2	0	0	0	0	0	0	8	4	2
2^{nd}	1	1	1	2	0	1	1	1	1	1	1	1	0	8	4
3^{rd}	2	2	2	4	1	4	2	2	2	2	2	2	4	2	1
4^{th}	4	4	4	0	2	0	4	4	8	4	4	4	1	1	0
5^{th}	8	8	8	1	4	8	8	8	4	8	8	8	2	0	8
B_ϕ AREA															
1^{st}	0	0	0	0	0	0	8	4	4	0	0	0	0	4	0
2^{nd}	1	1	1	1	1	1	0	2	2	1	1	1	1	2	2
3^{rd}	2	2	2	2	2	2	1	1	1	2	2	2	2	1	1
4^{th}	4	4	4	4	4	4	4	0	0	4	4	4	8	0	4
5^{th}	8	8	8	8	8	8	2	8	8	8	8	8	4	8	8

DOI: 10.2312/GFZ.b103-08029

APPENDIX D

Plots of the Axial Moment Rate of Change

DOI: 10.2312/GFZ.b103-08029

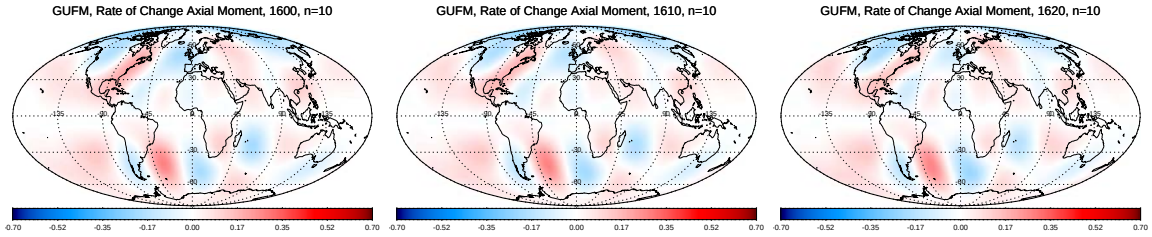

(a) 1600 (b) 1610 (c) 1620

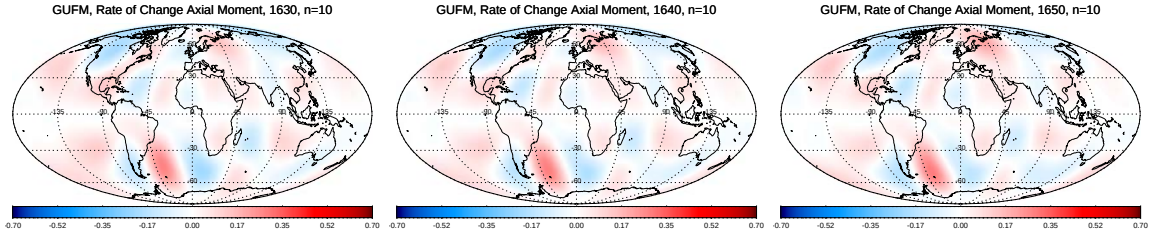

(d) 1630 (e) 1640 (f) 1650

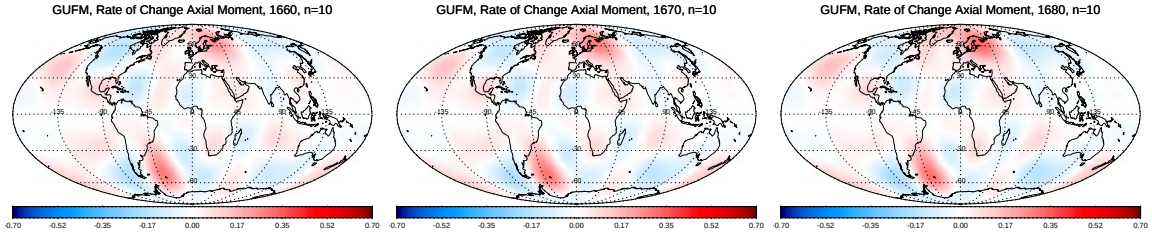

(g) 1660 (h) 1670 (i) 1680

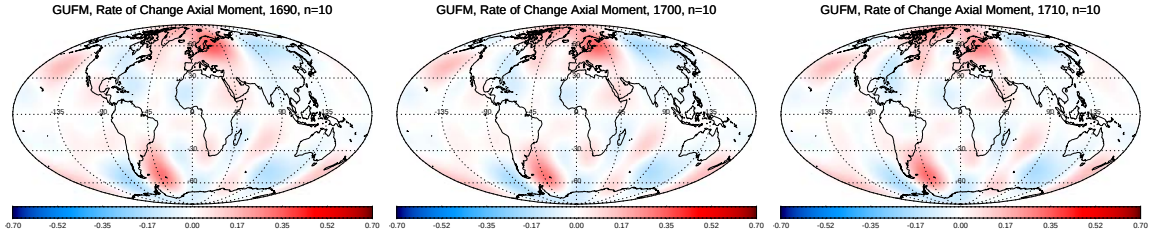

(j) 1690 (k) 1700 (l) 1710

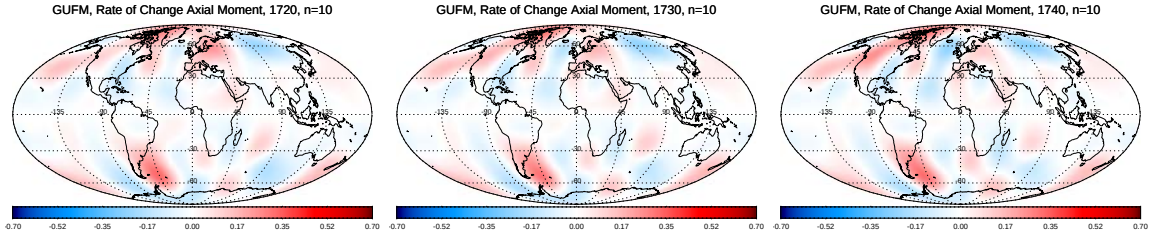

(m) 1720 (n) 1730 (o) 1740

Figure D.1: The gufm1 Rate of Change of the Axial Moment for every 10 years between 1600 and 1740 at the CMB for spherical harmonic degree n=10 in units of mT/century.

DOI: 10.2312/GFZ.b103-08029

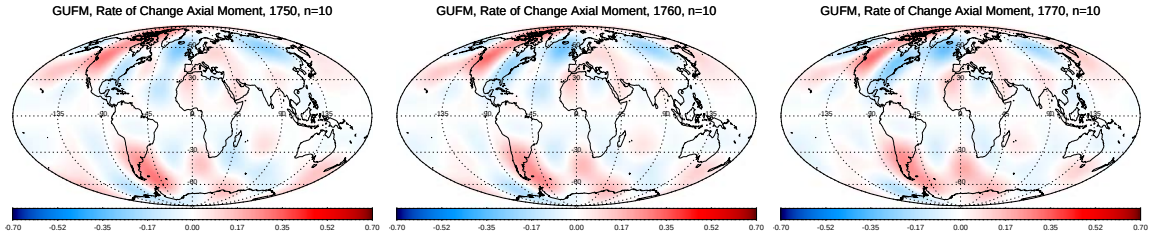

(a) 1750 (b) 1760 (c) 1770

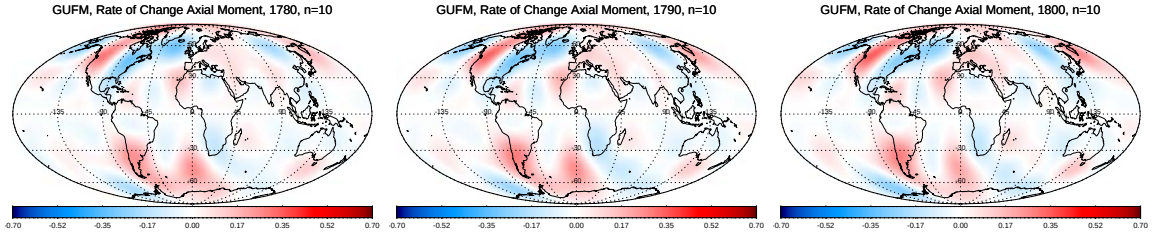

(d) 1780 (e) 1790 (f) 1800

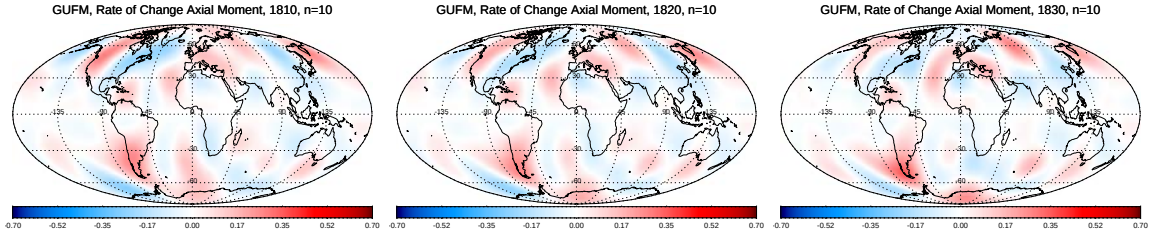

(g) 1810 (h) 1820 (i) 1830

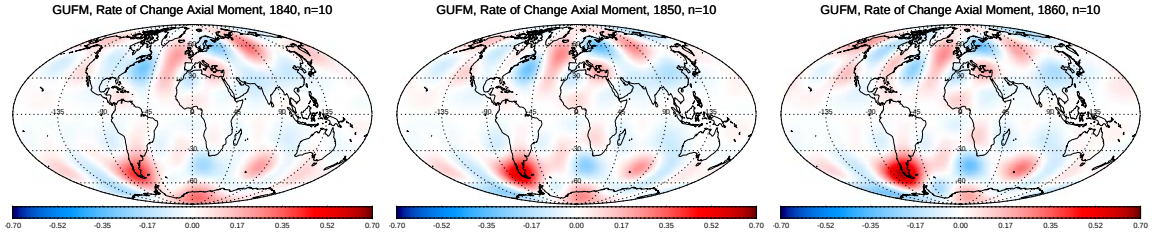

(j) 1840 (k) 1850 (l) 1860

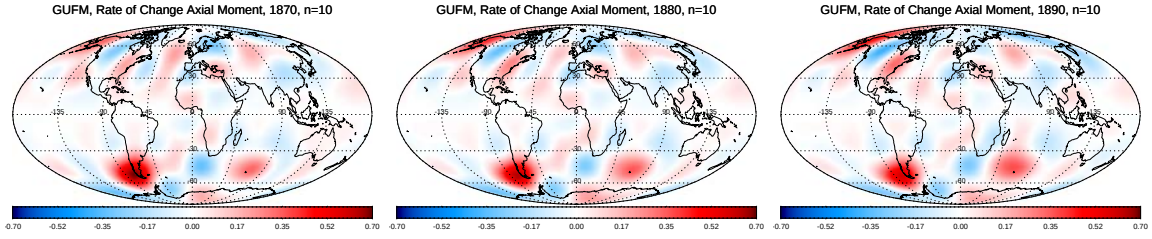

(m) 1870 (n) 1880 (o) 1890

Figure D.2: The gufm1 Rate of Change of the Axial Moment for every 10 years between 1750 and 1890 at the CMB for spherical harmonic degree n=10 in units of mT/century.

DOI: 10.2312/GFZ.b103-08029

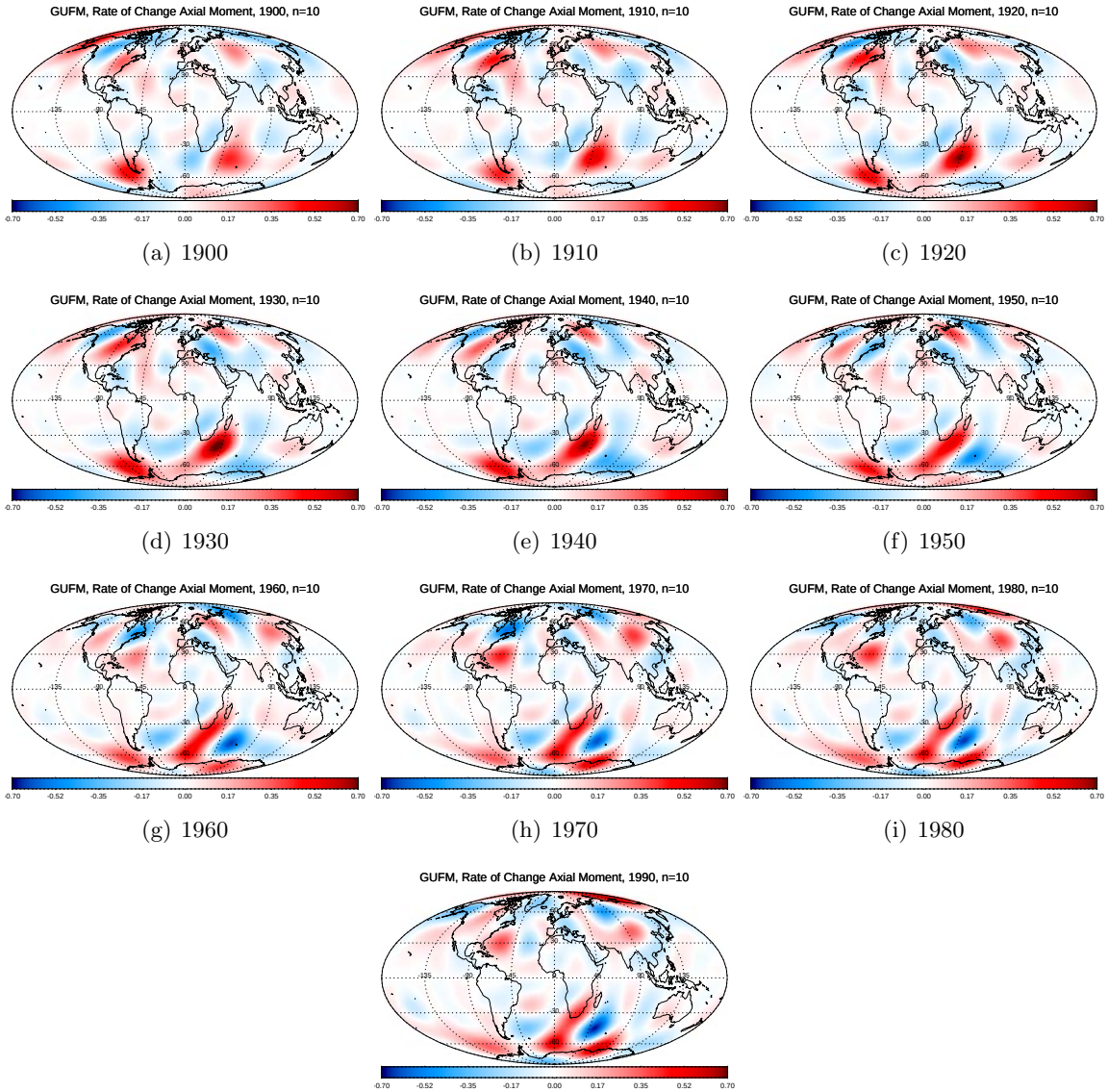

(a) 1900 (b) 1910 (c) 1920

(d) 1930 (e) 1940 (f) 1950

(g) 1960 (h) 1970 (i) 1980

(j) 1990

Figure D.3: The gufm1 Rate of Change of the Axial Dipole Moment for every 10 years between 1900 and 1990 at the CMB for spherical harmonic degree n=10 in units of mT/century.

DOI: 10.2312/GFZ.b103-08029

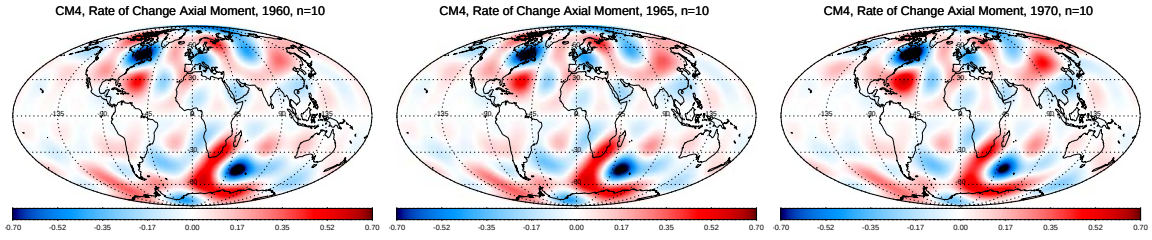

(a) CM4, 1960, n=10 (b) CM4, 1965, n=10 (c) CM4, 1970, n=10

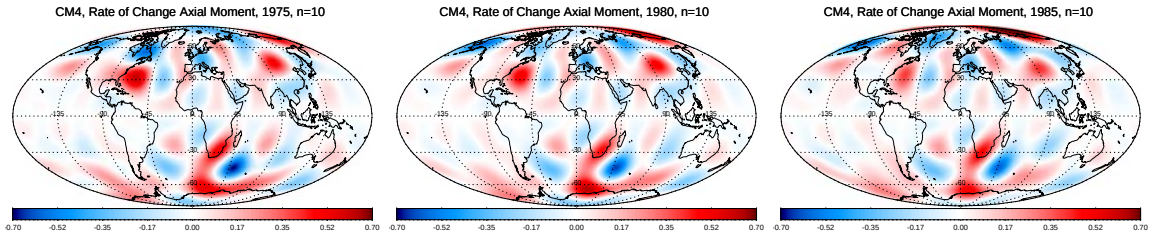

(d) CM4, 1975, n=10 (e) CM4, 1980, n=10 (f) CM4, 1985, n=10

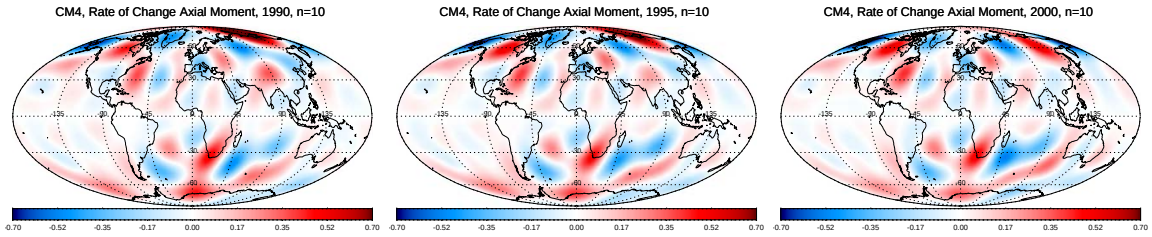

(g) CM4, 1990, n=10 (h) CM4, 1995, n=10 (i) CM4, 2000, n=10

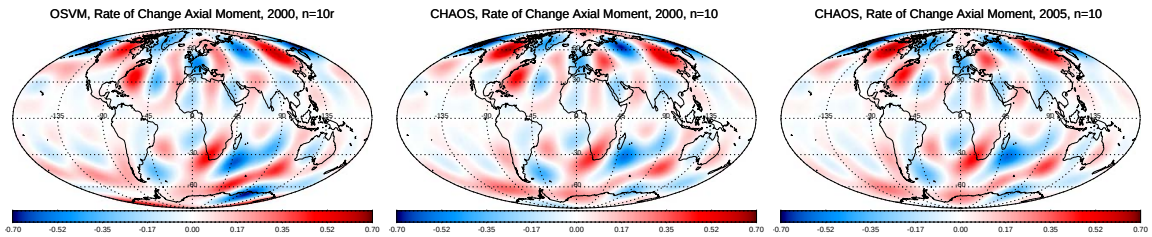

(j) OSVM, 2000, n=10 (k) CHAOS, 2000, n=10 (l) CHAOS, 2005, n=10

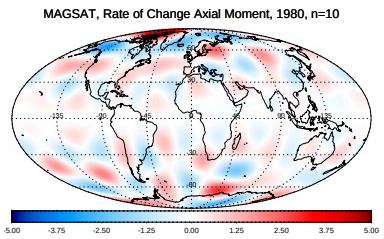

(m) Magsat, 1980, n=10

Figure D.4: Rate of Change of the Axial Dipole Moment for the CM4, CHAOS, OSVM and Magsat at the CMB for spherical harmonic degree n=10 in units of mT/century.

DOI: 10.2312/GFZ.b103-08029

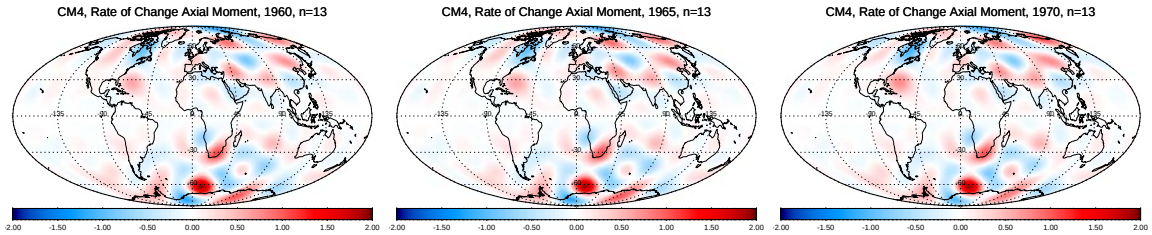

(a) CM4, 1960, n=13 (b) CM4, 1965, n=13 (c) CM4, 1970, n=13

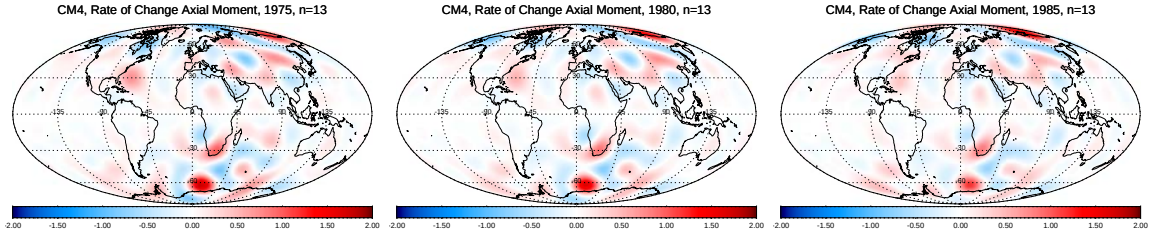

(d) CM4, 1975, n=13 (e) CM4, 1980, n=13 (f) CM4, 1985, n=13

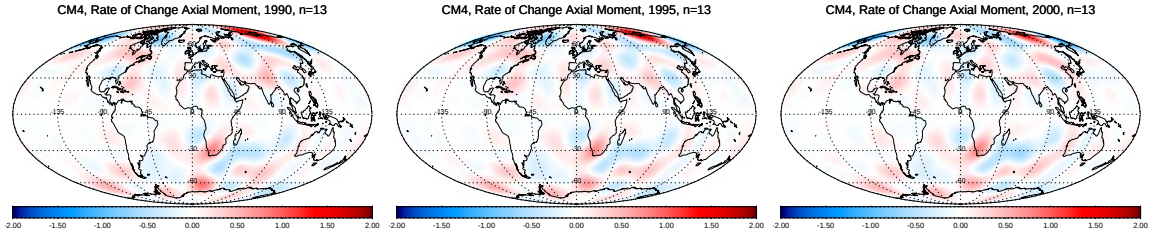

(g) CM4, 1990, n=13 (h) CM4, 1995, n=13 (i) CM4, 2000, n=13

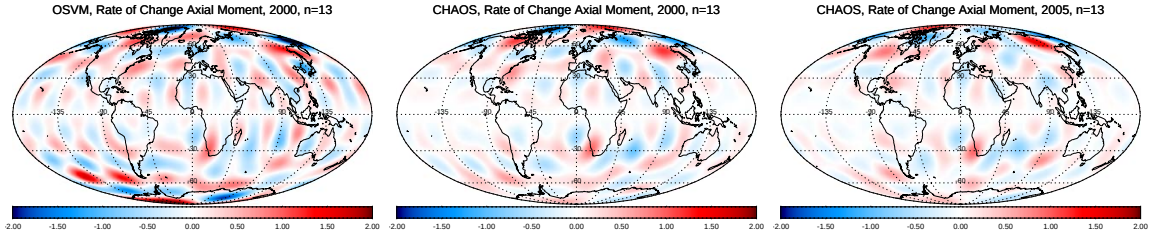

(j) OSVM, 2000, n=13 (k) CHAOS, 2000, n=13 (l) CHAOS, 2005, n=13

Figure D.5: Rate of Change of the Axial Dipole Moment for the CM4, CHAOS, OSVM and Magsat at the CMB for spherical harmonic degree n=13 in units of mT/century.

DOI: 10.2312/GFZ.b103-08029

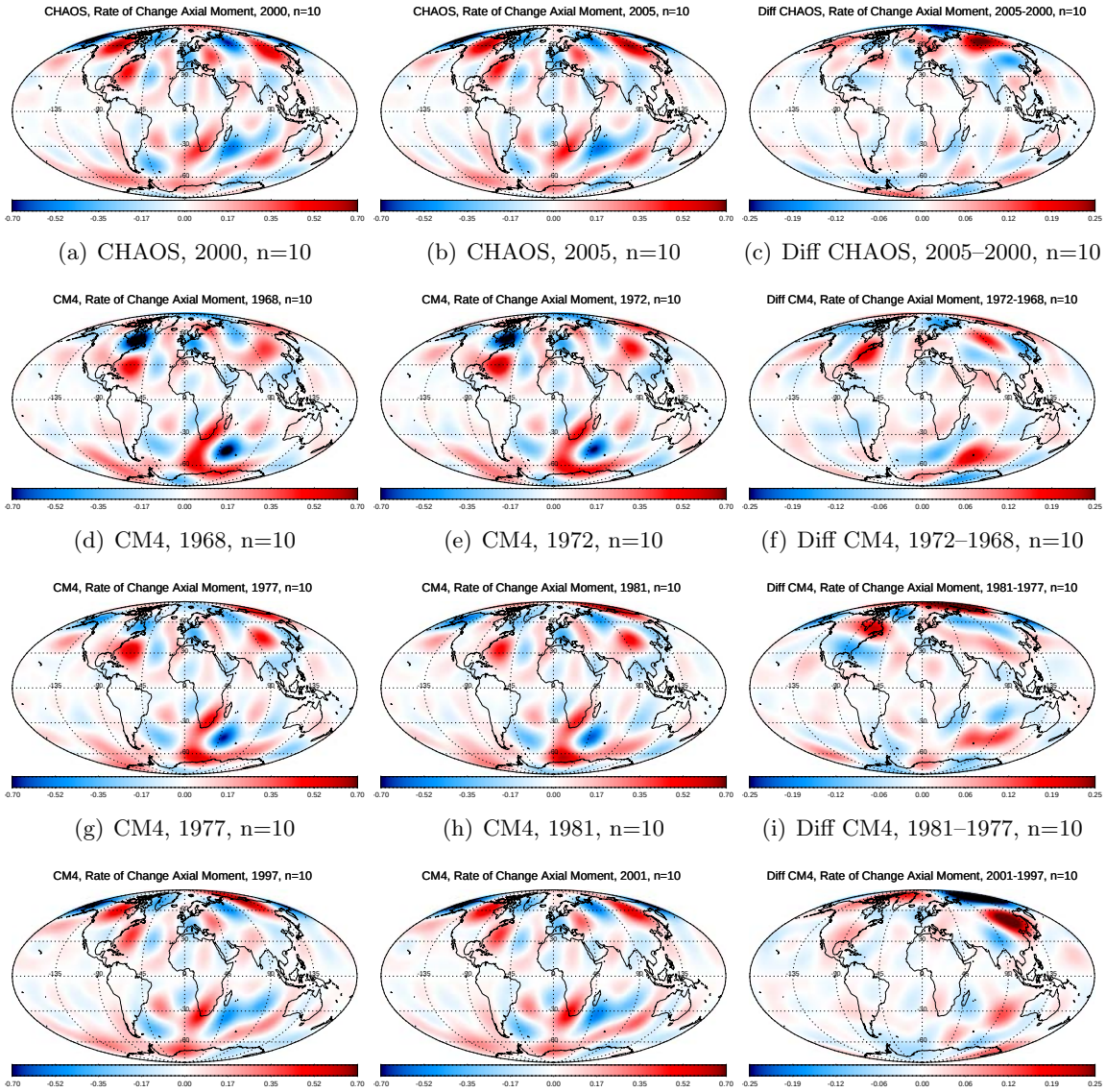

(a) CHAOS, 2000, n=10 (b) CHAOS, 2005, n=10 (c) Diff CHAOS, 2005–2000, n=10

(d) CM4, 1968, n=10 (e) CM4, 1972, n=10 (f) Diff CM4, 1972–1968, n=10

(g) CM4, 1977, n=10 (h) CM4, 1981, n=10 (i) Diff CM4, 1981–1977, n=10

(j) CM4, 1997, n=10 (k) CM4, 2001, n=10 (l) Diff CM4, 2001–1997, n=10

Figure D.6: The Rate of Change of the Axial Dipole Moment for CHAOS and CM4 models and the difference at the CMB for spherical harmonic degree n=10 in units of mT/century.

DOI: 10.2312/GFZ.b103-08029

REFERENCES

[1] R. T. Merrill, M. W. McElhinny, and P. L. McFadden. *The magnetic field of the Earth – International Geophysics Series, vol 63*. Academic Press, San Diego CA, 1998. 1.1, 1.3, 1.5.1

[2] P. H. Roberts and G. A. Glatzmaier. The Geodynamo, Past, Present and Future. *Geophys. Astrophys. Fluid Dynamics*, 94:47–84, 2001. 1.1

[3] G. Glatzmaier and P. Roberts. Simulating the geodynamo. *Contemporary Physics*, 38(4):269–288, 1997. 1.1

[4] P. Roberts and G. Glatzmaier. Geodynamo theory and simulations. *Rev. Mod. Phys.*, 72(4):1081–1123, 2000. 1.1, 3.6

[5] R. H. Tyler, S. Maus, and H. Lühr. Satellite observations of magnetic fields due to ocean tidal flow. *Science*, 299:239–241, 2003. 1.1

[6] A. D. Richmond, E. C. Ridley, and R. G. Roble. A thermosphere ionosphere general circulation model with coupled electrodynamics. *Geophys. Res. Letts.*, 19:601–604, 1992. 1.1, 1.7.2, 2.1, 2.1.1

[7] N. Olsen, H. Lühr, T. J. Sabaka, M. Mandea, M. Rother, L. Tøffner-Clausen, and S. Choi. CHAOS – A Model of Earth's Magnetic Field derived from CHAMP, Ørsted, and SAC–C magnetic satellite data. *Geophys. J. Int.*, 166:67–75, 2006. 1.1, 1.4.2, 1.7.2, 2.1, 2.1.2, 3.3

[8] A. Jackson, A. R. T. Jonkers, and M. R. Walker. Four centuries of geomagnetic secular variation from historical records. *Philos. Trans. R. Soc. Lond.*, 358:957–990, 2000. 1.1, 1.4, 1.5.1, 1.7.2, 3.3, 3.5, 3.6

[9] L. J. Lanzerotti, R. A. Langel, and A. D. Chave. Geoelectromagnetism. In G. L. Trigg, editor, *Encyclopedia of Applied Physics, Vol 7*, pages 109–123. VCH Publishers, New York, 1993. 1.1, 1.5.2

[10] M. M. Walker, T. E. Dennis, and J. L. Kirschvink. The magnetic sense and its use in long-distance navigation by animals. *Curr. Opin. Neurobiol.*, 12:735–744, 2002. 1.1, 1.2

[11] J. C. Cain and R. Sweeney. The POGO data. *J. Atmos. and Terr. Phys.*, 35:1231, 1973. 1.2, 1.4.2

[12] R. A. Langel and R. H. Estes. The near-Earth magnetic field at 1980 determined from MAGSAT data. *J. Geophys. Res.*, 90:2495–2509, 1985. 1.2, 1.4.2

DOI: 10.2312/GFZ.b103-08029

[13] T. Neubert, M. Mandea, G. Hulot, R. von Frese, F. Primdahl, J. L. Jørgensen, E. Friis-Christensen, P. Stauning, N. Olsen, and T. Risbo. Ørsted Satellite Captures High-Precision Geomagnetic Field Data. *Eos Trans. AGU*, 82(7):81, 2001. 1.2, 1.4.2

[14] C. Reigber, H. Lühr, and P. Schwintzer. CHAMP Mission Status. *Adv. Space Res.*, 30(2):129–134, 2002. 1.2, 1.4.2

[15] CONAE. SAC–C.
http://www.conae.gov.ar/sac-c/, 2007. 1.2

[16] J. C. Cain, B. B. Ferguson, and D. T. Mozzoni. An n = 90 internal potential function of the Martian crustal magnetic field. *J. Geophys. Res.*, 108(E2):5008, 2003. 1.2, 1.21, 1.7.1

[17] G. Backus, R. Parker, and C. Constable. *Foundations of Geomagnetism*. Cambridge University Press, Cambridge, 1996. 1.3, 1.5.2, 1.6.2

[18] C. T. Russell. A brief history of solar-terrestrial physics. In M. G. Kivelson and C. T. Russell, editors, *Introduction to Space Physics*, pages 1–26. Cambridge University Press, Cambridge, 1995. 1.3, 1.13, 1.14

[19] P. J. Smith and J. Needham. Magnetic Declination in Mediaeval China. *Nature*, 214:1213–1214, 1967. 1.3

[20] P. J. Smith. Pre-Gilbertian conceptions of terrestrial magnetism. *Tectonophysics*, 6:499–510, 1968. 1.3

[21] S. Pumfrey. William Gilbert. In P. Harman and S. Mitton, editors, *Cambridge Scientific Minds*, pages 6–20. Cambridge University Press, Cambridge, 2002. 1.3

[22] William Gilbert. On the Magnet by William Gilbert translated by Silvanus Thompson for the Gilbert Club of London.
http://rack1.ul.cs.cmu.edu/is/gilbert/, 2007. 1.3

[23] D. P. Stern. A Millennium of Geomagnetism. *Rev. Geophys.*, 40(3):1–30, 2002. 1.3, 1.5.2

[24] R. J. Walker and C. T. Russell. Solar-wind interactions with magnetized planets. In M. G. Kivelson and C. T. Russell, editors, *Introduction to Space Physics*, pages 164–182. Cambridge University Press, Cambridge, 1995. 1.3

[25] M. Alexandrescu, V. Courtillot, and J.-L. Le Mouël. High-resolution secular variation of the geomagnetic field in western Europe over the last 4 centuries: Comparison and integration of historical data from Paris and London. *J. Geophys. Res.*, 102(B9):20245–20258, 1997. 1.4, 3.7

[26] M. Korte, C.G. Constable, A. Genevey, U. Frank, and E. Schnepp. Continuous geomagnetic field models for the past 7 millennia: 1. A new global data compilation. *Geochem., Geophys., Geosys.*, 6:Q02H15, 2005. 1.4, 1.5.1, 1.7.2, 3.3

[27] A. Jonkers, A. Jackson, and A. Murray. Four centuries of geomagnetic data from historical records. *Rev. Geophys.*, 41(2):1006, 2003. 1.4, 1.7.2, 3.3

DOI: 10.2312/GFZ.b103-08029

[28] M. Mandea. Magnetic satellite missions: where have we been and where are we going? *C. R. Geoscience*, 338:1002–1011, 2006. 1.4, 3.7

[29] INTERMAGNET. Participating Observatories (Map). http://www.intermagnet.org, 2007. 1.4.1, 1.4

[30] M. Mandea and N. Olsen. A new approach to directly determine the secular variation from magnetic satellite observations. *Geophys. Res. Lett.*, 33:L15306, 2006. 1.4.1

[31] R. Regan. The Reduction and Analysis of Satellite Magnetometer Data. *J. Geophys. Res.*, 3(4):331–349, 1979. 1.4.2

[32] N. Olsen, R. Holme, G. Hulot, T. Sabaka, T. Neubert, L. Tøffner-Clausen, F. Primdahl, J. Jørgensen, J.-M. Léger, D. Barraclough, J. Bloxham, J. Cain, C. Constable, V. Golovkov, A. Jackson, P. Kotzé, B. Langlais, S. Macmillan, M. Mandea, J. Merayo, L. Newitt, M. Purucker, T. Risbo, M. Stampe, A. Thomson, and C. Voorhies. Ørsted Initial Field Model. *Geophys. Res. Lett.*, 27(22):3607–3610, 2000. 1.4.2

[33] N. Olsen. A Model of the Geomagnetic Field and its Secular Variation for Epoch 2000. *Geophys. J. Int.*, 149(2):454–462, 2002. 1.4.2, 3.5, 3.7

[34] GeoForschungsZentrum Potsdam. GFZ's Challenging Minisatellite Payload for Geophysical Research and Application (CHAMP) Home Page. http://www.gfz-potsdam.de/pb1/op/champ/index_CHAMP.html, 2006. 1.4.2, 1.4.2, 1.5, 1.6

[35] S. Maus, M. Rother, C. Stolle, W. Mai, S. Choi, H. Lühr, D. Cooke, and C. Roth. Third generation of the Potsdam Magnetic Model of the Earth (POMME). *Geochem. Geophys. Geosyst.*, 7(7):Q07008, 2006. 1.4.2

[36] S. Maus, M. Rother, K. Hemant, C. Stolle, H. Lühr, A. Kuvshinov, and N. Olsen. Earth's lithospheric magnetic field determined to spherical harmonic degree 90 from CHAMP satellite measurements. *Geophys. J. Int.*, 164:319–330, 2006. 1.4.2

[37] S. Maus, H. Lühr, M. Rother, K. Hemant, G. Balasis, P. Ritter, and C. Stolle. Fifth-generation lithospheric magnetic field model from CHAMP satellite measurements. *Geochem. Geophys. Geosyst.*, 8:Q05013, 2007. 1.4.2

[38] M. Mandea and M. Purucker. Observing, Modeling, and Interpreting Magnetic Fields of the Solid Earth. *Surveys in Geophysics*, 26(4):415–459, 2005. 1.7

[39] GeoForschungsZentrum Potsdam. History of Adolf-Schmidt-Observatory. http://www.gfz-potsdam.de/pb2/pb23/Niemegk/en, 2007. 1.9

[40] L. Newitt, M. Mandea, L. McKee, and J. Orgeval. Recent Acceleration of the North Magnetic Pole Linked to Magnetic Jerks. *Eos Trans. AGU*, 83:381–388, 2002. 1.5.1

[41] N. Olsen and M. Mandea. Will the Magnetic North Pole wind up in Siberia? *Eos Trans. AGU*, 88(29):293, 2007. 1.5.1

[42] D. Gubbins, A. L. Jones, and C. C. Finlay. Fall in Earth's Magnetic Field is Erratic. *Science*, 312:900–902, 2006. 1.5.1

DOI: 10.2312/GFZ.b103-08029

[43] British Geological Survey. The Earth's Magnetic Field - An Overview. http://www.geomag.bgs.ac.uk/earthmag.html, 2007. 1.10

[44] S. Macmillan. A geomagnetic jerk for the early 1990's. *Earth Planet. Sci. Lett.*, 137:189–192, 1996. 1.5.1

[45] S. Zatman J. Bloxham and M. Dumberry. The origin of geomagnetic jerks. *Nature*, 420:65–68, 2002. 1.5.1, 3.7

[46] R. Holme and O. de Viron. Geomagnetic jerks and a high-resolution length-of-day profile for core studies. *Geophys. J. Int.*, 160(3):435–439, 2005. 1.5.1

[47] GeoForschungsZentrum Potsdam. Magnetic Field Model MF5. http://www.gfz-potsdam.de/pb2/pb23/SatMag/litmod5.html, 2006. 1.12

[48] M. Hamoudi, E. Thébault, V. Lesur, and M. Mandea. GeoForschungsZentrum Anomaly Magnetic Map (GAMMA): A candidate model for the World Digital Magnetic Anomaly Map. *Geochem. Geophys. Geosyst.*, 8:Q06023, 2007. 1.5.1

[49] S. Maus, T. Sazonova, K. Hemant, J. D. Fairhead, and D. Ravat. National Geophysical Data Center candidate for the World Digital Magnetic Anomaly Map. *Geochem. Geophys. Geosyst.*, 8:Q06017, 2007. 1.5.1

[50] Southwest Research Institute. IMAGE Glossary Website. http://pluto.space.swri.edu/IMAGE/glossary/glossary_intro.html, 2003. 1.5.2, 1.5.2

[51] W. D. Gonzalez, J. A. Joselyn, Y. Kamide, H. W. Kroehl, G. Rostoker, B. T. Tsurutani, and V. M. Vasyliunas. What is a geomagnetic storm? *J. Geophys. Res.*, 99(A4):5771–5792, 1994. 1.5.2

[52] T. P. O'Brien and R. L. McPherron. Forecasting the ring current index dst in real time. *Journal of Atmospheric and Solar-Terrestrial Physics*, 62(14):1295–1299, 2000. 1.5.2, 1.5.3

[53] J. G. Luhmann. Ionospheres. In M. G. Kivelson and C. T. Russell, editors, *Introduction to Space Physics*, pages 183–202. Cambridge University Press, Cambridge, 1995. 1.5.2

[54] M. Menvielle. Derivation and dissemination of geomagnetic indices. *Revista geofisica*, 48:51–66, 1998. 1.5.3

[55] GeoForschungsZentrum Potsdam. Indices of Global Geomagnetic Activity. http://www.gfz-potsdam.de/pb2/pb23/GeoMag/niemegk/kp_index, 2006. 1.16, 1.5.3

[56] J. Bartels, N. H. Heck, and H. F. Johnston. The three-hour-range index measuring geomagnetic activity. *J. Geophys. Res.*, 44:411–454, 1939. 1.5.3

[57] J. Reda and J. Jankowski. Three-hour activity index based on power spectra estimation. *Geophys. J. Int.*, 157(1):141–146, 2004. 1.5.3

[58] R. L. McPherron. Magnetospheric Dynamics. In M. G. Kivelson and C. T. Russell, editors, *Introduction to Space Physics*, pages 1–26. Cambridge University Press, Cambridge, 1995. 1.5.3, 1.5.3, 2.4, 2.3

DOI: 10.2312/GFZ.b103-08029

[59] The Dominion Radio Astrophysical Observatory. Solar radio monitoring programme. http://www.drao-ofr.hia-iha.nrc-cnrc.gc.ca, 2006. 1.5.3

[60] GeoForschungsZentrum Potsdam. International Q-Days and D-Days. http://www.gfz-potsdam.de/pb2/pb23/niemegk/kp_index/quietdst, 2006. 1.5.3

[61] Kyoto World Data Center for Geomagnetism. Geomagnetic Data Service. http://swdcwww.kugi.kyoto-u.ac.jp/index.html, 2007. 1.17

[62] M. Sugiura. Hourly values of equatorial Dst for the International Geophysical Year. *Ann. Int. Geophys. Year*, 35:945–948, 1964. 1.5.3

[63] W. H. Campbell. Geomagnetic storms, the Dst ring-current myth and lognormal distributions. *J. Atmos. Terr. Phys.*, 58(10):1171–1187, 1996. 1.5.3

[64] USGS National Geomagnetism Program. A Brief Introduction to Geomagnetism. http://geomag.usgs.gov/intro.php, 2007. 1.18

[65] A. D. Richmond. Ionospheric electrodynamics using magnetic apex coordinates. *J. Geomagn. Geoelectr.*, 47:191–212, 1995. 1.6.1, 2.1.1, 2.1.1, 2.5

[66] T. E. VanZandt, W. L. Clark, and J. M. Warnock. Magnetic apex coordinates: A magnetic coordinate system for the ionospheric F2 layer. *J. Geophys. Res.*, 77:2406–2411, 1972. 1.6.1

[67] M. Mandea. Main Field Modelling. In D. Gubbins and E. Herrero-Bervera, editors, *Encyclopaedia of Geomagnetism and Paleomagnetism*, pages 679–683. Springer, 2007. 1.6.2

[68] R. A. Langel. The Main Field. In J. A. Jacobs, editor, *Geomagnetism, vol. 1, chap. 4*, pages 249–512. Academic Press, London, 1987. 1.6.2

[69] J. C. Cain, B. Holter, and D. Sandee. Numerical experiments in geomagnetic modeling. *J. Geomagn. Geoelectr.*, 42(9):973–987, 1990. 1.6.2, 3.5

[70] F. J. Lowes. Spacial power spectrum of the main geomagnetic field and extrapolation to the core. *Geophysical Journal of the Royal Society*, 36:717–730, 1974. 1.6.2

[71] J. C. Cain, D. T. Mozzoni, B. B. Ferguson, and O. Ajayi. Geomagnetic secular variation 1995-2000. *J. Geophys. Res.*, 108(B3):2161, 2003. 1.7.1, 2.8.2

[72] M. Purucker. Personal communication, 2003. 1.21

[73] A. D. Richmond. Modeling the Ionosphere Wind Dynamo: A Review. *PAGEOPH*, 131(3):413–435, 1989. 1.7.2, 2.1.1

[74] T. J. Sabaka, N. Olsen, and M. E. Purucker. Extending comprehensive models of the Earth's magnetic field with Ørsted and CHAMP data. *Geophys. J. Int.*, 159:521–547, 2004. 1.7.2, 3.3

[75] S. Maus, S. Macmillan, T. Chernova, S. Choi, D. Dater, V. Golovkov, V. Lesur, F. Lowes, H. Lühr, W. Mai, S. McLean, N. Olsen, M. Rother, T. Sabaka, A. Thomson, and T. Zvereva. The 10th-Generation International Geomagnetic Reference Field. *Geophys. J. Int.*, 161:561–565, 2005. 1.7.2, 2.1.1, 3.3

DOI: 10.2312/GFZ.b103-08029

[76] M. Korte and C.G. Constable. Continuous geomagnetic field models for the past 7 millennia: 2. CALS7K. *Geochem., Geophys., Geosys.*, 6:Q02H16, 2005. 1.7.2, 3.3

[77] D. Mozzoni, M. Mandea, and J. C. Cain. CHAMP and TIE-GCM magnetic perturbation comparisons. In *Proceedings of the First Swarm International Science Meeting 3-5 May 2006, Nantes, France (ESA WPP-261, July 2006)*, page 112. ESA, 2006. 2.1

[78] D. T. Mozzoni, M. Mandea, and J. Cain. Magnetic perturbations seen by CHAMP and evaluated using the TIE–GCM. *Ann. Geophys.*, 25:1543–1554, 2007. 2.1

[79] M. E. Hagan and J. M. Forbes. Migrating and nonmigrating diurnal tides in the middle and upper atmosphere excited by tropospheric latent heat release. *J. Geophys. Res.*, 107(D24):4754, 2002. 2.1.1

[80] M. E. Hagan and J. M. Forbes. Migrating and nonmigrating semidiurnal tides in the upper atmosphere excited by tropospheric latent heat release. *J. Geophys. Res.*, 108(A2):1062, 2003. 2.1.1

[81] A. Maute, A. Richmond, T. Sabaka, and N. Olsen. Comparison of ionospheric dynamo currents and magnetic perturbations modeled by the TIEGCM with CM3e model results. In *EGS-AGU-EUG Joint Assembly 6-11 April 2003, Nice, France (EAE03-A-04686)*, 2003. 2.1.1, 2.3

[82] GeoForschungsZentrum Potsdam. CHAOS - A Model of Earth's Magnetic Field derived from CHAMP, /Orsted, and SAC-C magnetic satellite data. http://www.gfz-potsdam.de/pb2/pb23/Models/CHAOS/index.html, 2007. 2.1.2

[83] Danish National Space Center. CHAOS - A Model of Earth's Magnetic Field derived from CHAMP, /Orsted, and SAC-C magnetic satellite data. http://www.spacecenter.dk/files/magnetic-models/CHAOS/, 2007. 2.1.2

[84] P. K. Seidelmann. *Explanatory Supplement to the Astronomical Almanac*. University Science Books, Sausalito CA, 2005. 2.2

[85] G. Moyer. The Origin of the Julian Day System. *Sky and Telescope*, 61:311–313, 1981. 2.2

[86] R. A. Heelis, P. C. Kendall, R. J. Moffett, D. W. Windle, and H. Rishbeth. Electrical coupling of the E- and F-regions and its effect on F-region drifts and winds. *Planet. Space Sci.*, 22(5):743–756, 1974. 2.3

[87] W. D. Parkinson. *Introduction to Geomagnetism*. Scottish Academic Press, Edinburgh, 1983. 2.3

[88] A. D. Richmond. Ionospheric Electrodynamics. In H. Volland, editor, *Handbook of Atmospheric Electrodynamics, Volume II*, pages 249–290. CRC Press, Boca Raton, 1995. 2.4

[89] A. D. Richmond. Modeling the geomagnetic perturbations produced by ionospheric currents, above and below the ionosphere. *J. Geodyn.*, 33:143–156, 2002. 2.5

DOI: 10.2312/GFZ.b103-08029

[90] A. I. Maute, A. D. Richmond, M. E. Hagan, and R. G. Roble. Ionospheric Dynamo Currents and Magnetic Perturbations at the Ground and Above the Ionosphere Modeled by the TIEGCM. In *American Geophysical Union - Fall Meeting 6-10 December 2002, San Francisco, USA (SA72B-0525)*, 2002. 2.5

[91] A. D. Richmond. The computation of magnetic effects of field-aligned magnetospheric currents. *J. Atmos. Terr. Phys.*, 36:245–252, 1974. 2.5

[92] V. Lesur. Personal communication, 2006. 2.8.1

[93] M. Mandea, M. Korte, D. Mozzoni, and P. Kotzé. The magnetic field changing over the southern African continent: a unique behaviour. *accepted by South African Journal of Geology*, accepted. 3, 3.6

[94] D. T. Mozzoni and M. Mandea. Total Unsigned Flux Evolution at the Core-Mantle Boundary and Geomagnetic Jerks. *submitted to Geophys. Res. Lett.*, 2007. 3

[95] National Oceanic and Atmospheric Administration. Relative Intensities of NOAA POES Energetic Particles.
poes.ngdc.noaa.gov, 2006. 3.1

[96] European Space Agency Space Environments and Effects. The Radiation Environment.
http://image.gsfc.nasa.gov/poetry/tour/vanallen.html, 2006. 3.2

[97] J. K. Hargreaves. *The Solar-Terrestrial Environment: An Introduction to Geospace - the Science of the Terrestrial Upper Atmosphere, Ionosphere, and Magnetosphere*. Cambridge University Press, Cambridge, 1992. 3.1

[98] P. Olson and H. Amit. Changes in earth's dipole. *Naturwissenschaften*, 93:519–542, 2006. 3.1, 3.5, 3.5, 3.5

[99] O. Pinto, W. D. Gonzalez, I. R. C. A. Pinto, A. L. C. Gonzalez, and O. Mendes. The South Atlantic Magnetic Anomaly: three decades of research. *J. Atmos. Terr. Phys.*, 54:1129–1134, 1992. 3.1, 3.4, 3.4

[100] J. R. Heirtzler. The future of the South Atlantic anomaly and implications for radiation damage in space. *J. Atmos. Solar Terr. Phys.*, 64:1701–1708, 2002. 3.1, 3.4

[101] G. D. Badhwar. Drift rate of the South Atlantic Anomaly. *J. Geophys. Res.*, 102(A2):2343–2350, 1997. 3.1, 3.4

[102] J. Lean. Living with a variable sun. *Phys Today*, 58(6):32–38, 2005. 3.1

[103] J. R. Heirtzler, J. H. Allen, and D. C. Wilkinson. Ever-present South Atlantic anomaly damages spacecraft. *Eos Trans. AGU*, 83(15):165, 2002. 3.1

[104] M. J. Golightly, K. Hardy, and W. Quam. Radiation dosimetry measurements during U.S. space shuttle missions with the RME-III. *Radiation Measurement*, 23(1):25–42, 1994. 3.1

[105] T. J. Sabaka, N. Olsen, and R. A. Langel. A comprehensive model of the quiet-time, near-Earth magnetic field: phase 3. *Geophys. J. Int.*, 151(1):32–68, 2002. 3.3

DOI: 10.2312/GFZ.b103-08029

[106] IAGA Division V-MOD. International Geomagnetic Reference Field. http://www.ngdc.noaa.gov/IAGA/vmod/igrf.html, 2007. 3.3

[107] M. Korte and C.G. Constable. Continuous global geomagnetic field models for the past 3000 years. *Phys. Earth Planet. Inter.*, 140:73–89, 2003. 3.3

[108] S. Chapman and J. Bartels. *Geomagnetism*. Oxford University Press, London, 1940. 3.4

[109] D. Heynderickx. Comparison between methods to compensate for the secular motion of the South Atlantic anomaly. *Radiation Measurement*, 26(3):369–372, 1996. 3.4

[110] SIDC-team. The International Sunspot Number. *Monthly Report on the International Sunspot Number, online catalogue*, 1770-2007. 3.4

[111] I. G. Usoskin, S. K. Solanki, and M. Korte. Solar activity reconstructed over the last 7000 years: The influence of geomagnetic field change. *Geophys. Res. Lett.*, 33(8):L08103, 2006. 3.4, 3.4

[112] J. Zhang, X. Song, Y. Li, P. G. Richards, X. Sun, and F. Waldhauser. Inner Core Differential Motion Confirmed by Earthquake Waveform Doublets. *Science*, 309:1357–1360, 2005. 3.4

[113] Z. G. Wei and W. Y. Xu. Westward drift in secular variation of the main geomagnetic field inferred from IGRF. *Earth Planets Space*, 55:131–137, 2003. 3.4

[114] A. I. Laptukhov. Mechanism of the Effect of Solar Activity on the Speed of the Daily Rotation of the Earth. *Geomagnetism and Aeronomy*, 20(4):465–467, 1980. 3.4

[115] Yu. D. Kalinin and V. M. Kiselev. Relation between Geomagnetic Activity, Solar-Wind Velocity, and the Irregular Daily Rotation of the Earth. *Geomagnetism and Aeronomy*, 20(6):702–704, 1980. 3.4

[116] R. Hide. How to locate the electrically conducting fluid core of a planet from external magnetic observations. *Nature*, 271:640–641, 1978. 3.6

[117] E. Benton. Magnetic probing of planetary interiors. *Physics of The Earth and Planetary Interiors*, 20:111–118, 1979. 3.6

[118] R. Hide and S. R. C. Malin. On the determination of the size of the earth's core from observations of geomagnetic secular variation. *Proc. R. Soc. Lond. A*, 374:15–33, 1981. 3.6

[119] T. J. Shankland, J. Peyronneau, and J.-P. Poirier. Electrical conductivity of the Earth's lower mantle. *Nature*, 366:453–455, 1993. 3.6

[120] C. Finlay. Hydromagnetic waves in Earth's core and their influence on geomagnetic secular variation. *Thesis*, 2005. 3.6, 3.6

[121] J. Bloxham, D. Gubbins, and A. Jackson. Geomagnetic secular variation. *Phil. Trans. R. Soc. Lond. A*, 329(1606):415–502, 1989. 3.6

[122] D. Gubbins. Mechanism for geomagnetic polarity reversals. *Nature*, 326:167–169, 1987. 3.6

DOI: 10.2312/GFZ.b103-08029

[123] P. H. Roberts and S. Scott. On analysis of the secular variation (i) a hydromagnetic constraint: Theory. *J. Geomagn. Geoelectr.*, 17:137–151, 1965. 3.6

[124] R. Holme and N. Olsen. Core surface flow modelling from high-resolution secular variation. *Geophys. J. Int.*, 166(2):518–528, 2006. 3.6

[125] G. E. Backus. Kinematics of geomagnetic secular variation in a perfectly conducting core. *Phil. Trans. R. Soc. Lond.*, 263(1141):239–266, 1968. 3.6

[126] E. Dormy and M. Mandea. Tracking geomagnetic impulses down to the core-mantle boundary. *Earth Planet. Sci. Lett.*, 237:300–309, 2005. 3.6

[127] M. Mandea, E. Bellanger, and J.-L. Le Mouël. A geomagnetic jerk for the end of 20th century? *Earth Planet. Sci. Lett.*, 183:369–373, 2000. 3.6

[128] V. Courtillot, J. Ducruix, and J.-L. Le Mouël. Sur une accélérations récente de la variation séculaire du champ magnétique terrestre. *C.R. Acad. Sci. Paris*, D287:1095–1098, 1978. 3.7

[129] S. R. C. Malin and B. M. Hodder. Was the 1970 geomagnetic jerk of internal or external origin? *Nature*, 296:726–728, 1982. 3.7

[130] J. Gavoret, D. Gibert, M. Menvielle, and J.-L. Le Mouël. Long-term variations of the external and internal components of the earths magnetic field. *J. Geophys. Res.*, 91:4787–4796, 1986. 3.7

[131] D. Gubbins and L. Tomlinson. Secular variation from monthly means from Apia and Amberley magnetic observatories. *Geophys. J. Int.*, 86(2):603–616, 1986. 3.7

[132] M. Alexandrescu, D. Gibert, G. Hulot, J.-L. Le Mouël, and G. Saracco. Worldwide wavelet analysis of geomagnetic jerks. *J. Geophys. Res.*, 101(B10):21975–21994, 1996. 3.7

[133] P. De Michelis, R. Tozzi, and A. Meloni. Geomagnetic jerks: observation and theoretical modeling. *Mem. S.A.It.*, 76:957–960, 2005. 3.7

[134] A. Chambodut and M. Mandea. Evidence for geomagnetic jerks in comprehensive models. *Earth Planets Space*, 57(2):139–149, 2005. 3.7

[135] N. Olsen and M. Mandea. Investigation of a secular variation impulse using satellite data: The 2003 geomagnetic jerk. *Earth and Planetary Science Letters*, 255:94–105, 2007. 3.7

[136] V. Courtillot, J.-L. Le Mouël, J. Ducruix, and A. Cazenave. Geomagnetic secular variation as a precursor of climatic change. *Nature*, 297:386–387, 1982. 3.7

[137] R. Schachtschneider, G. Balasis, M. Rother, and M. Mandea. Wavelet-based selection of satellite data for geomagnetic core field modeling. In *Proceedings of the First Swarm International Science Meeting 3-5 May 2006, Nantes, France (ESA WPP-261, July 2006)*, page 78. ESA, 2006. 4.1

[138] European Space Agency. ESA's magnetic field mission Swarm. http://www.esa.int/esaLP/ESA3QZJE43D_LPswarm_0.html, 2007. 4.1

DOI: 10.2312/GFZ.b103-08029

[139] E. Friis-Christensen, H. Lühr, and G. Hulot. Swarm: A constellation to study the Earth's magnetic field. *Earth Planets Space*, 58:351–358, 2006. 4.2

[140] H. J. Linthe, P. Kotzé, M. Mandea, and H. Theron. Keetmanshoop A New Observatory in Namibia. *Publs. Inst. Geophys. Pol. Acad. Sc.*, C-99:38–45, 2007. 4.2

[141] Florida State University. School of Computational Science. http://www.scs.fsu.edu, 2006. A.1

DOI: 10.2312/GFZ.b103-08029

BIOGRAPHICAL SKETCH

David T. Mozzoni

David T. Mozzoni was born August 21, 1976 in Warwick, Rhode Island. In the spring of 1999, he completed Bachelors degrees in Mathematics and Physics at The Florida State University. He enrolled in the doctoral program at FSU in the fall of 1999 and under the advisement of Prof. Joseph C. Cain, he obtained his Masters degree in fall 2005 from the Department of Physics.

DOI: 10.2312/GFZ.b103-08029